

NOVEL BIMETALLIC MESOPOROUS CATALYSTS FOR HYDROGEN PRODUCTION
THROUGH STEAM REFORMING OF ETHANOL

A THESIS SUBMITTED TO
THE GRADUATE SCHOOL OF NATURAL AND APPLIED SCIENCES
OF
MIDDLE EAST TECHNICAL UNIVERSITY

BY

CANAN ŞENER

IN PARTIAL FULFILLMENT OF THE REQUIREMENTS
FOR
THE DEGREE OF DOCTOR OF PHILOSOPHY
IN
CHEMICAL ENGINEERING

SEPTEMBER 2012

Approval of the thesis:

**NOVEL MESOPOROUS BIMETALLIC CATALYSTS FOR HYDROGEN PRODUCTION
THROUGH STEAM REFORMING OF ETHANOL**

submitted by **CANAN SENER** in partial fulfillment of the requirements for the degree of
**Doctor of Philosophy in Chemical Engineering Department, Middle East Technical
University** by,

Prof. Dr. Canan Özgen
Dean, Graduate School of **Natural and Applied Sciences**

Prof. Dr. Deniz Üner
Head of Department, **Chemical Engineering**

Prof. Dr. Timur Doğu
Supervisor, **Chemical Engineering Dept., METU**

Prof. Dr. Gulsen Dogu
Co-Supervisor, **Chemical Engineering Dept., Gazi University**

Examining Committee Members:

Prof. Dr. H. Önder Özbege
Chemical Engineering Dept., METU

Prof. Dr. Timur Doğu
Chemical Engineering Dept., METU

Prof. Dr. Nail Yasyerli
Chemical Engineering Dept., Gazi University

Assoc. Prof. Dr. Naime Asli Sezgi
Chemical Engineering Dept., METU

Assoc. Prof. Dr. Nuray Oktar
Advanced Technologies, Gazi University

Date: 12.09.2012

I hereby declare that all information in this document has been obtained and presented in accordance with academic rules and ethical conduct. I also declare that, as required by these rules and conduct, I have fully cited and referenced all material and results that are not original to this work.

Name, Last name : Canan Şener

Signature :

ABSTRACT

NOVEL BIMETALLIC MESOPOROUS CATALYSTS FOR HYDROGEN PRODUCTION THROUGH STEAM REFORMING OF ETHANOL

Şener, Canan

Ph.D., Department of Chemical Engineering

Supervisor: Prof. Dr. Timur Doğu

Co-Supervisor: Prof. Dr. Gülşen Doğu

September 2012, 208 pages

Hydrogen is considered as an alternative clean energy source due to the depletion of fossil fuels and related environmental problems. Steam reforming of bio-ethanol, has excellent potential for hydrogen production, with CO₂ neutrality. Ni, Pd and Pt are the most active metals for steam reforming of ethanol. Improving catalytic activity of supported Ni catalyst by incorporating small amount of Pd or Pt is a successful method for increasing activity and stability of the catalyst. Development of active and stable catalysts with low coke formation and high hydrogen yield attracted major attention of researchers in recent decades.

MCM-41 supported bimetallic mesoporous catalytic materials containing well dispersed Ni and Pd nanoballs were synthesized following an impregnation procedure. TEM images and XRD analysis of these materials indicated the formation of nickel and palladium nanoballs of 15-25 nm and 5-8 nm respectively, within the synthesized materials. These materials have quite narrow pore-size distributions in the range of 1-5 nm. In the calcined materials, nickel was in Ni⁺³ and Ni⁺² states, however in the reduced sample most of the nickel was in Ni⁰ state, together with some NiO. Formation of NiO_x crystals takes place after the calcination step. Impregnation of palladium into Ni/MCM-41 caused a decrease in the reduction temperature of NiO for about 50°C. Activity of the catalytic materials were tested in the reaction of steam reforming of ethanol. All the catalysts showed high conversion and quite high hydrogen yield over 400 °C. PdNi impregnated MCM-41 supported catalysts showed higher conversion of ethanol but lower hydrogen yield than Ni impregnated catalysts due to methane formation in the case of Pd incorporation.

However, MCM-41 does not show enough hydrothermal stability for steam reforming of ethanol reaction. SBA-15 has very similar physical properties of MCM-41 with larger pores and high hydrothermal stability. Ceria also has widespread applications in catalysis area with its excellent oxygen buffering capacity. It can be used as catalyst support and also an improving agent for silica supports.

Mesoporous silica SBA-15 with ordered pore structure was synthesized following a hydrothermal procedure and then bimetallic Ni-Ce and Pd-Ni-Ce incorporated mesoporous silica catalysts were prepared and tested in steam reforming of ethanol. On the other hand, ceria enriched silica structures i.e cerium/silicate composites were also synthesized. However the syntheses were unsuccessful due to the thermal sintering of ceria.

Addition of ceria to the support structure decreased coke formation significantly.. According to the thermal gravimetric analysis studies conducted after ethanol steam reformin reaction at 600 °C, coke formation with Ni-SBA-15 (Ni/Si=0.10) catalyst was 40% and it was 10% with NiCe-SBA-15 (Ni/Si=0.10, Ce/Si=0.50) Activity test results obtained with Ni incorporated silica catalysts in steam reforming of ethanol gave high hydrogen yield over 4 (max. 6) and complete conversion of ethanol at 600 °C. SBA-15 found to be more stable catalyst than MCM-41 in the steam reforming of ethanol reaction.

The highest hydrogen yield values were achieved by AIMCM-41 supported Ni-Ce impregnated catalysts. Aluminum in the silica matrix (3% wt.) increased the catalytic activity significantly, by giving acidic properties to the catalyst. Simultaneous and consecutive Ni and Ce impregnation were also examined. AIMCM-41 supported, consecutively Ce and Ni impregnated catalysts with Ce/Si and Ni.Si molar ratio sof 0.10, showed very high catalytic activity (5.8 at the beginning). AIMCM-41 supported catalyst were less stable because of high activity and consequently coke formation.

Keywords: Mesoporous, nanocomposite material, MCM-41, Pd-MCM-41, SBA-15, Mesoporous Cerium/Silica, Hydrogen Production, Ethanol Steam Reforming

ÖZ

ETANOLÜN SU BUHARI İLE REFORMLANMASI İLE HİDROJEN ÜRETİMİ İÇİN YENİ ÇİFT METALLİ MEZO-GÖZENEKLI KATALİZÖRLER

Şener, Canan

Yüksek Lisans, Kimya Mühendisliği Bölümü

Tez Yöneticisi: Prof. Dr. Timur Doğu

Ortak Tez Yöneticisi : Prof. Dr. Gülşen Doğu

Eylul 2012, 208 sayfa

Hidrojen, fosil yakıtların tükenişi ve buna bağılı çevre problemleri nedeniyle, yeni bir alternatif enerji kaynağı olarak kabul edilmektedir. Biyo-etanolun buharla reformlanması yüksek CO₂ nötrülüğü ile hidrojen üretimi için yüksek potansiyele sahiptir. Ni, Pd ve Pt metalleri, etanolün buhar reformlama reaksiyonu için en aktif metallerdir. Nikelin destek katalizörlere küçük miktarlarda Pd veya Pt eklenmesi, katalitik aktivitenin ve kararlılığın artırılması için başarılı bir yöntemdir. Düşük kok oluşumu ve yüksek hidrojen verimi gösteren aktif ve kararlı katalizörlerin geliştirilmesi son yıllarda araştırmacıların ilgisini çekmektedir.

Çift metalli, MCM-41 tipi, iyi dağılmış Ni ve Pd nano topları içeren mezogözenekli katalitik malzemelerin sentezi, emdirme teknikleriyle gerçekleştirilmiştir. Bu malzemelerin TEM fotoğrafları ve XRD analizleri, 15-25 nm ve 5-8 nm çaplarında Ni ve Pd nanotopları oluşumunu göstermiştir. Bu malzemeler, 1-5 nm aralığında çok dar gözenek boyut dağılımına sahiptir. Kalsine edilmiş örneklerde, nikelin oksitlenme seviyesi Ni⁺³ ve Ni⁺², indirgenmiş örneklerde ise çoğunlukla Ni⁰ mevcut iken Ni⁺² de bulunmaktadır. Kalsinasyon sonrasında NiO_x kristalleri oluşumu gerçekleşmiştir. Ni/MCM-41'e nikel emdirilmesi NiO'nin indirgenme sıcaklığında 50 °C'lik düşüşe neden olmuştur. Katalitik malzemelerin aktiviteleri etanolün su ile buharlanması reaksiyonunda test edilmiştir. Tüm katalizörler 400°C'nin üstünde yüksek dönüşüm ve yüksek hidrojen verimi göstermiştir. PdNi emdirilmiş MCM-41 ile desteklenmiş katalizörler yüksek dönüşüm göstermişlerdir, fakat Pd eklenmesindeki metan oluşumundan dolayı daha düşük hidrojen verimi göstermiştir.

MCM-41 etanolun buharla reformlanması reaksiyonu için yeterli hidrotermal kararlılığı gösterememektedir. SBA-15, MCM-41 ile çok benzer özellikler göstermektedir ve daha geniş gözenekler ile daha yüksek hidrotermal kararlılığa sahiptir. Seryumun mükemmel oksijen

tamponlama özelliği ile katalizör alanında çok farklı uygulamaları bulunmaktadır. Seryum hem kataliz destek malzemesi olarak hem de iyileştirici bir ajan olarak kullanılabilir.

Mezogözenekli silika bazlı ve düzenli gözenek yapılı SBA-15, hidrotermal sentez yöntemi takip edilerek hazırlanmış, Pd-Ni ve Pd-Ni-Ce ile emdirilmiş mezogözenekli silika katalizörleri hazırlanmış ve etanol buhar reformlama reaksiyonunda denemistir. Bir diğer yandan, seryum ile zenginleştirilmiş silika yapılar, yani seriya/silika kompozitler sentezlenmiştir. Ancak seriyanın termal sinterleşmesinden dolayı bu sentezler başarısız olmuştur.

Seryumun destek malzeme yapısına eklenmesiyle kok oluşumu ciddi şekilde düşmüştür. 600 °C'de gerçekleştirilen etanolun su buharı ile reformlanması reaksiyonu sonrası yapılan termal gravimetrik analizler, Ni-SBA-15 (Ni/Si=0.10) katalizöründe kok oluşumunu %40 iken NiCe-SBA-15 (Ni/Si=0.10, Ce/Si=0.50) katalizöründe %10 olduğunu göstermiştir. NiCe emdirilmiş silika katalizörlerle yürütülen aktivite çalışmaları 600 °C'de tam etanol dönüşümü ve 4'ten yüksek hidrojen verimi göstermiştir (en fazla 6). SBA-15 etanolün su buharı ile reformlama reaksiyonlarında MCM-41'den daha kararlı olduğu bulunmuştur.

En yüksek hidrojen verimi NiCe emdirilmiş AIMCM-41 destekli katalizörlerle elde edilmiştir. Silika matriksindeki alumina (3% kütlece) katalizöre asidik özellikler vermesi sayesinde katalitik aktiviteyi artırmıştır. Eş ve ardışık zamanlı Ni ve Ce emdirilmeleri de incelenmiştir. Ce/Si ve Ni/Si molar oranları 0.10 olan AIMCM-41 destekli, ardışık Ce ve Ni emdirilmiş katalizör çok yüksek katalitik aktivite (başlangıçtaki hidrojen verimi 5.8) göstermiştir. AIMCM-41 destekli katalizör yüksek aktivite ve bu nedenle kok oluşmasından dolayı daha az kararlıdır.

Anahtar Kelimeler: Mezo-gözenek, nano-kompozit malzeme, MCM-41, Pd-MCM-41, SBA-15, Mezogözenekli Seryum/Silika, Hidrojen Üretimi, Etanol Su Buharı Reformlama

To My Family & Friends,

ACKNOWLEDGEMENTS

I would like to express my sincere thanks to my supervisor Prof. Dr. Timur Dođu for his inspiring guidance, help supervising this research work, outstanding motivation and support with deep sense of gratitude and appreciation.

I am also very grateful to my co-supervisor Prof Dr. Gölşen Dođu for her great help, continuous encouragement and endless support.

I would like to thank Prof. Dr. Onder Ozbelge for his valuable advices, confidence, support and encouragement.

I would like to thank Prof. Dr. Nail Yasyerli for his valuable comments and kindness.

Special thanks are due to Gokhan Celik and Seval Gunduz for their friendship, support and motivation. Without them, this study could not be completed.

Special thanks are due to METU Central Laboratories for characterization. Pinar Tokmakkaya for XRD analyses, Dr. Kemal Behlulgil for nitrogen physisorption analyses, Sedat Canli for SEM/EDS analyses and Hikmet Eren for his great helps.

Technicians of our department Turgut Aksakal, Selahattin Uysal, Gölten Orakçı, Mihrican Açıkgöz were always ready to help, helpful and kind. I want to thank them for their technical and friendly supports.

I would like to thank my best friends Zeynep Obali, Zeynep Ozaydin and Ceren Oktar Doganay for all their support. I also thank Duygu Gerceker and Okan Ozkok for their friendship.

I would like to present my sincere thanks to Prof. Dr. Brent Shanks from Iowa Sate University for accepting me his laboratories and allowed me to work in a project and enabled me to improve my material science skills.

An important part of this study was completed within a scope of the project which was carried out by our department and Bulgarian Academy of Sciences, Institute of Catalysis. I would like to thank TUBITAK and Bulgarian Academy of Sciences for financial support and Dr. Katia Arishtirova and Prof. Dr. Sonia Damyanova for their good partnership.

Governmental Planning Organization was also gratefully acknowledged for the research fund BAP-08-11-DPT.2002K120510 for financial support.

Special thanks to my parents Ayse Sener and Yunus Sener and brother Furkan Sener for their endless support, love and life they have given to me.

TABLE OF CONTENTS

ABSTRACT.....	iv
ÖZ	vi
ACKNOWLEDGEMENTS.....	ix
TABLE OF CONTENTS	xi
LIST OF FIGURES.....	xvi
LIST OF TABLES.....	xxv
CHAPTERS	
1. INTRODUCTION.....	1
1.1. WORLD ENERGY PROBLEMS AND HYDROGEN AS AN ENERGY CARRIER 1	
1.2. MESOPOROUS CATALYSTS	5
1.3. OBJECTIVES	6
2. FUEL OF THE FUTURE: HYDROGEN.....	8
2.1. PROPERTIES OF HYDROGEN	8
2.2. HYDROGEN PRODUCTION TECHNIQUES	11
3. STEAM REFORMING OF ETHANOL	18
3.1. REACTION AND CONDITIONS.....	18
3.2. CATALYSTS FOR STEAM REFORMING OF ETHANOL.....	21
4. SILICEOUS AND NON-SILICEOUS MESOPOROUS MATERIALS AS CATALYST SUPPORT	24
4.1. ORDERED MESOPOROUS MOLECULAR SIEVES	24
4.2. SYNTHESIS OF MESOPOROUS MATERIALS	25

4.2.1. Formation Mechanism of MCM-41	30
4.3. TYPICAL MESOPOROUS STRUCTURES	32
4.4. AN ALTERNATIVE SUPPORT MATERIAL FOR ETHANOL-STEAM REFORMING REACTION CATALYSTS: CERIA (CeO ₂)	35
4.5. SYNTHESIS OF CERIA-BASED NANOMATERIALS	38
4.5.1. Ceria Nanomaterials	38
4.5.2. CeO ₂ -ZrO ₂ Solid Solution Nanomaterials	39
4.5.3. Other Ceria Based Nanocrystals	40
4.5.4. Controlled Synthesis	40
4.5.4.1. Assembly of Ceria Based Nanomaterials	40
5. MODIFICATION OF SUPPORT MATERIALS FOR CATALYTICE	42
6. CATALYST CHARACTERIZATION METHODS	44
6.1. X-Ray Diffraction (XRD)	44
6.2. Nitrogen Physisorption	45
6.3. Transmission Electron Microscopy (TEM)	45
6.4. Scanning Electron Microscopy (SEM)	46
6.5. X-Ray Photoelectron Spectroscopy (XPS)	46
7. THERMODYNAMIC ANALYSIS	47
8. EXPERIMENTAL	51
8.1. CATALYST DESIGN & PREPARATION	51
8.1.1. MCM-41 SYNTHESIS	51
8.1.2. SBA-15 SYNTHESIS	52
8.1.3. SYNTHESIS OF MCM-41 SUPPORTED CATALYSTS	53
8.1.3.1. SYNTHESIS OF Ni@MCM-41	53
8.1.3.2. SYNTHESIS OF PdNi@MCM-41	54
8.1.4. SYNTHESIS OF SBA-15 SUPPORTED CATALYSTS	55
8.1.4.1. SYNTHESIS OF Ni@SBA-15 CATALYST	55

8.1.4.2. SYNTHESIS OF NiCe@SBA-15 CATALYST	55
8.1.4.3. SYNTHESIS OF PdNiCe@SBA-15 CATALYST	56
8.1.5.1. SYNTHESIS OF Ni@AIMCM-41 CATALYST	56
8.1.5.2. SYNTHESIS OF Ce@AIMCM-41 CATALYST	57
8.1.5.3. SYNTHESIS OF NiCe@AIMCM-41 CATALYSTS.....	57
8.2. CHARACTERIZATION OF SYNTHESIZED MATERIALS.....	57
8.2.1. X-Ray Diffraction (XRD).....	58
8.2.2. Transmission Electron Microscopy (TEM)	58
8.2.3. Nitrogen Physisorption.....	58
8.2.4. Energy Dispersive Spectroscopy (EDS)/Scanning Electron Microscopy (SEM)58	
8.2.5. X-ray Photoelectron Spectroscopy (XPS).....	58
8.2.6. Temperature Programmed Reduction (TPR) Studies	58
8.2.7. Thermal Gravimetric (TGA) Analysis.....	59
8.3. STEAM REFORMING OF ETHANOL TEST REACTION	59
8.3.1. Experimental Set-up	59
8.3.2. System Parameters	60
8.4. DRY REFORMING OF METHANE WITH CARBON DIOXIDE	60
9. RESULTS AND DISCUSSION	61
9.1. Ni AND PdNi IMPREGNATED MCM-41 CATALYSTS.....	61
9.1.1. CHARACTERIZATION RESULTS OF PREPARED CATALYSTS	61
9.1.1.2. CHARACTERIZATION OF Ni@MCM-41 CATALYSTS	64
9.1.1.2.1. EDS Analysis.....	64
9.1.1.2.2. XRD Analysis.....	66
9.1.1.2.3. Nitrogen Adsorption Desorption Analysis.....	69
9.1.1.2.4. SEM Analyses	71
9.1.1.2.5. Thermal Analysis (TGA/DTA).....	72
9.1.1.2.6. Temperature Programmed Reduction – TPR Studies	73
9.1.1.3. CHARACTERIZATION OF PdNi@MCM-41 CATALYSTS	74

9.1.1.3.1. EDS Analysis.....	74
9.1.1.3.5. TGA Analysis.....	80
9.1.2. ETHANOL-STEAM REFORMING REACTION RESULTS WITH Ni AND Ni-Pd IMPREGNATED MCM-41.....	88
9.1.2.1. ETHANOL CONVERSION	88
9.2.1.2. HYDROGEN YIELD.....	89
9.1.2.3. PRODUCT DISTRIBUTION OF Ni AND Pd-Ni INCORPORATED CATALYSTS	91
9.2.1.4. COMPARISON OF Ni & PD-NI INCORPORATED CATALYSTS	97
9.2. Ni, NiCe and PdNiCe IMPREGNATED SBA-15 CATALYSTS	108
9.2.1. CHARACTERIZATION RESULTS OF SBA-15 SUPPORTED CATALYSTS	108
9.2.1.1. Characterization of SBA-15.....	109
9.2.1.2. Characterization of SBA-15 Supported Catalysts.....	113
9.2.2. ACTIVITIES OF SBA-15 SUPPORTED CATALYST IN ETHANOL STEAM REFORMING REACTION	123
9.2.3. CHARACTERIZATION OF SBA-15 SUPPORTED CATALYSTS AFTER STEAM REFORMING OF ETHANOL REACTION	131
9.3. Ni, Ce and NiCe IMPREGNATED COMMERCIAL AIMCM-41 CATALYSTS.....	137
9.3.1. CHARACTERIZATION OF AIMCM-41 SUPPORTED CATALYSTS	138
9.3.1.1. Characterization of Commercial AIMCM-41	138
9.3.1.2. Characterization of Ni, Ce and NiCe Impregnated AIMCM-41 Supported Catalysts	141
9.3.1.3. Ethanol-Steam Reforming Reaction Results.....	150
9.3.1.4. Characterization of AIMCM-41 Supported Catalysts After Ethanol Steam Reforming Reaction.....	159
9.4. Ni IMPREGNATED COMMERCIAL CeO ₂ CATALYST	163
9.4.1. CHARACTERIZATION OF THE CATALYST	163
9.4.1.2. Activity of Ni Impregnated CeO ₂ Catalyst	166
9.4.3. Characterization of Ni/CeO ₂ After Reaction.....	168

10.CONCLUSIONS.....	170
REFERENCES	172
APPENDICES.....	181
A.1. SUMMARY OF THE CATALYSTS	181
A.2. CALIBRATION OF GAS CHROMATOGRAPHY	182
A.3. SAMPLE CALCULATION.....	183
A.3. SELECTION OF FLOWRATE	186
A.4. ACTIVITY OF Ni@MCM-41 AND PdNi@MCM-41 CATALYSTS IN DRY REFORMING OF METHANE REACTION	189
A.4.1. EXPERIMENTAL.....	189
A.4.2. RESULTS	189
A.5. REACTION PARAMETERS OF THE CATALYSTS TESTED IN STEAM REFORMING OF ETHANOL REACTION	192
CURRICULUM VITAE	203

LIST OF FIGURES

Figure 1.1.1. Illustration of possible global problems (adapted from (Midilli A. 2005)).....	2
Figure 2.2.1. Relation of production techniques and types of utilization of hydrogen (adapted from Midilli et al., 2005).....	12
Figure 2.2.2. Fuel processing of gaseous, liquid and solid fuels for hydrogen production (adapted from (Halladay J.D. 2009))	13
Figure 4.1.1. M41S family materials (Huo Q. 2011)	25
Figure 4.2.1. Schematic representation of different types of silica-surfactant interfaces (taken (Huo Q. 2011)).....	28
Figure 4.2.2. Schematical representation of surfactant (Gao C. 2009).....	29
Figure 4.2.3. Liquid-crystal templating (LCT) mechanism proposed by Beck et al. (1992) showing two possible pathways for the formation ofMCM-41: (1) liquid- crystal-initiated and (2) silicate-initiated.....	31
Figure 4.2.4. Cooperative formation pathway (Firouzi D. 1995)	32
Figure 4.3.1. (a) Schematical representation of MCM-41 (b) TEM image of MCM-41 (taken from (Sener 2006)).....	34
Figure 4.3.2. Structure of SBA-15 (Zhao D. 1998).....	35
Figure 4.4.1. Structure of Ceria (taken from (Bumajdad A. 2009))	36
Figure 4.5.1. Alcohothermal mechanism for synthesis of CeO ₂ nanocrystals (Yuan Q. 2009).....	39
Figure 4.5.2. The illustration of self-assembly process of surface modified ceria nanoparticles (taken from (Yuan Q. 2009)).....	41
Figure 6.1.1. Schematical representation of pores of MCM-41 (Sener 2006)	45
Figure 8.1.1. Synthesis procedure of MCM-41	52
Figure 8.1.2. Synthesis procedure of SBA-15.....	53
Figure 8.1.3. Schematical representation of Ni impregnated MCM-41-supported catalysts	53
Figure 8.1.4. Schematical representation of Pd and Ni impregnated MCM-41 catalysts.....	54

Figure 8.3.1. Schematical representation of experimental set-up.....	59
Figure 9.1.1. X-ray diffraction pattern of MCM-41 material.....	62
Figure 9.1.2. Schematical representation of MCM-41 material.....	62
Figure 9.1.3. Nitrogen adsorption-desorption isotherms of MCM-41 material.....	63
Figure 9.1.4. Pore size distribution curve of MCM-41 material.....	64
Figure 9.1.5. Energy dispersive spectra of Ni@MCM-41 samples (a) B1, (b) B2, (c) B3.....	64
Figure 9.1.6. Small and high-angle X-ray diffraction patterns of Ni@MCM-41 samples before calcination (B7, B8, B9)	66
Figure 9.1.7. Small and high-angle X-ray diffraction patterns of Ni@MCM-41 samples after calcination (B1, B2, B3)	66
Figure 9.1.8. Nitrogen adsorption-desorption isotherms of Ni@MCM-41 catalysts (a) B2, (b) B3, (c) B1.....	70
Figure 9.1.9. Pore size distribution curves of Ni@MCM-41 catalysts.....	71
Figure 9.1.10. SEM images of (a) B1 sample, (b) B2 sample (c) B3 sample (d) B7 sample, (e) B8 sample, (f) B9 sample	72
Figure 9.1.11. DTA plot of B7 sample	73
Figure 9.1.12. (a) TGA (b) dTGA plots of B7 sample.....	73
Figure 9.1.13. TPR profiles of Ni@MCM-41 samples.....	74
Figure 9.1.14. EDS patterns of B4, B5 ve B6 samples	74
Figure 9.1.15. Small and high angle X-ray diffraction patterns of Pd-Ni@MCM-41 catalysts before calcination.....	76
Figure 9.1.17. Nitrogen adsorption-desorption isotherms of PdNi@MCM-41 catalysts (a) B5 (b) B6 (c) B4.....	78
Figure 9.1.18. Pore size distribution curves of Pd-Ni@MCM-41 catalysts.....	79
Figure 9.1.19. SEM images of PdNi@MCM-41 samples (a) B4, (b) B5 (c) B6 (d) B10, (e) B11, (f) B12.....	80
Figure 9.1.20. DTA plot of B10 sample	81
Figure 9.1.21. TGA plot of B10 sample	81
Figure 9.1.22. TPR profiles Pd-Ni@MCM-41 catalysts.....	83

Figure 9.23. TEM image of B6 sample (1).....	84
Figure 9.1.24. TEM image of B6 sample (2).....	84
Figure 9.1.25. TEM image of B6 sample (3).....	85
Figure 9.1.26. TEM image of B6 sample (4).....	85
Figure 9.1.27. XPS patterns of Pd-Ni dual catalysts for NiO region.....	87
Figure 9.1.28. XPS patterns of Pd-Ni dual catalysts for PdO region.....	87
Figure 9.1.40. Change of ethanol conversion with temperature for Ni incorporated catalysts	88
Figure 9.1.41. Change of ethanol conversion with temperature for Pd-Ni incorporated catalysts	89
Figure 9.1.42. Change of hydrogen yield with temperature for Ni incorporated catalysts.....	90
Figure 9.1.43. Change of hydrogen yield with temperature for PdNi incorporated catalysts	91
Figure 9.1.44. Carbon dioxide selectivity for Ni impregnated MCM-41 catalysts	92
Figure 9.1.45. Carbon dioxide selectivity for Pd Ni impregnated MCM-41 catalysts	92
Figure 9.1.46. Carbon monoxide selectivity of Ni impregnated MCM-41	93
Figure 9.1.47. Carbon monoxide selectivity of PdNi impregnated MCM-41.....	93
Figure 9.1.48. Methane selectivity of Ni impregnated MCM-41 catalysts	94
Figure 9.1.49. Methane selectivity of PdNi impregnated MCM-41 catalysts	94
Figure 9.1.50. Product distribution of B1 catalyst.....	95
Figure 9.1.51. Product distribution of B2 catalyst.....	95
Figure 9.1.52. Product distribution of B3 catalyst.....	95
Figure 9.1.53. Product distribution of B4 catalyst.....	96
Figure 9.1.54. Product distribution of B5 catalyst.....	96
Figure 9.1.55. Product distribution of B6 catalyst.....	96
Figure 9.1.56. Change of ethanol conversion with temperature for B1 and B4 catalysts	97
Figure 9.1.57. Change of hydrogen yield by temperature for B1 and B4 catalysts.....	98
Figure 9.1.58. Change of carbon monoxide selectivity with temperature for B1 and B4 catalysts	98

Figure 9.1.59. Change of methane selectivity with temperature for B1 and B4 catalysts.....	99
Figure 9.1.60. Change of CO ₂ selectivity of B1 ve B4 catalysts with temperature	99
Figure 9.1.68. Low and high-angle x-ray diffraction patterns of B1, B2 and B3 after reaction (▲ NiO, ● C).....	101
Figure 9.1.69. Low and High-angle X-ray diffraction patterns of B4, B5 and B6 catalysts after reaction (● C)	102
Figure 9.1.70. Nitrogen adsorption desorption isotherms of B1, B2 and B3 catalysts after reaction	103
Figure 9.1.71. Nitrogen adsorption desorption isotherms of B4, B5 and B6 catalysts after reaction	104
Figure 9.1.72. Pore size distribution curves of B1, B2 and B3 catalysts after reaction.....	105
Figure 9.1.73. Pore size distribution curves of B4, B5 and B6 catalysts after reaction.....	105
Figure 9.1.74. TGA profile of B1	106
Figure 9.1.75. TGA profile of B2	106
Figure 9.1.76. TGA profile of B3	107
Figure 9.1.77. TGA profile of B4	107
Figure 9.2.1. Typical XRD pattern of SBA-15 catalysts.....	109
Figure 9.2.2. Nitrogen adsorption-desorption isotherm and pore size distribution curve of SBA-15 (a) calcine (b) extracted	111
Figure 9.2.3. Pore size distribution of SBA-15.....	111
Figure 9.2.4. SEM images of SBA-15 with different magnifications.....	112
Figure 9.2.5. Low angle XRD pattern of Ni impregnated SBA-15 supported catalyst Ni@SBA-15.....	113
Figure 9.2.6. Nitrogen adsorption-desorption isotherm of Ni impregnated SBA-15 catalyst Ni@SBA-15.....	115
Figure 9.2.7 . Pore size distribution curve of Ni impregnated SBA-15 catalyst Ni@SBA- 15.....	115
Figure 9.2.9. XRD pattern of Ni and Ce impregnated SBA-15 catalyst.....	117

Figure 9.2.10. XRD pattern of Pd, Ni and Ce impregnated SBA-15 catalyst. PdNiCe(0.5)@SBA-15 (R)	118
Figure 9.2.11. N ₂ adsorption desorption isotherm of Ni and Ce impregnated SBA-15 catalyst (a) NiCe(0.50)@SBA-15 (b) PdNiCe(0.50)@SBA-15.....	120
Figure 9.2.12. Pore size distribution of Ni and Ce impregnated SBA-15 catalyst.....	121
Figure 9.2.13. SEM images of nickel and ceria impregnated SBA-15 supported catalyst, NiCe(0.50)@SBA-15	122
Figure 9.2.14. SEM images of nickel, ceria and palladium impregnated SBA-15 supported catalyst, NiCe(0.50)@SBA-15	122
Figure 9.2.15 . Ethanol conversion and hydrogen yield of Ni impregnated SBA-15 catalyst, Ni @ SBA-15 at 600 °C.....	124
Figure 9.2.16. Ethanol conversion and hydrogen yield of Ni and Ce impregnated SBA-15 catalyst with Ce/Si=0.10, NiCe(0.10)@SBA-15 at 600 °C	124
Figure 9.2.17. Ethanol conversion and hydrogen yield of Ni and Ce impregnated SBA-15 catalyst with Ce/Si=0.50, NiCe(0.50)@SBA-15 at 600 °C	125
Figure 9.2.18. Ethanol conversion and hydrogen yield for Pd, Ni and Ce impregnated SBA-15 catalyst, PdNiCe(0.5)@SBA-15 at 600 °C	125
Figure 9.2.19. Composition of gas product stream for Ni impregnated SBA-15 catalyst, Ni@SBA-15.....	126
Figure 9.2.20. Composition of gas product stream of Ni and Ce impregnated SBA-15 catalyst with Ce/Si=0.10, NiCe(0.10)@SBA-15	126
Figure 9.2.29. Low angle x-ray diffraction pattern of reduced Ni@SBA-15 and after reaction at 600 °C.....	131
Figure 9.2.30. High angle x-ray diffraction pattern of Ni@SBA-15 before and after reaction at 600 °C (▲ NiO, ● C).....	132
Figure 9.2.31. Low angle x-ray diffraction pattern of NiCe(0.10)@SBA-15 before and after reaction at 600 °C.....	132
Figure 9.2.32. High angle x-ray diffraction pattern of NiCe(0.10)@SBA-15 before and after reaction at 600 °C.....	133

Figure 9.2.33. Wide angle x-ray diffraction pattern of NiCe(0.50)@SBA-15 before and after reaction at 600 °C.....	133
Figure 9.2.34. SEM images of NiCe(0.50)@SBA-15 after reaction at 600 °C.....	134
Figure 9.2.35. SEM images of PdNiCe(0.50)@SBA-15 after reaction at 600 °C	135
Figure 9.2.36. TGA profile of Ni@SBA-15 after reaction at 600 °C	136
Figure 9.2.37. TGA profile of NiCe(0.10)@SBA-15 after reaction at 600 °C.....	136
Figure 9.2.38. TGA profile of NiCe(0.50)@SBA-15 after reaction at 600 °C.....	137
Figure 9.3.1. Low angle x-ray diffraction pattern of AIMCM-41	139
Figure 9.3.3. Nitrogen adsorption-desorption isotherm of AIMCM-41.....	140
Figure 9.3.4. Pore size distribution curve of AIMCM-41	141
Figure 9.3.5. Low angle x-ray diffraction pattern of reduced nickel impregnated AIMCM-41, Ni@AIMCM-41.....	142
Figure 9.3.6. Low angle x-ray diffraction pattern of reduced nickel impregnated AIMCM-41, Ni@AIMCM-41.....	142
Figure 9.3.7. High angle x-ray diffraction patterns of Ni and NiCe impregnated AIMCM-41 supported catalysts (▲ CeO ₂ , ● NiO).....	143
Figure 9.3.8. Nitrogen adsorption-desorption isotherms of Ni, and NiCe impregnated AIMCM-41 catalysts.....	145
Figure 9.3.9. Low angle x-ray diffraction patterns of Ce, Ni and NiCe impregnated AIMCM-41.....	146
Figure 9.3.10. High angle x-ray diffraction patterns of Ce and NiCe impregnated AIMCM-41 catalysts.....	147
Figure 9.3.11. High angle x-ray diffraction pattern of cerium impregnated and consequently cerium and nickel impregnated AIMCM-41 catalysts	147
Figure 9.3.12. SEM images of Ni@[Ce@AIMCM-41]	148
Figure 9.3.13. SEM images of Ce@AIMCM-41	148
Figure 9.3.14. SEM images of NiCe(0.10)@AIMCM-41.....	149
Figure 9.3.15. SEM images of NiCe(0.50)@AIMCM-41.....	149

Figure 9.3.15. Ethanol conversion and hydrogen yield of Ni impregnated AIMCM-41 catalyst, Ni@AIMCM-41 at 600 °C	151
Figure 9.3.16. Ethanol conversion and hydrogen yield of sequentially Ni and Ce impregnated AIMCM-41 catalyst, Ni@[Ce@AIMCM-41] at 600 °C.....	151
Figure 9.3.17. Ethanol conversion and hydrogen yield of Ni and Ce impregnated AIMCM-41 with Ce/Si=0.10, NiCe(0.10)@AIMCM-51 at 600 °C.....	152
Figure 9.3.18. Ethanol conversion and hydrogen yield of Ce@AIMCM-41 at 600 °C.....	152
Figure 9.3.19. Ethanol conversion and hydrogen yield of NiCe(0.50)@AIMCM041 at 600 °C	153
Figure 9.3.20. Comparison of hydrogen yields of Ni and NiCe impregnated AIMCM-41 supported catalysts.....	153
Figure 9.2.21. Composition of gas product stream of Ni impregnated AIMCM-41 catalyst, Ni@AIMCM-41 at 600 °C	154
Figure 9.3.22 . Composition of gas product stream of sequentially Ni and Ce impregnated AIMCM-41 catalyst, Ni@[Ce@AIMCM-41] at 600 °C.....	155
Figure 9.3.23. Composition of gas product stream of Ni and Ce impregnated AIMCM-41 with Ce/Si=0.10, NiCe(0.10)@AIMCM-51 at 600 °C	155
Figure 9.3.24. Composition of gas product stream of Ni and Ce impregnated AIMCM-41 with Ce/Si=0.50, NiCe(0.50)@AIMCM-51 at 600 °C	156
Figure 9.3.25. Composition of gas product stream of Ce@AIMCM-41 at 600 °C.....	156
Figure 9.3.26. Selectivities of products with the catalyst Ni@AIMCM-41 at 600 °C	157
Figure 9.3.27 . Product selectivities of sequentially Ni and Ce impregnated AIMCM-41 catalyst, Ni@[Ce@AIMCM-41] at 600 °C	157
Figure 9.3.28. Product selectivities of Ni and Ce impregnated AIMCM-41 with Ce/Si=0.10, NiCe(0.10)@AIMCM-41 at 600 °C	158
Figure 9.3.29. Product selectivities of Ni and Ce impregnated AIMCM-41 with Ce/Si=0.50, NiCe(0.50)@AIMCM-41 at 600 °C	158
Figure 9.3.30. Product selectivities of Ce impregnated AIMCM-41 with Ce@AIMCM-41 at 600 °C	159

Figure 9.3.31. Low angle x-ray diffraction pattern of reduced Ni@[Ce@AIMCM-41] and after reaction at 600 °C.....	160
Figure 9.3.32. Wide angle x-ray diffraction pattern of reduced Ni@[Ce@AIMCM-41] and after reaction at 600 °C (▲C, ◆NiO).....	160
Figure 9.3.33. SEM images of NiCe(0.10)@AIMCM-41 after reaction at 600 °C	161
Figure 9.3.34. SEM images of NiCe(0.50)@AIMCM-41 after reaction at 600 °C	161
Figure 9.3.35. SEM images of Ce@AIMCM-41 after reaction at 600 °C.....	162
Figure 9.3.36. Thermal gravimetric analysis of consecutively ceria and nickel impregnated AIMCM-41 supported catalyst, Ni@[Ce@AIMCM-41] after reaction at 600 °C.....	162
Figure 9.4.1. X-ray diffraction pattern of CeO ₂ and Ni@CeO ₂	163
Figure 9.4.2. Nitrogen adsorption-desorption isotherms of commercial CeO ₂ and as-synthesized Ni/CeO ₂	164
Figure 9.4.3. SEM image of reduced/CeO ₂	165
Figure 9.4.4. SEM images of reduced Ni/CeO ₂	165
Figure 9.4.4.5. Ethanol conversion and hydrogen yield of NiCeO ₂ at 600 °C	166
Figure 9.4.6. Composition of gas product stream yield of Ni/CeO ₂ at 600 °C	167
Figure 9.4.7. Selectivities of products with Ni/CeO ₂ at 600 °C	167
Figure 9.4.8. SEM images of Ni@CeO ₂ after reaction at 600 °C.....	168
Figure 9.4.9. Thermal gravimetric analysis of Ni/CeO ₂	169
Figure A.3.1. Ethanol conversion versus temperature for different space times for B5 catalyst.....	186
Figure A.3.2. Hydrogen yield versus temperature for different space times for B5 catalyst.....	186
Figure A.3.3. Carbon dioxide selectivity versus temperature for different space times for B5 catalyst.....	187
Figure A.3.4. Carbon monoxide selectivity versus temperature for different space times for B5 catalyst.....	187

Figure A.3.5. Methane selectivity versus temperature for different space times for B5 catalyst.....	188
Figure A.3.6. Formaldehyde selectivity versus temperature for different space times for B5 catalyst.....	188
Figure A.4.1. Methane conversion of Ni@MCM-41 samples	190
Figure A.4.2. Hydrogen yield of Ni@MCM-41 samples	190
Figure A.4.3. Methane conversion of PdNi@MCM-41 samples	191
Figure A.4.4. Hydrogen yield of PdNi@MCM-41 samples	191

LIST OF TABLES

Table 1.1.1. Energy conversion and usage options with respect to energy source (adapetd from (Panwar N.L. 2011)).....	3
Table 1.1.2. Global renewable energy scenerio (adapted from (Panwar N.L. 2011))	4
Table 2.1.1. Properties of Hydrogen (adapted from (Midilli A. 2005))	9
Table 2.1.2. Comparison of key properties of hydrogen and other fuels (adapted from (Midilli A. 2005))	10
Table 2.2.1. Major thermal, biological, and electrochemical methods for hydrogen production (adapted from (Hydrogen Production Overview n.d.)).....	15
Table 2.2.2. Comparison of reforming Technologies (taken from Holladay et al.2009)	17
Table 3.1.1. Possible reaction pathways of ethanol steam reforming (adapted from (Ni M. 2007)).....	20
Table 3.2.1. Nobel metal catalystsfor steam reforming of ethanol (adapted from (Ni M. 2007)).....	22
Table 3.2.2. Non-nobel metal catalystsfor steam reforming of ethanol (taken from (Ni M. 2007)).....	23
Table 4.2.1. Surfactants for the synthesis of mesostructures (adapted from (Wieslaw J. 2005)).....	27
Table 4.2.2. Structures and packing parameter of mesoporous materials (adapted from (Gao C. 2009))	29
Table 4.3.1. Structure and pore diameter of typical mesoporous silica materials (adapted from (adapted from (Gao C. 2009))	33
Table 7.1. Constant pressure heat capacity coefficients of chemicals involved in steam reforming of ethanol (Sandler S.I. 1999).....	47
Table 7.2. Standard enthalpies of formation and standard Gibbs energy of formation at 25 °C.....	48

Table 8.1.1. Nomenclature of Ni@MCM-41 and Pd-Ni@MCM-41 catalysts synthesized by impregnation procedure	55
Table 8.1.2. Prepared SBA-15 supported catalysts	56
Table 8.1.3. AIMCM-41 supported catalysts	57
Table 8.3.1. Temperature programme for gas chromatography	60
Table 8.3.2 Chromatograph Parameters	60
Table 9.1.1. Nitrogen adsorption data for MCM-41 support material	63
Table 9.1.2. Chemical Compositions by Energy Dispersive Spectroscopy	65
Table 9.1.3. Ni/Si ratios of Ni@MCM-41 samples	65
Table 9.1.4. XRD peaks of Ni@MCM-41 catalysts caused by MCM-41 structure	67
Table 9.1.6. NiO particle sizes in Ni@MCM-41 samples	69
Table 9.1.7. Nitrogen adsorption-desorption analysis results of the prepared catalysts	71
Table 9.1.8. Chemical compositions by energy dispersive spectroscopy	75
Table 9.1.9. Nitrogen adsorption analysis results of prepared catalysts after calcination	77
Table 9.1.10. XPS parameters of the samples	86
Table 9.1.11. Physical Properties of the Catalysts After Reaction	100
Table 9.1.12. Weight loss of used catalysts	107
Table 9.2.1. Prepared SBA-15 supported catalysts	109
Table 9.2.2. X-ray diffraction analysis of SBA-15 samples	110
Table 9.2.3. Nitrogen physisorption analysis of SBA-15 samples	110
Table 9.2.4. X-ray diffraction analysis of Ni@SBA-15 sample	114
Table 9.2.5. Nitrogen physisorption analysis of Ni@SBA-15 sample	114
Table 9.2.6. Metal particle sizes of Ni, NiCe and PdNiCe impregnated SBA-15 catalysts ..	118
Table 9.2.7. Nitrogen physisorption analysis of NiCe and PdNiCe impregnated SBA-15 catalysts	120
Table 9.2.9. Weight loss of Ni and NiCe impregnated SBA-15 catalysts by TGA after reaction at 600 °C	137
Table 9.3.1. AIMCM-41 supported catalysts	138
Table 9.3.2. X-ray diffraction peaks and related parameters for AIMCM-41	139

Table 9.3.3. Composition of AIMCM-41 obtained by EDS	140
Table 9.3.4. Nitrogen physisorption analysis of AIMCM-41	140
Table 9.3.5. X-ray diffraction analysis of nickel and nickel-ceria impregnated AIMCM-41 catalysts	143
Table 9.3.6. NiO and CeO ₂ particle sizes	144
Table 9.3.7. Nitrogen physisorption analysis of nickel and nickel-ceria impregnated AIMCM-41 samples	144
Table 9.3.5. X-ray diffraction analysis of nickel and nickel-ceria impregnated AIMCM-41 catalysts	146
Table 9.4.1 Surface area of CeO ₂ and Ni/CeO ₂	165
Table A.2.1. Calibration parameters of reaction gases	182
Table A.5.1. Reaction parameters of B1	192
Table A.5.2. Reaction Parameters of B2	192
Table A.5.3. Reactin parameters of B3.....	192
Table A.5.4. Reaction parameters of B4.....	193
Table A.5.5. Reaction parameters of B5.....	193
Table A.5.6. Reaction parameters of B6.....	193
Table A.5.7. Reaction parameters of Ni@SBA-15 at 600 °C.....	194
Table A.5.8. Gas stream product composition of Ni@SBA-15 at 600 °C.....	194
Table A.5.9. Reaction parameters of NiCe(0.10)@SBA-15 at 600 °C	194
Table A.5.10. Gas stream product composition of NiCe(0.10)@SBA-15 at 600 °C.....	195
Table A.5.11. Reaction parameters of NiCe(0.50)@SBA-15 at 600 °C	195
Table A.5.12. Gas stream product composition of NiCe(0.50)@SBA-15 at 600 °C.....	196
Table A.5.13. Reaction parameters of PdNiCe(0.50)@SBA-15 at 600 °C	196
Table A.5.14. Gas stream product composition of PdNiCe(0.50)@SBA-15 at 600 °C	197
Table A.5.15. Reaction parameters of Ni@AIMCM-41 at 600 °C	198
Table A.5.16. Gas stream product composition of Ni@AIMCM-41 at 600 °C.....	198
Table A.5.17. Reaction parameters of NiCe(0.10)@AIMCM-41 at 600 °C.....	199
Table A.5.18. Gas stream product composition of NiCe(0.10)@AIMCM-41 at 600 °C	199

Table A.5.19. Reaction parameters of Ni@[Ce@AIMCM-41] at 600 °C.....	200
Table A.5.20. Gas stream product composition of Ni@[Ce@AIMCM-41] at 600 °C.....	200
Table A.5.21. Reaction parameters of Ce@AIMCM-41.....	201
Table A.5.22. Gas stream product composition of Ce@AIMCM-41.....	201
Table A.5.23. Reaction parameters of NiCe(0.50)@AIMCM-41	202
Table A.5.24. Gas stream product composition of NiCe(0.50)@AIMCM-41.....	202

CHAPTER 1

INTRODUCTION

1.1. WORLD ENERGY PROBLEMS AND HYDROGEN AS AN ENERGY CARRIER

Depletion of fossil fuels and pollutions are the world encountered problems in the last two decades. Energy requirement of the world has been increased due to the technological development and increasing population. For future world stability, investigations of alternative energy strategies of the world have gained importance and environmental compatibility of alternative energy sources is the most important property.

Midilli et al. defines the most important three world energy problems as follows (Midilli A. 2005) :

1. As the world population increases, energy demand increases. Additionally, new technological developments also increase the energy demand. These facts cause depletion of fossil fuels.
2. Due to the increase of concentration of carbon dioxide in the atmosphere, global climate changes occur.
3. Due to the instability of prices of energy, conflicts and wars may occur and living standards decrease.

Illustration of possible global problems from increasing use of fossil fuels and the consequent need for hydrogen energy systems is presented in Figure 1.1.1. The major problems are shown at the top. The first pathway (shown on the left) follows a way of increasing use of renewable and sustainable energy, while the second pathway (right) allows for increasing use of fossil fuels and the problems related to that path.

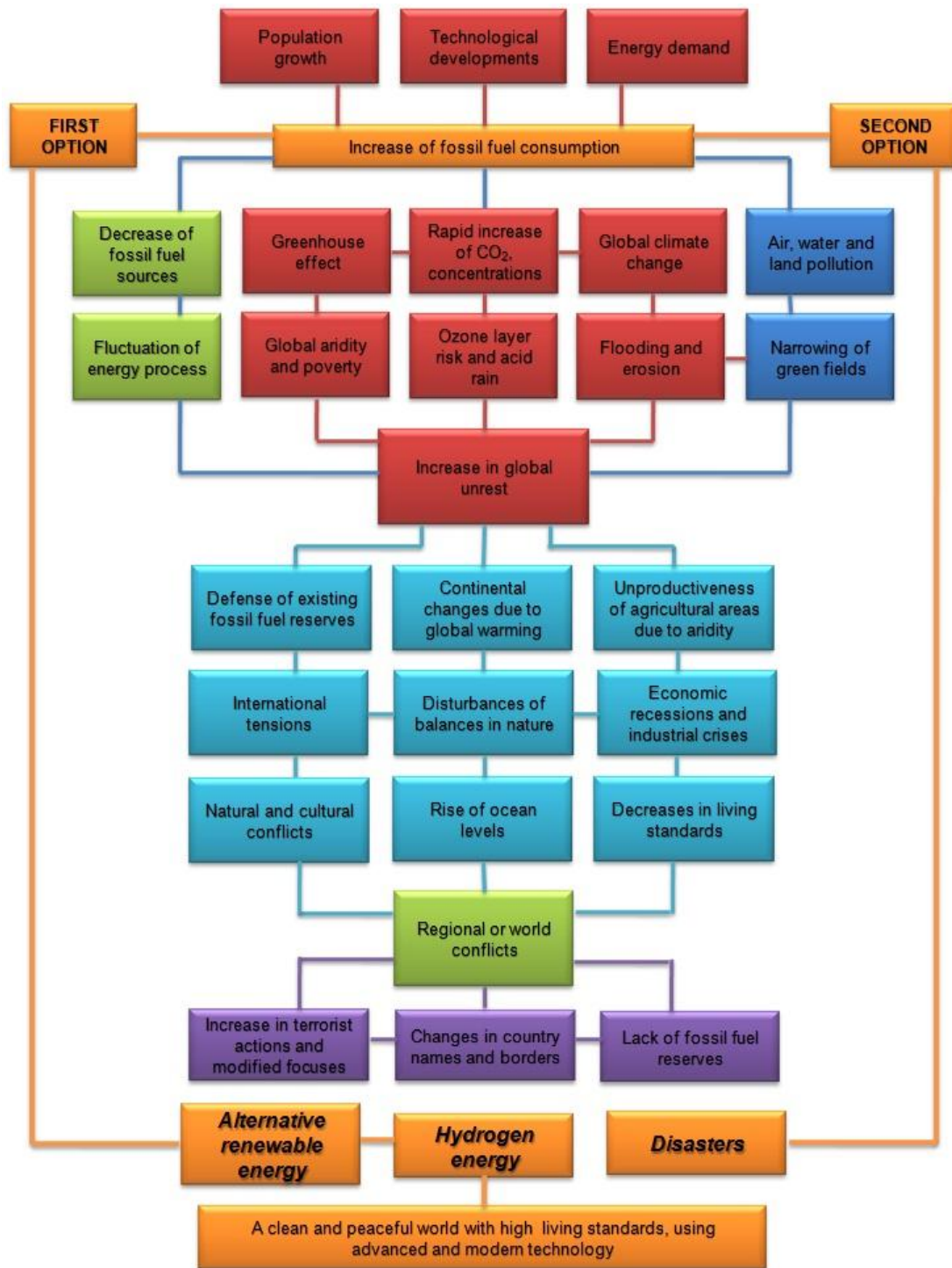


Figure 1.1.1. Illustration of possible global problems (adapted from (Midilli A. 2005))

In the world's future, renewable energy resources will play an important role. The energy sources can be split into three categories:

- renewable resources
- fossil fuels
- nuclear resources

Alternative types of energy are the solar energy, wind energy, biomass energy, geothermal energy, etc. and are used to obtain endless production of energy. Zero or almost zero emissions of air pollutants and greenhouse gases are provided with renewable energy sources which meet the domestic energy requirements. By development of renewable energy systems, several crucial tasks such as fuel economy, energy supply and supply reliability, increasing the standard of living and level of employment of the local population, implementation of the obligations of the countries with regard to fulfilling the international agreements relating to environmental protection, solving problems of local energy and water supply, ensuring sustainable development of the remote regions in the desert and mountain zones could be resolved. Moreover, job opportunities can be created in rural areas by the development and implementations of renewable energy and by this way, migration towards to urban areas can be minimized. The rural and small scale energy needs can be met by harvesting the renewable energy in decentralized manner as an affordable and environmentally sustainable option (Table 1.1.1) (Panwar N.L. 2011).

Table 1.1.1. Energy conversion and usage options with respect to energy source (adapeted from (Panwar N.L. 2011))

Energy source	Energy conversion and usage options
Modern biomass	Pyrolysis, dogestion, heat and power generation, gasification
Hydropower	Power generation
Solar	Solar dryers, solar home system, solar cookers
Geothermal	Urban heating, hydrothermal power generation
Wind	Power generation, windmills, wind generators, water pumps
Direct solar	Photovoltaic water heaters, thermal power generation
Wave	Numerous design, barrage, tidal streams

The conversion of hydrocarbons to hydrogen will play an important role in the 21st century, ranging from large hydrogen plants for refineries, fuel gas plants etc. to small units providing

hydrogen for fuel cells. Fuel cells are becoming more and more attractive power sources, especially for the motor vehicles. Direct use of hydrogen in the fuel cells is considered as a preferred option for the hydrogen energy system (Table 1.1.2) (Ni M. 2007), (Demirbas 2006).

Table 1.1.2. Global renewable energy scenerio (adapted from (Panwar N.L. 2011))

	2001	2010	2020	2030	2040
Total consumption (million tons oil equivalent)	10 038	10 549	11 425	12 352	13 310
Biomass	1080	1313	1791	2483	3271
Large hydro	22.7	266	309	341	358
Geothermal	43.2	86	186	333	493
Small hydro	9.5	19	49	106	189
Wind	4.7	44	266	542	688
Solar thermal	4.1	15	66	244	480
Photovoltaic	0.1	2	24	221	784
Solar thermal electricity	0.1	0.4	3	16	68
Marine (tidal/wave/ocean)	0.05	0.1	0.4	3	20
Total RES	1 365.5	1 745.5	2 964.4	4289	6351
Renewable energy source contribution (%)	13.6	16.6	23.6	34.7	47.7

The forecasts show that hydrogen will become a major source of energy in the future. It is considered as the “fuel of the future” and it offers a potentially non-polluting, inexhaustible and efficient energy source. It also has the advantage of not causing greenhouse effect. The efforts of the researchers are dedicated to develop practical and economically competitive hydrogen technologies and systems to meet the energy needs.

Currently, hydrogen is used in the chemical industry, but in the near future it will become a significant fuel. There are several hydrogen production processes. With increasing demand for hydrogen, production from renewable sources, is of great importance. Bio-ethanol offers a promising source of hydrogen due to its low toxicity, ease of handling and availability from different sources (Demirbas 2006).

Development of active and stable catalysts for such dry and steam reforming reactions attracted major attention of researchers in recent decades (O. U. Matter P.H. 2005), (B. D. Matter P.H. 2004), (Pawelec B. 2007), (Parizotto N.V. 2007).

Nickel and palladium are among the most active metals tested in catalytic steam and dry reforming reactions, to produce synthesis gas and hydrogen from natural gas and alcohols (Duan S. 2005), (Gheno S.M. 2003), (Portugal U.L. 2002), (Takahashi R. 2005), (N. N. Pompeo F. 2005). Autothermal catalytic reforming of alcohols [(Gutierrez A. 2011), (Lattner J.R. 2007)] is also considered as an attractive alternate for hydrogen production for fuel cell derived cars. Supported Pd catalysts also have wide application in hydrogenation and organic synthesis reactions (Panpranot J. 2004), (Albertazzi S. 2003), (M. I. Kosslick H. 2001).

1.2. MESOPOORUS CATALYSTS

After the discovery of the M41S family silicate structured mesoporous materials (Kresge C.T. 1992) significant research was focused to improve the catalytic performance of such materials by the incorporation of metals or metal oxides into their structure, following one-pot or post synthesis procedures. In our group's recent studies (Gucbilmez Y. 2006), (Sener C.(*) 2006) synthesis of metal and metal oxide incorporated MCM-41 type catalytic materials by direct hydrothermal synthesis and impregnation procedures were investigated and catalytic activity of V-MCM-41 in selective oxidation of ethanol was studied (Gucbilmez Y. 2006).

Heterogeneous catalyst design is an important phenomena. Not only the control of surface chemistry is important but also surface geometry in which scales of catalysts are macroscale, mesoscale or microscale. Any active catalyst must have high active phase dispersions or high surface area. Moreover, mass transfer of products and reactant from and to catalytic sites should be fast (On D.T. 2001).

Mesoporous molecular sieves (MMSs) have the benign catalytic properties and they have introduced a new conception in catalysts. They have the high surface area (up to 1600 m²/g for silica based mesostructured catalysts) and pore diameters in the mesoporous range (2-

50 nm). In mesoporous materials, channels which mimics the liquid crystals formed in the catalyst preparation by the use of surfactants are arranged stereoregularly. Mesoporous materials have wide application areas. Three kinds of mesoporous materials have been obtained by different preparation methods. First kind of materials is M41S family. The most important members of M41S family consist of MCM-41 which is hexagonal, MCM-48 which is cubic, and MCM-50 which is lamellar. Second kind of mesoporous materials was first synthesized by the group Pinnavaia and called as HMS and MSU. These materials are silicate based, hexagonal, less ordered. Their pore geometry is worm hole like. This type of materials offers thicker pore walls, higher thermal stability, monodispersed pore diameters, and fast diffusion of reactants. Last kind of mesoporous materials was invented by Stucky and co-workers. In their new synthesis route, amphiphilic di and tri block copolymers were used as structure directing agents and these materials were called as SBA. Having long range order, thicker walls from 3 nm to 9 nm, and large mesodispersed mesopores, these materials are hydrothermally and thermally stable. In these materials, calcination or solvent extraction is easier due to the ionic surfactants. Calcination temperature of M41S family members can be much higher than SBA-15 (On D.T. 2001).

1.3. OBJECTIVES

The subject of this work focused on the development of active and stable catalysts for hydrogen production by reforming of biomass derivatives, such as methane and bio-ethanol.

The main objective of the work is to develop novel catalysts with high activity for the production of hydrogen by reforming of bio-ethanol. To achieve this objective, the scope of the work covers the following studies:

- To find suitable supports for reforming catalysts, resistant to the high reaction temperature and to maintain the metal dispersion of the catalyst during operation.
- To find the suitable metal components (such as Pd, Ni, Ce) and additives as active catalytic components and to find the optimal ratio between them.
- Synthesis of Pd and Ni incorporated MCM-41 type mesoporous catalytic materials for reforming reactions.
- Synthesis of Ni, Ni-Ce, Pd-Ni-Ce incorporated SBA-15 type mesoporous catalytic materials for steam reforming of ethanol reaction.

- Synthesis of Ni, Ce and Ni-Ce incorporated AlMCM-41 type mesoporous catalytic materials for steam reforming of ethanol reaction.

- To find the appropriate working conditions for the reactions offering good catalytic properties.

CHAPTER 2

FUEL OF THE FUTURE: HYDROGEN

2.1. PROPERTIES OF HYDROGEN

Over 60 % of the earth's surface is composed of bounded hydrogen. It is the key part of water. The name 'Hydrogen' is the combination of Greek words "hydro" meaning water and "genes" meaning "generator". Hydrogen appears in different forms in plants, animals, humans, fossil fuels, and other chemical compounds.

In the 16th century, Paracelsus and Van Helmot described Hydrogen as a special gas with the property of inflammability. In 17th century, Robert Boyle produced hydrogen gas while experimenting with iron and acids. Hydrogen was first recognized as a distinct element by Henry Cavendish, and it was named by Lavoisier in 18th century. In the 19th century, the idea of hydrogen could be an energy carrier was developed. In this century, hydrogen also used in production of fertilizer by Carl Bosh. Hydrogen was used in vehicles by Kordesch in 20th century (Midilli A. 2005).

In the 20th century, hydrogen was extensively used in the manufacture of

- Methanol
- Ammonia
- Heating oil
- Gasoline
- Fertilizers
- Glass
- Refined metals
- Vitamins
- Cosmetics
- Semi-conductor circuits
- Lubricants
- Cleaners
- Margarine
- Rocket fuel

After 1974, many studies were conducted to investigate the uses for hydrogen energy and facilitate its penetration as an energy carrier. Subsequently, many industries worldwide began developing and producing hydrogen, hydrogen-powered vehicles, hydrogen fuel cells.

There are several attributes of hydrogen as an energy carrier related to the energy demand, application fields, production techniques, and the following: renewable, clean, securely storable and transportable, not harmful to the environment or life, producible by different techniques and from various sources, broadly utilizable in various applications, and economically usable. The properties and attributes of hydrogen and a comparison of hydrogen with other fuels are presented in Tables 2.1.1 and 2.1.2. Hydrogen is an advantageous transportation fuel because of its utilization efficiency factor, versatility and safety. Water is the only waste emerging from hydrogen oxidation. Therefore, only pollutant of hydrogen fueled vehicle is the engine lubricants.

Table 2.1.1. Properties of Hydrogen (adapted from (Midilli A. 2005))

Property	Value	Unit
Density	0.0838	kg/m ³
Density (liquid)	70.8	kg/m ³
HHV and LHV	141.9-119.90	MJ/kg (liquid)
HHV and LHV	11.89-10.05	MJ/m ³ (volumetric)
Boiling point	20.41	K
Freezing point	13.97	K
Diffusion coefficient in air	0.61	cm ² /s
Specific heat at constant pressure	14.89	kJ/kg K
Ignition limits in air	4-75	% (volume)
Ignition energy in air	0.02	millijoule
Ignition temperature	585	K
Flame temperature in air	2318	K
Explosion energy	58.823	kJ/ g TNT
Flame emissivity	17-25	%
Stoichiometric mixture in air	29.53	%
Stoichiometric air/fuel	34.3/1	kg/kg
Flame velocity	2.75	cm/s

Table 2.1.2. Comparison of key properties of hydrogen and other fuels (adapted from (Midilli A. 2005))

Fuel type	Energy per unit mass (J/kg)	Energy per unit volume (J/m³)	Specific carbon emission (kg C/kg fuel)
Liquid hydrogen	141.90	10.10	0.00
Gaseous hydrogen	141.90	0.013	0.00
Fuel oil	45.50	38.65	0.84
Gasoline	47.40	34.85	0.86
Jet fuel	46.50	35.30	-
LPG	48.80	24.40	-
LNG	50.00	23.00	-
Methanol	22.30	18.10	0.50
Ethanol	29.90	23.60	0.50
Bio diesel	37.00	33.00	0.50
Natural gas	50.00	0.04	0.46
Charcoal	30.00	-	0.50

Advantages of hydrogen are summarized by Midilli et al. as the following:

- Hydrogen is a clean energy carrier and non-toxic .
- There are many production processes for hydrogen including electrolysis of water, sunlight utilization, direct and indirect thermal decomposition, and fossil fuel based processes such as gasification of coal or other heavy hydrocarbons and steam reforming of natural gas or other light hydrocarbons.
- On a mass basis, hydrogen is of a high specific energy (e.g., the energy content of 2.6 kg gasoline is equivalent to that of 1 kg of hydrogen)
- Use of hydrogen as a chemical feedstock is advantageous in the petrochemical, microelectronics, food, ferrous and non-ferrous metal, metallurgical process industries, chemical and polymer synthesis, and as an energy carrier in clean sustainable energy systems.
- Hydrogen can be safely transported in pipelines.
- Hydrogen can be generated from various energy sources, including most renewable ones.

- Compared to electricity, hydrogen can be stored over relatively long periods of time.
- Hydrogen produces non-toxic exhaust emissions upon combustion except at some equivalence ratios
- Utilization of hydrogen in all parts of the economy is possible (e.g., as an automobile fuel and to generate electricity via fuel cells).

Some disadvantages of hydrogen can be summarized as follows:

- Hydrogen, when mixed with air, can burn in lower concentrations and safety concerns could arise.
- Hydrogen storage in liquid form is difficult since liquefaction temperature of it is very low (Midilli A. 2005).

2.2. HYDROGEN PRODUCTION TECHNIQUES

Conventional hydrogen production methods can be summarized by Steinberg et al. as ;

- (1) steam reforming of natural gas,
- (2) gasification of coal by the Texaco process,
- (3) partial oxidation of residual oil,
- (4) steam-iron process,
- (5) gasification of coal by the Koppers-Totzek process,
- (6) water electrolysis.

The advanced processes are given in that study as

- (1) high temperature electrolysis of steam,
- (2) integrated coal gasification and high temperature electrolysis,
- (3) coal gasification and electrochemical shift,
- (4) the HYDROCARB thermal conversion of coal,
- (5) thermal cracking of natural gas (Steinberg M. 1989)

Relation of production techniques and types of utilization of hydrogen is presented schematically in Figure 2.1.1. Figure 2.2.2 shows the conceptual flow sheet of hydrogen production technologies.

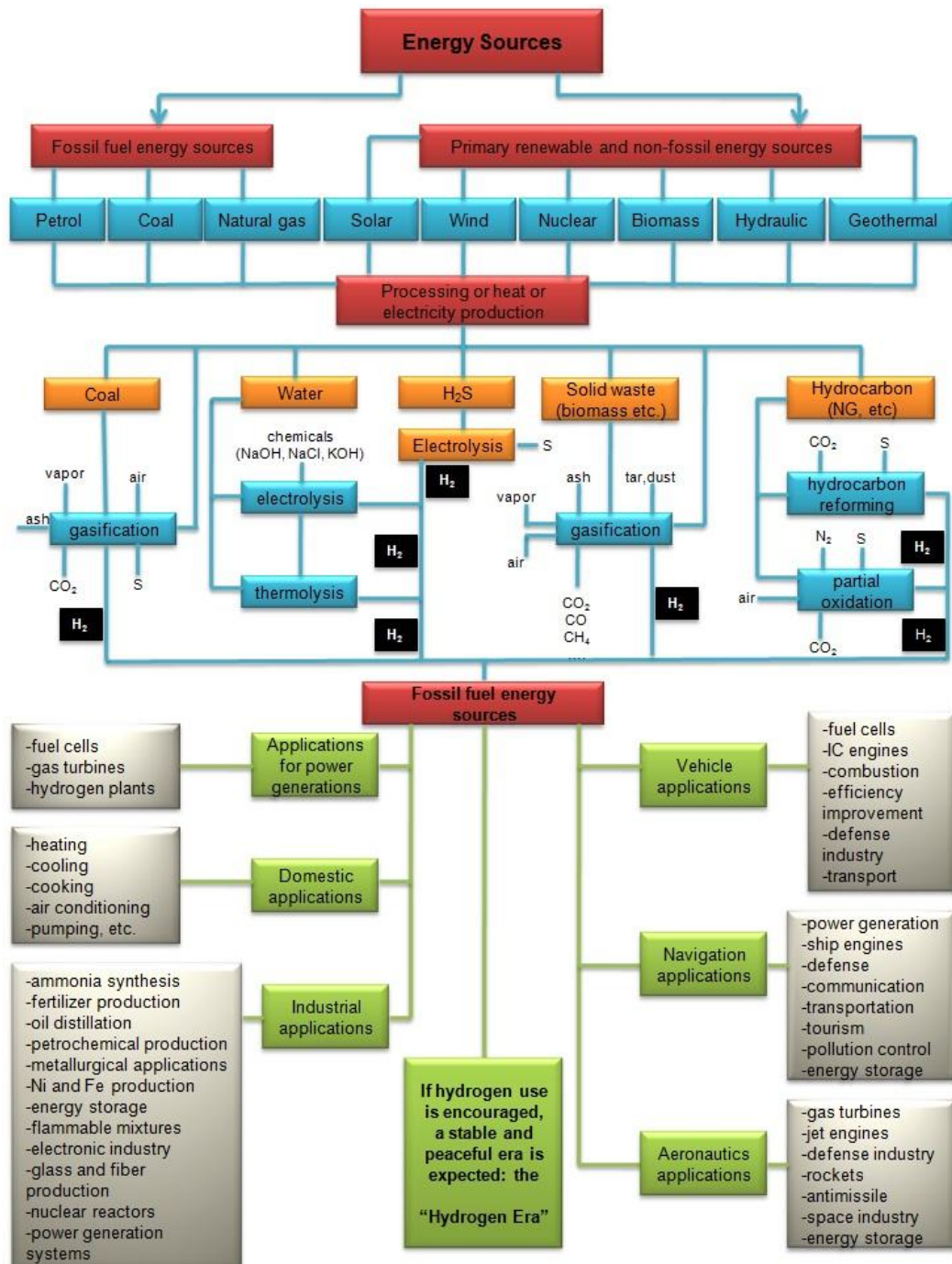


Figure 2.2.1. Relation of production techniques and types of utilization of hydrogen (adapted from Midilli et al., 2005).

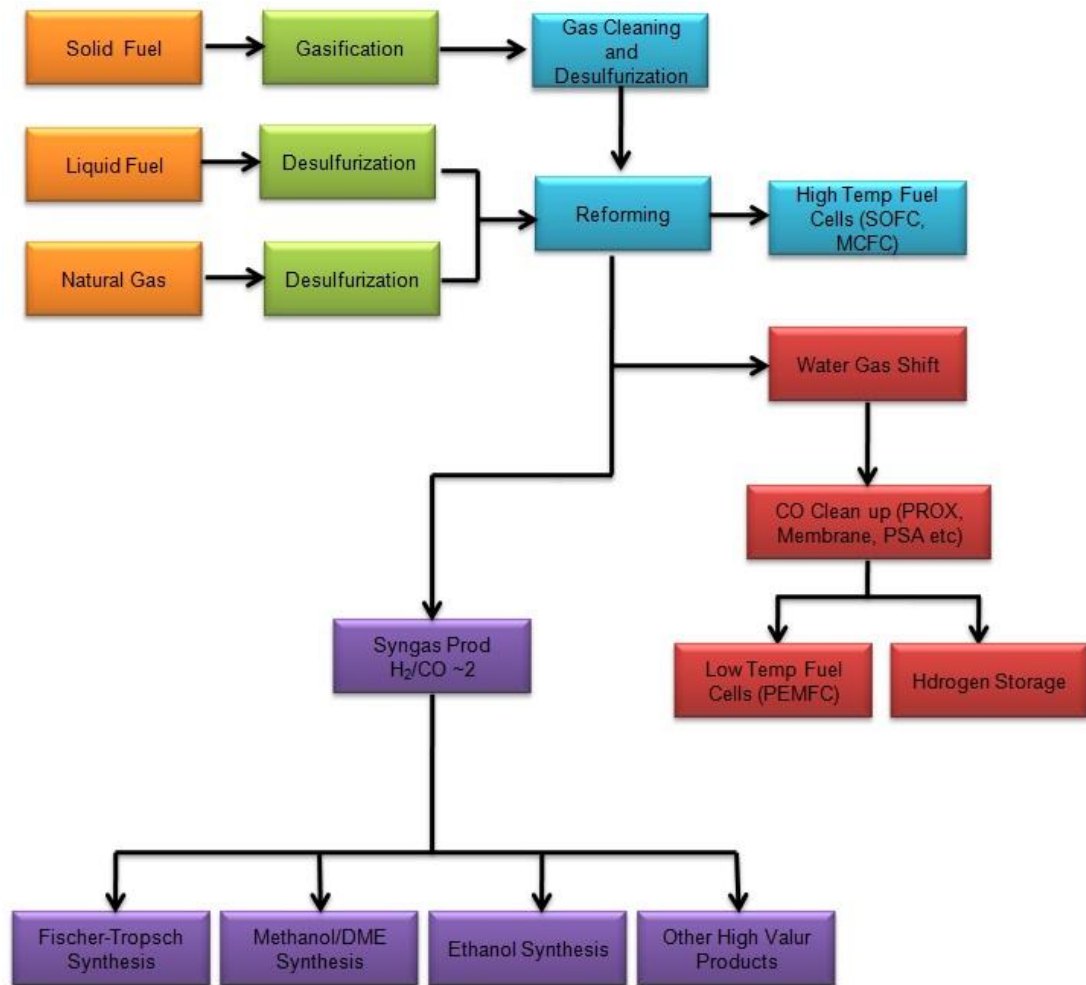
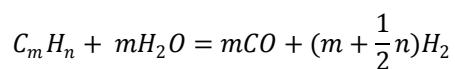


Figure 2.2.2. Fuel processing of gaseous, liquid and solid fuels for hydrogen production (adapted from (Halladay J.D. 2009))

Hydrocarbon reforming reactions

The reforming, WGS, and oxidation reactions can be generalized as follows for hydrocarbon and methanol fuels (Halladay J.D. 2009):

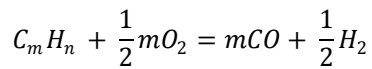
Steam reforming



ΔH = hydrocarbon dependent, endothermic



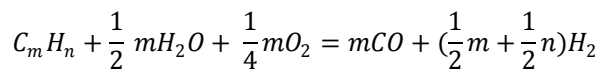
Partial oxidation



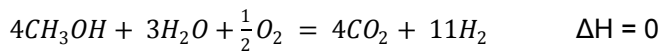
ΔH = hydrocarbon dependent, exothermic



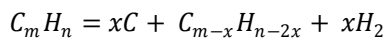
Autothermal reforming



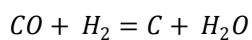
ΔH = hydrocarbon dependent, thermally neutral



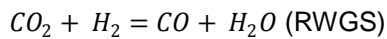
Carbon (coke) formation



ΔH = hydrocarbon dependent



Water-gas-shift



CO oxidation



Thermochemical water splitting, plasma and solar photovoltaic-water electrolysis, high energy nuclear radiation, and by-product hydrogen from the chemical industry are also methods under research and development. Another classification for hydrogen production according to the primary method is given in Table 2.2.1 .

Table 2.2.1. Major thermal, biological, and electrochemical methods for hydrogen production (adapted from (Hydrogen Production Overview n.d.))

Primary Method	Process	Feedstock	Energy
Thermal	Steam Reformation	Natural Gas	High temperature steam
	Gasification	Coal, Biomass	Steam and oxygen at high temperature and pressure
	Thermochemical Water Splitting	Water	High temperature heat from advanced gas-cooled nuclear reactors
	Pyrolysis	Biomass	Moderately high temperature steam
Biological	Photobiological	Water and algae strains	Direct sunlight
	Fermentative Microorganisms	Biomass	High temperature heat
	Anaerobic Digestion	Biomass	High temperature heat
Electrochemical	Electrolysis	Water	Electricity from wind, solar, hydro and nuclear
	Photoelectrochemical	Water	Direct sunlight
	Electrolysis	Water	Electricity from coal or natural gas

Steam reforming is a method for hydrogen production which separates hydrogen from the carbon components in methane, methanol and ethanol etc. by using thermal energy. Fuels with carbon components react with steam on the catalytic surface. Decomposition of carbon compounds into hydrogen and carbon monoxide is followed by a shift reaction which causes

conversion of carbon monoxide and water to carbon dioxide and hydrogen (Fatsikostas A.N. 2004).

Electrolysis is a method of hydrogen production by separating the elements of water-H and oxygen (O)-by charging water with an electrical current. Conductivity of the water is improved by the addition of an electrolyte such as salt and increased the efficiency (Pierre R. Roberge 2012)

Steam electrolysis is a variational electrolysis process to the conventional one. To split the water in the steam electrolysis, heat is supplied to split the water and this makes the steam electrolysis process more efficient than conventional electrolysis (Pierre R. Roberge 2012).

Assisted by heat, bromine or iodine chemicals are used in thermochemical splitting of water and water molecule is, therefore, splitted. Entire process is completed usually in several steps, usually three.

Photoelectrochemical processes use two types of electrochemical systems for hydrogen production. Soluble metal complexes are used as catalysts in one process while in the other process, semiconductor surfaces are used. Water splitting reaction is driven by electrical charge produced from the absorption of solar energy upon dissolved soluble metal complex. This process mimics photosynthesis. (Halladay J.D. 2009)

Algae and bacteria are used by biological and photobiological processes to produce hydrogen. Solar energy is absorbed by the pigments in certain types under specific conditions. In water splitting, the function of the enzyme in the cell is a catalyst. Although some bacteria are able to produce hydrogen, they need a substrate to grow on. These organisms not only produce hydrogen but also reduce the pollution as well.

Catalytic reforming of methane has also increasing interest for syngas production (Rostrup-Nielsen et al., 1993). Nobel metal supported catalysts (Ferreira A.P. 2007); (Gheno S.M. 2003), supported Ni catalysts (A. K. Sener C. 2008) and Dual catalysts like PtNi (Pawelec B. 2007) were studied in this process.

Steinberg et al. concluded that the most economic near-term process among the conventional processes is the steam reforming of methane. They also stated that coal gasification and partial oxidation processes are two to three times more expensive than the steam reforming of natural gas (Steinberg M. 1989).

(Steinberg M. 1989) also summarized new technologies economy as "New gas separation processes, such as pressure swing adsorption, improve the economics of these conventional

processes. Integration of hydrogen production with other end-use processes has an influence on the overall economics of the system. The advanced high temperature electrochemical systems suffer from high electrical energy and capital cost requirements. The thermochemical and high energy water splitting techniques are inherently lower in efficiency and more costly than the thermal conversion processes. The thermal cracking of methane is potentially the lowest cost process for hydrogen production. This is followed closely by the HYDROCARB coal cracking process. To reach full potential, the thermal cracking processes depend on taking credit for the clean carbon fuel by-product. As the cost of oil and gas inevitably increases in the next several decades, emphasis will be placed on processes making use of the world's reserve of coal.”

There are three primary techniques used to produce hydrogen from hydrocarbon fuels: steam reforming, partial oxidation (POX), and autothermal reforming (ATR). Table 2.2.2 summarizes the advantages and disadvantages of these processes. At the end of the reforming process, a gas stream composed of hydrogen, carbon monoxide and carbon dioxide.

Table 2.2.2. Comparison of reforming Technologies (taken from Holladay et al.2009)

Technology	Advantages	Disadvantages
Steam reforming	Most extensive industrial experience Oxygen not required Lowest process temperature Best H ₂ /CO ratio for H ₂ production	Highest air emissions
Autothermal reforming	Lower process temperature than POX Low methane slip	Limited commercial experience Requires air or oxygen
Partial oxidation	Decreased desulfurization requirement No catalyst required Low methane slip	Low H ₂ /CO ratio Very high processing temperatures Soot formation/handling adds process complexity

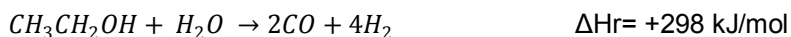
CHAPTER 3

STEAM REFORMING OF ETHANOL

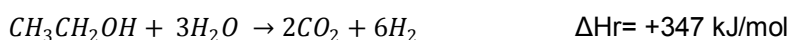
3.1. REACTION AND CONDITIONS

When compared with other fuels such as gasoline, methanol, methane, LPG, and dimethyl ether, ethanol is a promising candidate as a source for renewable hydrogen with several advantages. The mature process to produce ethanol is the fermentation of glucose and economics of this process are known. Lower carbon dioxide emissions, ease of storage and distribution, and environmental friendliness are the attractive attributes of ethanol. Furthermore, ethanol is the most available bio-fuel of nowadays. The greenhouse gas emissions of ethanol produced from corn or sugar cane is slightly lower than the conventional gasoline. However, less amount of petroleum inputs are necessary for production of ethanol compared to gasoline. In a substantial way, ethanol produced from cellulosic materials could reduce both petroleum inputs and gas emissions. There are increasing number of usage of ethanol at conventional vehicles in Asia, Europe, and America. Therefore, investigation of different options of hydrogen production from ethanol is very reasonable because infrastructure and supply for ethanol distribution is building up today .

Steam reforming is an endothermic process

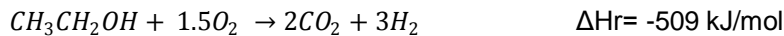
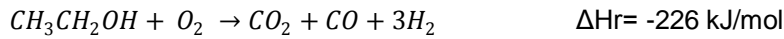
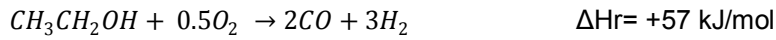


Complete steam-reforming operation is given by the following reaction

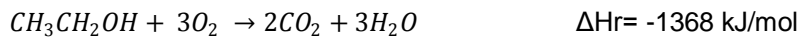


whereas the maximum hydrogen yield of ethanol steam reforming can be fixed by 6 mole H₂ / mole ethanol.

Partial oxidation is as indicated by the name, the incomplete oxidation of the feed. This incomplete oxidation generates heat and fractionates the feed to smaller molecules.



As the oxygen content in the feed stream is increased, the feed is completely oxidized and the maximum heat output is achieved.



Steam reforming of ethanol have been studied extensively in the literature by means of the reaction pathways and thermodynamics of [(Fatsikostas A.N. 2004), (Ni M. 2007), (Ni M. 2007) have summarized the possible reaction pathways of ethanol steam reforming (Table 3.1.1). It can be seen that hydrogen production varies significantly with different reaction pathways. In order to maximize hydrogen production, it is crucial to ensure sufficient supply of steam and to minimize ethanol dehydration and decomposition.

Ni et al. reported that catalysts play a crucial role in the reactivity toward complete conversion of ethanol. However, each catalyst induces different pathways and, therefore, the selection of a suitable catalyst plays a vital role in ethanol steam reforming for hydrogen production. Active catalysts should maximize hydrogen selectivity and inhibit coke formation as well as CO production (Ni M. 2007).

Table 3.1.1. Possible reaction pathways of ethanol steam reforming (adapted from (Ni M. 2007))

Reaction	Equation	Remarks
Sufficient steam supply	$C_2H_5OH+3H_2O \rightarrow 2CO_2+6H_2$	Ideal pathway, the highest hydrogen yield
Insufficient steam supply	$C_2H_5OH+H_2O \rightarrow 2CO+4H_2$ $C_2H_5OH+2H_2 \rightarrow 2CH_4+H_2O$	Undesirable products, lower hydrogen production
Dehydrogenation	$C_2H_5OH \rightarrow C_2H_4O+H_2$	Reaction pathways for hydrogen production in practice
Acetaldehyde decomposition	$C_2H_4O \rightarrow CH_4+CO$	
Acetaldehyde steam reforming	$C_2H_4O+H_2O \rightarrow 3H_2+2CO$	
Dehydration	$C_2H_5OH \rightarrow C_2H_4+H_2O$	Undesired pathway, coke formation
Coke formation	$C_2H_4 \rightarrow \text{polymeric deposits(coke)}$	
Decomposition	$C_2H_5OH \rightarrow CO+ CH_4+H_2$ $C_2H_5OH \rightarrow CO+ CH_4+H_2$ $2C_2H_5OH \rightarrow C_3H_6O+ CO+3H_2$ $C_2H_5OH \rightarrow 0.5CO_2+ 1.5CH_4$	Coke formation, low hydrogen production
Reaction of decomposition products		
Methanation	$CO+3H_2 \rightarrow CO+ CH_4+H_2$	
	$CO_2+4H_2 \rightarrow CH_4+2H_2O$	
Methane decomposition	$CH_4 \rightarrow 2H_2+C$	
Boudouard reaction	$2CO \rightarrow CO_2+C$	
Water gas shift reaction (WGSR)	$CO+ H_2O \rightarrow CO_2+H_2$	Reduce coke formation, enhance hydrogen production

3.2. CATALYSTS FOR STEAM REFORMING OF ETHANOL

Noble metal catalysts are well known for their high catalytic activities. For ethanol steam reforming, Rh, Ru, and Pt have been extensively investigated by (Liguras D.K. 2003), (Sheng P.Y. 2007), (Erdohelyi A. 2006), (Liberatori J.W.C. 2007), (Tosti S. 2008).

At high temperatures, ethanol steam reforming occurs rather than methanol steam reforming and the carbon monoxide in the effluent is higher in the former. There are many studies focused on steam reforming whereas few of them deal with partial oxidation reforming and autothermal reforming (Table 3.2.1, 3.2.2).

For practical use, one of the key factors in ethanol reforming catalysts is the durability. The main reasons for deactivation are the metal sintering and coke formation. When the appropriate reforming operating conditions are chosen, deactivation can be suppressed. Although several reports have calculated the thermodynamic compositions of the ethanol steam reforming process including coke formation, a thorough investigation of autothermal ethanol steam reforming and partial oxidation were not included.

As reported by Duan and Senkan (Duan S. 2005) noble metals like Pt and Pd are also quite active in ethanol conversion. Besides ethanol conversion activity, hydrogen selectivity, stability and minimization of coke formation are some of the desired properties of ethanol reforming catalysts. Besides the reforming reaction, dehydration, dehydrogenation and cracking reactions of ethanol are expected to yield ethylene, acetaldehyde and methane, respectively. Formation of these side products are generally considered to favor coke formation. Addition of small amounts of noble metals to nickel based catalysts was considered to have a positive effect on the minimization of coke formation (Profeti L.P.R. 2009). Our recent work on dry reforming of methane with Pd and Ni impregnated bimetallic MCM-41 type catalysts also showed the positive effect of Pd incorporation on catalyst stability (P. B. Damyanova S. 2009).

Table 3.2.1. Nobel metal catalysts for steam reforming of ethanol (adapted from (Ni M. 2007))

Catalyst	Support	Temperature (K)	Steam/Ethanol molar ratio	Ethanol conversion (%)	Hydrogen selectivity (%)	Reference
Rh (1 wt%) (2 wt%)	γ -Al ₂ O ₃	1073	3:1	100	~95	(Liguras D.K. 2003)
Ru (1 wt%) (5 wt%)				100	~96	
Pt (1 wt%)				60	~65	
Pd (1 wt%)				55	~50	
Rh (5 wt%)	γ -Al ₂ O ₃		8:4:1	100% at the beginning 43% 100 h after operation	Unknown	(Cavallaro S. 2003)
Rh (3 wt%)	MgO	923	8:5:1	99 (10 h)	91	(Frusteri F. 2004)
Pd (3 wt%)				10 (10 h)	70	
Ni (21 wt%)				42 (10 h)	97	
Co (21 wt%)				55 (10 h)	92	
Ru (1 wt%)	CeO ₂	723	Not known		57 (20 min) 25 (100 min)	(Erdohelyi A. 2006)
Rh (1 wt%)					82 (20 min) 56 (80 min)	

Table 3.2.2. Non-nobel metal catalysts for steam reforming of ethanol (taken from (Ni M. 2007))

Catalyst	Support	Temperature (K)	Steam/Ethanol molar ratio	Ethanol conversion (%)	Hydrogen selectivity (%)	Reference	
Ni (20 wt%)	La ₂ O ₃	773	3:1	35	70	(Fatsikostas A.N. 2004)	
		1073		~100	95		
	γ-Al ₂ O ₃	973		77	87		
		1073		100	96		
Ni (20.6 wt%)	Y ₂ O ₃	523	3:1	81.9	43.1	(Sun J. 2004)	
Ni (16.1 wt%)	γ-Al ₂ O ₃			76	44		
Ni (15.3 wt%)	La ₂ O ₃			80.7	49.5		
Ni (35 wt%)	γ-Al ₂ O ₃	773	6:1	100	91	(Comas J. 2004)	
Ni (3.8 wt%)	Al ₂ O ₃ (heat treatment at 823 K)	723	3:1	96.6	61.5	(Akande A.J. 2005)	
		923		100	89.0		
	Al ₂ O ₃ (heat treatment at 973 K)	723		100	0		
		823		99.2	67.3		
		923		100	87.4		
Ni (10 wt%)	γ-Al ₂ O ₃	923	8:1	100	78.2	(Aboudheir A. 2006)	
				100	82.2		
	La ₂ O ₃			100	89.3		
	ZnO			100	89.1		
Co (10 wt%)	ZnO	623	4:1	100 (75 h)	73.4	(P. P. Llorca J. 2003)	
Co (10 wt%), addition with Na	ZnO	673	13:1				
				Na (0.06 wt%)	100		72.1
				Na (0.23 wt%)	100		73.4
Co (8 wt%) (18 wt%) (8 wt%) (18 wt%)	Al ₂ O ₃	673	3:1	74	60-70	(Batista S.B. 2004)	
				99	63-70		
	SiO ₂			89	62-70		
				97	69-72		

CHAPTER 4

SILICEOUS AND NON-SILICEOUS MESOPOROUS MATERIALS AS CATALYST SUPPORT

4.1. ORDERED MESOPOROUS MOLECULAR SIEVES

In the past half century, development of inorganic porous materials has been so fastly despite the fact of crystalline or amorphous structure of inorganic porous materials. These materials find wide applications as catalyst, adsorbent, energy material, ion exchanger, etc. Their adsorption and catalytic abilities were enhanced by high surface area and open structure and synthesis of desirable property and structure is possible. Zeolites, pure silica molecular sieves, microporous phosphates are the examples of inorganic porous materials.

Porous materials are classified with respect to their pore size diameters. According to International Union of Pure and Applied Chemistry notation, materials with pore diameters less than 2 nm are microporous materials and materials with pore diameters greater than 50 nm are macroporous materials. Mesoporous materials have the pore diameters in between. The advantages of mesoporous materials come from their pore size and they break the diffusion limitations of microporous materials. Pore size and shape properties of porous materials could be tuned and controlled and pore properties are the most significant structural parameters of porous materials. Pore properties could be studied with nitrogen adsorption (Kresge C.T. 1992).

M41S mesoporous materials have large uniform channels ranging from 1.5 to 10 nm. There are three main members of M41S family which are MCM-41 (short for Mobil Crystalline Matter No.41) with a one dimensional hexagonal array of uniform mesopores, MCM-48 with three dimensional cubic channels, and MCM-50 with uniform lamellar phases [(Taguchi 2005), (Oye G. 2001), (Ciesla U. 1999)]. Among these mesoporous materials, MCM-41 and MCM-48 have very potential in catalytic applications. The mesoporous structure of the lamellar phase, MCM-50, was reported to collapse upon calcination. These mesoporous materials have long range order, and high surface area values, above 700 m²/g These

properties make them as attractive catalyst supports. Therefore, they are very promising for catalysis applications (Xu J. 1999).

Studies of mesoporous materials were started as early as 1970s and synthesis of these materials have taken attractions after the report of M41S family. M41S materials are shown in Figure 4.1.1.

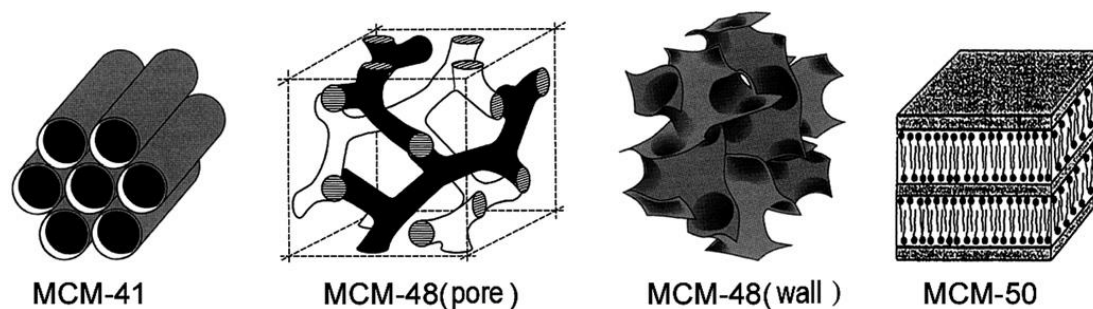


Figure 4.1.1. M41S family materials (Huo Q. 2011)

M41S family materials offer a pore diameter of 2 nm to 20 nm and have an amorphous pore walls. Their structure is ordered and synthesis of them is conducted in a temperature range of 25-150 °C. To synthesize mesoporous silica, template was the surfactant which is an amphilic molecule. Surfactant molecules turn into micelles to keep the energy minimum and these micelles serve as real templates for mesoporous materials.

The properties of mesoporous materials which differentiate mesoporous materials from other porous materials are as follows,

- Well- defined pore system
- Various framework composition
- High thermal and hydrothermal stability
- Various controllable morphologies
- Wide application potential

4.2. SYNTHESIS OF MESOPOROUS MATERIALS

In synthesis of mesoporous materials, four major component are necessary; inorganic precursor, organic template molecule, solvent, and acid or base catalyst. By arranging relative rates of delicate interplay of basic processes, desired structure and morphology can

be obtained. These processes are self assembly of organic template molecules, sol-gel chemistry, and specific interaction, namely.

Mobil researchers have shown that final pore structure of the mesoporous materials was affected by the relative concentration of species which are present in the synthesis solution (Kresge C.T. 1992), (Beck J.S. 1992). Optimal conditions of modified MCM-41 synthesis have been found and studied by many researchers

There are several silica sources such as silica gel, tetraethyl orthosilicate (TEOS), ludox, fumed silica, sodium silicate ($\text{Na}_4\text{O}_4\text{Si}$) and sodium meta-silicate (Na_2SiO_3) used in the synthesis of mesoporous materials. Among the silica sources, TEOS is the usually used for acidic conditions and other sources are used for the basic conditions in mesoporous material synthesis [(Oye G. 2001), (Gucbilmez Y. 2006)].

Surfactant which stands for surface active agent is an amphiphilic chemical compound and composed of two parts. One part is polar which is hydrophilic and dipole or charged group and other part is non-polar which is hydrophobic and generally hydrocarbon or halocarbon chain. Due to the its hydrophilic and hydrophobic nature, surfactant molecule organizes itself in solution in such a way as to minimize contact between incompatible ends (Sener 2006)

The most commonly used templating agents for the synthesis of MCM-41 are the ionic surfactants such as cetyltrimethylammonium bromide (CTMABr) and cetyltrimethylammonium chloride (CTMACl). MCM-41 formation is resulted from the use of low molecular weight amphiphiles with the molecular formula $\text{C}_n\text{H}_{2n+1}(\text{CH}_3)_3\text{N}^+$ ($n=8-22$) or $\text{C}_n\text{H}_{2n+1}\text{C}_5\text{H}_5\text{N}^+$ ($n=12$ or 16). Electrostatic interactions between the silicate species which are negatively charged and surfactants which are positively charged in solution play a key role in formation mechanism of MCM-41 (Huo Q. 2011).

By changing the alkyl chain length of the surfactant molecules, modification of the pore sizes of MCM-41 in the range of 2 nm – 10 nm is possible. As the lengths of the surfactant alkyl chains increase, pore diameters increase (Beck J.S. 1992).

In then synthesis of the mesoporous materials, several types of surfactants are used. They are classified as cationic, anionic and neutral surfactants. The types of surfactants are listed in Table 4.2.1. Alkyltrimethylammonium hydroxides are mostly used surfactants. Depending on the synthesis conditions, they give rise the hexagonal, cubic or lamellar structures (Sayari A. 1996)

Table 4.2.1. Surfactants for the synthesis of mesostructures (adapted from (Wieslaw J. 2005))

Surfactant Charge	Surfactant Type	Interaction Type	Examples/Structures
Cationic	Alkyl-NR ₃ ⁺	S ⁺ I ⁻	M41S (MCM-41, MCM-48, MCM-50) FSM-16
	Alkyl-NR ₃ ⁺	S ⁺ XI ⁺	SBA-3
	Alkyl-NR ₃ ⁺ , R=Et	S ⁺ XI ⁺	SBA-1
	Di-(N-quaternary) ²⁺	S ⁺ I ⁻	MCM-48, SBA-6, SBA-8
Anionic	Alkyl-OPO ₃ H ₂ ⁻	S ⁺ I ⁻	Mainly lamellar or disordered; Al, Pb, Fe, Mn, Ni, Co, etc.
	R-CO ₂ H	S ⁺ I ⁻	Al (sec-OBu) ₃ – organized mesoporous alumina
Neutral	Amine	N ⁰ I ⁰	HMS and MSU silicas (worm-like structures, similar to M41S and can be modified similarly)
	Poly(ethylene)oxide Alkyl-(EO) _n , EO=ethylene oxide	S ⁰ I ⁰	With TMOS (true LCT)
	Amine	S ⁰ I ⁰	Ligand assisted; amine bonding to Nb and Ta alkoxides
	Alkyl-(EO) _n , EO=ethylene oxide	(S ⁰ H ⁺)(XI ⁺)	SBA-11, SBA-12, SBA-14
	Triblock copolymers	(S ⁰ H ⁺)(XI ⁺)	SBA-15, SBA-16, FDU-1
		S ⁰ I ⁰	Al(sec-OBu) ₃ (organized mesoporous alumina)

Interaction of silica and surfactant interfaces (synthesis pathways) according to the type of interaction between organic template and inorganic precursor is shown in Figure 4.2.1.

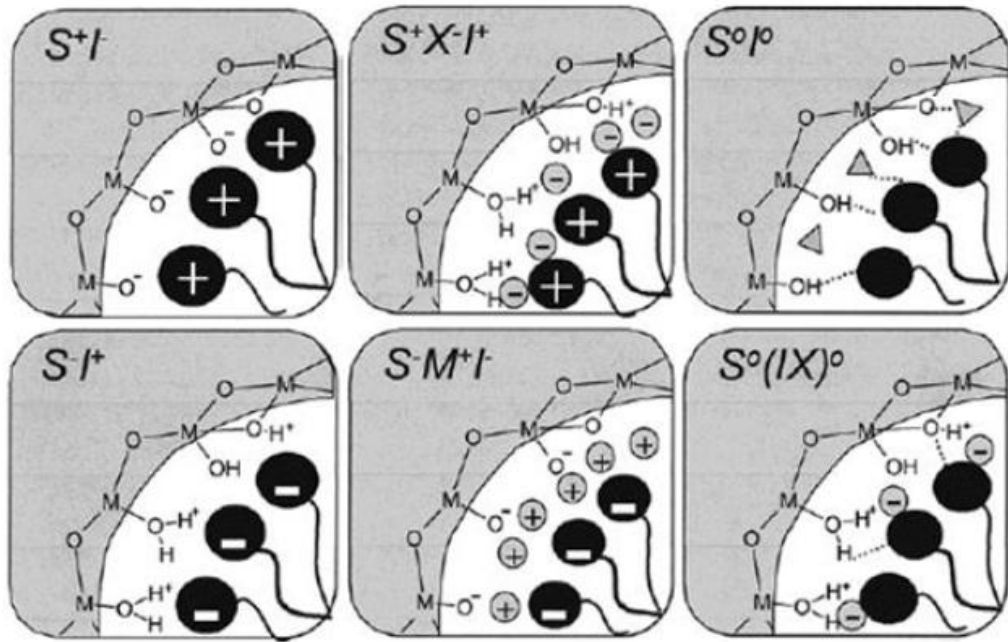


Figure 4.2.1. Schematic representation of different types of silica-surfactant interfaces (taken (Huo Q. 2011))

In the synthesis of ordered mesoporous materials, Taguchi et al. has reported that polyethylene oxide which is a versatile surfactant was used. Use of poly mono ethers were recommended to be used in the material synthesis since they could result in unordered worm-like or ordered hexagonal pore sizes around 5 nm. Ability to form liquid crystal structures were supplied with generally used surfactant of the tri-block co-polymers consisting of poly(ethylene oxide)_x-poly-(propylene oxide)_y-poly(ethylene oxide)_x, (PEO)_x(PPO)_y-(PEO)_x, (trade name: Pluronic). Use of these surfactants in the mesoporous material synthesis have shown that different ordered products can be obtained with various framework compositions. Here, mesostructured assembly was formed by the interaction of cationic silicate species and EO (ethylene oxide) unit (Taguchi 2005).

Surfactant packing parameter g , is used in order to predict the mesophases to an extent. The parameter is defined by the formula (Taguchi 2005)

$$g = V/a_0h \quad (\text{eqn. 4.2.1})$$

where V is the volume of hydrophobic tail, a_0 is the effective headgroup area and h is the kinetic length of the hydrophobic tail of the surfactant (Figure 4.2.2).

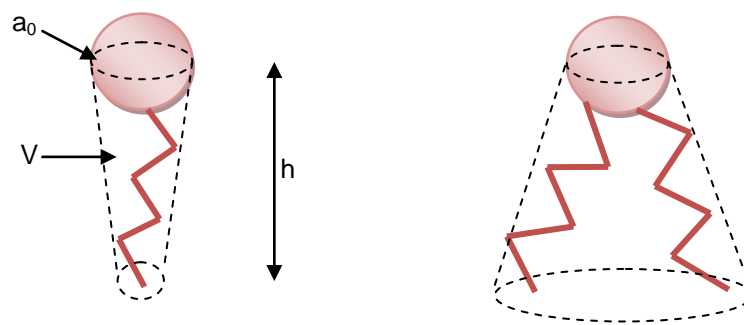


Figure 4.2.2. Schematical representation of surfactant (Gao C. 2009)

There are different structures of mesophases. These structures are summarized in Table 4.2.2 by means of plane groups. In lamellar phases removal of the surfactant cause the collapse of the structure. 2D hexagonal structure is formed by the arrangement of cylindrical mesopores. In the bicontinuous cubic structure hydrophilic/hydrophobic interface curvature is low and mean curvature is zero. Cage type cubic structures are formed by spherical micelles of surfactants and curvature of hydrophilic/hydrophobic interface is high. Cage type hexagonal structures intergrow with Fm3m due to the similarity of these structures in the packing model. Also there are other mesophases with the space groups of $P4_2/mnm$, $P4/mmm$, $c2mm$ and $Pmmm$ etc.

Table 4.2.2. Structures and packing parameter of mesoporous materials (adapted from (Gao C. 2009))

Structure	Plane Groups	g	Examples
Lamellar (L)	L	1	MCM-50
2D Hexagonal	$P6mm$	1/2	MCM-41, SBA-15, SBA-3, AMS-3
Bicontinuous Cubic	$Ia3d$, $Pn3m$, $Im3m$	1/2-2/3	MCM-48, KIT-6, FDU-5, AMS-6
Cage-Type Cubic	$Pm3n$, $Fm3m$, $Im3m$, $Fd3m$	1/3	SBA-1, SBA-6, SBA-16
Cage-Type Hexagonal	$P6_3/mmc$	1/3	

From the discovery of M41S family materials (MCM-41, 48, 50), several other mesostructured materials with different morphologies and compositions in a wide synthetic range from strongly acidic conditions to highly basic conditions by using several surfactants.

Among the mesoporous materials, two dimensional hexagonal morphologies were obtained with MCM-41, SBA-15, FSM-16, and SBA-3. A typical MCM-41 was synthesized by the surfactant $C_{16}H_{33}(CH_3)_3OH/Cl$ solution with sodium silicate as silicate source. A high quality MCM-41 material exhibits a main peak at around 2° and several $hk0$ diffraction peaks at small angle as shown in Figure 3. N_2 adsorption desorption isotherm of MCM-41 is a type IV isotherm. MCM-41 has very large surface area ($>1000\text{ m}^2/\text{g}$) and pore volume ($>0.7\text{ cm}^3/\text{g}$).

In MCM-41 synthesis, solvent is the water and amount of water in the synthesis mixture is critical.

Acids or bases can be used as mineralizing agents and function of mineralizing agent is to mineralize the silica sources into soluble species with suitable morphologies. These morphologies could form various periodic mesophases by associating with surfactant molecules. Examples to basic additives are sodium hydroxide, tetraethylammonium hydroxide, or tetramethylammonium hydroxide whereas examples to acidic additives are HNO_3 , HCl , or HF (Oye G. 2001).

4.2.1. Formation Mechanism of MCM-41

The original MCM-41 synthesis was carried out in water under alkaline conditions. The function of surfactants which are organic molecules as templates is to form an ordered inorganic-organic composite material. Porous silicate based structural network is obtained after calcination in which surfactant is removed. In the formation of the inorganic-organic composite materials, electrostatic interactions between the surfactants which are positively charged and silicate species which are negatively charged play a very important role (Beck J.S. 1992).

For the MCM-41 synthesis, first formation mechanism was proposed and described by Beck et al. (1992) and this mechanism was called as liquid crystal templating (LCT) mechanism which is shown in Figure 4.2.3. Beck et al. proposed that in the formation of MCM-41, surfactant molecules are organized into the liquid crystals and liquid crystals serve as templates. As a first step, formation of a micellar rod is occurred and formations of hexagonal array of rods from inorganic silica-alumina or silica are incorporated around rod-

like structures (Figure 4.2.3). Alternative pathway was also proposed by Beck et al. and formation of MCM-41 is shown in Figure 4.2.3. This mechanism is a silicate anion initiated mechanism and supermolecular structure is formed by the combination of surfactant molecules with anionic silicate species.

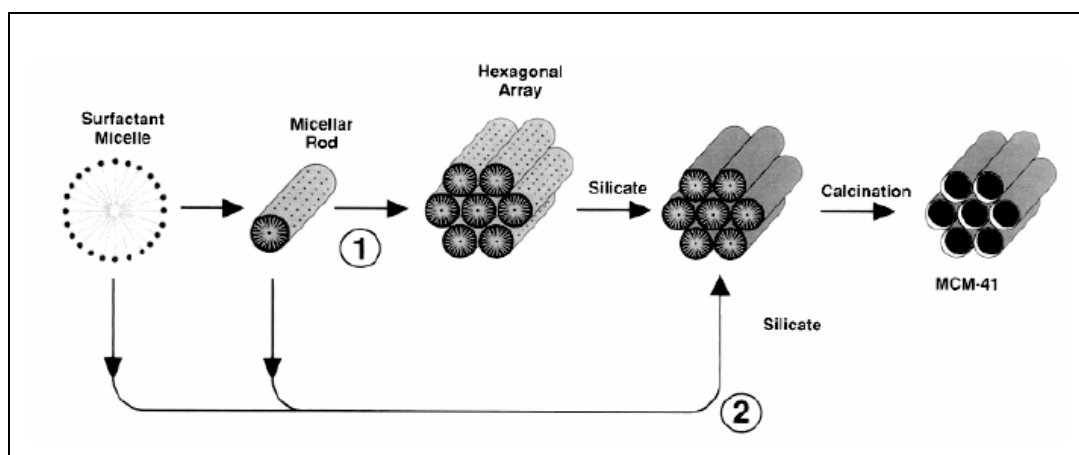


Figure 4.2.3. Liquid-crystal templating (LCT) mechanism proposed by Beck et al. (1992) showing two possible pathways for the formation of MCM-41: (1) liquid-crystal-initiated and (2) silicate-initiated.

Stucky and coworkers (Monnier 1993), (Firouzi D. 1995) proposed a formation mechanism and named as cooperative organization of organic and inorganic molecular species into three dimensional structured arrays. Proposed formation mechanism consists of three reaction steps (Figure 4.2.4). In the first reaction step, dynamic equilibrium between cylindrical or spherical micelles and single molecules is assumed to occur and silica addition is made. In the second reaction step, exchange of OH^- or Br^- anions with silicate species occurs after the addition of silica source and inorganic-organic ion pairs are formed by aggregation of the ion pairs into a new mesophase and dissociation of the organic micelles. In the third and last reaction step, number of surfactant molecules are controlled by the multidentate interaction of silicatropic liquid crystal assembly process and interface packing density and biphas morphology can be determined (Xu J. 1999)

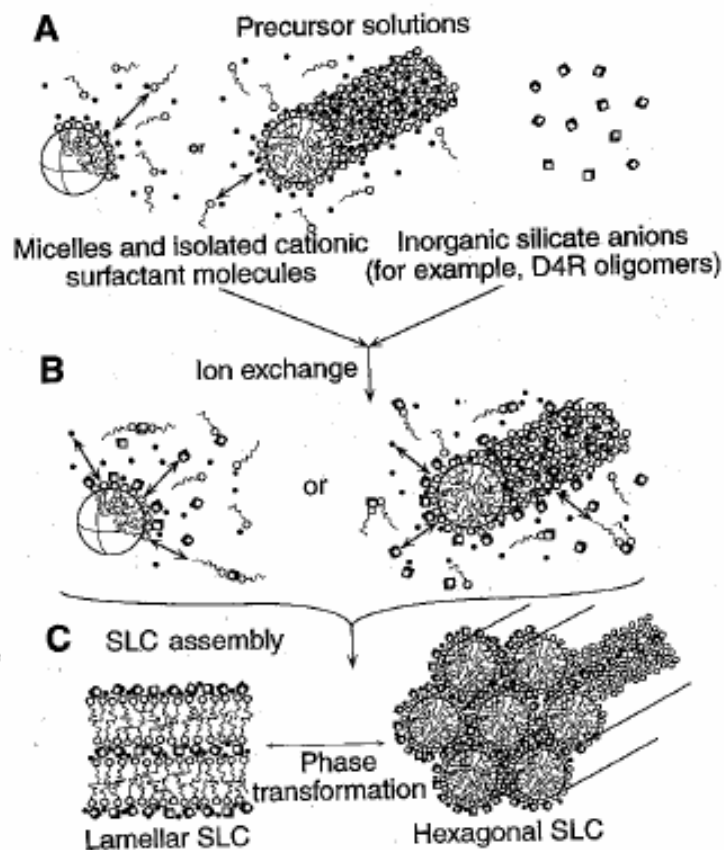


Figure 4.2.4. Cooperative formation pathway (Firouzi D. 1995)

Length of the alkyl chain of the surfactant used in the experiments usually controls the mesopore size of these kinds of materials, primarily. However, addition of organic molecules such as n-alkanes, aromatics, or fatty acid could enlarge the pores and expansion of pores could occur. Tuning of the pore size between the short and long chain surfactants is possible with mixing two alkyl ammonium surfactants having different chain lengths.

4.3. TYPICAL MESOPOROUS STRUCTURES

Mesoporous structures of materials can be determined and classified with respect to their pores and their arrangement in the structure. Synthesis conditions such as materials source and Ph and surfactant family types used in the material preparation can also be used in classification of these structures. Different than zeolites, order of atoms is not considered in the classification of mesoporous materials (Collart O. 2003).

Synthesis of mesoporous materials in the acidic media has been made by Stucky and his coworkers. They identified and named these materials as the cubic SBA-1, SBA-11, and SBA-16 (Huo Q.(***) 1994), hexagonal SBA-3 and SBA-15 (Zhao D. 1998), the 3D

hexagonal SBA-2 and SBA-12 and the rectangular SBA-8 (SBA is the short form of Santa Barbara acid and the number following is the internal agreements of the Santa Barbara laboratory) (Taguchi 2005).

Different structured materials have been also synthesized such as MSU, KIT-1, and HSM. Mesoporous structure is obtained in these materials. However, distribution of mesopores is more random than the other types of mesoporous materials. Some researchers detected the porosity of these materials as wormholes (Collart O. 2003)(Table 4.3.1).

Table 4.3.1. Structure and pore diameter of typical mesoporous silica materials (adapted from (adapted from (Gao C. 2009))

Mesoporous Solid	Space Group	Pore Diameter (nm)	Structure
MCM-41	<i>P6mm</i>	2-5	Hexagonal 1D channel
MCM-48	<i>la3d</i>	2-5	Bicontinuous 3D
SBA-15	<i>P6mm</i>	5-10	Hexagonal 1D channel
MSU	<i>P6mm</i>	2-5	2D hexagonal
HMS	<i>P6mm</i>	2-5	Hexagonal

MCM-41

Among the M41S family members, MCM-41 is one of the most discussed and characterized structures in the literature because of promising and interesting structural properties. MCM-41 is composed of an amorphous silicate framework with hexagonal pores(Figure 4.3.1.a) Its structure is unidirectional and arranged in a honeycomb structure. Such a special arrangement can be well observed with TEM analysis as shown in Figure 4.3.1.b [(Ciesla U. 1999), (Kresge C.T. 1992), (Beck J.S. 1992)].

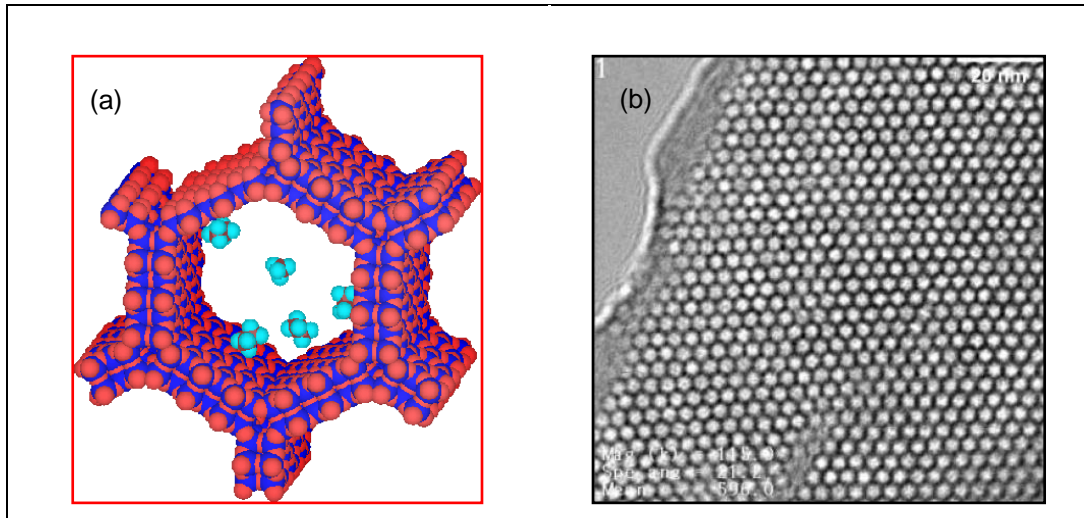


Figure 4.3.1. (a) Schematical representation of MCM-41 (b) TEM image of MCM-41 (taken from (Sener 2006))

SBA-15

SBA-15 is the best known member of SBA family and it has cylindrical two dimensional hexagonally ordered pores. Synthesis begins with dissolving a PEO-PEO-PEO triblock copolymer (Pluronic 123) in strongly acidic aqueous medium and adding TEOS at 35 °C following subsequent aging step at higher temperatures (60-90 °C) for hours to day. To create ordered structure, a pH below the isoelectric point of silica is necessary. For the long range order, a charge matching pathway involving van der Waals and Coulombic forces is responsible as suggested by Zhao et al. (1998). This pathway was described as $(S^0H^+)(X^-I^+)$, with S^0 the neutral surfactant, X^- , an halide anion e.g. chlorine and I^+ the cationic silicate species that is protonated below the isoelectric point. SBA-15 materials offer the opportunity of tuning pore sizes in a broad range, the possibility of chemical functionalization of the pore walls, and controlling over particle morphology [Martens et al. (2011)].

SBA-15 has additional micropores in the silica walls resulting from the network of silica and hydrophilic EO chains formed during the synthesis. Due to the unique bimodal pore structure, SBA-15 is used in advanced applications provided that methods of selective deposition of functional groups or guest species in either one or the other pore system are developed (Hsu Y-C. 2007).

The need to create additional diffusion channels is even more crucial for SBA-15 generally having a macroscopic morphology of rope-like, micrometer-sized aggregates.

A typical TEM image is presented in Figure 4.3.2. Hexagonal pore structure and a typical XRD pattern of SBA-15 are also seen in the figure (Zhao D. 1998). The structure is very similar to MCM-41 but having larger pores.

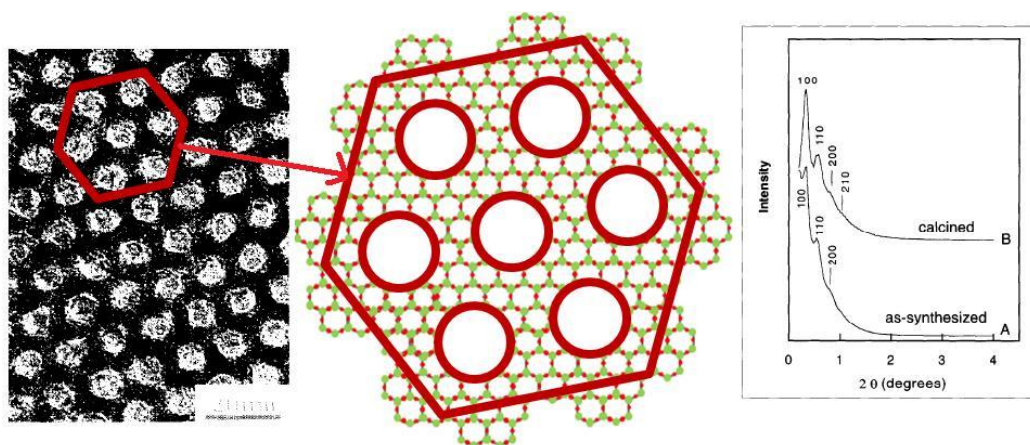


Figure 4.3.2. Structure of SBA-15 (Zhao D. 1998)

MCM-48

MCM-48 structure is much more complex than the MCM-41 or SBA-15. Two 3D independent pore systems are created by the two identical, cubic but separate compartments of the surface cells. Unit cell of MCM-48 is of cubic symmetry. Two independent pore systems of MCM-48 never join or cross each other and interlocked. They run along [100] and [111] directions. Toward the [100] direction, micelle rods which represents the pore systems progress in spirals around each other. XRD pattern of MCM-48 is quite complicated due to the complex symmetry as explained (Kumar et al., 2001; Collart 2003). Pore diameter of MCM-48 varies with respect to synthesis conditions and Collart reported that pore diameter changed between 2.7 nm and 4.6 nm and average pore wall thickness was about 0.9 nm (2003).

4.4. AN ALTERNATIVE SUPPORT MATERIAL FOR ETHANOL-STEAM REFORMING REACTION CATALYSTS: CERIA (CeO₂)

Ceria is a promising support material which has increasing applications in many areas. Oxygen storage capacity, metal-ceria interactions, structural and chemical properties attracted the attention of the researchers (Rao G.R. 2003).

Ceria is a solid material which has yellow colour due to $O^{2-} \leftarrow Ce^{4+}$ charge transfer. It crystallizes in the structure of fluorite (CaF_2) with a space group of $Fm\bar{3}m$. Schematic representation of unit cell is presented in Figure 4.4.1. In the face centered cubic (FCC) structure of ceria, Ce^{4+} ions form a cubic close packing arrangement and all the tetrahedral sites are occupied by the oxide ions whereas the octahedral sites remain vacant. The unit cell of ceria can be considered as a simple cube, in which the face center positions and corners are occupied by oxide ions and the alternate corners are occupied by Ce^{4+} ions (Rao G.R. 2003).

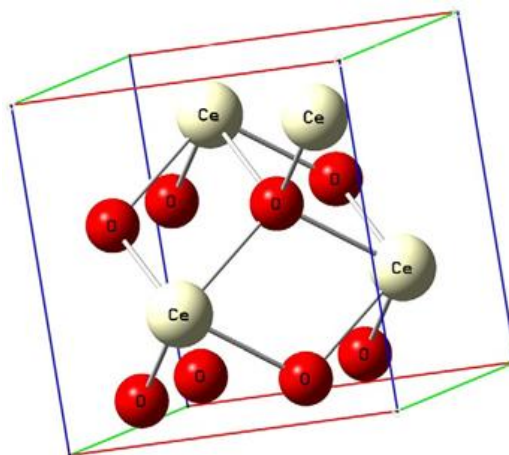


Figure 4.4.1. Structure of Ceria (taken from (Bumajdad A. 2009))

Ceria is being preferred to the other support materials, because (Bumajdad A. 2009)

1. It has a promising oxygen buffering property. This is caused by high tolerance to reversible 36nda re36e36n/deoxygenation cycles without disruption of the fluorite lattice-structure.
2. If it is prepared as nanoparticles, its electric conductivity increases and carbon monoxide oxidation boosts.
3. It has a high melting point (2400 °C), so can be used in high temperature applications.
4. Nanocrystalline CeO_2 has size-dependent and improved properties.
5. Mesoporous ceria is a good support material for many reactions due to the high surface area.

Bumajdad et al. (2009) also summarized the application areas as listed below,

- Solid oxide fuel cells
- High refractive index materials
- Insulators
- Polishing materials

- UV blockers
- High-temperature-oxidation resistance
- Free radical scavengers
- Gas sensors
- Catalysts
- Catalyst promoters
- Catalyst supports

The metal/CeO₂ systems have been extensively used as catalysts for several industrially and environmentally important chemical reactions (Rao G.R. 2003). The most important reason for choosing Cerium as the support material is its high tolerance to reversible oxygenation/deoxygenation cycles, i.e., ceria has a promising oxygen buffering property (Bumajdad A. 2009). This property was examined by many researchers in ESR reaction, (Frusteri F. 2004), (Jalowiecki-Duhamel L. 2010), (Jacobs G. 2007)]. In these studies, Addition of ceria was found to improve the catalytic stability as well as activity primarily due to the higher oxygen mobility of ceria and less coke formation was observed [(Ciambelli P. 2010), (Song H.(*) 2009)]. Very high oxygen selectivities (Frusteri F. 2004) stability more than 600 h for hydrogen production (W. Y. Sun J. 2010) were achieved. Cerium oxide and also doped and mixed cerias can be prepared by different techniques. Some of them are listed below:

- Pyrolysis (low T or spray)
- Aqueous precipitation with different precipitating agents (hexamethylenetetramine, ammonia solution etc.)
- Solution methods
- Thermodecomposition
- Mechanochemical methods
- Sol-gel methods
- Solid combustion methods
- Microwave heating
- Sonochemical methods
- Gas condensation
- Electrochemical methods (Cerovic L. 2010), [Wang et al., (2008)]

For the synthesis of mesoporous CeO₂ as a catalyst support can be also achieved by novel synthesis approaches. Recently published novel techniques are hard-templating [(Ying F. 2011), (Puertolas B. 2010)], microwave-assisted techniques (Zawadzki M., 2008); and reverse micelle methods [(Gu F. 2007)]; Son et al. (2008)].

Successful procedures to the synthesis of ceria nanoparticles in aqueous media were performed by (Luo J-X. 2009), (Terribile D. 1998) and (Lundberg M. 2002). In the study of Terribile et al. (1998), CTMABr was used as structure directing agent. Cationic surfactants were expected to be favorably adsorbed on ceria nanoparticles, primarily due to the high electronegativity of the oxygen atoms of ceria. Ceria nanoparticles with the surface areas of 50-300 m²/g and high porosity and less agglomeration were synthesized, i.e. improved resistance to sintering. Non-ionic polymeric surfactant P123 ((EO)₂₀(PO)₇₀(EO)₂₀) was used to synthesize mesoporous thin films of ceria with high surface area (150 m²/g) and pore diameter of 3.5 nm by Lundberg et al. (Lundberg M. 2002). In this study, tunnel structures was found to be disordered due to the forced removal of surfactant aggregates by ceria crystallization during calcination.

Another novel technique for the synthesis of mesoporous CeO₂ nanoparticles is the “hard-template approach” [(Ying F. 2011), (Luo J-X. 2009)]. In this technique, a mesoporous material (e.g. MCM-48) is used as hard template. CeO₂ is impregnated to the template, and removal of silica is achieved by hot NaOH solution. So the reverse replica of the porosity structures of the template is obtained. Synthesized CeO₂ nanoparticles are smaller in particle size, much larger in surface area and in portion of surface oxygen reducible at low T.

Catalytic features of Ceria-based catalysts prepared by novel techniques were also examined and found to be successful especially in steam reforming reactions.

4.5. SYNTHESIS OF CERIA-BASED NANOMATERIALS

Ceria based materials, i.e. ceria, ceria-zirconia solids solution, ceria–titania, doped ceria, and others, can be synthesized at high temperatures and low temperatures with solution based routes which allow easy control and use of simple apparatus. Tailoring the nanostructure of ceria based materials are dependent on the methods of preparation such as hydrothermal method, solvothermal method, and precipitation in high boiling solvent and the experimental conditions such as the concentration, temperature, reaction time, and acidity (Yuan Q. 2009).

4.5.1. Ceria Nanomaterials

Studies on nanostructured ceria, CeO₂ started at as early as 1988. At that time, CeO₂ spheres with uniform size distribution were prepared by forced hydrolysis of cerium salts in an acidic media (Hsu W.P. 1988)]. Hydrolysis of Ce⁴⁺ salt at a very low pH has also resulted in CeO₂ particles (Chane-Ching J.Y. 1987). There were lots of methods have been used in

synthesizing the CeO₂ powders and the most advanced method is the aqueous phase synthesis method.

Alcoholthermal method is used in the synthesis of uniform ceria nanocrystals with sizes ranging from 2.6 to 6.9 nm resulting in high surface area and high degree of crystallinity. The hydrolytic route in the alcoholthermal method is as follows

- i. The formation of Ce³⁺ and Ce⁴⁺ ions when Ce (3) and Ce(4) nitrates are dissolved
- ii. The formation of polymers of cerium hydroxide coordinated with ethanol
- iii. The transition of hydroxides to hydrated and alcoholized CeO_{2-δ}
- iv. CeO_{2-δ} nanocrystals obtained through alcohol treatment

By adding the poly vinyl pyrrolidone (PVP) as the stabilizer, the synthesis method is improved. A tentative mechanism for the formation of CeO₂ colloids is given in Figure 4.5.1. The PVP molecule is adsorbed on the Ce³⁺ ions with coordination between cerium cations and the O atoms in PVP. Then, the OH⁻ ions are released by the hydrolysis of the dropped alkylamine with water from Ce(NO₃)₃.6H₂O and ethanol. In this condition, the oxygen in the air oxidized the Ce(3) to Ce(4). The following alcohol treatment supplies enough energy for the complete conversion of Ce(OH)₄ nuclei into CeO₂ via dehydration and the subsequent growth of highly crystallized CeO₂ nanocrystals (Hirano M. 1996).

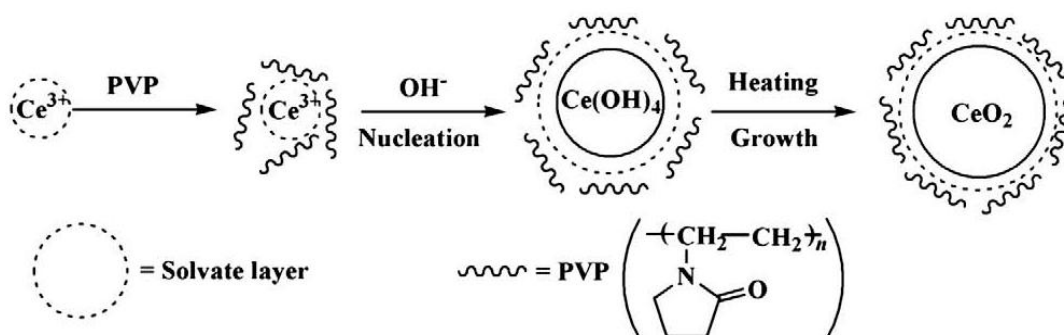


Figure 4.5.1. Alcoholthermal mechanism for synthesis of CeO₂ nanocrystals (Yuan Q. 2009)

4.5.2. CeO₂-ZrO₂ Solid Solution Nanomaterials

Incorporation of zirconia to ceria is well known to enhance the oxygen storage capacity, thermal stability and to increase the surface area. Ceria-zirconia solid solution has some problems in determining the structural properties. X-Ray diffraction and Raman spectra are incapable of detecting the heterogeneity. A more powerful tool for determining the oxygen

positions in oxides, Pulsed Neutron Diffraction technique, is adapted to study the atomic structure of $\text{CeO}_2\text{-ZrO}_2$. It is seen that, there are heterogeneities in the ceria matrix associated with the zirconia formation (Mamontov E. 2000).

It is possible to obtain ceria-zirconia in cubic phase, fluorite type phase and monoclinic phase. Depending on the concentration, metastable cubic phase and ordered arrangement of cations can be obtained (Otsuka-Yao-Matsuo S. 1995). Urea hydrolysis based coprecipitated catalyst were prepared (Pengpanich S. 2002). However, zirconia and ceria oxides were not homogeneous but segregated in micro domains. The homogeneity of mixed oxide catalyst is exchanged by doping the trivalent rare earth metals. Addition of these metals has also good effect on stability and surface area (Yuan Q. 2009).

For the reactions in which size effect is important, the use of $\text{CeO}_2\text{-ZrO}_2$ is difficult since the nuclei formation and aggregation rate is uncontrollable in the preparation of ceria-zirconia solid solutions. In addition to this, the morphology is another problem since it is not possible to tune the sizes, shapes, and composition of the catalysts. (W. X. Liang X. 2008). On the other hand, when spherical ceria clusters are used as precursors, spherical nanocages are obtained; whereas when cubic clusters are used as precursors, cubic nanocages are obtained.

4.5.3. Other Ceria Based Nanocrystals

Metal doped ceria based catalysts have found great applications in fuel cells and catalysis applications. Versatile metals such as Ca, Sr, Bi, Y, Gd are used as dopants. The ceria-titania catalyst has some promising properties in the catalysis applications. It is possible for the ceria and titania ions to coexist in the mixed oxides due to the difference in the ionic radius. Increase in the Ce/Ti ratio is found to have good effect in photocatalytic applications. Moreover, alumina supported ceria based catalysts can function well for acid catalysis (Arias A.M. 2000). Alumina is a very good support for the reactions. The interaction between the alumina and ceria is strong resulting in the oxidizing conditions and CeAlO_3 at the interface causes the stabilization of the textural properties.

4.5.4. Controlled Synthesis

4.5.4.1. Assembly of Ceria Based Nanomaterials

Self-organization of spherical particles having the same diameter to the 2D and 3D ordered structures are one of the natural phenomena occurring in nature. The self-assembled are different than their isolated particles and corresponding bulk phase.

4.5.4.1.1. Two-Step Assembly

The colloids or nanoparticles having uniform shape and size are used as building blocks for the assembled structures. This is called as two-step assembly. With this strategy, the 2D and 3D structures with large surface area can be obtained. In two-step assembly, two key parameters are particle size distribution and particle-particle interaction. Chane-Ching et al. developed a method for the synthesis of self-assembly of functionalized nanoparticles (C. F. Chane-Ching J.Y. 2005). In their work, difunctional amino acid is used to provide suitable ceria interactions with $\text{CH}_2\text{CH}_2\text{O}$ groups of surfactants. Based on the co-operative self-assembly of colloidal nanoparticles, hexagonal CeO_2 is obtained and catalyst structure is preserved after heating to 500°C . The self-assembly process of surface-modified ceria nanoparticles are illustrated with Figure 4.5.2.

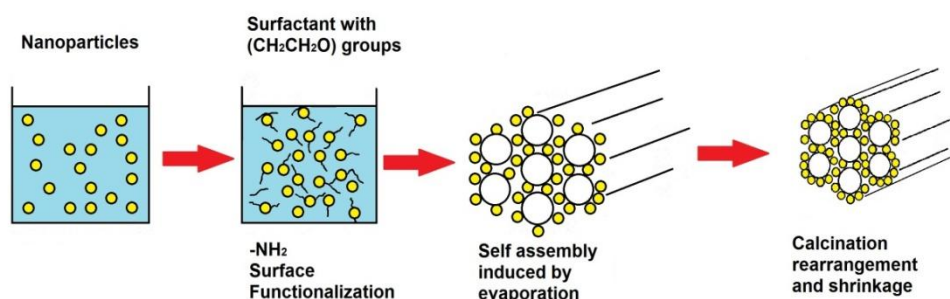


Figure 4.5.2. The illustration of self-assembly process of surface modified ceria nanoparticles (taken from (Yuan Q. 2009))

4.5.4.1.2. One-Step Assembly

The self-assembly process occurs at the same time when no crystals are formed and no previous synthesis of nanocrystals has to be done. This is called as one-step assembly. The factors affecting the final assembled structure are synthesis condition including precursor sort and concentration, solvent, composition, solvent composition, surfactant or template concentration, reaction temperature, reaction time, and others. The mesoporous ceria-zirconia catalyst was obtained via non-template hydrothermal route (Zhang F. 2002). The found catalyst exhibits long range disorder and short range order, as a result from the natural agglomeration of uniform particles upon hydrothermal treatment. Prepared catalyst powders have high surface area ($232\text{--}281\text{ m}^2/\text{g}$) and narrow pore size distributions ($3.5\text{--}4.0\text{ nm}$). Such catalysts are good candidates for the application in catalysis.

CHAPTER 5

MODIFICATION OF SUPPORT MATERIALS FOR CATALYTIC PURPOSES

Siliceous or non-siliceous support materials are not considered as active catalysts and sorbents for many reactions and sorption processes. Additional catalytic functions are introduced to the support by incorporation of active sites to its structure. Active sites are incorporated into the support structure by direct addition during the synthesis, or by the modification of the support after the desired structure has been synthesized.

Widely used post-synthesis methods are, impregnation, grafting, adsorption and ion-exchange. (On D.T. 2001)

Impregnation is one of the widely used catalytic material preparation methods in which active component is impregnated to porous support or active component's solution of the catalyst. Impregnation steps are quite simple unless there are specific interactions between support and components of impregnation (Wiingaarden R.J. 1998).

In impregnation, solution of active component is added slowly to the suspension of porous structured support or catalyst and concentration is an important factor in adsorption of active component and penetration of it. Water is in excess after adsorption is completed and it should be removed in order to preserve the active component in the pores of the support. Water removal is important because migration of the metal salts to the exterior surface is possible in presence of water. After water is removed completely, calcination is used to convert the metal salts to metal oxides. Quality of adsorption depends on the adsorption properties of solvent and carrier and uniformity is an important phenomenon (Wiingaarden R.J. 1998).

Use of different solvents could result in different concentration gradients. Chromatographic effect plays an important role in uneven distribution of the components in multicomponent

impregnation. So as to avoid such an effect, impregnation could be conducted in different orders and places and adsorption capabilities must be considered. For the components having low adsorption capacity, adsorption occurs in the pores and for the components having high adsorption capacity, surface adsorption occurs. Keeping the impregnated catalyst in moist state also prevents uneven distribution of active component by allowing more time to reach equilibrium (Wiingaarden R.J. 1998).

CHAPTER 6

CATALYST CHARACTERIZATION METHODS

6.1. X-Ray Diffraction (XRD)

Crystal structures of solids can be well described by x-ray diffraction (Dumesic J.A. 1993)c, 1993). X-ray diffraction is one of the most important characterization techniques for the ordered material structures. MCM-41 type catalytic materials can be characterized by this method. Ordered channel walls causes diffraction peaks rather than the crystal structure in the atomic range. In a well ordered, hexagonally structured, two dimensional catalyst structure exhibits a sharp (100) plane diffraction peak and (110),(200), and (210) diffraction peaks of higher Miller index planes (Sener 2006).

Pore structure of materials can be also investigated by XRD. Mesoporous materials give the reflection peaks at low angles, i.e. 2θ is lower than 10 and no peak at higher angles. Based on diffraction profile, it can be concluded that pore walls are mainly amorphous. The ordering lies in the pore structure and indexes of different lattices are in the low angle diffraction peaks (Sener, 2006). d_{100} value is used in calculation of parameter a in a hexagonal lattice by using the formula

$$a = 2 \times d_{100} / \sqrt{3} \quad (6.1.1)$$

Unit cell parameter a and d_{100} are shown in Figure 4.1.1. Pore wall thickness δ can be calculated from the formula given below

$$\delta = a - 2 \times r \quad (6.1.2)$$

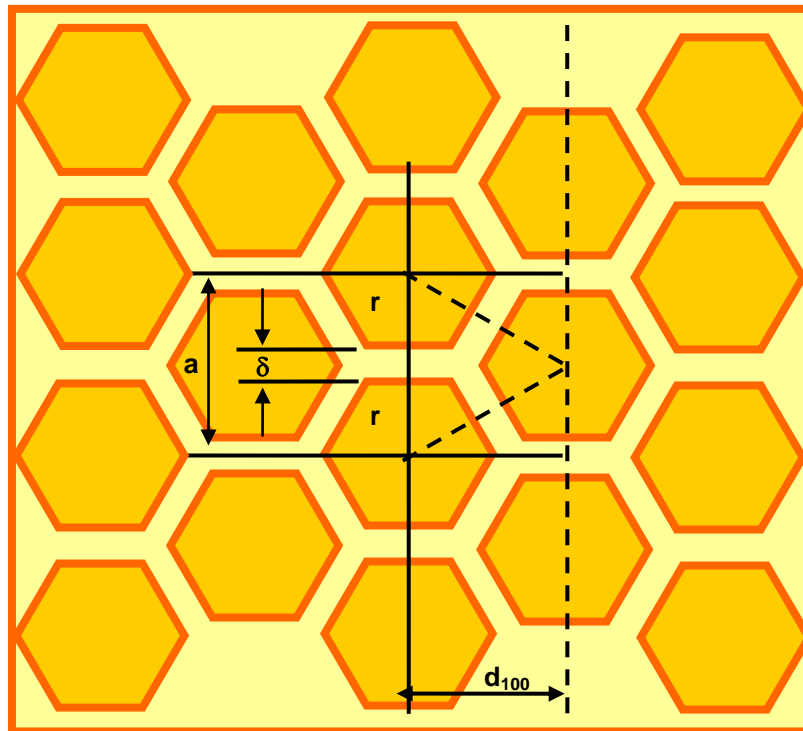


Figure 6.1.1. Schematic representation of pores of MCM-41 (Sener 2006)

6.2. Nitrogen Physisorption

Physisorption is a major technique for characterization of porous materials. The mesoporous materials have uniform mesopores and have been characterized extensively by N_2 physisorption .

In nitrogen physisorption analysis, temperature is reduced to the normal liquefaction point (77 K for nitrogen) and amount of nitrogen is measured with respect to pressure. Pore size information such as surface area, pore size, and pore size distribution are obtained from the resulting isotherm. MCM-41 materials have a sharp step in the mesopore range of $P/P_0=0.2$ to 0.5, corresponding to the liquid condensation of nitrogen in the uniform mesopore structure. As the step gets sharper, the pore size becomes more uniform (Yao, 2006).

6.3. Transmission Electron Microscopy (TEM)

One standard method to characterize the ordered structure of materials is transmission electron microscopy (TEM). In this method, a high energy beam (100-200 keV) is used to image a thin material specimen. The high-energy electron beam transmits the sample grids

and casts an image of the sample's precise structure of MCM-41, the channels, pores and the hexagonal structure (Sener 2006).

6.4. Scanning Electron Microscopy (SEM)

Scanning electron microscopy involves detection of back-scattered and secondary electrons as well as X-rays that are back-scattered from the sample, This technique can be used on thick samples, and it is effective for monitoring catalyst morphology (Sener, 2006).

6.5. X-Ray Photoelectron Spectroscopy (XPS)

Electron spectroscopy for chemical analysis (ESCA) is one of the most widely used surface characterization methods. This method could also be named as X-ray photoelectron spectroscopy (XPS). XPS is a very popular method due to its flexibility in addressing a wide variety of samples and its high information content (Wickerman, 2003). Among the attributes of XPS, a quantitative analysis of the surface composition is the most important ability of this technique since bulk composition and surface composition of catalysts may differ (Dumesic J.A.1993).

XPS is based on the "photoelectric effect". Photons with high energy hit the material with the consequent emission of electrons (photoelectrons). Einstein's law is behind this process and can describe the basic physics of XPS. The photoelectron kinetic energy, E_k , measured quantity in the experiment, is given by:

$$E_k = h\nu - E_b \quad (6.5.1)$$

where $h\nu$ is the energy of the incident radiation and E_b the binding energy of the electron in a particular level.

In the complete ESCA spectrum, peaks associated with the various elements (except H and He) which are present in the outer 10 nm of that materials can be observed. Percentage of each identified element can be detected from the area under these peaks by correcting them with appropriate instrumental factors.

CHAPTER 7

THERMODYNAMIC ANALYSIS

Thermodynamic analysis of steam reforming of ethanol is done at atmospheric pressure and in a temperature range of 100 °C – 900 °C. Overall steam reforming of ethanol reaction with the highest hydrogen production is as follows.



Thermodynamic analysis of this reaction is made as follows: Constant pressure heat capacities were found from literature as a function of temperature and given as in eq. 7.2.

$$C_p = a + b \times T + c \times T^2 + d \times T^3 \quad C_p [=] \text{ J/mol.K and } T [=] \text{ K} \quad (\text{eqn. 7.2})$$

Heat capacity coefficients of chemicals involved in steam reforming of ethanol is given in Table 7.1.

Table 7.1. Constant pressure heat capacity coefficients of chemicals involved in steam reforming of ethanol (Sandler S.I. 1999)

Chemicals	a	b×10 ¹	c×10 ⁵	d×10 ⁹
C ₂ H ₅ OH	9.014	2.141	-8.390	1.373
H ₂ O	32.24	0.019	1.055	-3.596
CO ₂	19.80	0.734	-5.602	17.15
H ₂	27.14	0.093	-1.381	7.645

Constant pressure heat capacity coefficients of the steam reforming of ethanol reaction can be calculated as in eq. 2. and heat capacity of the reaction is given with eq. 3.

$$\Delta a = \sum_i (v_i \times a_i) \quad (\text{eqn. 7.3})$$

$$\Delta C_p = \Delta a + \Delta b \times T + \Delta c \times T^2 + \Delta d \times T^3 \quad (\text{eqn. 7.4})$$

In a similar fashion, heat of reaction and gibbs free energy of reaction can be calculated at reference temperature of 25 °C. Standard enthalpies of formation and standard Gibbs energy of formations are given in Table 7.2.

Table 7.2. Standard enthalpies of formation and standard Gibbs energy of formation at 25 °C

Chemicals	\check{H}_f , kJ/mol	\check{G}_f , kJ/mol
C₂H₅OH	-235.0	-168.4
H₂O	-242.0	-228.8
CO₂	-393.8	-394.6
H₂	0	0

$$\Delta H^\circ_{\text{rxn}} = \sum_i (v_i \times H^\circ_{f_i}) \quad (\text{eqn. 7.5})$$

$$\Delta G^\circ_{\text{rxn}} = \sum_i (v_i \times G^\circ_{f_i}) \quad (\text{eqn. 7.6})$$

Heat of reaction at reaction conditions can be calculated by integrating the constant pressure heat capacity with respect to temperature as in eqn. 7.7.

$$\Delta H_{\text{rxn}} = \Delta H^\circ_{\text{rxn}} + \int \Delta C_p \cdot dT \quad (\text{eqn. 7.7})$$

After finding the heat of reaction as a function of temperature, equilibrium constant was found by integrating Van't Hoff relation over studied range of temperature. Differential form of Van't Hoff relation is given in equation 7.

$$d \ln K = \frac{\Delta H_{\text{rxn}}}{RT^2} \cdot dT \quad (\text{eqn. 7.8})$$

To be able to perform integration of equation 7, a boundary condition is needed. For this purpose, equilibrium constant at reference temperature can be calculated as in equation 8.

$$K_{298} = \exp\left(\frac{\Delta G^{\circ}_{\text{rxn}}}{RT}\right) \quad (\text{eqn. 7.9})$$

Equilibrium constant obtained from integrating equation 7.8 is equal to fraction based equilibrium constant since pressure is one bar. There is also no need to consider non-idealities because of low pressure and high reaction temperature.

$$K = K_y = \prod_i y_i^{\nu_i} = \frac{y_{\text{CO}_2}^2 \times y_{\text{H}_2}^6}{y_{\text{C}_2\text{H}_5\text{OH}} \times y_{\text{H}_2\text{O}}^3} \quad (\text{eqn. 7.10})$$

For the stoichiometric feed of ethanol and water, equilibrium conversion of ethanol with respect to temperature is given in Figure 7.1. As shown in this figure, equilibrium limitations are negligible at temperatures higher than 400 °C.

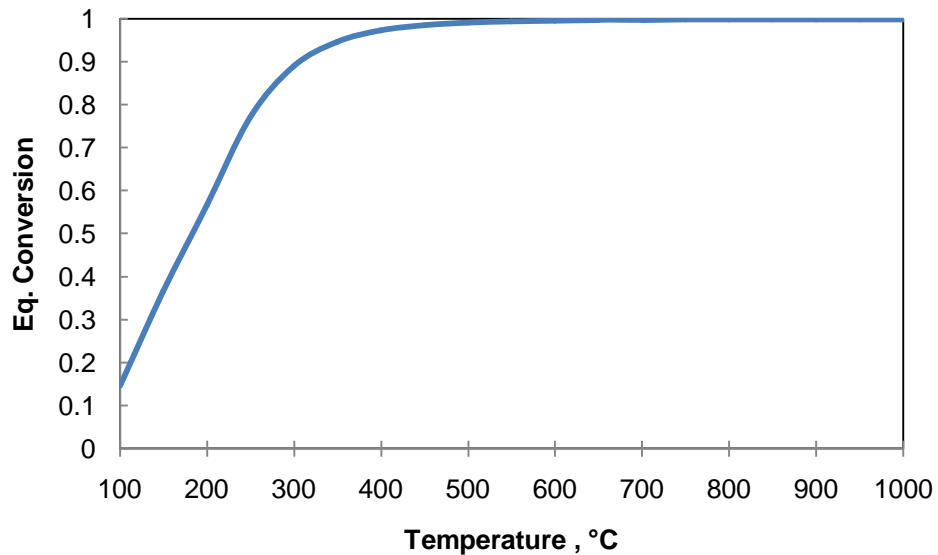


Figure 7.1. The equilibrium conversion curves for ethanol steam reforming reaction with respect to temperature for a feed ratio of $\text{H}_2\text{O}/\text{ETOH}=3$

Equilibrium conversion values of ethanol are also evaluated at different $\text{H}_2\text{O}/\text{Ethanol}$ ratios and results are shown in Figure 7.2. As it is expected, the increase of water to ethanol ratio in the feed stream caused an increase in equilibrium conversion.

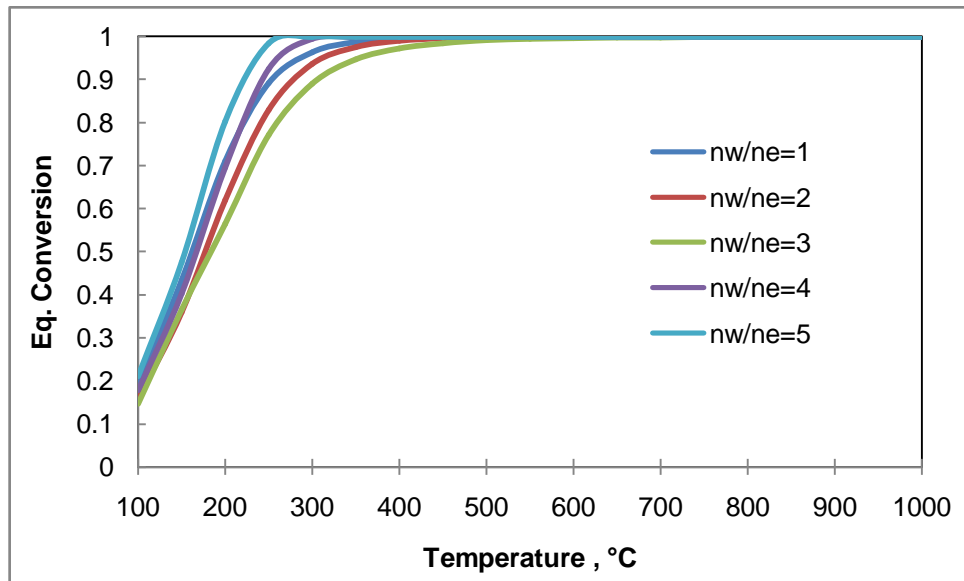


Figure 7.2. The equilibrium conversion curves for ethanol steam reforming reaction with respect to temperature for different feed ratios

CHAPTER 8

EXPERIMENTAL

Experimental work has four major steps;

- i) catalyst preparation
- ii) catalyst characterization
- iii) catalytic tests (ethanol steam reforming, dry reforming of methane)
- iv) characterization after reaction

Catalyst preparation investigations were carried out to find suitable supports (such as MCM-41, SBA-15, CeO₂, CeO₂/SiO₂ etc.) for reforming catalysts. Resistance of the catalyst to high reaction temperature and to maintain the metal dispersion during operation are quite important parameters in catalyst selection. To find suitable active metal components (such as Pd, Ce, Ni) and to find out the optimum active metal ratios are also important parameters considered in this work. Synthesis procedures were studied in order to have the optimum catalytic properties. Mainly, impregnation and direct hydrothermal synthesis procedures were taken into consideration.

Catalyst characterization provided structural, physical and chemical properties of the prepared nano-designed catalysts.

8.1. CATALYST DESIGN & PREPARATION

8.1.1. MCM-41 SYNTHESIS

MCM-41 was synthesized following a hydrothermal synthesis route (Sener et al., 2006; Gucbilmez et al., 2005) by using sodium silicate as the Si source and hexadecyltrimethylammonium bromide as the surfactant (Figure 8.1.1). First, a clear solution of surfactant was prepared by continuous stirring at 30°C. Then, sodium silicate solution was added dropwise to the surfactant solution, while stirring. The pH of the mixture was adjusted to 11 by using 4N H₂SO₄ and the resulting gel was stirred for 1 h. This gel was then transferred into a Teflon-lined autoclave and hydrothermal synthesis was carried out at

120°C for 96 hours. The resultant solid was recovered by filtration and thoroughly washed with deionized water until the pH of the wash water decreased to at least 8.0. The solid product was then calcined by heating from room temperature to 550°C at a rate of 1°C per minute and then by keeping at this temperature for 6 hours in a flow of dry air.

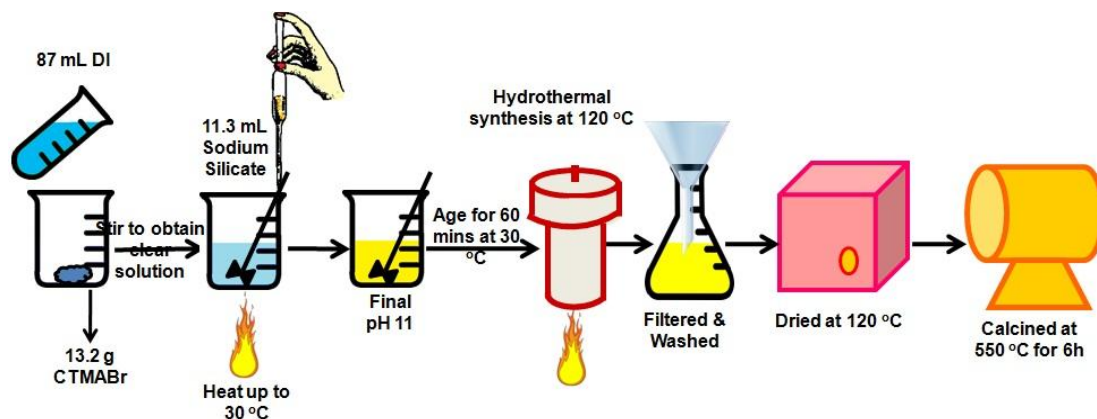


Figure 8.1.1. Synthesis procedure of MCM-41

8.1.2. SBA-15 SYNTHESIS

In the synthesis of SBA-15, procedure of Mbraka was used (Mbaraka J.K. 2003). Tetraethoxysilane was used as the silica precursor and Pluronic 123 was used as the surfactant. P123, which is a tri-block copolymer of polyethylene oxide-polypropylene oxide-polyethylene oxide with the molecular structure $\text{PEO}_{20}\text{-PPO}_{70}\text{-PEO}_{20}$, was used as purchased to tailor the textural properties of the mesoporous materials.

Synthesis procedure of SBA-15 is illustrated in Figure 8.1.2. In a typical synthesis, 4 g of P123 was dissolved in 125 ml of 1.9 M HCl at room temperature with stirring and subsequent heating to 40 °C before addition of TEOS (8.2 ml). The TEOS was prehydrolyzed for approximately 40 min before aging, thereafter aged for 24 h at 100 °C under static conditions. The resulting solid material was filtered and air-dried. For the removal of the surfactant, two different routes were followed. The first route is calcining the as-synthesized material at 550 °C for 6 hours with the heating rate of 1 °C/min. The other procedure is ethanol reflux. As-synthesized silica/surfactant composite was suspended in acidified ethanol (4 ml HCl in 400 ml ethanol) and refluxed for 24 hours at around 80 °C (i.e. near the boiling point of ethanol). The final product was washed with ethanol, air-dried and then stored in a desiccator (Figure 8.1.2).

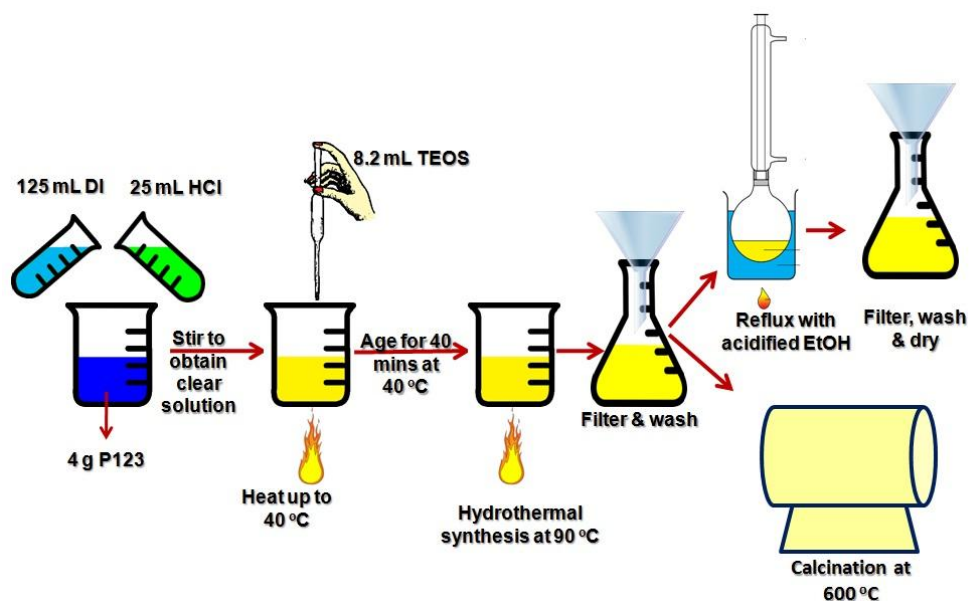


Figure 8.1.2. Synthesis procedure of SBA-15

8.1.3. SYNTHESIS OF MCM-41 SUPPORTED CATALYSTS

8.1.3.1. SYNTHESIS OF Ni@MCM-41

Ni impregnation to the MCM-41 support was achieved in Sofia Institute of Catalysis through the international collaborative project supported by TUBITAK. Schematic representation of the catalyst is presented in Figure 8.1.3.

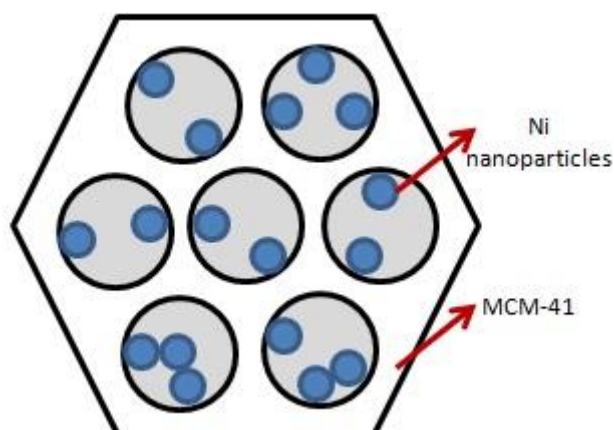


Figure 8.1.3. Schematical representation of Ni impregnated MCM-41-supported catalysts

In the preparation of MCM-41 supported Ni incorporated catalysts, $\text{Ni}(\text{NO}_3)_2 \cdot 6\text{H}_2\text{O}$ was used as the Ni source. Impregnation of the metal into the pores of MCM-41 was carried out in an impregnation procedure. A solution containing the desired amount of Ni was prepared and

MCM-41 was added to this solution. The mixture was stirred for three hours and evaporated to dryness in a rotating evaporator. The sample was dried overnight at 120°C. These materials were then calcined in flowing air using the following temperature programme:

- heat until 350°C within a time period of 60 min..
- keep at 350°C for 30 min.
- heat until 550°C at within a time period of 60 min.
- keep at 550°C for 4 hours.

8.1.3.2. SYNTHESIS OF PdNi@MCM-41

Similar to Ni@MCM-41 samples, PdNi@MCM-41 samples were also prepared in Sofia Institute of Catalysis.

For the impregnation of Pd into the Ni@MCM-41 material, first a solution of Pd(NO₃)₂ was prepared in deionized water. Synthesized Ni@MCM-41 samples were added into this solution and left there for 4 hours with continuous stirring. And then, the water was evaporated in a rotating evaporator. The samples were dried overnight at 120°C and calcined by the same procedure.

Catalyst design is shown in Figure 8.1.4.

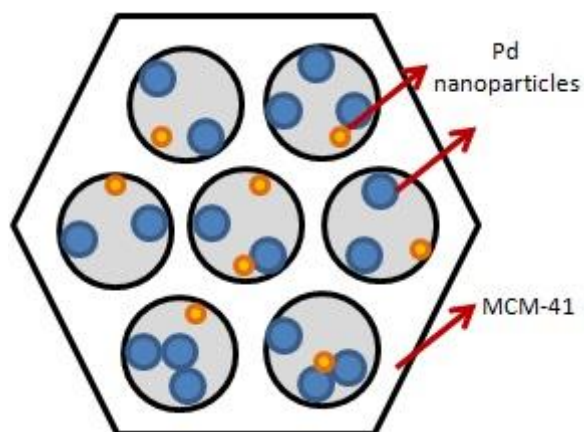


Figure 8.1.4. Schematical representation of Pd and Ni impregnated MCM-41 catalysts

Nomenclature and the compositions of the synthesized catalysts are given in Table 8.1.1.

Table 8.1.1. Nomenclature of Ni@MCM-41 and Pd-Ni@MCM-41 catalysts synthesized by impregnation procedure

Sample	Composition	Form
B1	8 wt. % Ni/MCM-41	Calcined
B2	16 wt. % Ni/MCM-41	Calcined
B3	24 wt. % Ni/MCM-41	Calcined
B4	0.6 wt. % Pd / 8 wt. % Ni/MCM-41	Calcined
B5	0.6 wt. % Pd / 16 wt. % Ni/MCM-41	Calcined
B6	0.6 wt. % Pd / 24 wt. % Ni/MCM-41	Calcined
B7	8 wt. % Ni/MCM-41	Dried
B8	16 wt. % Ni/MCM-41	Dried
B9	24 wt. % Ni/MCM-41	Dried
B10	0.6 wt. % Pd / 8 wt. % Ni/MCM-41	Dried
B11	0.6 wt. % Pd / 16 wt. % Ni/MCM-41	Dried
B12	0.6 wt. % Pd / 24 wt. % Ni/MCM-41	Dried

8.1.4. SYNTHESIS OF SBA-15 SUPPORTED CATALYSTS

8.1.4.1. SYNTHESIS OF Ni@SBA-15 CATALYST

In the preparation of Ni impregnated SBA-15, proper amount of SBA-15 was dried at 110 °C and suspended in a solution containing Ni(NO₃)₆.6H₂O. The mixture was stirred for 20 hours and evaporated to dryness. Ni impregnated SBA-15 catalyst was calcined for 3 hours at 600 °C with a heating rate of 5 °C/min. After calcination, Ni@SBA-15 was reduced by H₂ flow at 600 °C after purging with He. Ni/Si molar ratio was adjusted to 0.10.

8.1.4.2. SYNTHESIS OF NiCe@SBA-15 CATALYST

Proper amount of SBA-15 was dried at 110 °C and suspended in a solution containing desired amounts of Ce(NO₃)₃.6H₂O and Ni(NO₃)₆.6H₂O. The mixture was stirred for 20 hours

and evaporated to dryness. Ni and Ce impregnated SBA-15 catalyst was calcined for 3 hours at 600 °C for 3 hours with a heating rate of 5 °C/min. Ni/Si molar ratio was adjusted to 0.10 and Ce/Si molar ratio was 0.10 and 0.50.

Two different routes were followed for the impregnation procedure. In the first route, SBA-15 was impregnated by Ni and Ce simultaneously. In the second route, Ni and Ce were impregnated to SBA-15 consecutively, i.e., first Ce was impregnated and synthesized Ce@SBA-15 was calcined and Ni was impregnated to Ce@SBA-15.

8.1.4.3. SYNTHESIS OF PdNiCe@SBA-15 CATALYST

Proper amount of SBA-15 was dried at 110 °C and suspended in a solution containing $\text{Ce}(\text{NO}_3)_3 \cdot 6\text{H}_2\text{O}$ and $\text{Ni}(\text{NO}_3)_2 \cdot 6\text{H}_2\text{O}$. The mixture was stirred for 20 hours and evaporated to dryness. Ni and Ce impregnated SBA-15 catalyst was calcined for 3 hours at 600 °C for 3 hours with a heating rate of 5 °C/min. Ni/Si molar ratio was adjusted to 0.10 and Ce/Si molar ratio was 0.50. Pd was impregnated to the reduced catalyst with 1 % by weight loading.

Table 8.1.2. Prepared SBA-15 supported catalysts

Sample	Ni/Si	Ce/Si	% Pd	Impregnation
Ni@SBA-15	0.10	0	0	standard
NiCe(0.5)@SBA-15	0.10	0.50	0	simultaneously
Pd@[NiCe(0.5)@SBA-15	0.10	0.50	1	Ni and Ce simultaneously
NiCe(0.1)@SBA-15	0.10	0.10	0	simultaneously

8.1.5. SYNTHESIS OF AIMCM-41 SUPPORTED CATALYSTS

8.1.5.1. SYNTHESIS OF Ni@AIMCM-41 CATALYST

Commercial mesoporous Aluminasilicate was impregnated with Nickel. Al-MCM-41 has 3% by weight Aluminum content.

Proper amount of AIMCM-41 was dried at 110 °C and suspended in a solution containing $\text{Ni}(\text{NO}_3)_2 \cdot 6\text{H}_2\text{O}$. The mixture was stirred for 25 hours and evaporated to dryness. Ni

impregnated AIMCM-41 catalyst was calcined for 4 hours at 600 °C with a heating rate of 5 °C/min. Ni/Si molar ratio was adjusted to 0.10.

8.1.5.2. SYNTHESIS OF Ce@AIMCM-41 CATALYST

Proper amount of AIMCM-41 was dried at 110 °C and suspended in a solution containing Ce(NO₃)₃.6H₂O. The mixture was stirred for 25 hours and evaporated to dryness. Ni impregnated AIMCM-41 catalyst was calcined for 4 hours at 600 °C with a heating rate of 5 °C/min. Ce/Si molar ratio was adjusted to 0.10.

8.1.5.3. SYNTHESIS OF NiCe@AIMCM-41 CATALYSTS

Proper amount of AIMCM-41 was dried at 110 °C and suspended in a solution containing Ce(NO₃)₃.6H₂O and Ni(NO₃)₆.6H₂O. The mixture was stirred for 25 hours and evaporated to dryness. Ni impregnated AIMCM-41 catalyst was calcined for 4 hours at 600 °C with a heating rate of 5 °C/min. Ni/Si ratio was adjusted to 0.10 and Ce/Si molar ratio was adjusted to 0.10 and 0.50.

Table 8.1.3. AIMCM-41 supported catalysts

Catalyst	Ni/Si	Ce/Si	Procedure
Ni@AIMCM-41	0.10	0	Standard impregnation
NiCe(0.10)@AIMCM-41	0.10	0.10	Simultaneous impregnation
NiCe(0.50)@AIMCM-41	0.10	0.50	Simultaneous impregnation
Ce@AIMCM-41	0	0.10	Standard impregnation
Ni@[Ce@AIMCM-41]	0.10	0.10	Consecutive impregnation

A list of all catalysts is presented in Appendix A.1.

8.2. CHARACTERIZATION OF SYNTHESIZED MATERIALS

The synthesized materials are characterized by XRD, TEM, SEM-EDS, Nitrogen adsorption, TGA-DTA, XPS and TPR techniques.

8.2.1. X-Ray Diffraction (XRD)

X-ray diffraction for the identification of the crystalline phases were obtained. The XRD patterns of these materials were obtained by a Rigaku D/MAX2200 diffractometer with a $\text{CuK}\alpha$ radiation source in Metallurgical and Materials Engineering Department of METU and Rigaku Ultima-IV diffractometer in METU Central Laboratories. The scanning range of 2θ was set between 0.3° and 10° for low angle analysis and between 1° and 90° for wide angle analysis.

8.2.2. Transmission Electron Microscopy (TEM)

Jeol 2100F with attached Jeol EDX & HAADF detectors and GIF Tridem STEM Pack energy filtered unit was used for the TEM analysis.

8.2.3. Nitrogen Physisorption

Surface area (BET, BJH) and pore structure information were obtained by the nitrogen adsorption technique. These measurements were performed by Quantachrome Autosorb 1C at Central Laboratories of METU. Materials were prepared for the analyses by drying under vacuum at 100°C for 6 hours.

8.2.4. Energy Dispersive Spectroscopy (EDS)/Scanning Electron Microscopy (SEM)

For the SEM-EDS analysis, Jeol JSM-6400 was used in METU Central Laboratories.

8.2.5. X-ray Photoelectron Spectroscopy (XPS)

The XPS spectra of Ni/MCM-41 and Pd-Ni/MCM-41 materials before and after H_2 -reduction were obtained. The XPS measurements were performed with the X-Ray Photoelectron Spectroscopy instrument (SPECS) with $\text{MgK}\alpha$ and $\text{AlK}\alpha$ sources available in Central Laboratories in METU. The analyses were also made after ion bombardment (Ar^+) at 5000 eV for 2 min. The binding energy of the C is at 284.6 eV was taken as reference in the XPS measurements

8.2.6. Temperature Programmed Reduction (TPR) Studies

The TPR experiments with H_2 were carried out in the Micromeritics Chemisorb. The inlet total flow was $60\text{ cm}^3/\text{min}$ with a composition of 10% H_2 in Ar.

The experimental set-up consists of adsorbate (H₂) and diluent (Ar) gas cylinders joined to a sample tube placed into a temperature-controlled furnace and a TCD detector connected on line to the outlet stream leaving the sample tube for the simultaneous analysis of the products.

8.2.7. Thermal Gravimetric (TGA) Analysis

Thermal analysis of the uncalcined materials was carried out using Perkin-Elmer Pyris 1 TGA Thermal Analyzer instrument. Materials were treated with dry air by heating up to 900 °C with a heating ramp of 5 °C/min.

8.3. STEAM REFORMING OF ETHANOL TEST REACTION

8.3.1. Experimental Set-up

The catalytic experiments in the reaction of reforming of ethanol with steam were designed for working at atmospheric pressure. The reaction system consists of syringe pump, evaporator, furnace, fixed bed continuous flow reactor and gas chromatograph (Agilent Technologies 6850). Schematical representation of experimental set-up for ethanol-steam reforming reaction is shown in Figure 8.3.1.

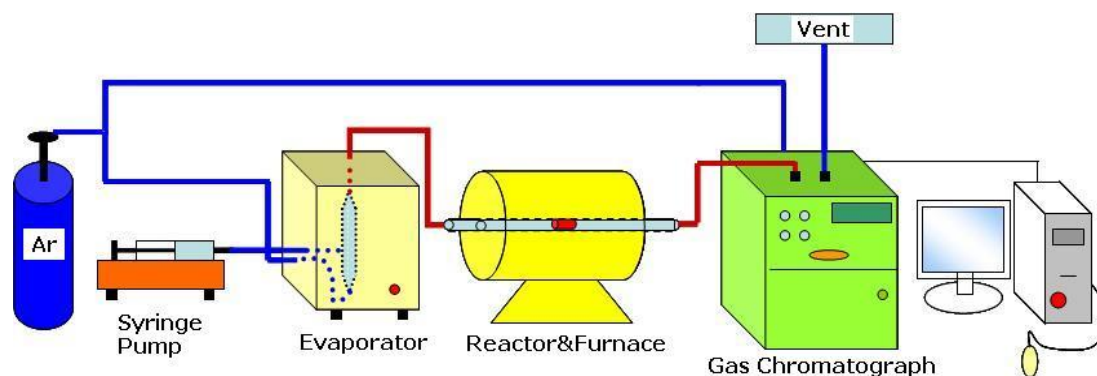


Figure 8.3.1. Schematical representation of experimental set-up

Reactor tube is a quartz tube with ¼ inch diameter. A porous filter is placed in the reactor tube not to enable the catalysts flow inside the system. Ethanol-water mixture (1:1 by volume) is pumped to the evaporator by syringe pump with a speed of 1.8 ml/hr. This flow corresponds to 40 ml/min in the gas phase. Argon carries the evaporated ethanol-steam mixture to the reaction system. All the pipe lines are heated up to 150 °C. Reaction takes place on the catalyst surface inside the quartz reactor. 0.10 or 0.15 grams of catalyst is used for each run (for MCM-41 supported catalysts 0.10 g catalyst was used, all the other

catalysts were tested with 0.15 g sample). Outlet streams of the reactor are analyzed by the gas chromatograph equipped with Porapak S (Altech) column.

8.3.2. System Parameters

The temperature program used in the analyses of the outlet stream is given in Table 8.3.1 Table 8.3.2 shows the gas chromatograph parameters.

The column was calibrated for the gases H₂, CO, CO₂, CH₄, C₂H₅OH, H₂O, C₂H₂. Calibration factors of the gases were calculated by taking the ethanol as basis (i.e. $\beta_{C_2H_5OH}=1$). Calibration factors and retention times for each compound is presented in Appendix A.2.

Table 8.3.1. Temperature programme for gas chromatography

Initial Temperature (°C)	Final Temperature (°C)	Temperature Ramp (°C/min)	Time (min)
35	35	-	3
35	175	20	
175	175	-	5
Total			15

Table 8.3.2 Chromatograph Parameters

Parameter	Set Value
Front Inlet Temperature	200°C
Front Inlet Pressure	22.5 psi
Reference Gas Flow Rate	40 ml/min
Front Detector Temperature	200°C

8.4. DRY REFORMING OF METHANE WITH CARBON DIOXIDE

The reaction of CH₄ reforming with CO₂ were performed in Bulgarian Academy of Sciences, Institute of Catalysis, Sofia by the research group there through our collaborative research project supported by TUBITAK. Experimental procedure of dry reforming of methane reaction tests, is presented in Appendix A.4.1.

CHAPTER 9

RESULTS AND DISCUSSION

9.1. Ni AND PdNi IMPREGNATED MCM-41 CATALYSTS

MCM-41 was synthesized by the procedure described in Section 8.1.1. After the preparation of crystalline silica structure, Ni impregnated metallic and PdNi impregnated bimetallic catalysts were synthesized with the MCM-41 support in Institute of Catalysis, Bulgarian Academy of Sciences by following the procedure described in Section 8.1.3.

Synthesized catalysts were characterized in detail and tested in steam reforming of ethanol reaction. The results are presented and discussed in this chapter.

9.1.1. CHARACTERIZATION RESULTS OF PREPARED CATALYSTS

MCM-41, Ni impregnated MCM-41 and PdNi impregnated MCM-41 samples were characterized by x-ray diffraction, energy dispersive spectroscopy, nitrogen physisorption, thermal gravimetric analysis, temperature programmed reduction, scanning electron microscopy, transmission electron microscopy and x-ray photoelectron spectroscopy techniques.

9.1.1.1. CHARACTERIZATION OF MCM-41

MCM-41 has the structure of amorphous SiO_2 with well-ordered and honeycomb structured pores. X-ray diffraction pattern of MCM-41 gives a major peak between 2° and 5° which is because of the ordering in the pore structure. Generally, this major peak is followed by 2 or 3 reflections. A typical XRD pattern of MCM-41 material is shown in Figure 9.1.1. XRD spectrum of the MCM-41 sample displayed a sharp (100) peak and three reflections, demonstrating that the sample have a two-dimensional hexagonal structure. This MCM-41 sample had a major peak at 2θ of 2.44° . Sharp and noise-free peaks of the MCM-41 sample indicate a successful synthesis of the desired structure.

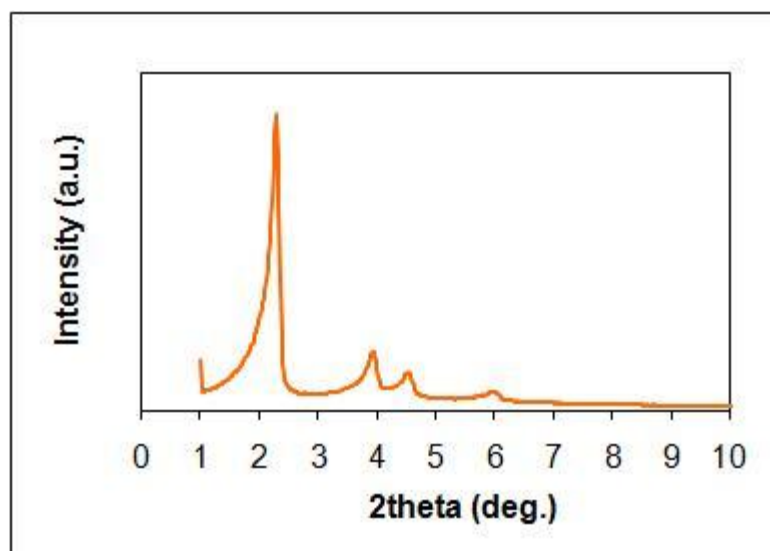


Figure 9.1.1. X-ray diffraction pattern of MCM-41 material.

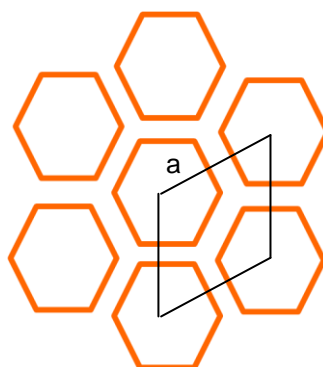


Figure 9.1.2. Schematical representation of MCM-41 material

Lattice parameter of MCM-41 is calculated by the formula $a = 2d_{(100)} / \sqrt{3}$ (Figure 9.1.2). $d_{(100)}$ value of the MCM-41 obtained from XRD analysis was 3.6 and “a” value was calculated as 4.2.

Nitrogen adsorption-desorption isotherms of MCM-41 is shown in Figure 9.1.3. According to the IUPAC classification, the Nitrogen adsorption-desorption isotherm is of Type IV. This type of isotherm is an indication of well-ordered mesoporous material.

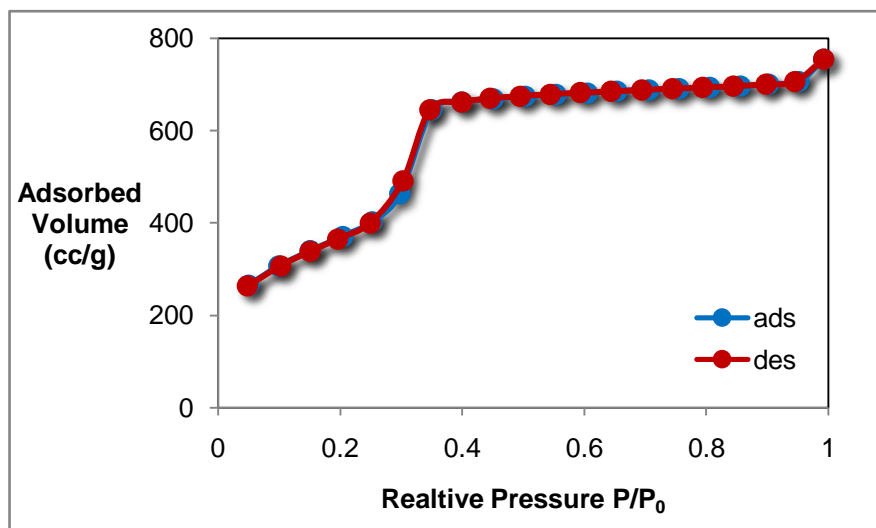


Figure 9.1.3. Nitrogen adsorption-desorption isotherms of MCM-41 material

The properties of MCM-41 support material obtained from Nitrogen adsorption-desorption analysis is summarized in Table 9.1.1. It is observed that MCM-41 has large surface area and mesopores having narrow pore size distribution (Figure 9.1.4)

Table 9.1.1. Nitrogen adsorption data for MCM-41 support material

BET surface area (m²/g)	1358
BJH adsorption surface area (m²/g)	1780
BJH desorption surface area (m²/g)	1798
Pore volume (cc/g)	1.168
Average pore diameter (nm)	3.43
BJH adsorption pore diameter (nm)	2.74
BJH desorption pore diameter (nm)	2.74

By using nitrogen adsorption analysis and x-ray diffraction analysis, pore wall thickness of MCM-41 was estimated as 1.77 nm.

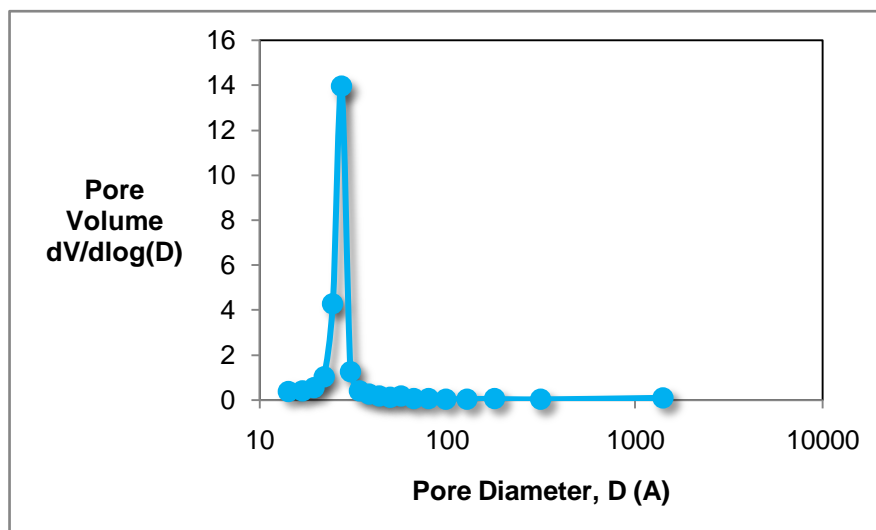


Figure 9.1.4. Pore size distribution curve of MCM-41 material

9.1.1.2. CHARACTERIZATION OF Ni@MCM-41 CATALYSTS

9.1.1.2.1. EDS Analysis

Bulk composition of the nanostructured catalysts were determined by quantitative EDS analysis. Energy dispersive spectra of the samples are shown in Figure 9.1.5, and the compositions of the catalysts from EDS are presented in Table 9.1.2.

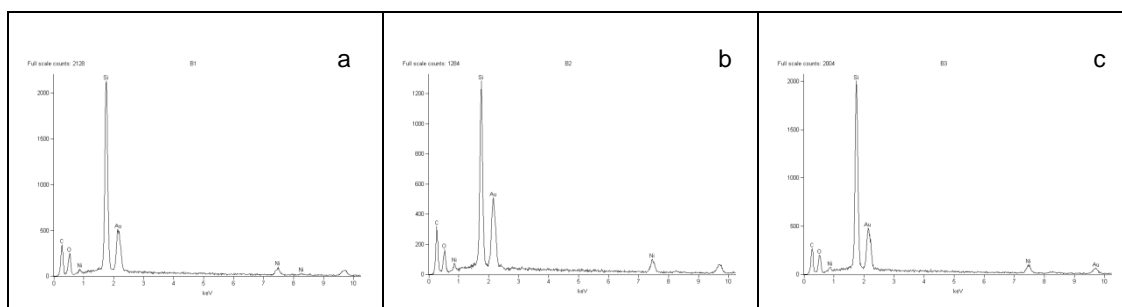


Figure 9.1.5. Energy dispersive spectra of Ni@MCM-41 samples (a) B1, (b) B2, (c) B3

Table 9.1.3 is a different presentation of the compositions of the dried and calcined Ni@MCM-41 samples by means of Ni/Si ratios.

Table 9.1.2. Chemical Compositions by Energy Dispersive Spectroscopy

Sample	Element	Weight Comp. % (EDS)	Atomic Comp. % (EDS)	Compound Comp. % (EDS)	Formula	Ni% (EDS)	Ni% (prep.)
B1	O	50.13	65.75	0.00			
	Si	42.16	31.50	90.19	SiO ₂	7.71	8
	Ni	7.71	2.75	9.81	NiO		
B2	O	46.42	64.53	0.00			
	Si	36.70	29.07	78.52	SiO ₂	16.88	16
	Ni	16.88	6.40	21.48	NiO		
B3	O	49.13	65.44	0.00			
	Si	40.69	30.87	87.06	SiO ₂	10.17	24
	Ni	10.17	3.69	12.94	NiO		

Table 9.1.3. Ni/Si ratios of Ni@MCM-41 samples

Sample	Calcination	Ni/Si (atomic)	Ni/Si (weight)
B1	After	0.104	0.22
B2	After	0.190	0.40
B3	After	0.134	0.28
B7	Before	0.100	0.210
B8	Before	0.210	0.440
B9	Before	0.120	0.250

9.1.1.2.2. XRD Analysis

Low-angle and high-angle x-ray diffraction patterns were obtained for Ni@MCM-41 samples and are shown in Figures 9.1.6 and 9.1.7, respectively.

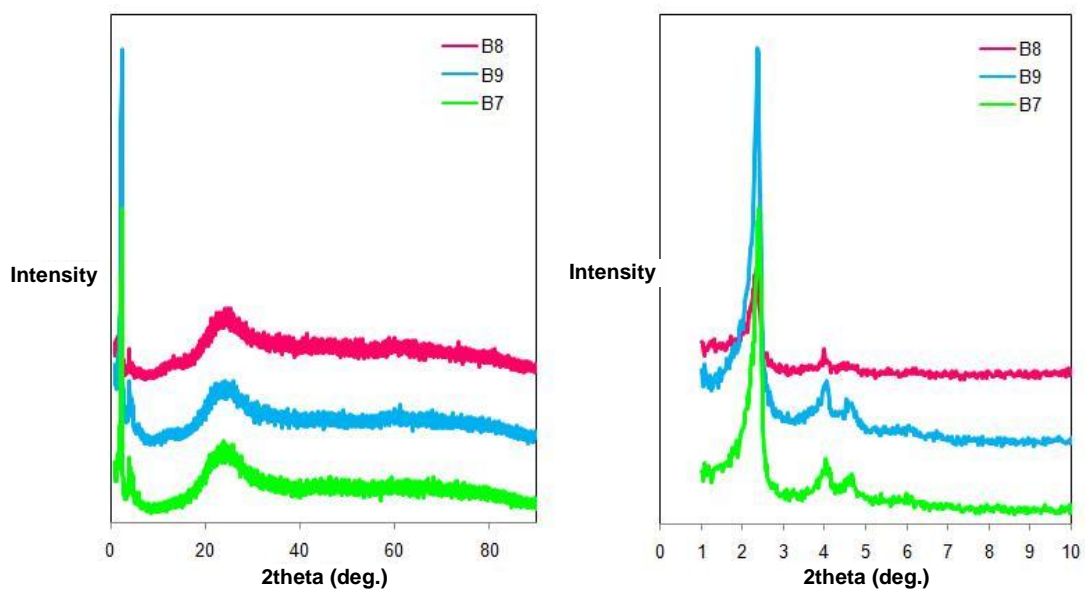


Figure 9.1.6. Small and high-angle X-ray diffraction patterns of Ni@MCM-41 samples before calcination (B7, B8, B9)

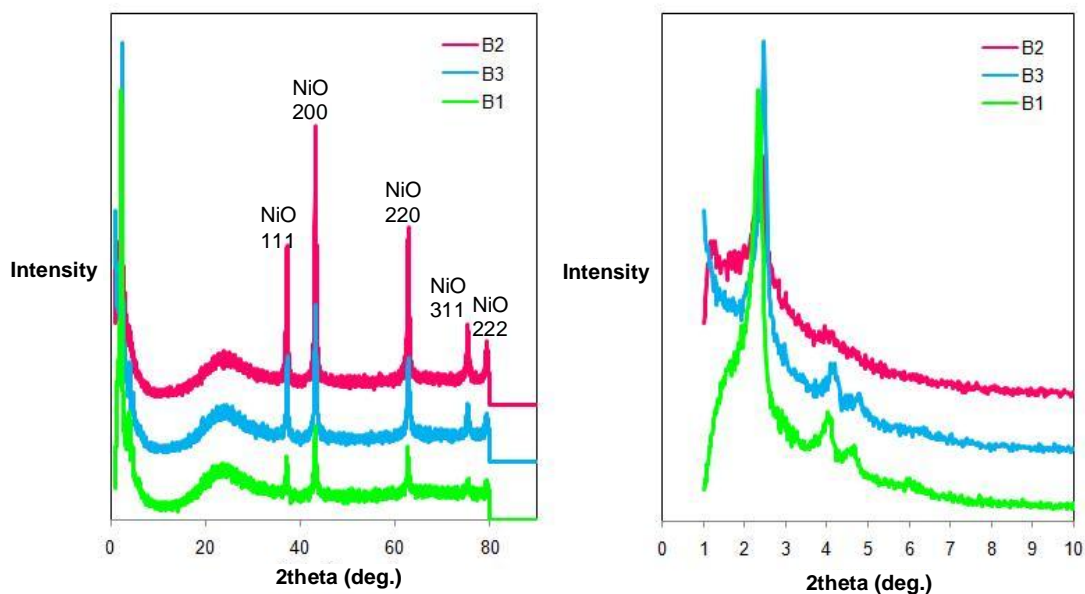


Figure 9.1.7. Small and high-angle X-ray diffraction patterns of Ni@MCM-41 samples after calcination (B1, B2, B3)

A careful inspection on Figures 9.1.6 and 9.1.7 gives that MCM-41 structure was partially deformed after the calcination step, and NiO particles were crystallized due to calcination. The main peak at 2theta of 43.2–43.4 is characteristic of NiO. The intensity of NiO peak increases with increasing Ni content.

Table 9.1.4 lists the peaks of MCM-41 for Ni@MCM-41 catalysts before and after calcination.

Table 9.1.4. XRD peaks of Ni@MCM-41 catalysts caused by MCM-41 structure

Sample	2theta	d-value	Sample	2theta	d-value
B1	2.340	37.7238	B7	2.380	37.09
	4.040	21.8529		4.040	21.85
	4.620	19.1107		4.620	19.11
B2	2.400	36.7809	B8	2.320	38.05
	4.140	21.3253		3.980	22.18
	-	-		-	-
B3	2.440	36.1780	B9	2.360	37.40
	4.160	21.2228		4.020	21.96
	4.780	18.4714		4.600	19.19

MCM-41 has a structure of amorphous silica, with well-ordered pores. These ordered pores causes MCM-41 give peaks at low angles in XRD analyses. For Ni@MCM-41 samples, a major peak was observed in 2.3-2.5° range followed by one or two reflections.

Lattice parameters were calculated as 4.35, 4.25 and 4.18 nm for B1, B2 and B3 samples, respectively. An inspection on high-angle X-ray diffraction patterns of the samples shows five signals which are caused by NiO species. Locations of these peaks are given in Table 9.1.6.

Table 9.1.5. XRD peaks of Ni@MCM-41 catalysts caused by NiO particles

Sample	2theta	d-value
B1	37.200	2.42
	43.220	2.09
	62.780	0.35
	75.360	1.26
	79.260	1.21
B2	37.260	2.41
	43.280	2.09
	62.860	1.48
	75.380	1.26
	79.360	1.21
B3	37.280	2.41
	43.320	2.09
	62.900	1.48
	75.460	1.26
	79.520	1.20

NiO particle sizes were also calculated by Sherrer equation by using wide-angle X-ray diffraction pattern data. Sherrer equation is given below

$$t = \frac{(0.9)(0.153)}{(FWHM)(\cos \theta)} \quad (E-9.1.2)$$

In this equation, FWHM is the full width at half maximum for the related peak. NiO particle sizes calculated by Scherrer equation are given in Table 9.1.6.

Table 9.1.6. NiO particle sizes in Ni@MCM-41 samples

Sample	d-value	2theta	Particle Size, nm
B1	2.0915	43.220	22.73
B2	2.0888	43.280	25.98
B3	2.0869	43.320	25.98

9.1.1.2.3. Nitrogen Adsorption Desorption Analysis

The representative adsorption-desorption isotherms of the samples are shown in Figure 9.1.8. The shape of the isotherms of supported Ni samples is similar to that of pure MCM-41. According to IUPAC classification the N₂ isotherms of all samples are of Type IV indicating a mesoporous structure (Figure 9.1.8). The shape of the isotherm becomes less inclined with increasing Ni content.

The textural properties of Ni@MCM-41 samples determined by N₂ adsorption-desorption isotherms are presented in Table 9.1.7. Table 9.1.7 demonstrates that after deposition of Ni on the surface of MCM-41 the surface areas, pore volumes and pore diameters of the samples decrease compared to that of the support. It was expected that an increasing amount of Ni would give lower surface area values due to plugging of the pores by the impregnated nickel. The higher surface area and the corresponding higher pore volume of the sample containing a Ni/Si ratio of 0.13 (Table 9.1.8) than the sample containing a Ni/Si ratio of 0.10 indicated that, impregnated nickel was better dispersed on the pore surfaces causing less pore plugging in the first case. The pore size distribution for MCM-41 and Ni@MCM-41 samples derived from the adsorption data using the Barret-Joyner-Halenda (BJH) method are shown in Figure 9.1.9. The pore size distribution for MCM-41 is centered at 2.7 nm and is typical for mesoporous material. After Ni addition a shift in the pore size distribution for MCM-41 was not observed. MCM-41 and Ni/MCM-41 samples have pore size distributions in the same narrow range. Therefore, the observed decrease in the textural properties of supported Ni samples is caused by blocking the pores of the carrier after Ni deposition.

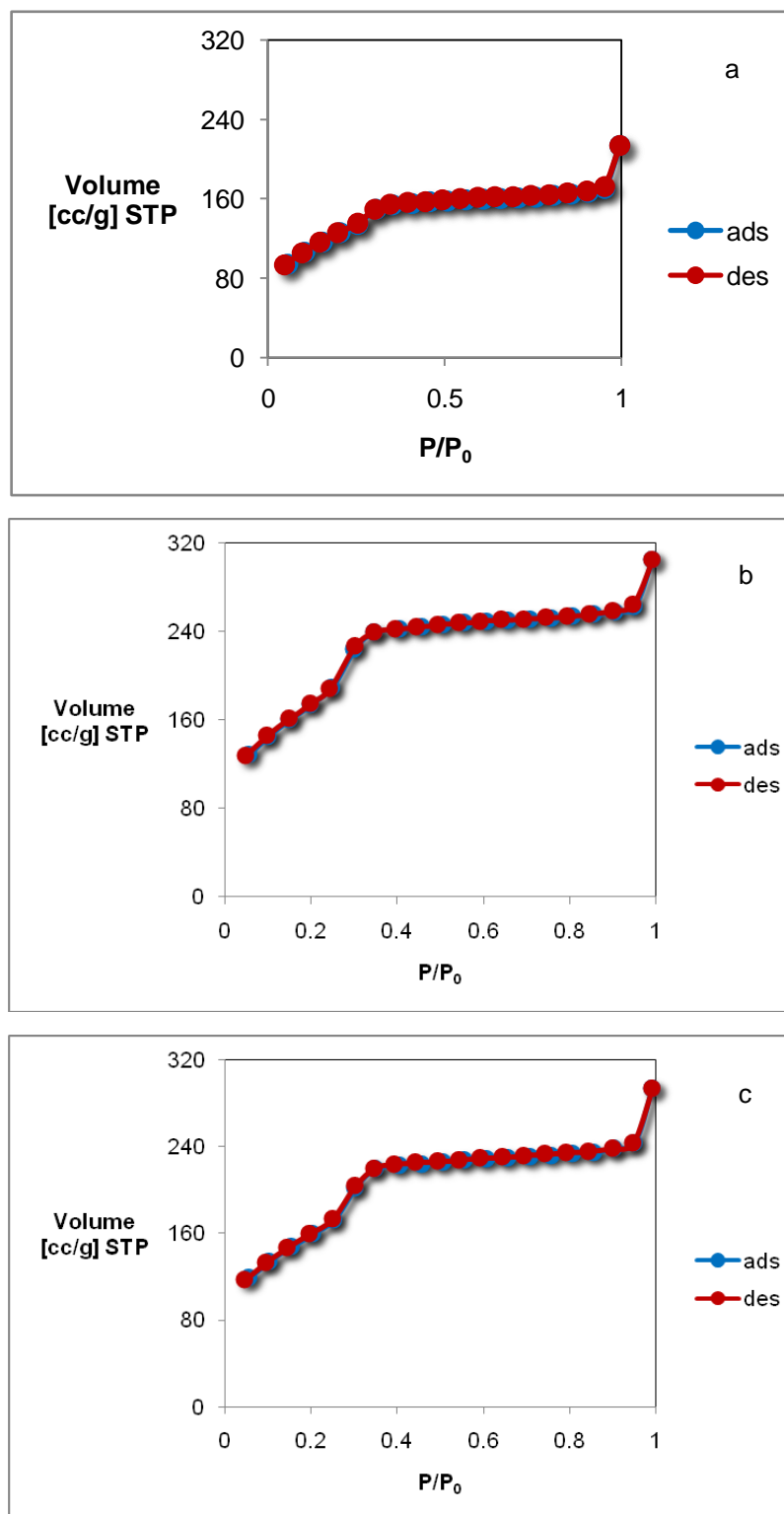


Figure 9.1.8. Nitrogen adsorption-desorption isotherms of Ni@MCM-41 catalysts (a) B2, (b) B3, (c) B1

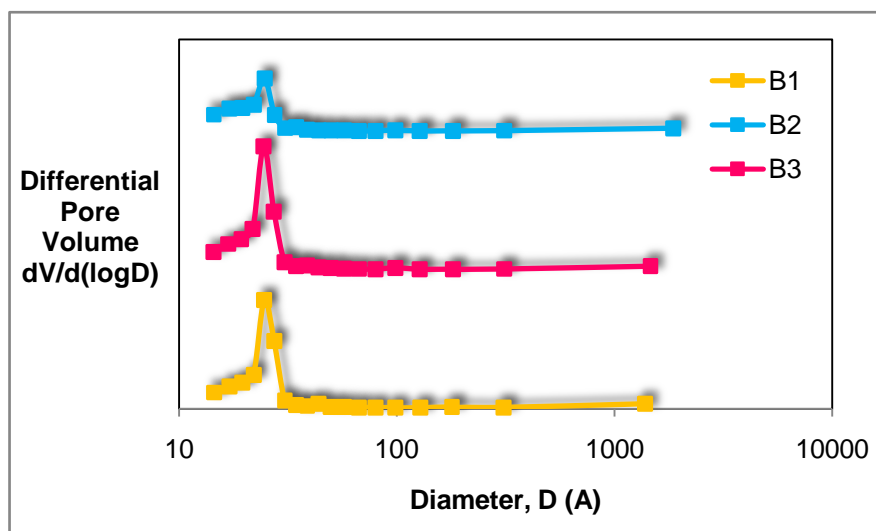


Figure 9.1.9. Pore size distribution curves of Ni@MCM-41 catalysts

Table 9.1.7. Nitrogen adsorption-desorption analysis results of the prepared catalysts

Sample	BET Surface Area (m ² /g)	BJH Ads. Surface Area (m ² /g)	Pore Volume (cc/g)	BJH Ads. Pore Diameter (nm)	Pore Wall Thickness (nm)
B1	583	591	0.4	2.5	1.9
B3	643	668	0.5	2.4	1.8
B2	464	408	0.3	2.5	1.7

9.1.1.2.4. SEM Analyses

SEM images shown in Figure 9.10 indicate the presence of agglomerated Ni particles in Ni@MCM-41 samples.

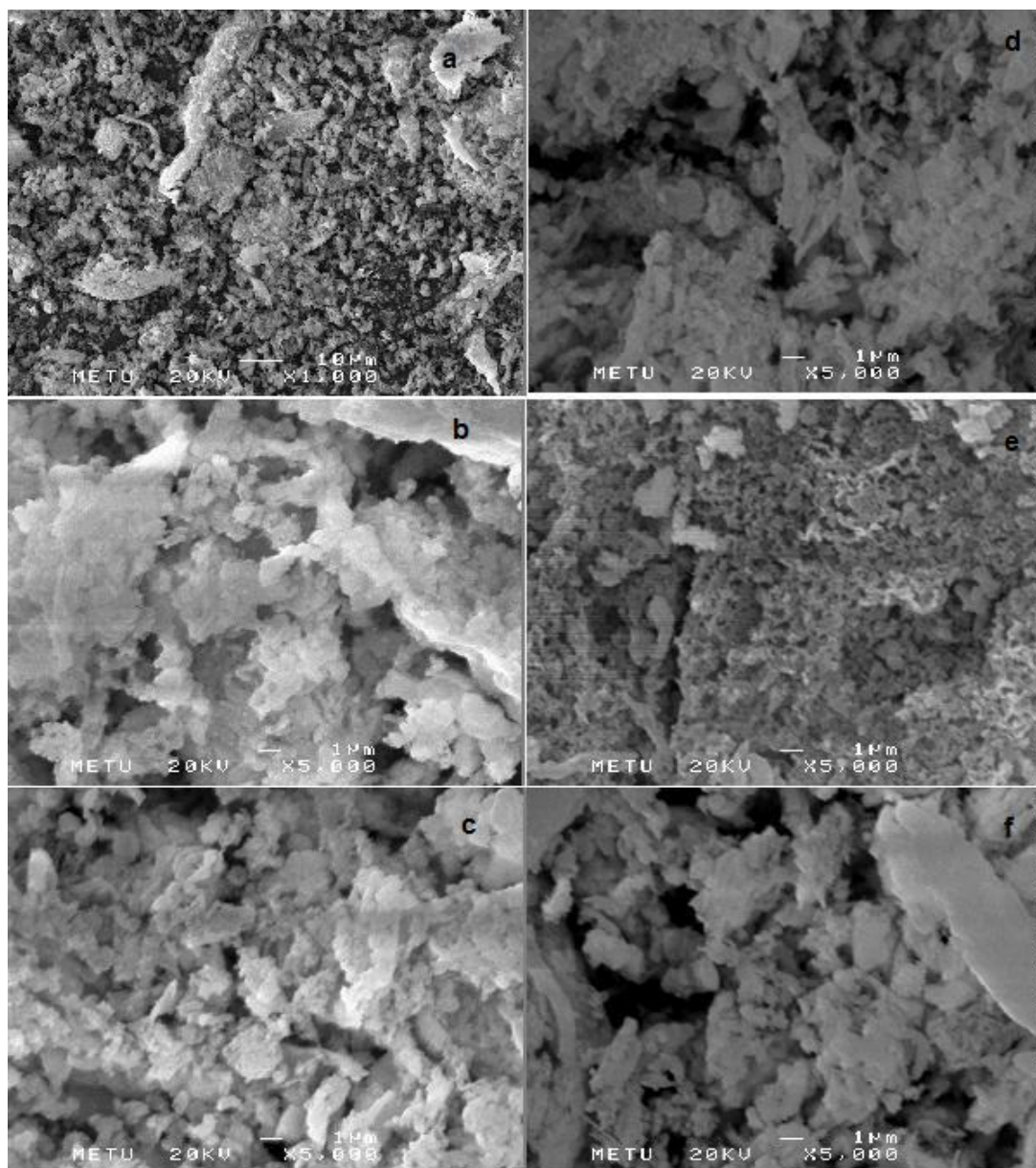


Figure 9.1.10. SEM images of (a) B1 sample, (b) B2 sample (c) B3 sample (d) B7 sample, (e) B8 sample, (f) B9 sample

9.1.1.2.5. Thermal Analysis (TGA/DTA)

The calcination temperature of the synthesized materials was determined by the thermal analysis of the uncalcined materials. Typical TGA and DTA plots of an uncalcined material (B7) (uncalcined form of B1) are shown in Figure 9.1.11 and Figure 9.1.12, respectively. These analyses indicated a change because of removal of the crystalline water and a decomposition step of the impregnated salts of Ni at around 200°C. TGA results showed that all decomposition steps were essentially completed before 400°C. However, considering the

future use of these synthesized materials in dry reforming of methane and steam reforming of alcohols in a temperature range extending upto 550°C, final calcination temperature was selected as 550°C.

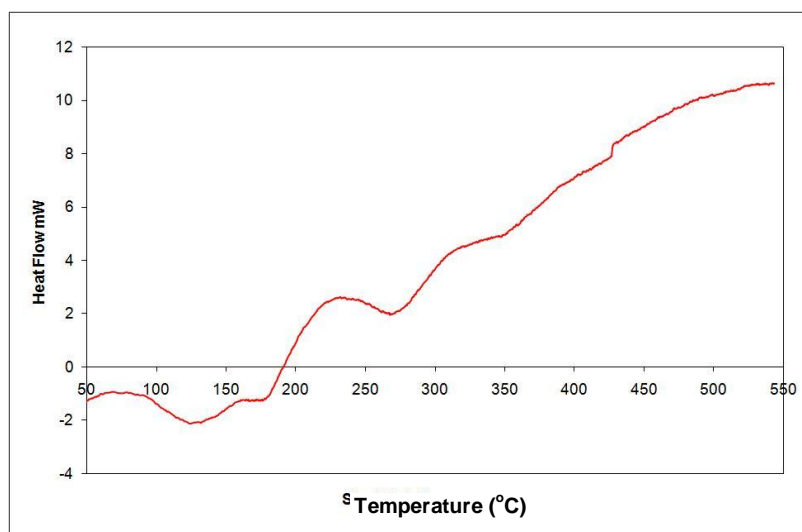


Figure 9.1.11. DTA plot of B7 sample

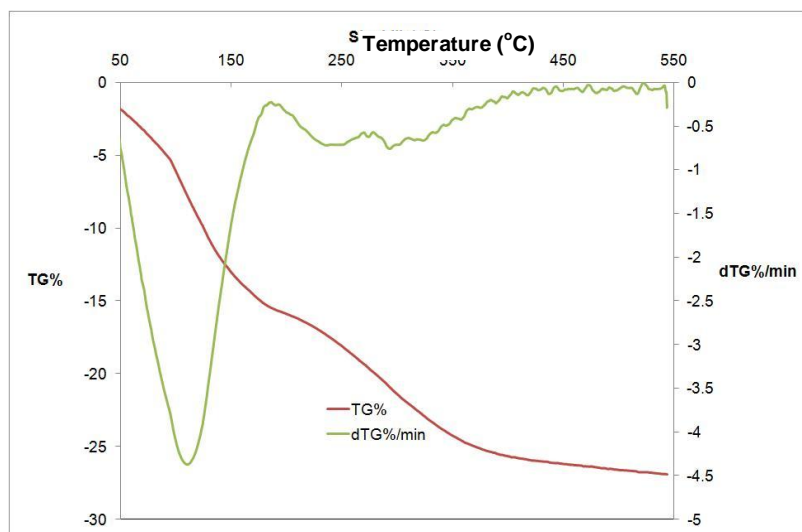


Figure 9.1.12. (a) TGA (b) dTGA plots of B7 sample

9.1.1.2.6. Temperature Programmed Reduction – TPR Studies

To understand the reducibility of the synthesized materials, TPR experiments were carried out using hydrogen as the reducing gas.

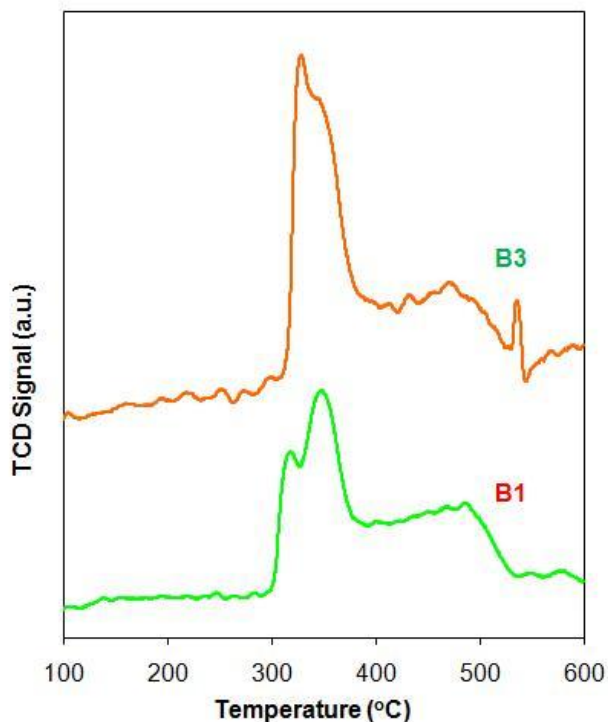


Figure 9.1.13. TPR profiles of Ni@MCM-41 samples

Temperature programmed reduction analyses of the samples B1 and B3 gives a two-step profile starting at around 300°C and ending at about 520°C (Figure 9.13). First peak is also deconvoluted by two sub-peaks. Formation of these steps may be due to the reduction of the outer atoms of Ni particles firstly, and then inner atoms after that. Major conclusion is that reduction of NiO is expected to be completed by 520 °C.

9.1.1.3. CHARACTERIZATION OF PdNi@MCM-41 CATALYSTS

9.1.1.3.1. EDS Analysis

Energy dispersive spectra of the samples are shown in Figure 9.1.14, and the compositions of the catalysts from EDS are presented in Table 9.1.8.

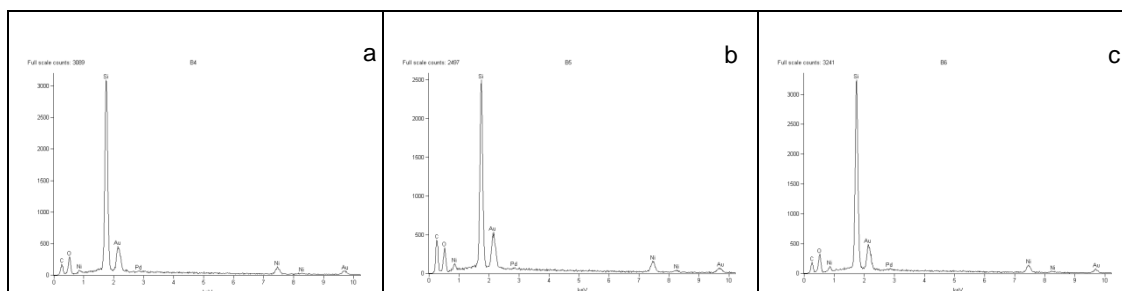


Figure 9.1.14. EDS patterns of B4, B5 ve B6 samples

Table 9.1.8. Chemical compositions by energy dispersive spectroscopy

Sample	Element	Weight Comp. % (EDS)	Atom Comp. % (EDS)	Ni/Si (atomic)	Ni/Si (weight)	Pd/Si (atomic)	Pd/Si (weight)
B4	Pd	1.76	0.52				
	Si	81.34	90.49	0.10	0.21	0.006	0.022
	Ni	16.90	9.00				
B5	Pd	2.26	0.70				
	Si	73.35	85.68	0.16	0.33	0.008	0.031
	Ni	24.39	13.63				
B6	Pd	2.53	0.75				
	Si	79.35	89.47	0.11	0.23	0.008	0.032
	Ni	18.12	9.77				

9.1.1.3.2. X-Ray Diffraction Analysis

Similar to Ni@MCM-41 samples, wide and low angle x-ray diffraction patterns for uncalcined and calcined forms of Pd-Ni@MCM-41 were plotted and shown in Figure 9.1.15 and Figure 9.1.16. XRD diffraction peaks observed at 2θ values of 37.2° (111 plane), 43.2° (200 plane) 62.8° (220 plane), 75.3° (311 plane) and 79.3° (222 plane) indicated the formation of NiO phase within the calcined materials B4, B5 and B6. Very small and broad XRD diffraction peak observed at a 2θ range of $34.1-34.3^\circ$ corresponds to PdO (101). The dimension of PdO crystals evaluated from the Scherrer equation ranged between 5-8 nm.

Comparison of the XRD patterns of the dried and calcined samples indicated that NiO and PdO crystals were formed within the matrix of the mesoporous materials after the calcination step. The sharp XRD peak observed at a 2θ value of about 2.4° in the XRD patterns of the

calcined materials and also in the XRD pattern of pure MCM-41 corresponds to the d_{100} of MCM-41 structure.

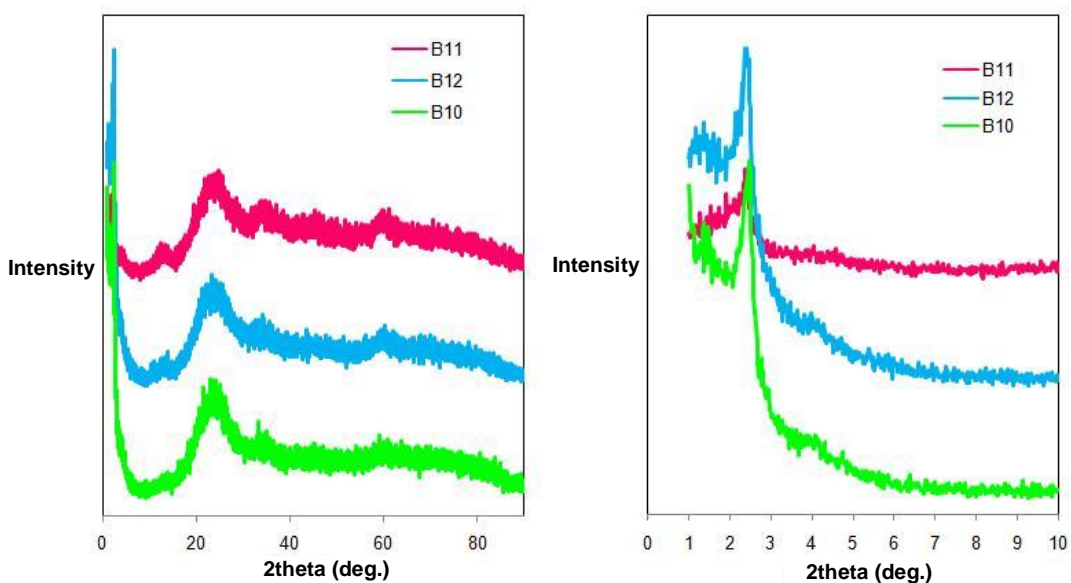


Figure 9.1.15. Small and high angle X-ray diffraction patterns of Pd-Ni@MCM-41 catalysts before calcination

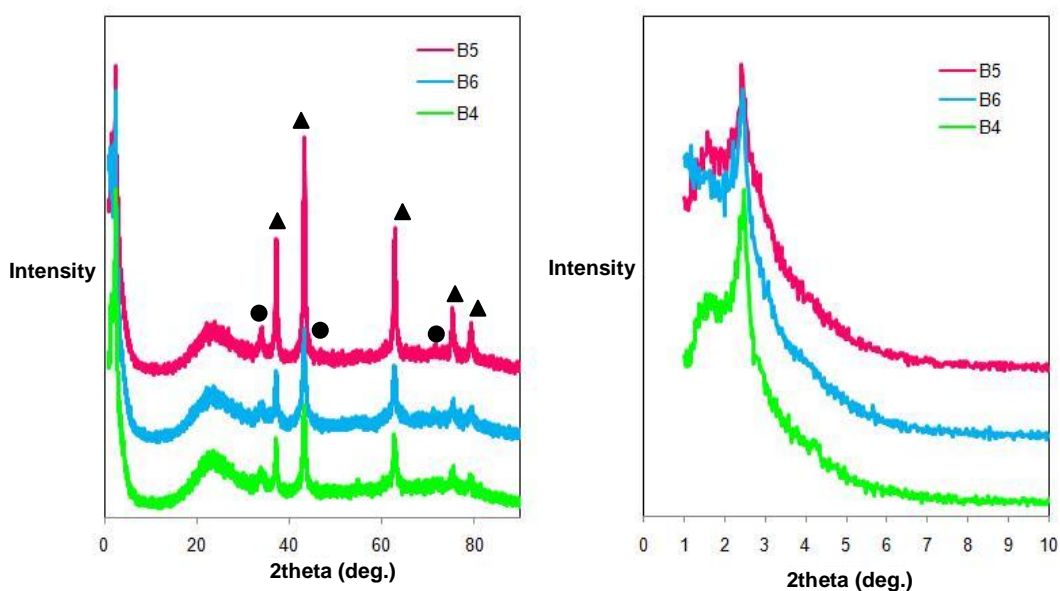


Figure 9.1.16. Small and high angle X-ray diffraction patterns of Pd-Ni@MCM-41 catalysts after calcination (▲ NiO, ● PdO)

9.1.1.3.3. Nitrogen Adsorption-Desorption Analysis

Surface area of PdNi@MCM-41 catalysts before and after calcination were measured and the results are presented in Table 9.1.9.

Table 9.1.9. Nitrogen adsorption analysis results of prepared catalysts after calcination

Sample	BET Surface Area (m ² /g)	BJH Ads. Surface Area (m ² /g)	Pore Volume (cc/g)	BJH Ads. Pore Diameter (nm)	Pore Wall Thickness (nm)
B4	633	615	0.47	2.18	1.97
B6	625	605	0.42	2.20	1.98
B5	577	563	0.40	2.45	1.73

The BET surface area values of the calcined bimetallic catalysts synthesized in this work were in the order of magnitude of 600 m²/g (Table 9.1.9), while the BET surface area of pure MCM-41 was 1358 m²/g. This decrease of surface area indicated closure of some of the pores of MCM-41 by the incorporated Ni and Pd clusters. The pore volume of pure MCM-41 was about 1.2 cc/g, while the pore volumes of the bimetallic catalysts were less than half of this value. Decrease of the pore volume of MCM-41 by the incorporation of Ni and Pd also indicated the closure of some of the pores. The surface area values of the uncalcined materials were also determined. N₂ adsorption-desorption results of uncalcined materials gave surface area and pore volume values in the ranges of 300 m²/g and 0.2 cm³/g, respectively. These values are about half of the corresponding values obtained after the calcination step. Decomposition of Pd(NO₃)₂ and NiNO₃ during the calcination process opens some of the pores of the nanocomposite materials, blocked by these salts of Pd and Ni.

Nitrogen adsorption-desorption isotherms of these bimetallic catalytic materials were close to Type IV, indicating mesoporous structure (Figure 9.1.17). Also pore size distributions were quite narrow in the range of 1-5 nm (Figure 9.1.18) with average pore diameters between 2.2-2.5 nm. (Table 9.1.9). These values were about 10-20% less than the average pore diameter of pure MCM-41. These results indicated the formation of a thin layer of metal on the surfaces of some of the pores. However, some of the pores are completely blocked by the Pd and Ni nanoballs causing significant reduction in the pore volume and the surface area.

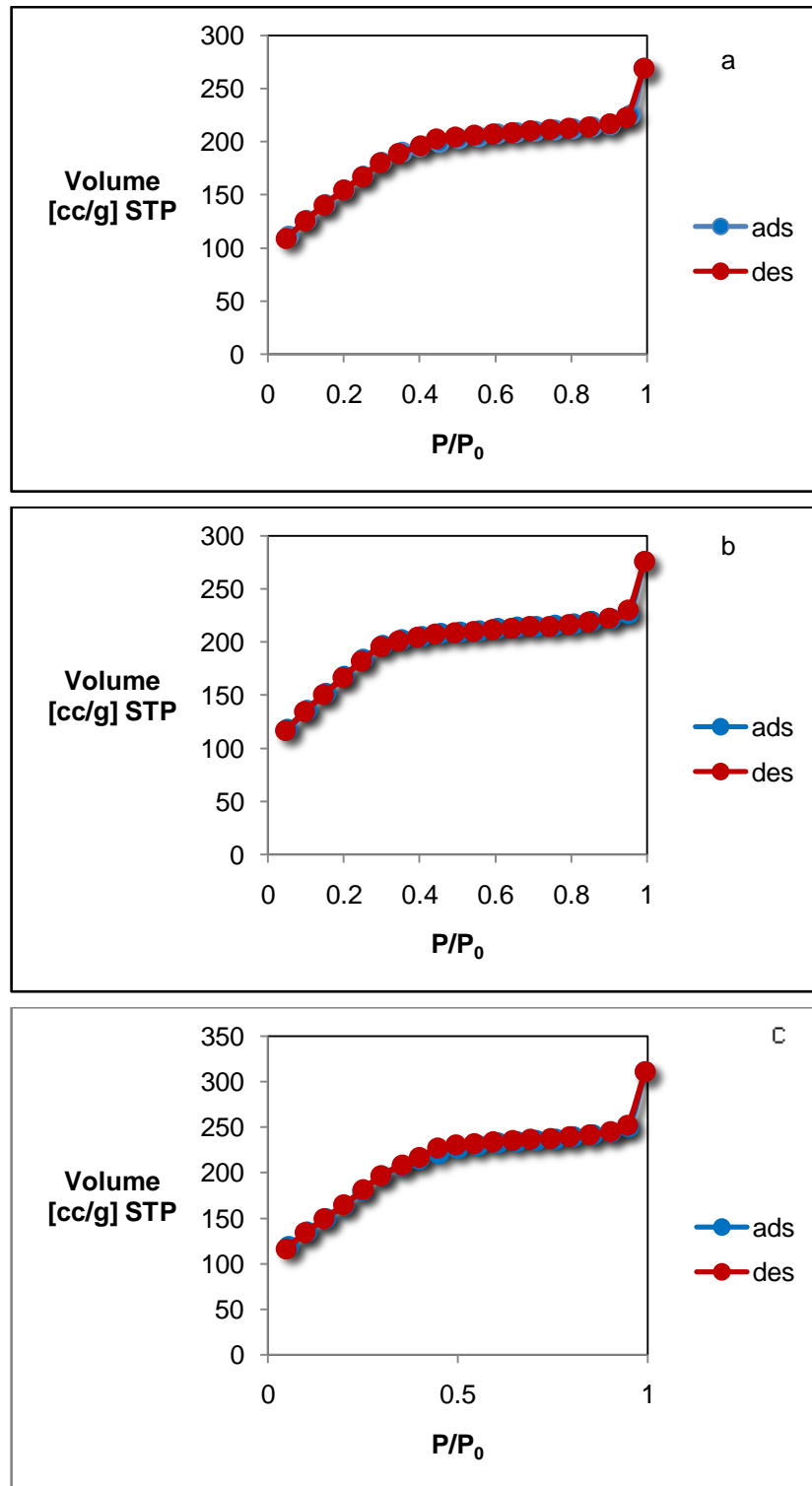


Figure 9.1.17. Nitrogen adsorption-desorption isotherms of PdNi@MCM-41 catalysts (a) B5 (b) B6 (c) B4

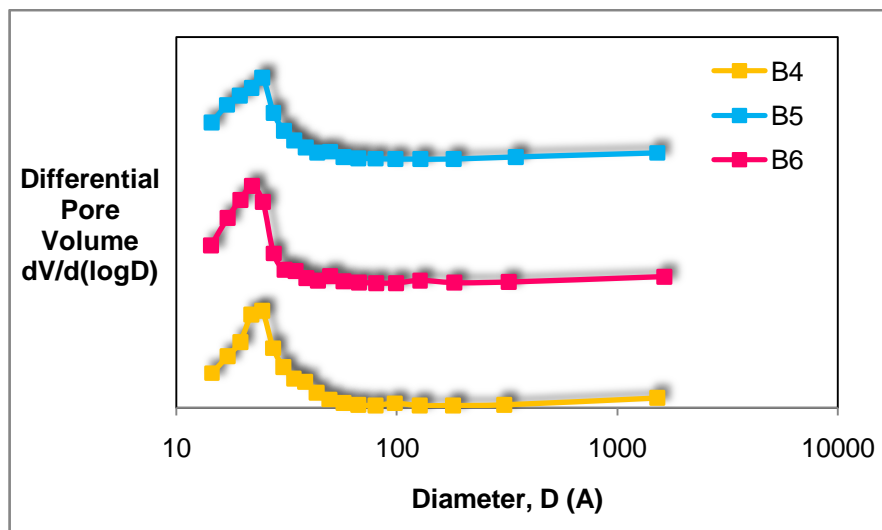


Figure 9.1.18. Pore size distribution curves of Pd-Ni@MCM-41 catalysts

9.1.1.3.4. SEM Analysis

Figure 9.1.19 is the presentation of the SEM images of Pd-Ni@MCM-41 catalysts before and after calcination. Agglomerated particles are observed in SEM images.

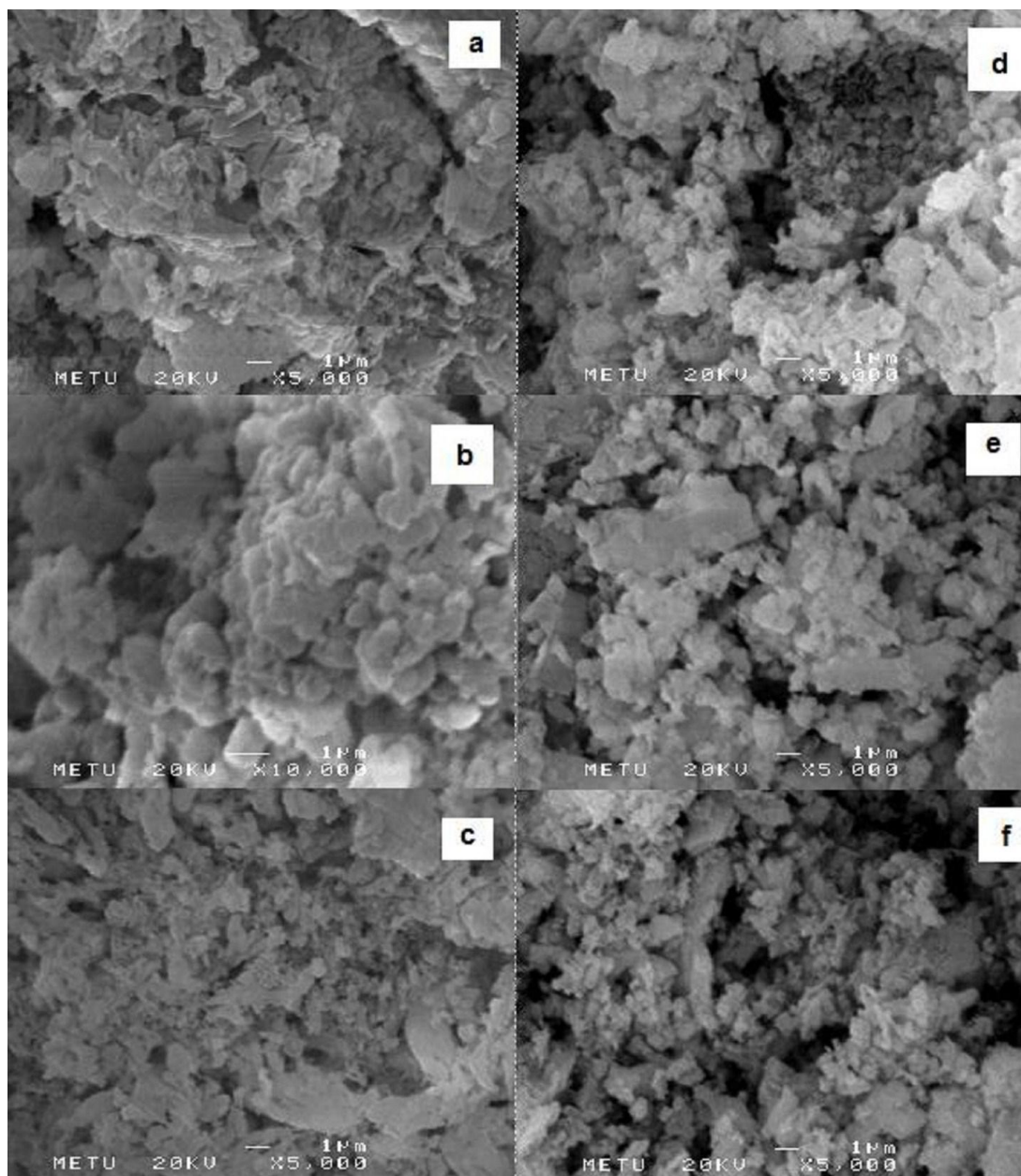


Figure 9.1.19. SEM images of PdNi@MCM-41 samples (a) B4, (b) B5 (c) B6 (d) B10, (e) B11, (f) B12

9.1.1.3.5. TGA Analysis

The calcination temperature of the synthesized materials was determined by the thermal analysis of the uncalcined materials. Typical TGA and DTA plots of an uncalcined material (uncalcined form of B4) are shown in Figure 5.20 and Figure 5.21. These analyses indicated two decomposition steps of the impregnated salts of Ni and Pd at around 200°C and 300°C. TGA results showed that all decomposition steps were essentially completed before 400°C. However, considering the future use of these synthesized materials in dry reforming of

methane and steam reforming of alcohols in a temperature range extending upto 550°C, final calcination temperature was selected as 550°C.

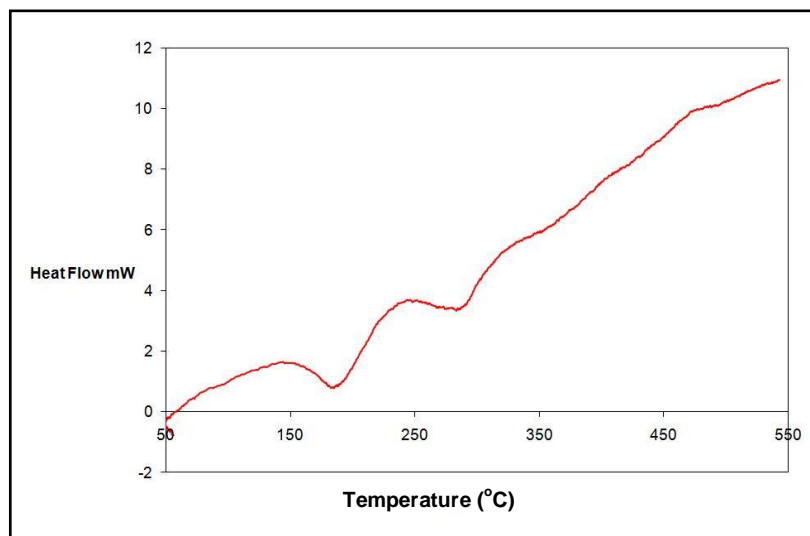


Figure 9.1.20. DTA plot of B10 sample

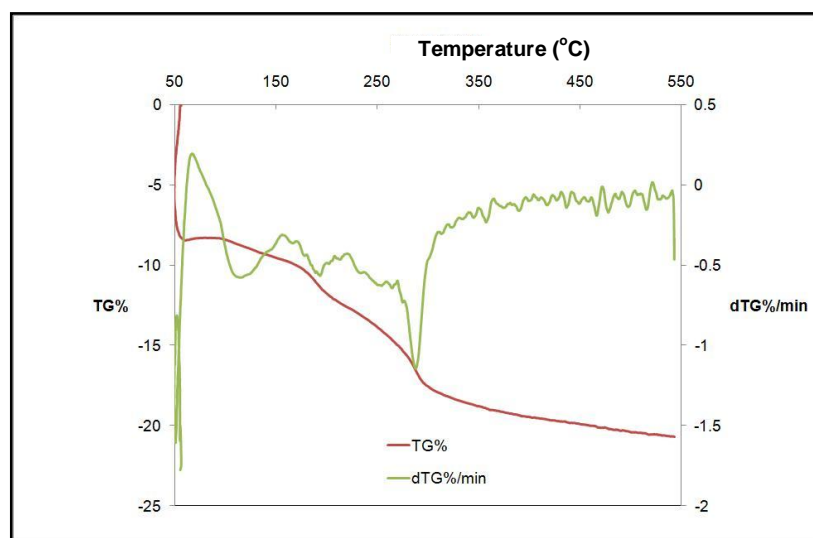


Figure 9.1.21. TGA plot of B10 sample

9.1.1.3.6. TPR Studies

Comparison of the TPR results of the bimetallic materials (B4, B6) (Figure 9.1.22) with the TPR results of materials containing only Ni in MCM-41 (B1, B3) (Figure 9.1.13) having about the same amount of Ni as in B4 and B6 (Figure 5.22), indicated a shift of the lower limit of

the reduction temperature to smaller values in the case of bimetallic materials. For materials not containing any Pd (Figure 9.1.13), reduction process started at about 300°C. However, the reduction of the bimetallic materials started at temperatures as low as 250°C. These results indicated that impregnation of small amount of Pd into the catalyst (Pd/Ni atomic ratio being between 0.05-0.07) caused a decrease in the reduction temperature. This is considered to be due to the promoting effect of Pd on the reduction of Ni species. A similar promoting effect of Pd on the reduction of NiO was also reported in the recent study of Mukainakano et al. , for Pd-Ni bimetallic catalysts impregnated into γ -Alumina. Our TPR results with the catalyst containing only Pd impregnated into MCM-41 also indicated completion of the reduction process of Pd-MCM-41 below 300°C. The main reduction peak observed between 300-380°C for B1 and B3 (catalysts containing only Ni in MCM-41) and between 250-350°C for the bimetallic catalysts B4 and B6 is actually composed of at least two overlapping peaks. As shown in Figure 9.1.22, a third wide TPR peak was also observed at higher temperatures (in the range of 400-520°C). Reduction of the isolated nickel oxide present on the surface of nanoballs is expected to be reduced very easily at lower temperatures. However, the reduction of nickel oxide species interacting strongly with the mesopore surfaces of the silicate structured support and reduction of nickel oxide present deep within the nanoballs are more difficult and these reduction processes take place at higher temperatures. These results agree with the results of (Pawelec B. 2007) and (Feio L.S.F. 2007) that reduction of nickel oxide species interacting strongly with the support take place at higher temperatures.

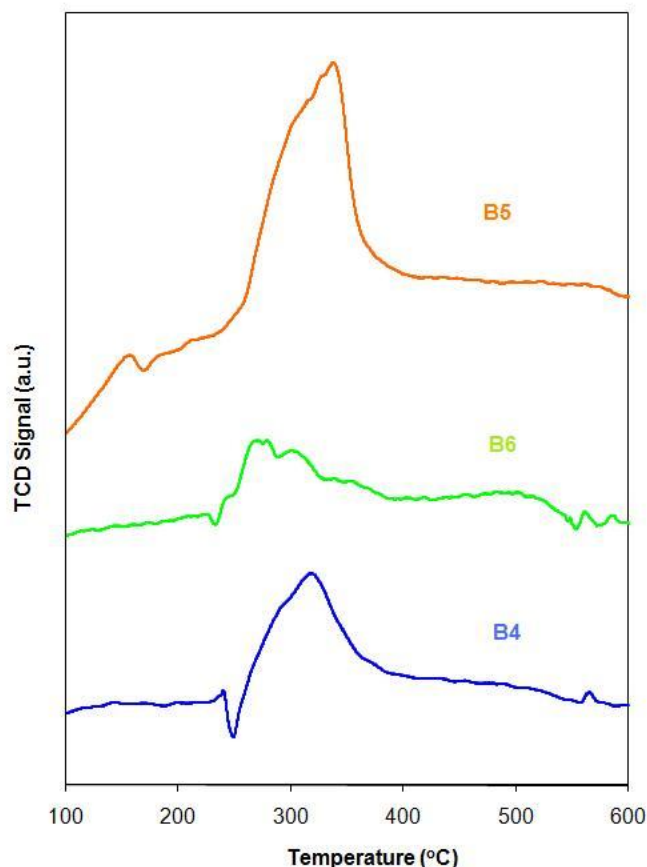


Figure 9.1.22. TPR profiles Pd-Ni@MCM-41 catalysts

9.1.1.3.7. Transmission Electron Microscopy-TEM Analysis

TEM images of the synthesized materials and the XRD analysis of the materials clearly showed the formation of NiO and PdO nanoballs within the MCM-41 matrix (Figures 9.1.23 and 9.1.24). As shown in Figure 9.1.23, nanoballs having diameters between 15-25 nm and 3-10 nm are distributed within the synthesized materials. A few of the larger nanoballs with diameters larger than 50 nm were also observed at some locations within the matrix of sample B6 (Figure 9.1.24).

The pore structure of B6 was seen in the high resolution TEM images given in Figure 9.1.25 and 9.1.26. Formation of nanoballs within the MCM-41 matrix are also seen in Figure 9.1.25. All TEM images showed that Ni and Pd were penetrated into most parts of the synthesized materials. However, as shown in Figure 9.1.26, penetration of Ni and Pd into some parts of the materials were not complete. The darker penetrated regions of the catalysts with Ni and Pd layers on the pore surfaces are seen in this figure.

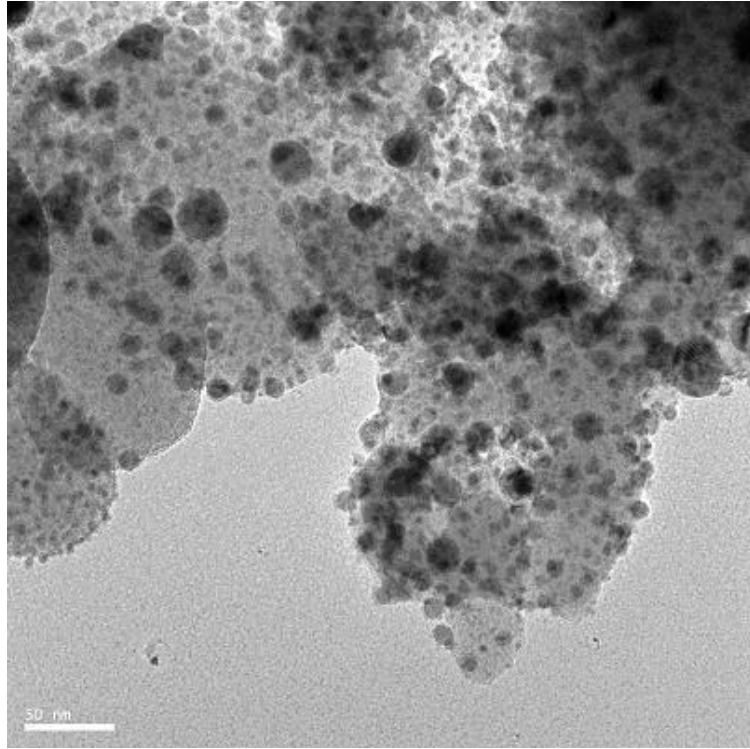


Figure 9.23. TEM image of B6 sample (1)

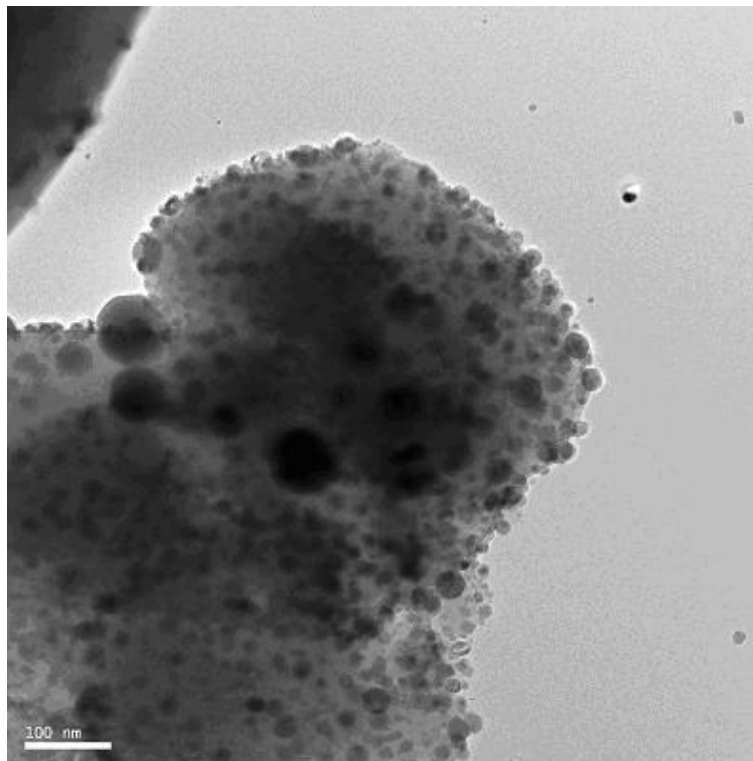


Figure 9.1.24. TEM image of B6 sample (2)

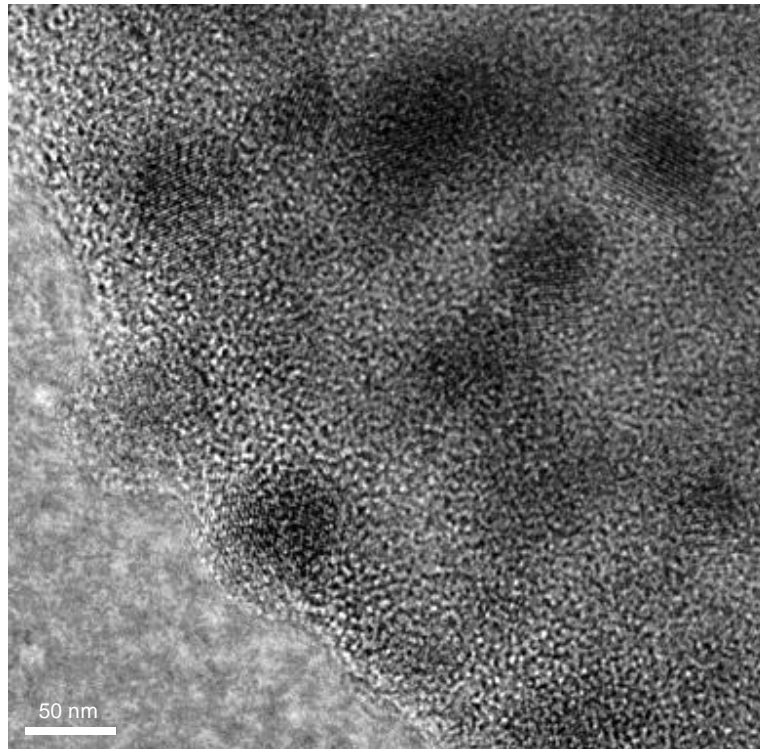


Figure 9.1.25. TEM image of B6 sample (3)

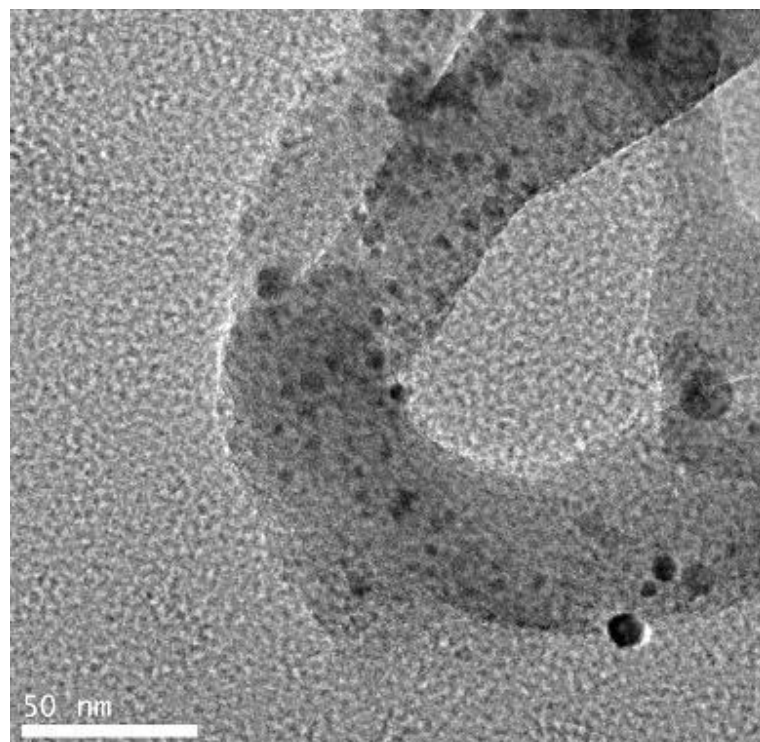


Figure 9.1.26. TEM image of B6 sample (4)

9.1.1.3.8. X-Ray Photoelectron Spectroscopy (XPS) Analysis

The XPS analysis of all the materials gave characteristic bands of O 1s and Si 2p at 103.2 eV and 532.5 eV, respectively (Table 9.1.10). For the bimetallic catalysts, the characteristic bands of Ni observed for the calcined and the reduced materials are given in Figure 5.27. As shown in this figure, the main band was observed at 855.7 eV and 855.3 eV for Ni 2p_{3/2} in the XPS spectra of B4 and B6, respectively. However, for the reduced material (in hydrogen) this band shifted to 852.5 eV. The binding energy values of Ni⁺³ (Ni₂O₃), Ni⁺² (NiO) and Ni⁰ were reported in the literature as 856.1 eV, 854.4 eV and 852.7 eV, respectively. Our results indicated that in the calcined materials nickel was partly in +3 and partly in +2 oxidation state. The Ni/Si atomic ratios evaluated from XPS analysis of the materials were also found to be quite close to the EDS analysis of these materials, indicating that distribution of nickel on the external surface and within the bulk of the synthesized materials were similar. For instance, the Ni/Si ratio of B5 evaluated from XPS was 0.097, while this ratio had been determined as 0.10 from EDS. XPS bands corresponding to palladium in the B4 and B5 materials are shown in Figure 5.28. This XPS analysis indicated a Pd/Si atomic ratio of 0.0072 in sample B5. For the same sample Pd/Si atomic ratio in the bulk of the material evaluated from EDS was 0.008. As shown in this figure, the main XPS band of Pd 3d₅ was observed at 335.7 eV and 336.1 eV, respectively. For PdO₂, PdO and Pd⁰, XPS bands are reported at 337.9 eV, 336.3 eV and 335.1 eV, respectively (Sener et al., 2006). Our results indicated that palladium was essentially in PdO form in the synthesized materials.

Table 9.1.10. XPS parameters of the samples

Sample	Binding Energy (eV)			
	Ni 2p _{3/2}	Pd 3d ₅	Si 2p	O 1s
B4 (calcined)	855.7	335.7	103.3	532.5
B5 (calcined)	855.3	336.1	102.9	532.5
B5 (reduced)	852.5	small	102.9	532.5

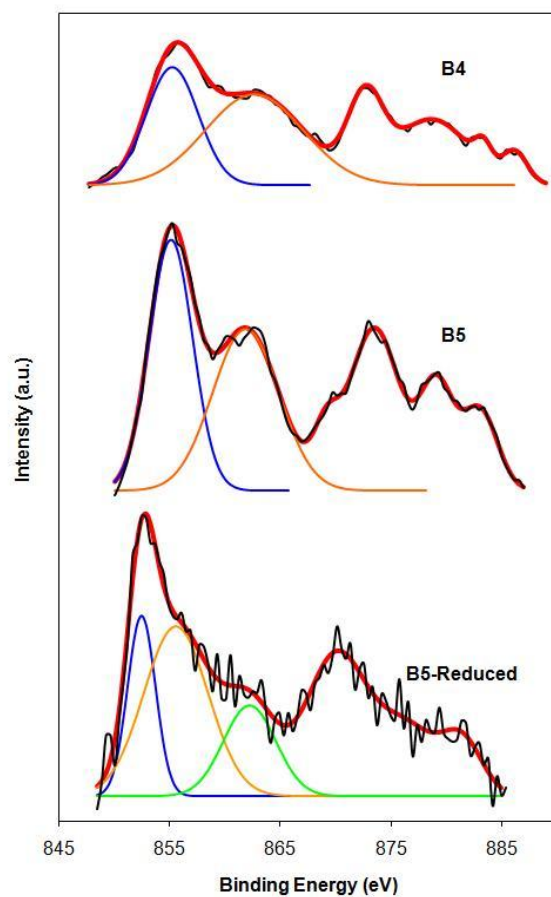


Figure 9.1.27. XPS patterns of Pd-Ni dual catalysts for NiO region

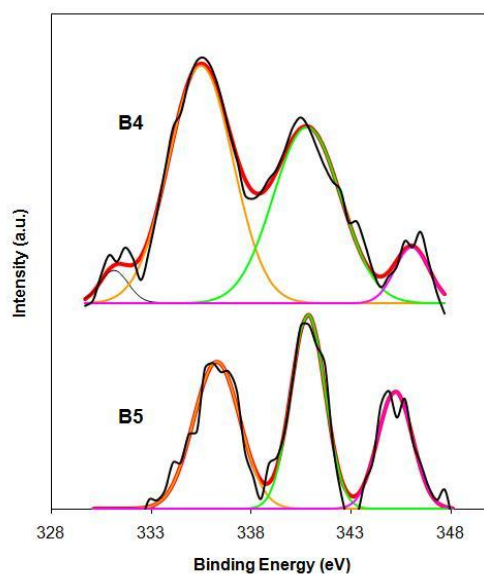


Figure 9.1.28. XPS patterns of Pd-Ni dual catalysts for PdO region

9.1.2. ETHANOL-STEAM REFORMING REACTION RESULTS WITH Ni AND Ni-Pd IMPREGNATED MCM-41

Ethanol-steam reforming reaction was performed with the synthesized catalysts as described in Section 8.3. Using the composition of the reactor effluent stream, ethanol conversion, selectivities of different products and hydrogen yield were examined.

The ethanol reforming reaction carried out in a temperature range of 200-550 °C by the catalysts showed that the main products were hydrogen and carbon monoxide. Besides H₂ and CO, formation of some carbon dioxide, methane and form aldehyde were also observed. Trace amounts of ethylene were also observed in some reactions.

9.1.2.1. ETHANOL CONVERSION

Conversion of ethanol was calculated according to the formula given below.

$$\text{Conversion of } C_2H_5OH (X_{EtOH}) = \frac{\text{Moles of ethanol converted}}{\text{Moles of ethanol fed to the reactor}}$$

A sample hand calculation is presented in Appendix A.3 Change of ethanol conversion with temperature is plotted in Figures 9.1.40 and 9.1.41 for Ni@MCM-41 and PdNi@MCM-41 catalysts, respectively.

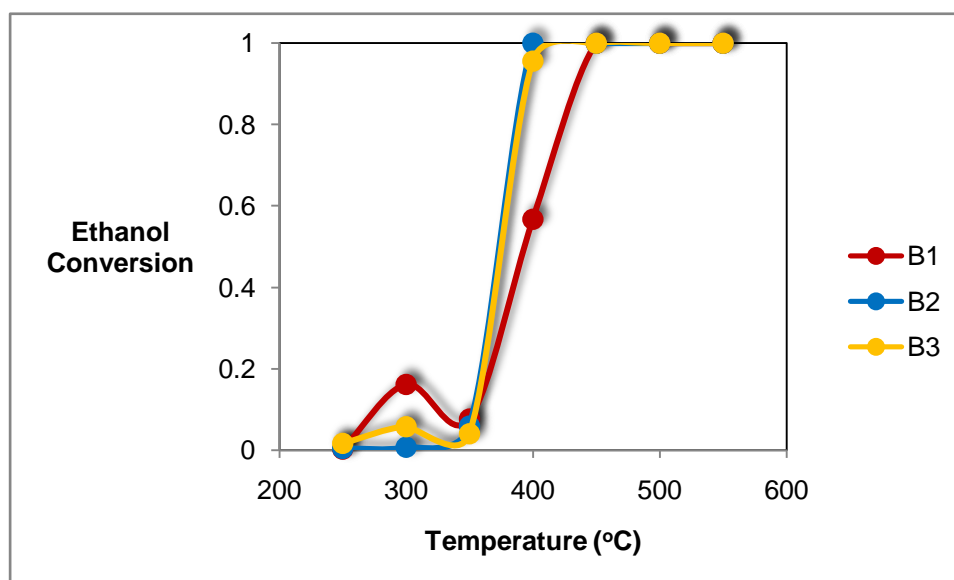


Figure 9.1.40. Change of ethanol conversion with temperature for Ni incorporated catalysts

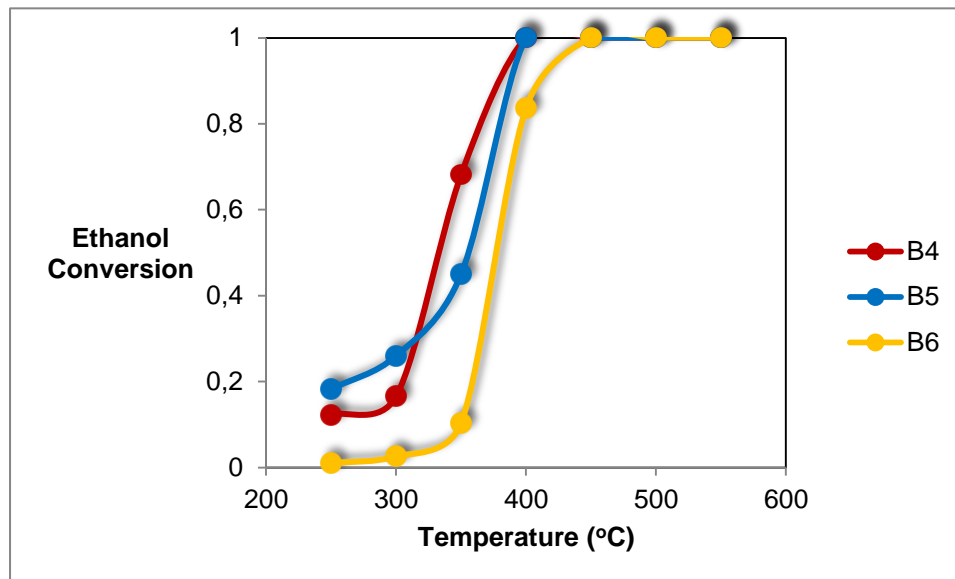


Figure 9.1.41. Change of ethanol conversion with temperature for Pd-Ni incorporated catalysts

As shown in Figure 9.1.40, ethanol conversion started at temperatures over 350 °C. It sharply increased with an increase in temperature, reaching to almost complete conversion over 400 °C for the reaction catalyzed by B2 and B3, i.e. the catalysts are highly active for ethanol-steam reforming reaction.

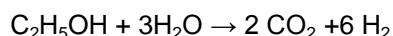
Pd incorporation to the Ni@MCM-41 catalysts caused some increase in the activity. The reaction starts over 200 °C in this case and goes to completion at 400 °C (Figure 9.1.41).

9.2.1.2. HYDROGEN YIELD

The most important product of ethanol-steam reforming reaction is the hydrogen. Yield of hydrogen is evaluated according to the formula below:

$$Yield\ of\ H_2O(Y_{Hydrogen}) = \frac{Moles\ of\ ehydrogen\ produced}{Moles\ of\ ethanol\ fed\ to\ the\ reactor}$$

The maximum Hydrogen yield that can be obtained for this reaction is 6.



The calculated reaction parameters are presented in Appendix A.5 for all catalysts.

However, producing 6 moles of hydrogen is not expected because of the possibilities of the side reactions, such as water-gas shift, ethylene formation by ethanol dehydration, acetaldehyde formation by dehydrogenation and coke formation.

The hydrogen yield increased with increasing temperature over 350°C for Ni incorporated MCM-41 catalysts (Figure 9.1.42). Hydrogen yield seems to be over 3 for B1 and B2 catalysts around 500°C.

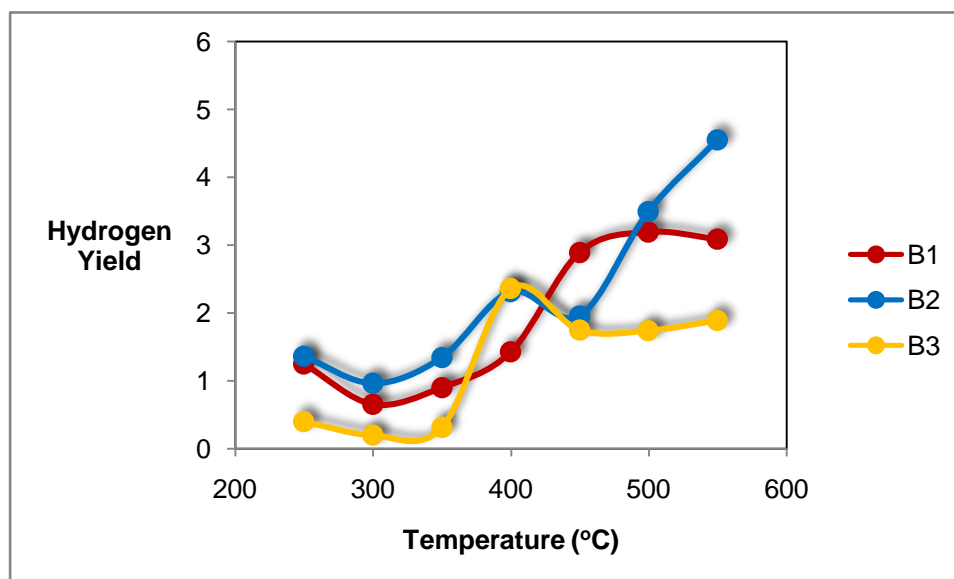


Figure 9.1.42. Change of hydrogen yield with temperature for Ni incorporated catalysts

PdNi impregnated catalysts shows a similar behavior for hydrogen yield to the Ni impregnated catalysts (Figure 9.1.43). B4 and B5 give almost the same hydrogen yield, B6 gives higher yield over 450 °C.

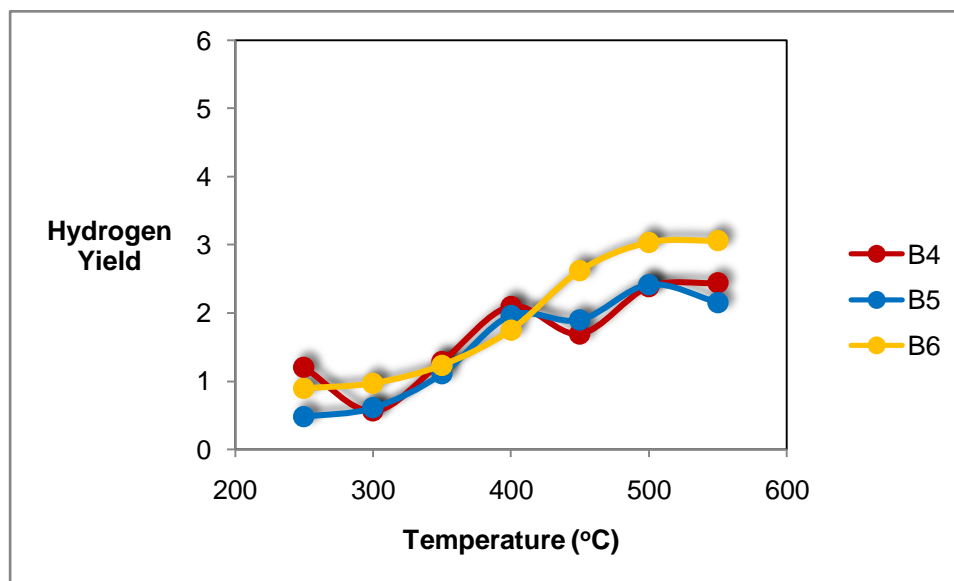


Figure 9.1.43. Change of hydrogen yield with temperature for PdNi incorporated catalysts

9.1.2.3. PRODUCT DISTRIBUTION OF Ni AND Pd-Ni INCORPORATED CATALYSTS

Selectivity of the products were calculated following equations and product distributions for the catalysts B1, B2, B3, B4, B5 and B6 were presented in Figures 9.1.44, 9.1.45, 9.1.46, 9.47, 9.48 and 9.49, respectively.

$$\text{CH}_4 - \text{Selectivity} = \frac{(0.5)(\text{CH}_4)_{\text{out}}}{(\text{C}_2\text{H}_5\text{OH})_{\text{converted}}} \quad (\text{E } 9.1.2)$$

$$\text{CO} - \text{Selectivity} = \frac{(0.5)(\text{CO})_{\text{out}}}{(\text{C}_2\text{H}_5\text{OH})_{\text{converted}}} \quad (\text{E } 9.1.3)$$

$$\text{CO}_2 - \text{Selectivity} = \frac{(0.5)(\text{CO}_2)_{\text{out}}}{(\text{C}_2\text{H}_5\text{OH})_{\text{converted}}} \quad (\text{E } 9.1.4)$$

Formation of some formaldehyde was observed for all the catalysts up to 400 °C and disappeared at higher temperatures. CH₄, CO and CO₂ are the carbon components appearing when the temperature increases over 450 °C. Methane formation increases with increasing temperature in the range of 450 °C and decreases over 450 °C. Methane formation is the result of C-C bond cracking and it is an unwanted side product. Methane-

steam reforming reaction is expected partially at higher temperatures. Pd incorporation increased Carbon Dioxide formation and this is a desirable behavior. Carbon Monoxide formation is at its maximum value between 350-400°C.

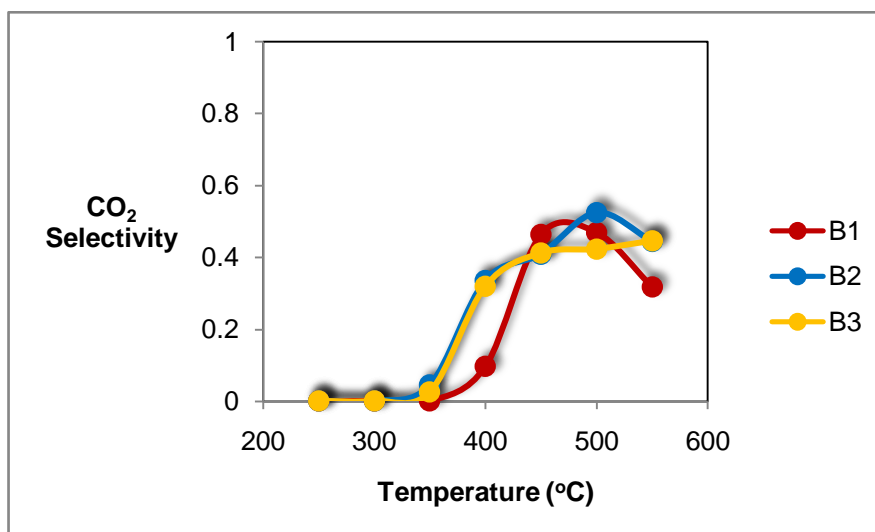


Figure 9.1.44. Carbon dioxide selectivity for Ni impregnated MCM-41 catalysts

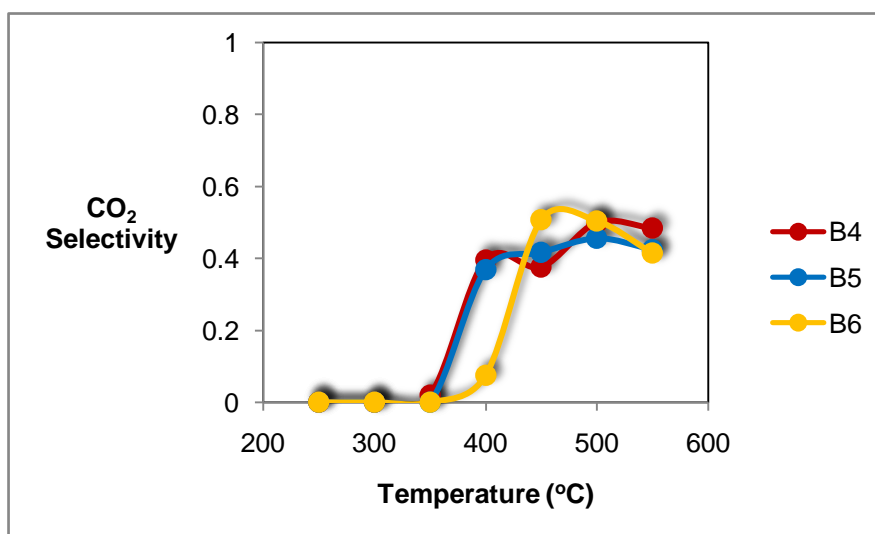


Figure 9.1.45. Carbon dioxide selectivity for Pd Ni impregnated MCM-41 catalysts

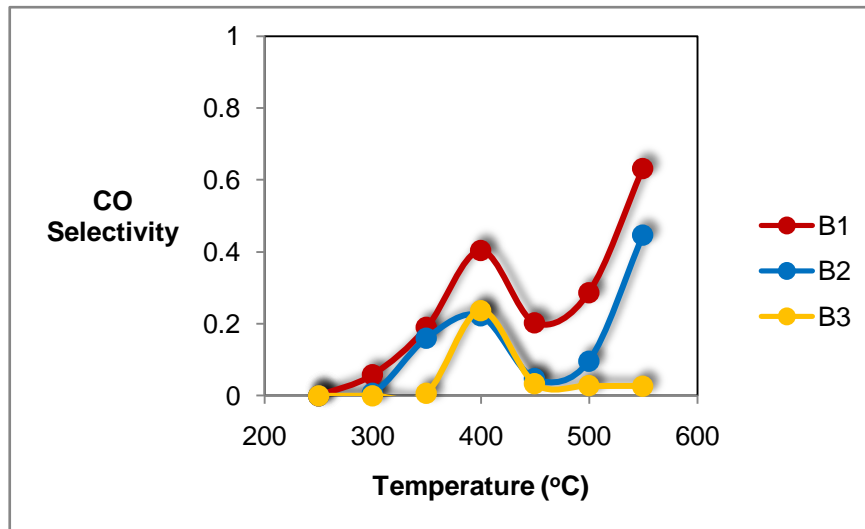


Figure 9.1.46. Carbon monoxide selectivity of Ni impregnated MCM-41

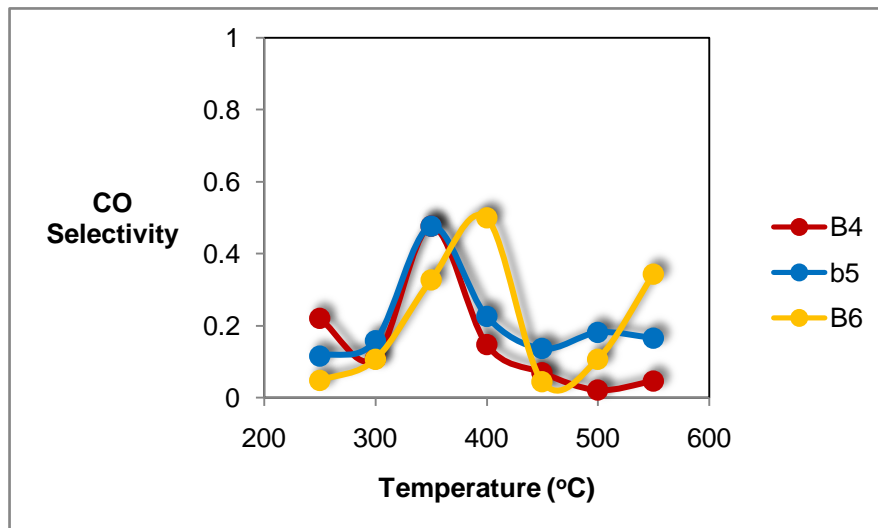


Figure 9.1.47. Carbon monoxide selectivity of PdNi impregnated MCM-41

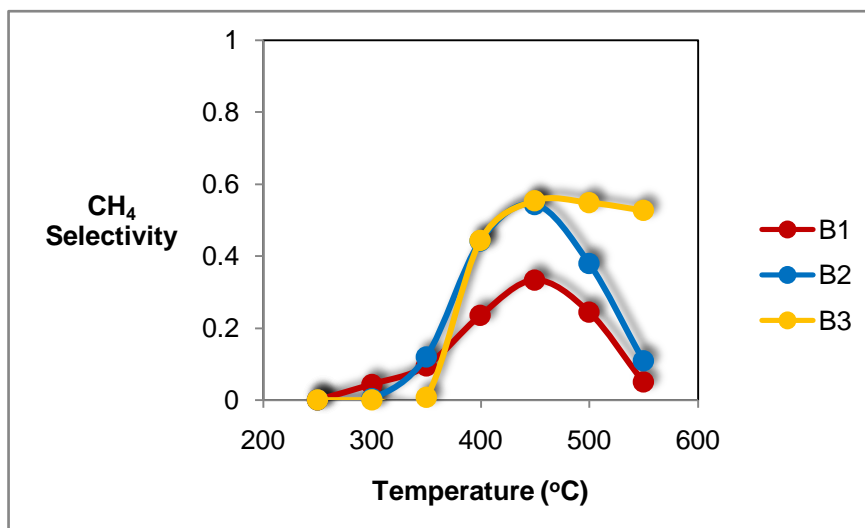


Figure 9.1.48. Methane selectivity of Ni impregnated MCM-41 catalysts

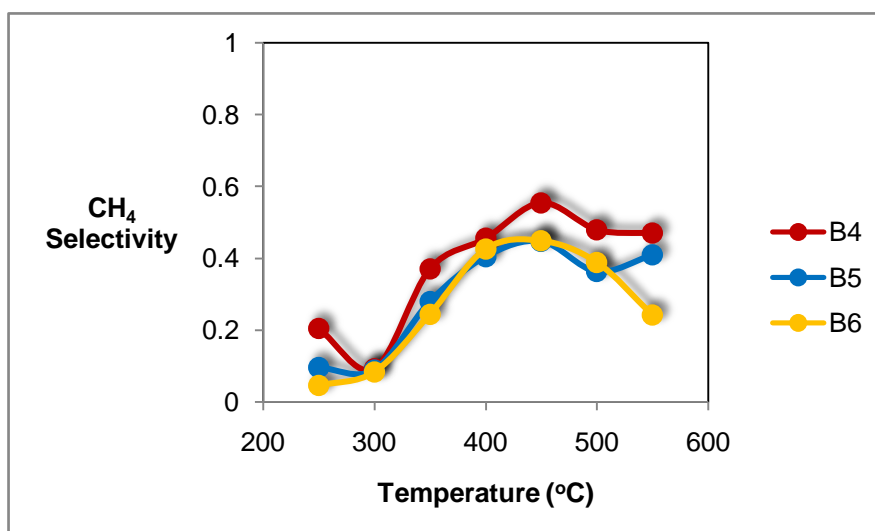


Figure 9.1.49. Methane selectivity of PdNi impregnated MCM-41 catalysts

Product distribution of each catalyst is given in Figures 9.1.50, 9.1.51, 9.1.52, 9.1.53, 9.1.54 and 9.1.55. Product composition at a specified temperature is obtained by following the temperature line. The plots are product selectivity versus temperature versus species plots. For all catalysts at 250 °C and 300 °C, acetaldehyde formation dominates and acetaldehyde concentration is high in product stream. At higher temperatures CH₄, CO and CO₂ concentrations increase.

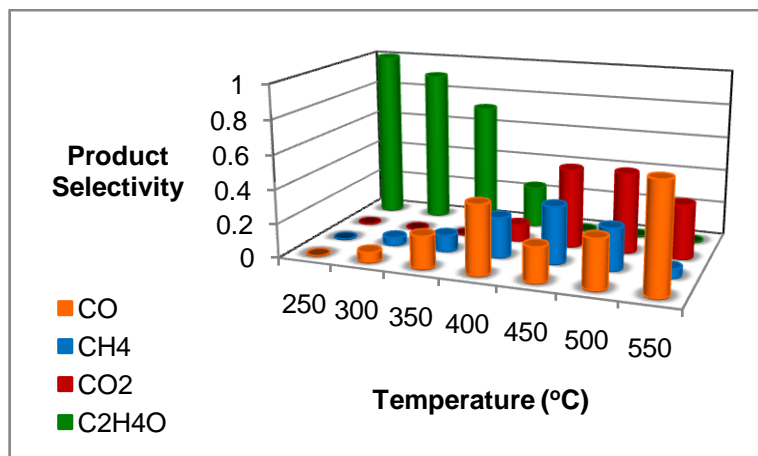


Figure 9.1.50. Product distribution of B1 catalyst

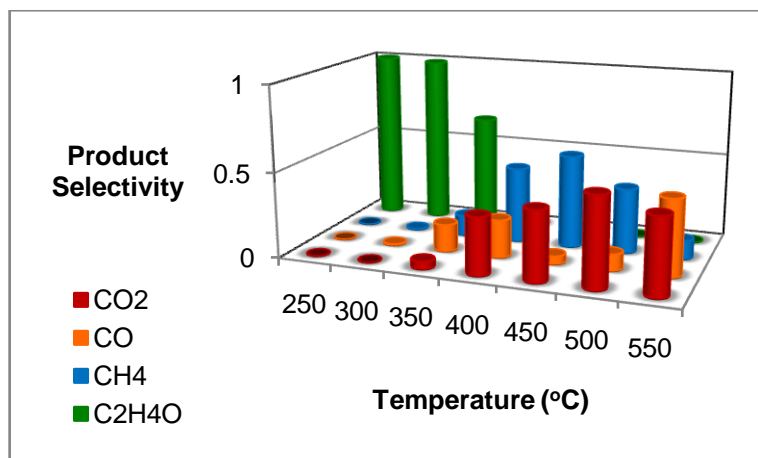


Figure 9.1.51. Product distribution of B2 catalyst

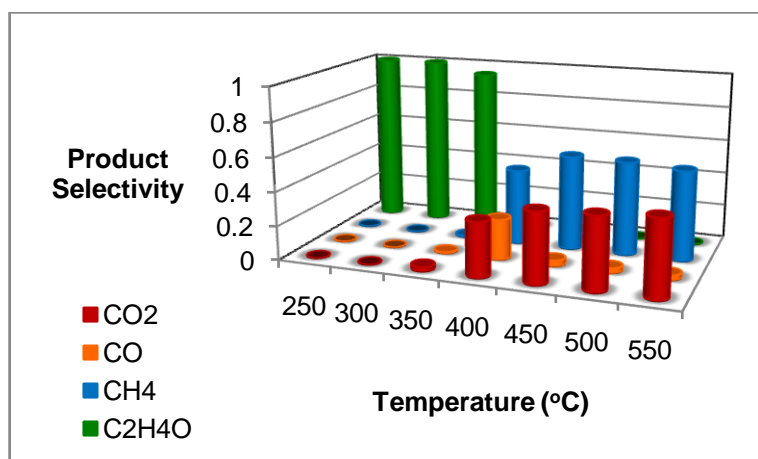


Figure 9.1.52. Product distribution of B3 catalyst

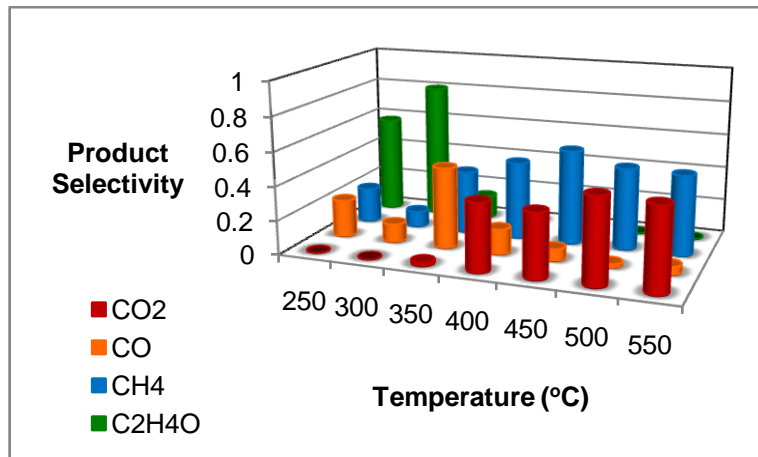


Figure 9.1.53. Product distribution of B4 catalyst

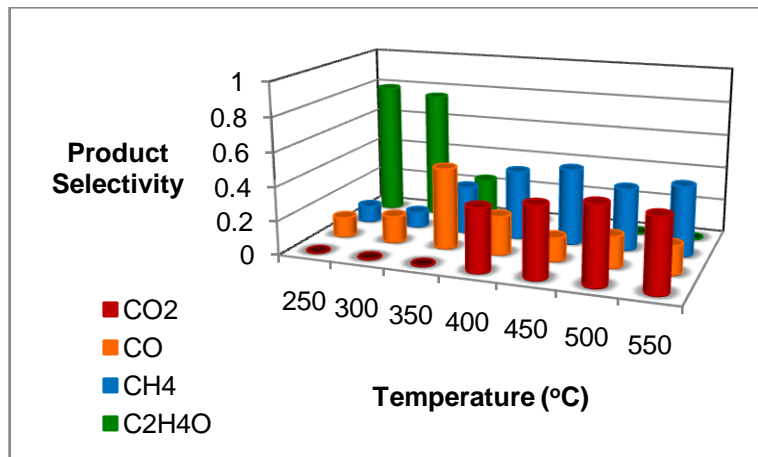


Figure 9.1.54. Product distribution of B5 catalyst

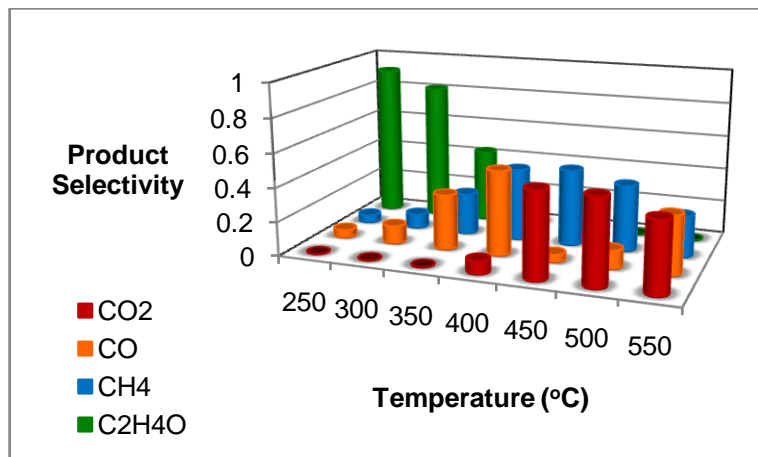


Figure 9.1.55. Product distribution of B6 catalyst

9.2.1.4. COMPARISON OF Ni & PD-NI INCORPORATED CATALYSTS

In this section, the catalysts before and after Pd impregnation were compared and the effect of Pd impregnation was examined.

In Figure 9.1.56, ethanol conversion curves for B1 and B4 were compared. B4 catalysts obtained by the impregnation of Pd to the B1 showed a very similar behavior in ethanol conversion versus temperature curve, but at 250 °C a shift was observed. At 350°C, while ethanol conversion by B1 was 5%, by B4 it increased up to 70%. It is clearly concluded that incorporation of Pd increased the catalysts activity in terms of ethanol conversion. Comparison of hydrogen yields of B1 and B4 catalysts are given in Figure 9.1.57. Impregnation of Pd decreased hydrogen yield due to the increased formation of CH₄ (Figure 9.1.59). Pd incorporation caused to favor ethanol decomposition instead of Steam reforming.

Carbon monoxide, methane and carbon dioxide selectivities of B1 and B4 were also compared in Figures 9.1.58, 9.1.59 and 9.1.60, respectively. Methane selectivity increased with Pd incorporation. CO selectivity of B4 at high temperatures was lower.

On the other hand, as mentioned before, these catalysts were also tested in dry reforming of methane with carbon dioxide in Bulgarian Academy of Sciences, Sofia Institute of Catalysis by Dr. Katia Arishtirova. According to carbon dioxide reforming of methane reaction results, addition of palladium increased the stability of the catalysts. These results are presented in Appendix A.4.

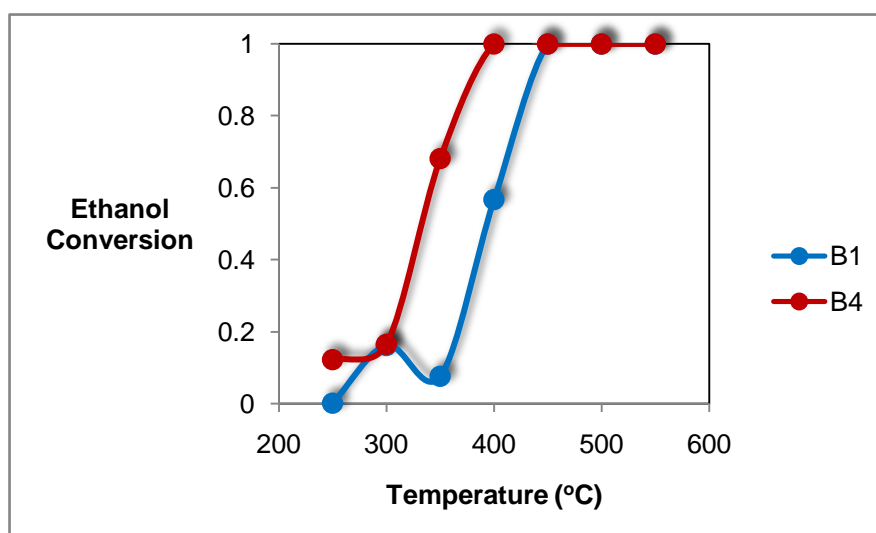


Figure 9.1.56. Change of ethanol conversion with temperature for B1 and B4 catalysts

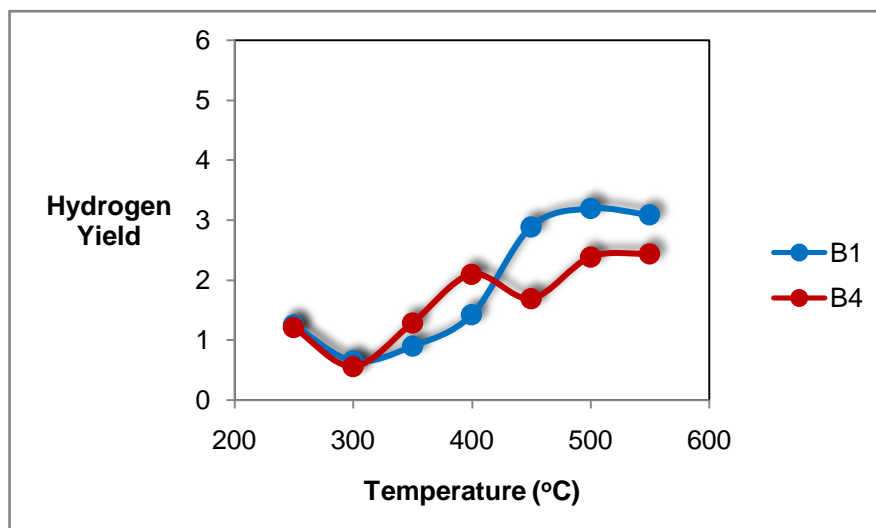


Figure 9.1.57. Change of hydrogen yield by temperature for B1 and B4 catalysts

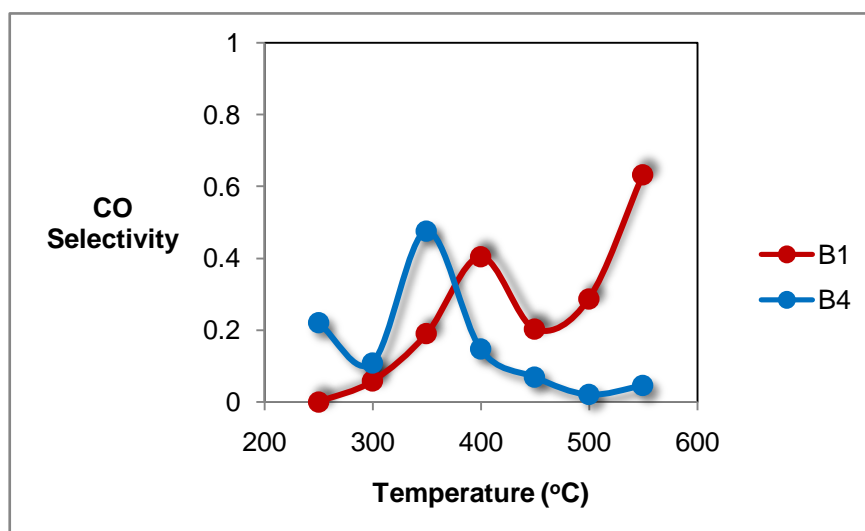


Figure 9.1.58. Change of carbon monoxide selectivity with temperature for B1 and B4 catalysts

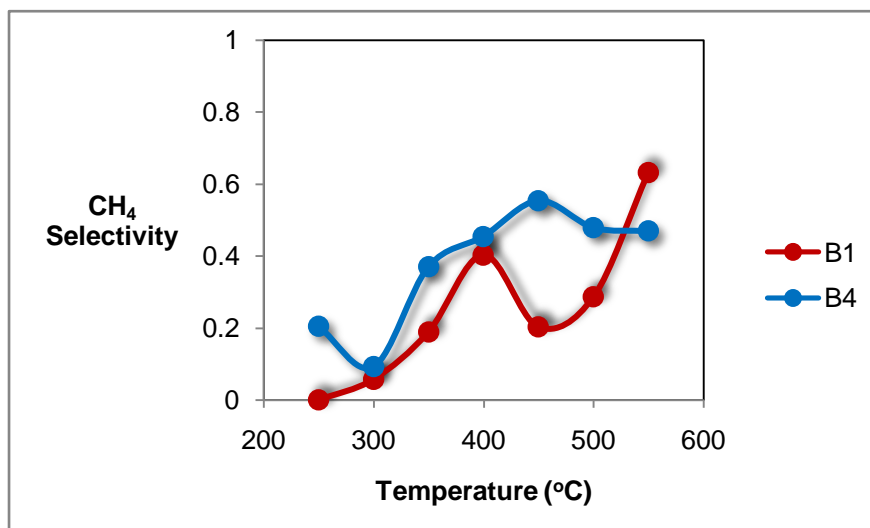


Figure 9.1.59. Change of methane selectivity with temperature for B1 and B4 catalysts

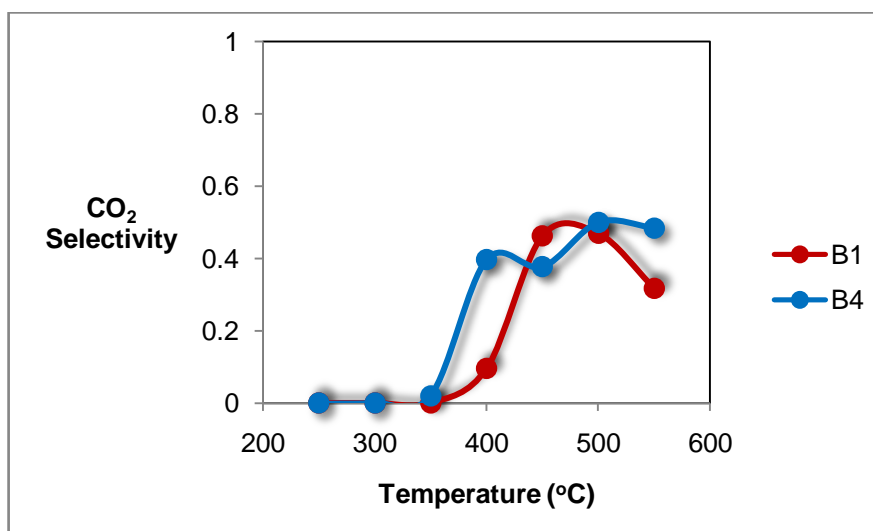


Figure 9.1.60. Change of CO₂ selectivity of B1 ve B4 catalysts with temperature

At the beginning of the experiments, in order to find proper reaction conditions, effect of flowrate to the conversion and hydrogen yield was tested. The results are presented in Appendix A.4. According to these results and the activity results presented above, Ni@MCM-41 catalysts show higher ethanol conversion and hydrogen yield at 550 °C with a total flow of 50 ml/min. Since the catalysts were calcined at 550 °C, activity tests above this temperature were not performed. By calcining at 600 °C, higher yield may be obtained by nickel impregnated MCM-41 catalysts.

9.1.3. CHARACTERIZATION RESULTS OF THE USED Ni AND PdNi IMPREGNATED CATALYST AFTER ETHANOL-STEAM REFORMING REACTION

The catalysts were re-characterized after reaction to have information about possible structural changes. Textural properties of the used catalysts are given in Table 9.1.11.

Table 9.1.11. Physical Properties of the Catalysts After Reaction

	B1	B2	B3	B4	B5	B6
Ni/Si atomic ratio (EDS)	0.10	0.18	0.12	0.10	0.18	0.10
Pd/Si atomic ratio (EDS)	-	-	-	0.010	0.004	0.002
BET surface area (m ² /g)	232.8	177.4	223.9	276.2	249.6	174.3
BJH surface area (m ² /g)	233.5	167.4	208.2	268.6	248.2	163.7
BJH pore volume (m ³ /g)	0.61	0.45	0.53	0.58	0.46	0.33
BJH average pore diameter (nm)	2.5	2.2	2.5	2.2	2.2	2.2

From Table 9.1.11, it is seen that, the surface area of the catalysts decreased and there was not a significant decrease in the content of Pd and Ni at the end of the reaction. Decrease in surface area is mainly due to the coke formation. X-ray diffraction patterns of Ni and Pd-Ni incorporated catalysts are given in Figures 9.68 and 9.69, respectively. Due to the filamentous carbon formation, carbon peak at a 2theta around 26 ° is observed in the x-ray diffraction patterns.

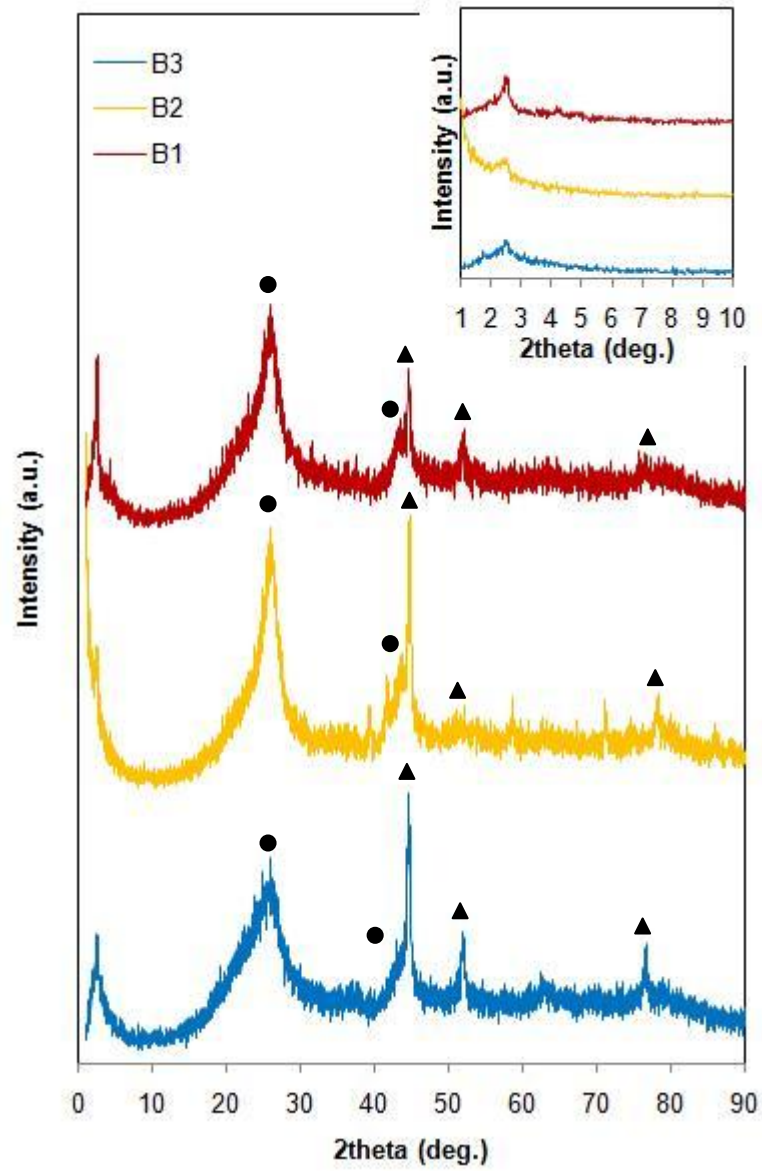


Figure 9.1.68. Low and high-angle x-ray diffraction patterns of B1, B2 and B3 after reaction (▲ NiO, ● C)

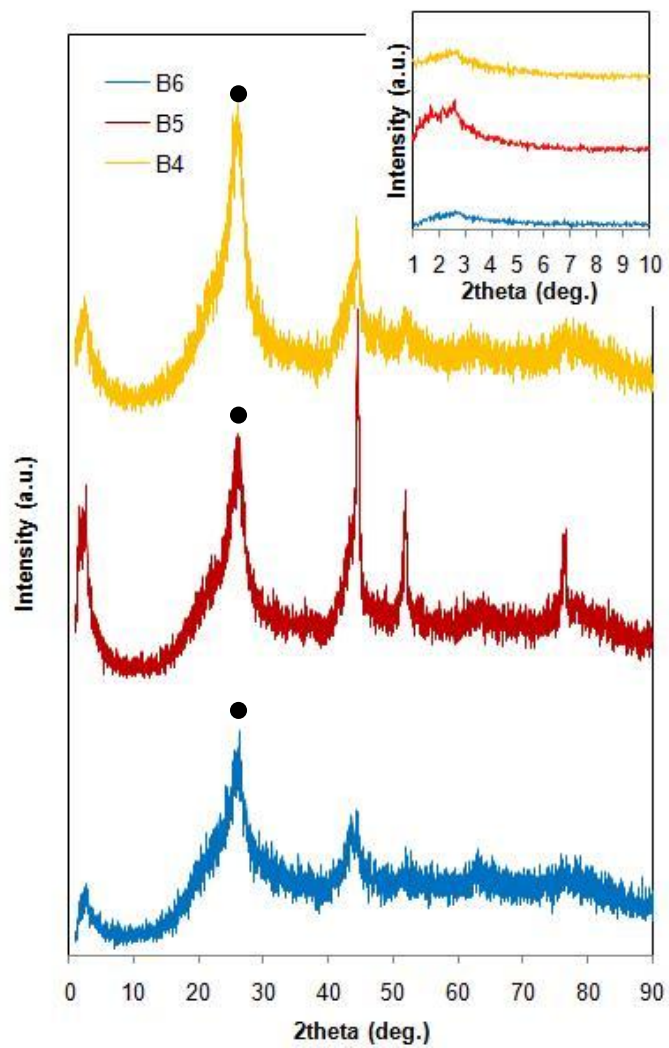


Figure 9.1.69. Low and High-angle X-ray diffraction patterns of B4, B5 and B6 catalysts after reaction (● C)

Nitrogen adsorption-desorption isotherms are presented in Figure 9.1.70 Figure 9.1.71.

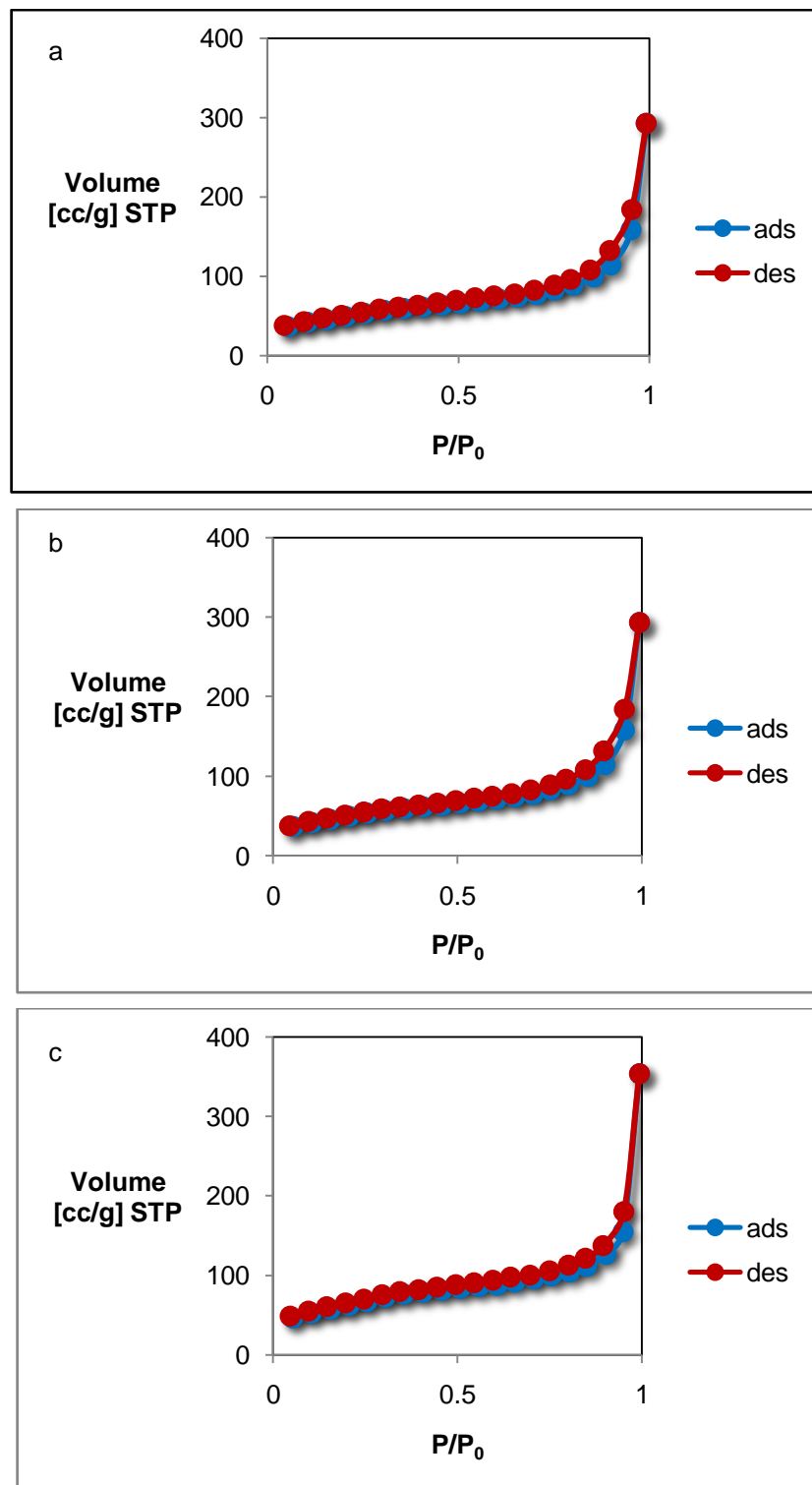


Figure 9.1.70. Nitrogen adsorption desorption isotherms of B1, B2 and B3 catalysts after reaction

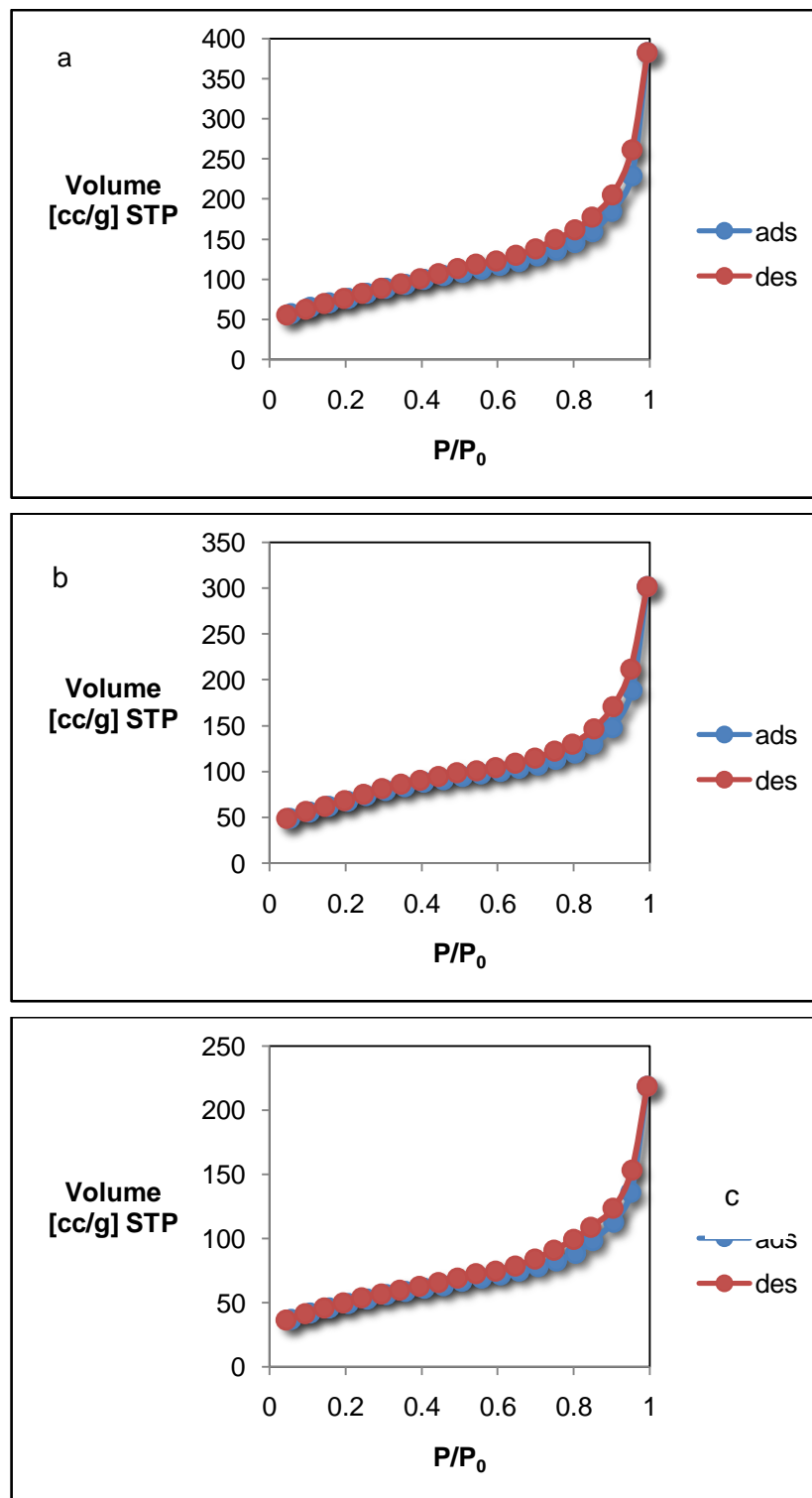


Figure 9.1.71. Nitrogen adsorption desorption isotherms of B4, B5 and B6 catalysts after reaction

After the reaction, the surface area of the catalysts varied between 170-235 m²/g. Changes occurred in the isotherms due to decrease in the surface area of the catalysts. Pore plugging occurred as a result of coke formation.

Pore size distribution of Ni and PdNi incorporated catalysts can be seen in graphs 9.1.72 and 9.1.73, respectively. Decrease in pore diameter occurred and the existence of macropores are observed.

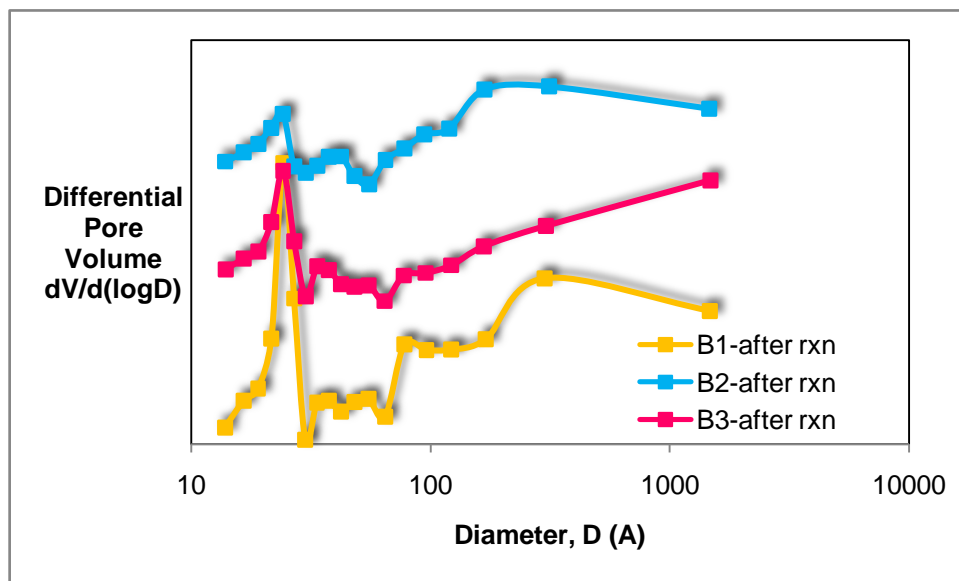


Figure 9.1.72. Pore size distribution curves of B1, B2 and B3 catalysts after reaction

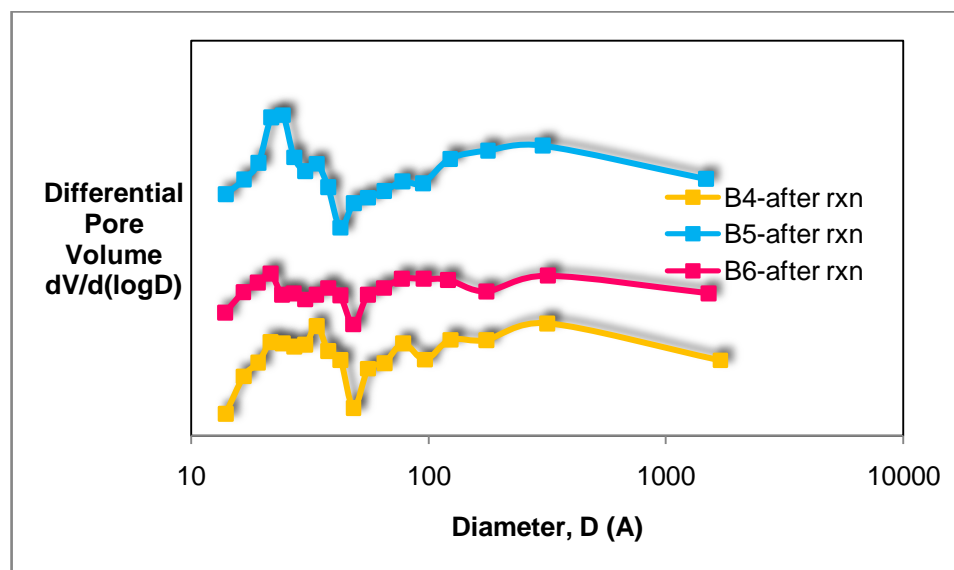


Figure 9.1.73. Pore size distribution curves of B4, B5 and B6 catalysts after reaction

Catalysts were analyzed by thermal gravimetric analysis (TGA) after reaction. Figures 9.1.74, 9.1.75, 9.1.76 and 9.1.77 for B1, B2 B3 and B4, respectively. Weight loss estimated by TGA are also summarized in Table 9.1.12. This weight loss corresponds to the carbon deposited on the catalyst surface during reaction.

In the TGA profiles, a small weight loss occurs at around 250 °C. Removal of deposited carbon takes place around 600 °C.

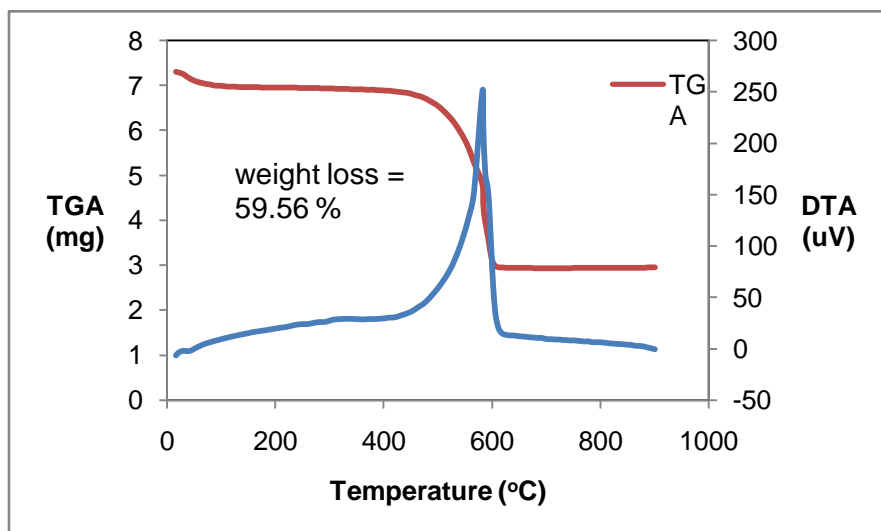


Figure 9.1,74. TGA profile of B1

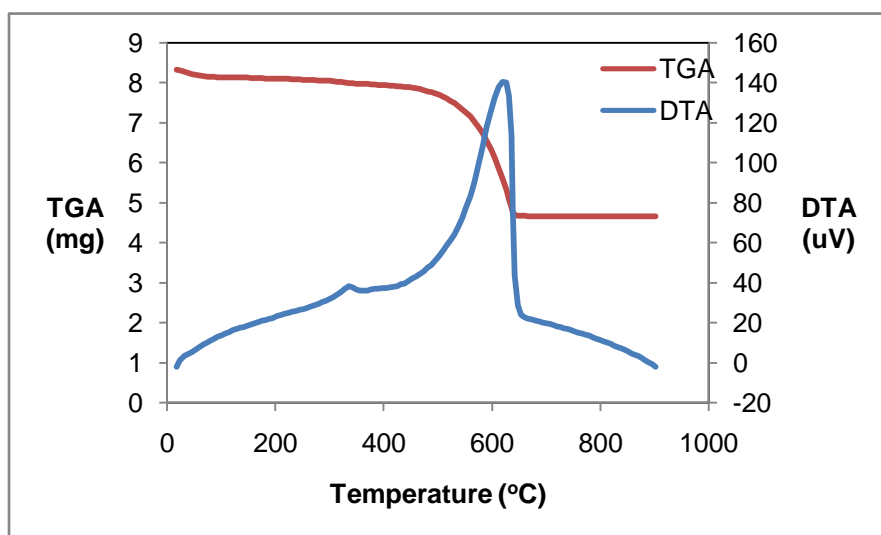


Figure 9.1.75. TGA profile of B2

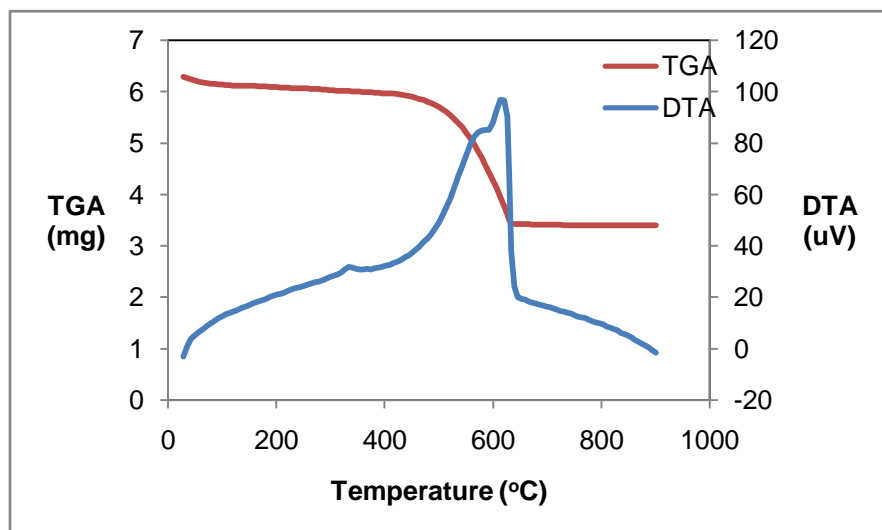


Figure 9.1.76. TGA profile of B3

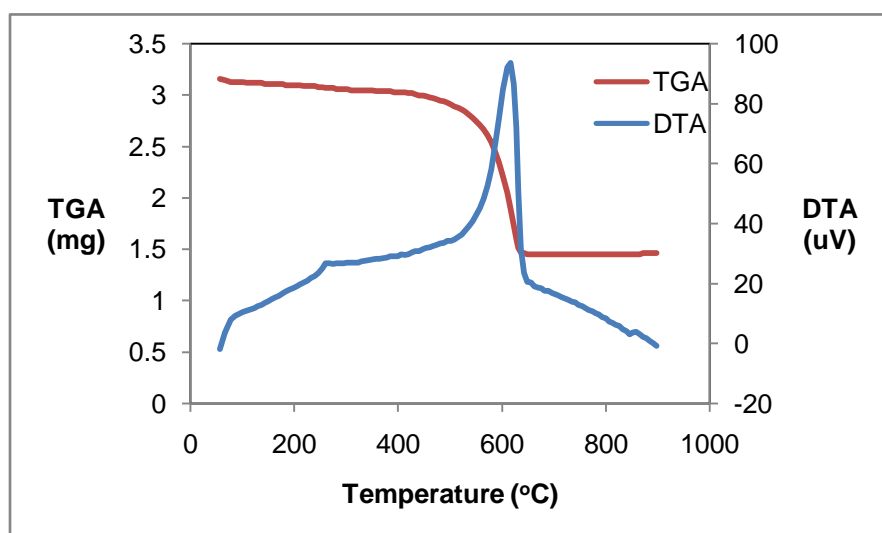


Figure 9.1.77. TGA profile of B4

Table 9.1.12. Weight loss of used catalysts

Sample	Weight Loss (%)
B1	59.56
B2	44.07
B3	45.83
B4	53.62

9.2. Ni, NiCe and PdNiCe IMPREGNATED SBA-15 CATALYSTS

In Section 9.1, it was observed that, Ni@MCM-41 is a quite active catalyst for steam reforming of ethanol reaction. However, MCM-41 is known to quite unstable in the presence of water at high temperatures. Also significant coke formation caused deformation in the catalyst structure. SBA-15 is also a mesoporous silica based support which has very similar structure to MCM-41, but having larger pores and pore walls with higher hydrothermal stability.

Cerium supports are also of great interest with their excellent oxygen buffering properties. However, thermal sintering occurs at high temperatures in the case of ceria support. Dispersing ceria on silica surface is an alternative which was tested for steam reforming of ethanol reaction. In this part of the study, SBA-15 was used as the support and it is enriched by ceria. Nickel was impregnated to SBA-15 and ceria enriched SBA-15.

9.2.1. CHARACTERIZATION RESULTS OF SBA-15 SUPPORTED CATALYSTS

In the preparation of SBA-15 supported catalysts, the support material SBA-15 was prepared by two different procedures. Removal of the surfactant was achieved by calcination and extraction procedures. The abbreviation SBA-15-C is used for the SBA-15 which is removed from surfactant by calcination and SBA-15-E is used for SBA-15 which is separated from surfactant by extraction.

Simultaneous and consecutive impregnation procedures were applied in order to prepare Ni, NiCe and PdNiCe incorporated SBA-15 catalysts. In the syntheses, Ce/Si ratio was adjusted to 0.10 and 0.50 in molar basis. When the Ce/Si ratio is 0.10, the catalyst can be considered as a dual catalyst with an equimolar amount of Ni. 0.10 for Ni/Si ratio is standard value and in the literature 20% is an ideal maximum for impregnation (Wiingaarden R.J. 1998)(Perego C. 1994). When the Ce/Si ratio is 0.50, it can be considered as SiO₂/CeO₂ composite. The effect of ceria loading is discussed in this part of the study. Effect of Pd impregnation is also discussed.

In the removal of surfactant from the silica structure, when extraction is applied, silanol groups remain on the surface of inner pores. In the calcination procedure, SiO₂ structure is formed. In order to examine the effect of surfactant removal procedure on the catalyst properties., Ni impregnation is applied on calcined and extracted SBA-15 samples. Prepared catalysts by using SBA-15 as support are summarized in Table 9.2.1.

Table 9.2.1. Prepared SBA-15 supported catalysts

Sample	Ni/Si	Ce/Si	% Pd	Impregnation
SBA-15-C	0	0	0	-
SBA-15-E				
Ni@SBA-15-C	0.10	0	0	standard
NiCe(0.5)@SBA-15-C	0.10	0.50	0	simultaneously
Pd@[NiCe(0.5)@SBA-15-C]	0.10	0.50	1	Ni and Ce simultaneously
NiCe(0.1)@SBA-15-E	0.10	0.10	0	simultaneously

9.2.1.1. Characterization of SBA-15

SBA-15 was synthesized as described in Section 8.1.2 and characterized by x-ray diffraction, scanning electron microscopy, energy dispersive spectroscopy and nitrogen physisorption techniques.

X-ray diffraction patterns of calcined and extracted SBA-15 samples are presented in Figure 9.2.1. As shown in this figure, well-ordered SBA-15 structure is successfully formed. Both calcined and the extracted samples give sharp peaks at a 2theta value of about 0.7° and two reflections in the x-ray diffraction pattern (Figure 9.2.1).

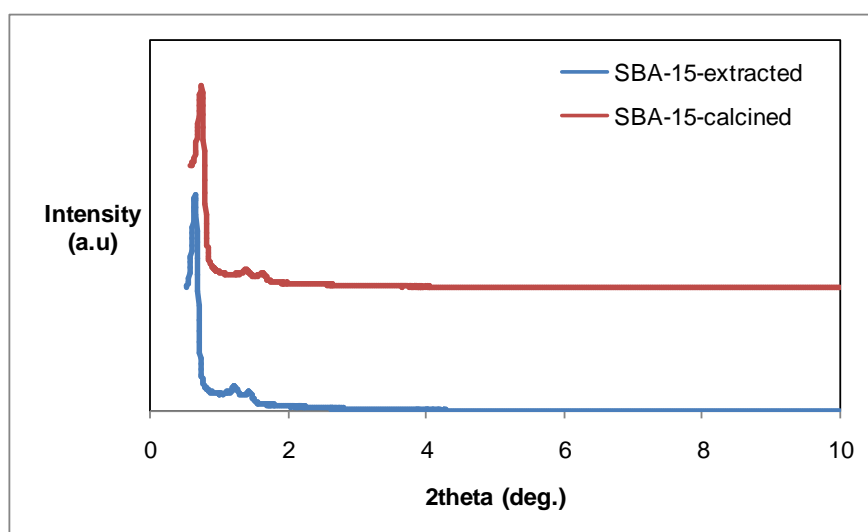


Figure 9.2.1. Typical XRD pattern of SBA-15 catalysts

Table 9.2.2. X-ray diffraction analysis of SBA-15 samples

Material	2theta (deg.)	2theta (deg.)	2theta (deg.)	$d_{p(100)}$ (Å)	Lattice Parameter
	1 st peak	2 nd peak	3 rd peak		
SBA-15-E	0.653	1.215	1.429	135.17	156.12
SBA-15-C	0.710	1.430	1.645	124.2	143.45

The calcined and extracted SBA-15 materials have almost the same structure. There is a very small shift in the peak locations (Table 9.2.3.). As expected, peak locations shift to the left by increasing pore diameter. Pore diameter, pore volume, surface area and pore wall thickness values for calcined and extracted SBA-15 are given in Table 9.2.3. Calcined sample has smaller surface area and smaller pore size than extracted sample.

Table 9.2.3. Nitrogen physisorption analysis of SBA-15 samples

SBA-15	BET Surface Area (m ² /g)	BJH Desorption Surface Area (m ² /g)	BJH Desorption Pore Volume (cc/g)	BJH Desorption Pore Diameter (Å)	Pore Wall Thickness (Å)
calcined	757.0	770.3	0.98	65.2	90.92
extracted	920.7	928.6	1.40	77.4	66.05

Scanning electron microscopy images of calcined SBA-15 are shown in Figure 9.2.4. Figure 9.2.4.a is an image with 500 000 times magnification. In his figure, the hexagonal structure of SBA-15 is clearly seen. Ordered channels are also observed. Pore diameter of the mesoporous silica structure can be estimated as around 6-7 nm, as obtained from nitrogen physisorption experiment. From the Figure 9.2.4.b, particle size of SBA-15 is estimated as 1.5 µm in height and 150 nm in radius. In Figure 9.2.4.c, hexagonal end of the particle is seen more clearly.

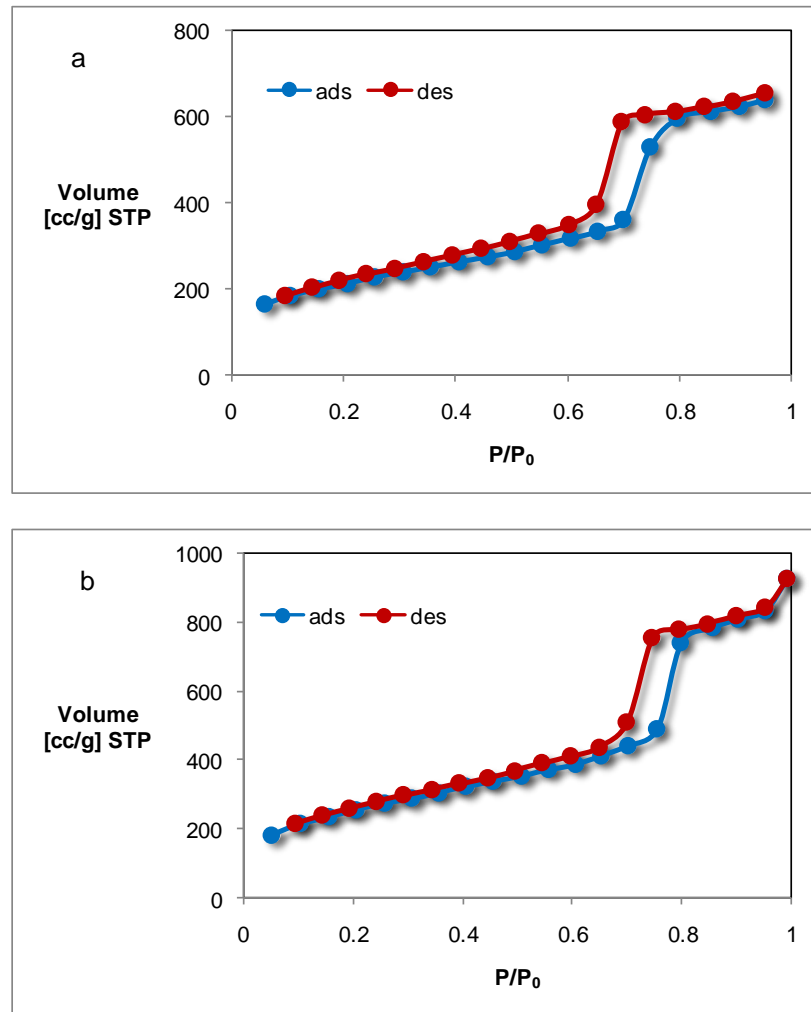


Figure 9.2.2. Nitrogen adsorption-desorption isotherm and pore size distribution curve of SBA-15 (a) calcine (b) extracted

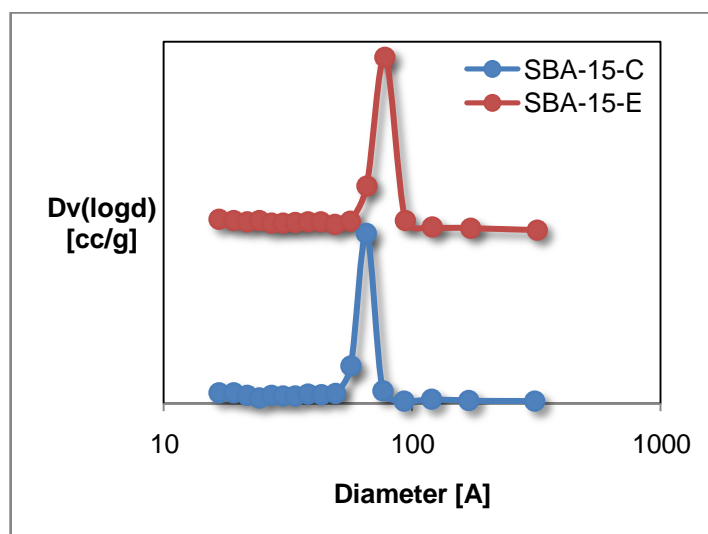


Figure 9.2.3. Pore size distribution of SBA-15

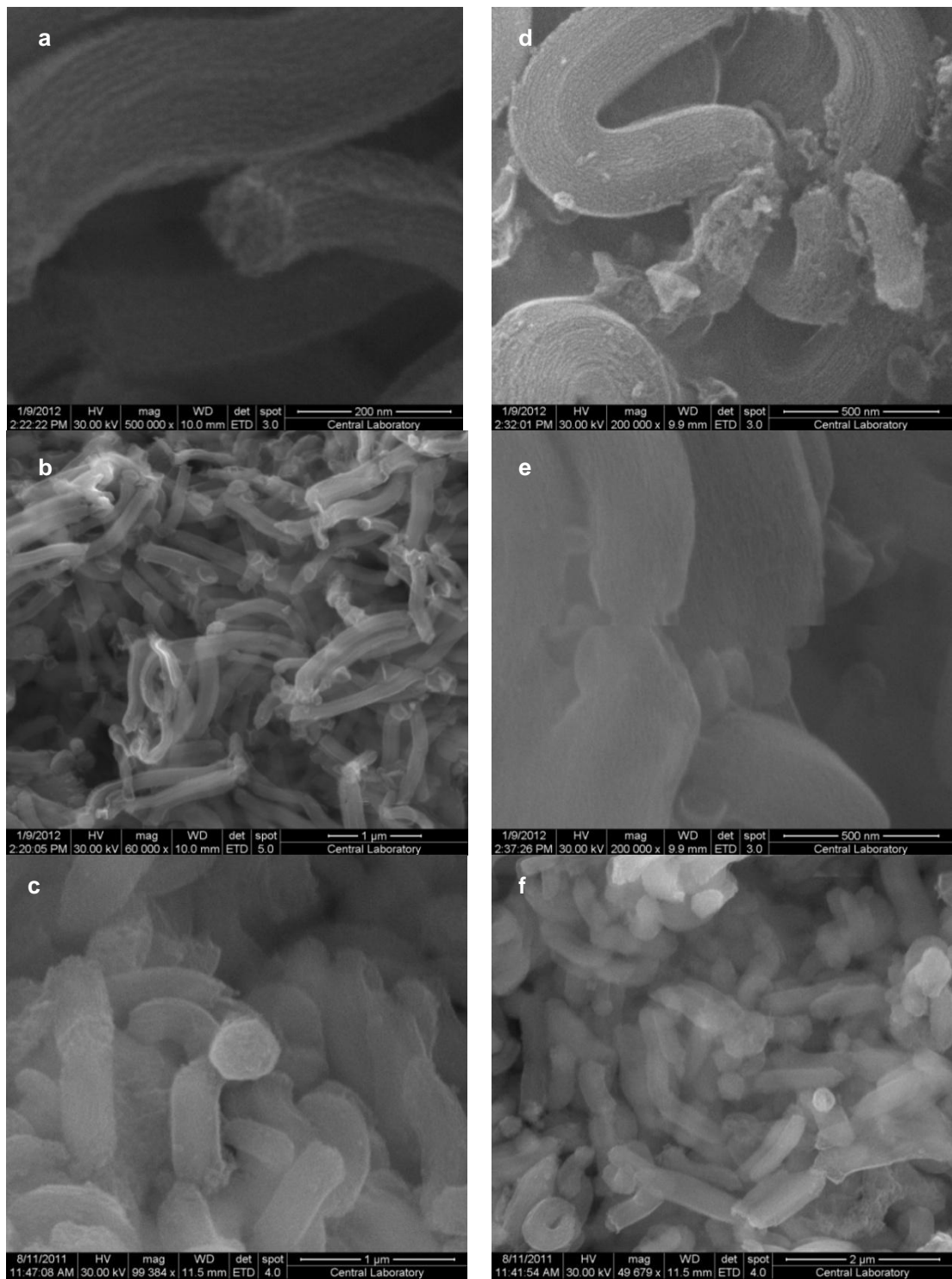


Figure 9.2.4. SEM images of SBA-15 with different magnifications

9.2.1.2. Characterization of SBA-15 Supported Catalysts

Synthesized SBA-15 type mesoporous silica was impregnated with nickel, ceria, nickel together with ceria and palladium and nickel with ceria according to the procedure described in Section 8. These catalysts were characterized by x-ray diffraction, nitrogen physisorption and scanning electron microscopy techniques. The changes in SBA-15 structure after impregnation is discussed and presented in this part.

Ni@SBA-15 is the catalyst prepared by impregnation of nickel to the calcined SBA-15 with the Ni/Si ratio of 0.10. X-ray diffraction pattern of Ni@SBA-15 is presented in Figure 9.2.5. Typical XRD pattern of SBA-15 is obtained after nickel impregnation with a small shift. After impregnation, a contraction in pore diameter is expected due to the incorporation of nickel oxide nanoparticles inside the pores. X-ray diffraction pattern indicates pore diameter contraction by this small shift in the location of peaks.

The major and reflection peaks are sharp with a high intensity in the first peak. Table 9.2.4 lists the peak locations and related characteristics of Ni@SBA-15 obtained from XRD analysis. From XRD analysis, it can be concluded that the structure of SBA-15 is preserved after impregnation. Wide angle x-ray diffraction pattern is also analyzed in order to have information about nickel incorporation and particle size. This analysis is presented in the next pages with nickel-ceria and palladium-nickel-ceria impregnated SBA-15 supported catalysts for comparison.

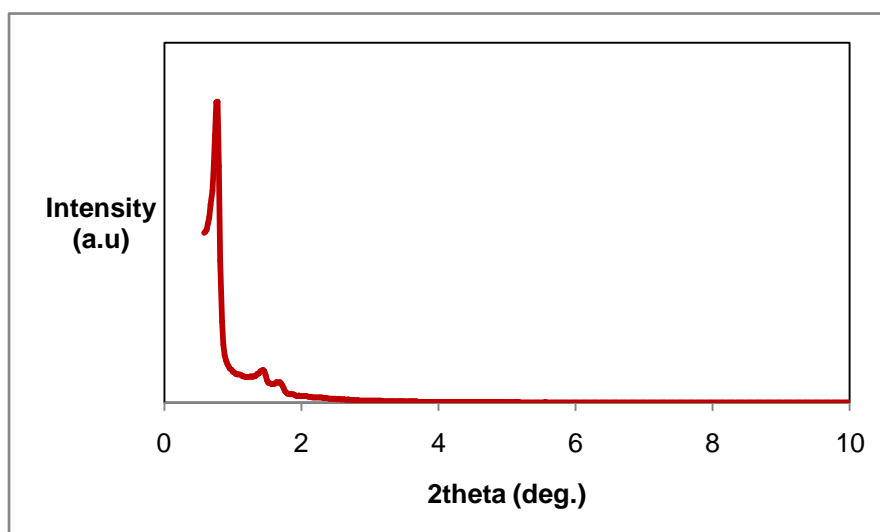


Figure 9.2.5. Low angle XRD pattern of Ni impregnated SBA-15 supported catalyst Ni@SBA-15

Table 9.2.4. X-ray diffraction analysis of Ni@SBA-15 sample

Material	2theta (deg.)	2theta (deg.)	2theta (deg.)	D(100) (Å)	Lattice Parameter
	1 st peak	2 nd peak	3 rd peak		
Ni@SBA-15	0.783	1.46	1.7	112.7	130.1

Nitrogen adsorption-desorption analysis indicates that after nickel impregnation the surface area of SBA-15 is decreased by around 40%. Surface area, pore volume and pore diameter values are given in Table 9.2.5. There is a slight decrease in pore diameter as a result of Ni impregnation as expected.

Nitrogen adsorption-desorption isotherm is presented in Figure 9.2.6. It is Type IV isotherm indicating mesoporous structure with hysteresis. Pore size distribution plot of Ni@SBA-15 is shown in Figure 9.2.7. Ni@SBA-15 has a narrow pore size distribution with a maximum at 6.49 nm.

Table 9.2.5. Nitrogen physisorption analysis of Ni@SBA-15 sample

Sample	BET Surface Area (m ² /g)	BJH Desorption Surface Area (m ² /g)	BJH Desorption Pore Volume (cc/g)	BJH Desorption Pore Diameter (nm)	Pore Wall Thickness (nm)
Ni@SBA-15	435.7	505.6	1.01	6.49	6.52

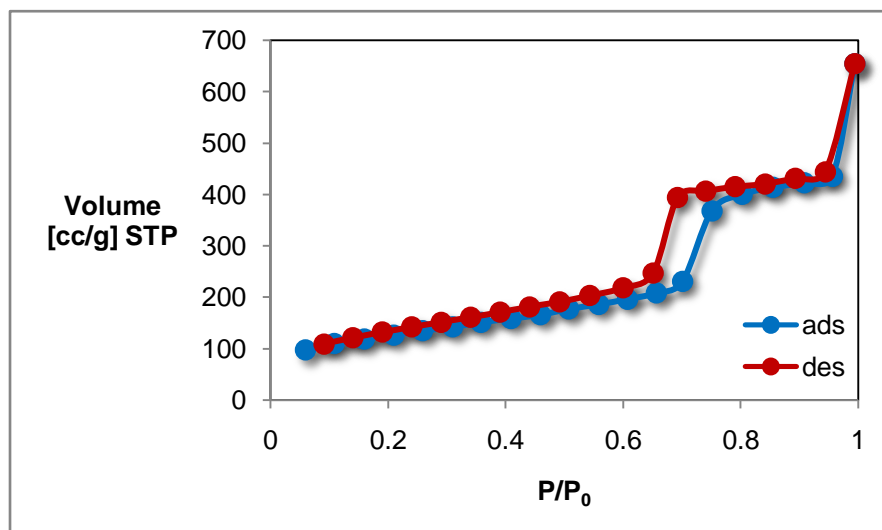


Figure 9.2.6. Nitrogen adsorption-desorption isotherm of Ni impregnated SBA-15 catalyst Ni@SBA-15

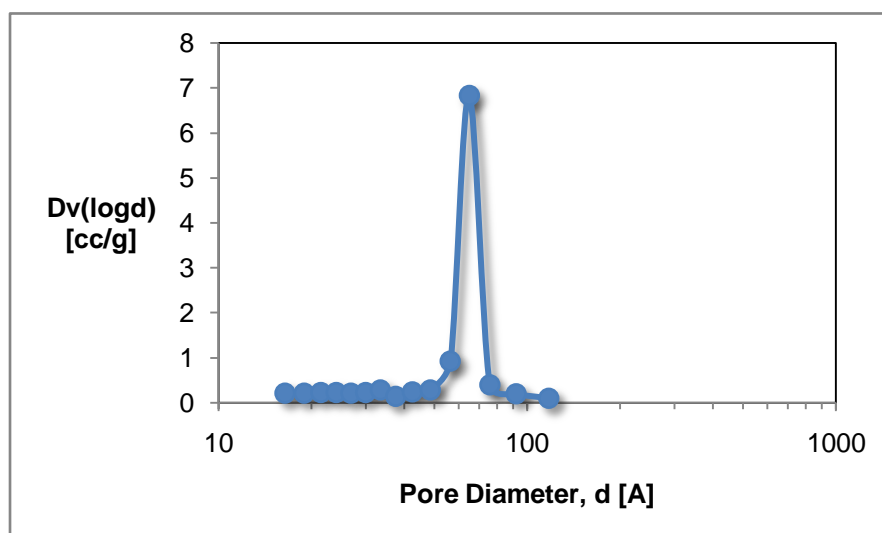


Figure 9.2.7 . Pore size distribution curve of Ni impregnated SBA-15 catalyst Ni@SBA-15

Surface morphology of Ni@SBA-15 is observed by scanning electron microscopy images and the images are presented in Figure 9.2.8. In the figure a, b and d is the SEM image of as-synthesized Ni@SBA-15, i.e. the material after impregnation and before final calcination. The images e, f and g belong to reduced Ni@SBA-15. There is not a significant difference in the morphology of Ni@SBA-15 before and after calcination. The structure is very similar to pure SBA-15.

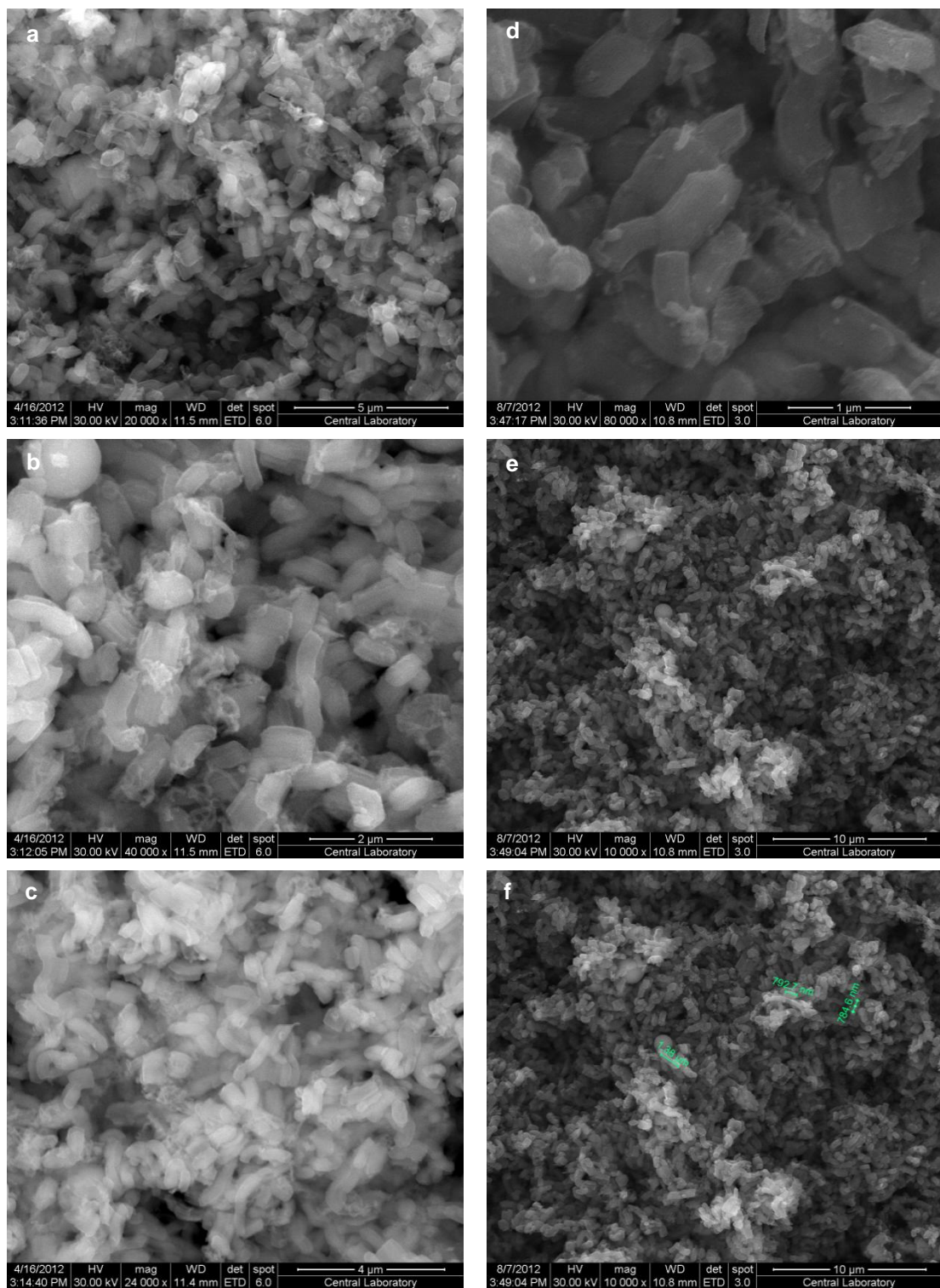


Figure 9.2.8. SEM images of Ni@SBA-15 (a) before calcination with 20 000 times magnification, (b) before calcination with 40 000 magnification, (c) before calcination with 24 000 magnification, (d) after calcination&reduction with 80 000 magnification, (e) after calcination&reduction with a magnification of 10 000, (f) after calcination&reduction with 10 000 magnification.

Nickel, ceria and palladium impregnated SBA-15 samples were summarized in Table 9.2.1 by means of preparation method and metal loading.

XRD pattern of NiCe(0.50)@SBA-15 catalyst is shown in Figure 9.2.9. Since the amount of impregnated ceria is high, mesoporous structure is deformed. In the x-ray diffraction pattern, a weak signal at 2theta of 0.78 is observed. This weak peak is an indication of preservation of the mesoporous structure, but the pores are blocked with metal nanoparticles. Second and third reflection peaks disappeared after ceria impregnation.

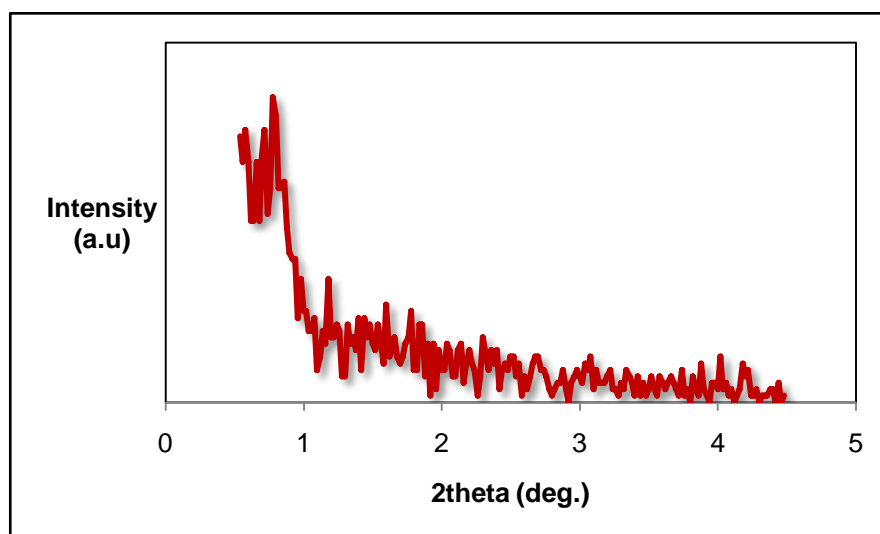


Figure 9.2.9. XRD pattern of Ni and Ce impregnated SBA-15 catalyst

Palladium impregnation was applied to the nickel and impregnated and reduced catalyst. Palladium loading was 1% on a weight basis. After a second calcination step and reduction procedure, the ordered mesoporous structure was significantly destroyed (Figure 9.2.10),

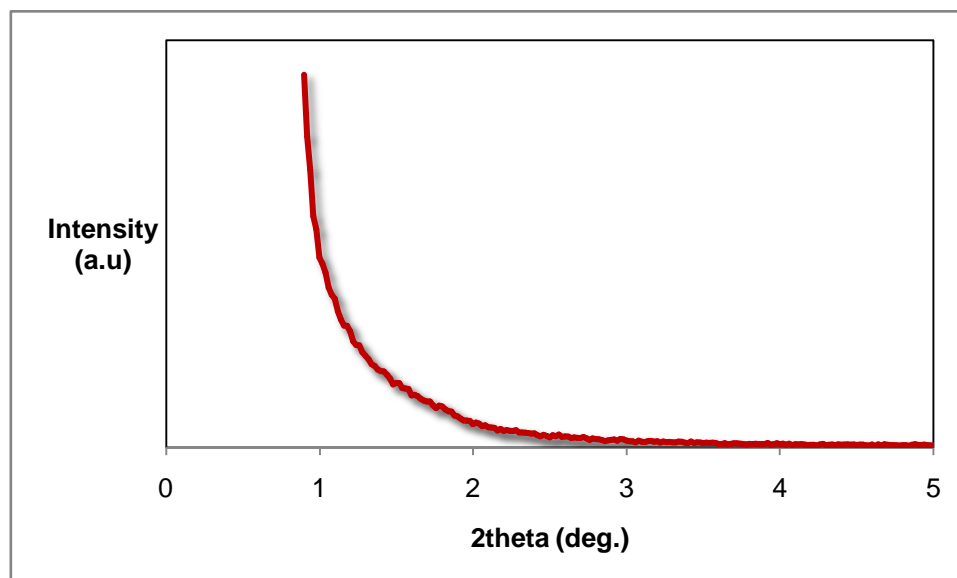


Figure 9.2.10. XRD pattern of Pd, Ni and Ce impregnated SBA-15 catalyst.
PdNiCe(0.5)@SBA-15 (R)

Wide angle x-ray diffraction patterns of Ni@SBA-15, NiCe(0.50)@SBA-15 and PdNiCe(0.50)@SBA-15 are shown in Figure 9.2.11. Peaks for crystalline NiO, CeO₂ and PdO are seen in this figure and they were indicated by triangle, circle and square, respectively. Crystalline sizes of the metals were calculated by Scherrer equation and listed in Table 9.2.6.

Table 9.2.6. Metal particle sizes of Ni, NiCe and PdNiCe impregnated SBA-15 catalysts

Catalyst	NiO Particle Size (nm)	CeO ₂ Particle Size (nm)	PdO Particle Size (nm)
Ni@SBA-15	16.1	-	-
NiCe(0.50)@SBA-15	6.28	7.58	-
PdNiCe(0.50)@SBA-15	6.39	7.59	36.4

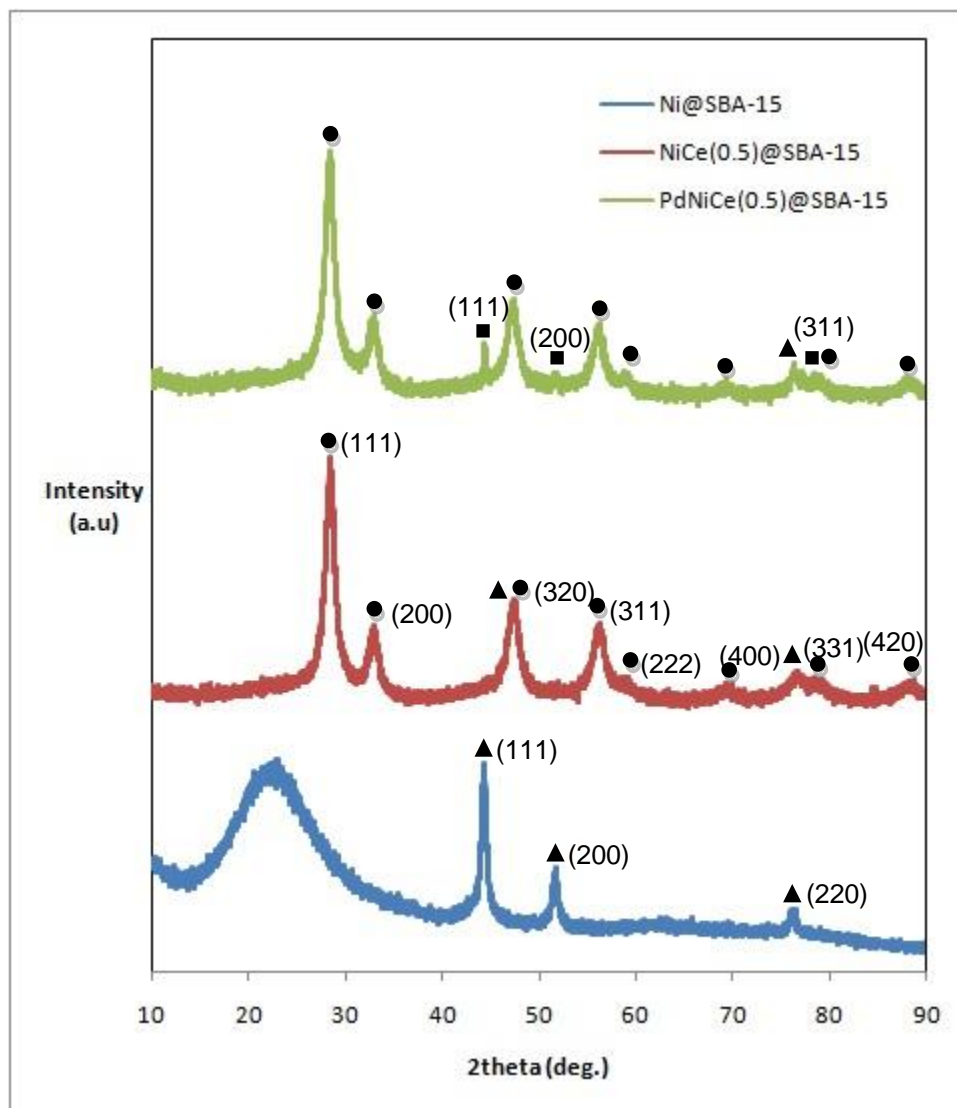


Figure 9.2.11. Wide angle x-ray diffraction patterns of Ni and Ce impregnated SBA-15 catalysts (● CeO₂, ▲ NiO, ■ PdO)

Nitrogen physisorption analysis indicates that nickel and ceria impregnated SBA-15 with high ceria loading has a lower surface area as expected. Impregnation of palladium to NiCe(0.5)@SBA-15 also decreased the surface area slightly. Due to the pore blocking of impregnated metals, NiCe(0.5)@SBA-15 and PdNiCe(0.5)@SBA-15 have smaller pore diameters and SBA-15 itself and nickel impregnated SBA-15 (Table 9.2.7). Figure 9.2.11 presents the nitrogen adsorption-desorption isotherms of NiCe(0.5)@SBA-15 and PdNiCe(0.5)@SBA-15. From the nitrogen adsorption-desorption isotherms, a H₂ type hysteresis loop associated with ill-defined pores measured for both catalysts. For SBA-15 and Ni@SBA-15 materials, nitrogen adsorption-desorption isotherm was Type IV, but for NiCe(0.5)@SBA-15 and PdNiCe(0.5)@SBA-15, it is not true to assume the isotherm as Type VI.

Table 9.2.7. Nitrogen physisorption analysis of NiCe and PdNiCe impregnated SBA-15 catalysts

Sample	BET	BJH	BJH	BJH
	Surface Area (m ² /g)	Desorption Surface Area (m ² /g)	Desorption Pore volume (cc/g)	Desorption Pore Diameter (nm)
NiCe(0.50)@SBA-15 (R)	199.8	234.7	0.38	3.77
PdNiCe(0.50)@SBA-15 (R)	128.5	162.4	0.31	3.81

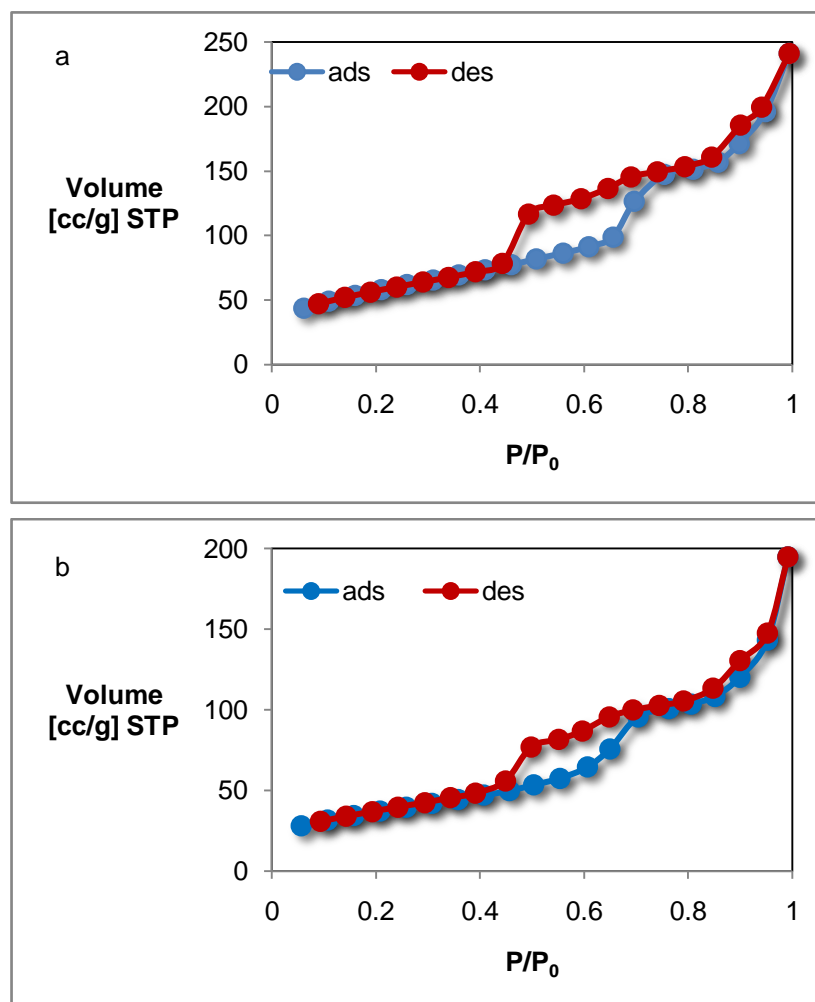


Figure 9.2.11. N₂ adsorption desorption isotherm of Ni and Ce impregnated SBA-15 catalyst (a) NiCe(0.50)@SBA-15 (b) PdNiCe(0.50)@SBA-15

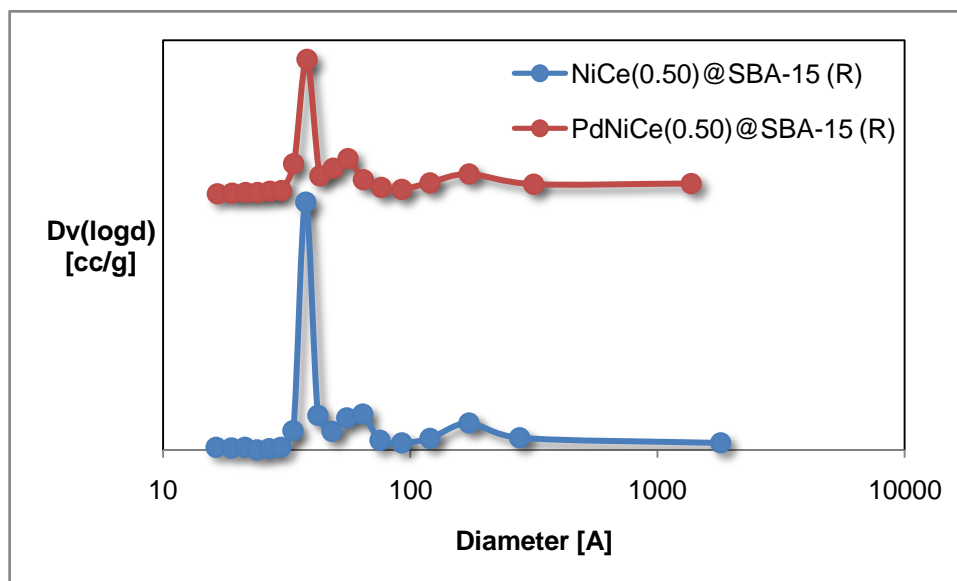


Figure 9.2.12. Pore size distribution of Ni and Ce impregnated SBA-15 catalyst

Pore size distribution curves of NiCe(0.50)@SBA-15 and PdNiCe(0.50)@SBA-15 are shown in Figure 9.2.8. For both catalysts, three different pore sizes were obtained from the pore size distribution curves giving maximums at 3.8, 5.6 and 17.2 nm for NiCe(0.50)@SBA-15 and 3.8, 6.4 and 17.3 for PdNiCe(0.50)@SBA-15

Scanning electron micrographs of NiCe(0.50)@SBA-15 and PdNiCe(0.50)@SBA-15 are shown in Figures 9.2.13 and 9.2.14, respectively. surface morphology of the catalysts are very similar to pure SBA-15. This can be assumed as an indication of the metals are locating inside pores with a high distribution and small particle sizes, not in the lattice as large particles.

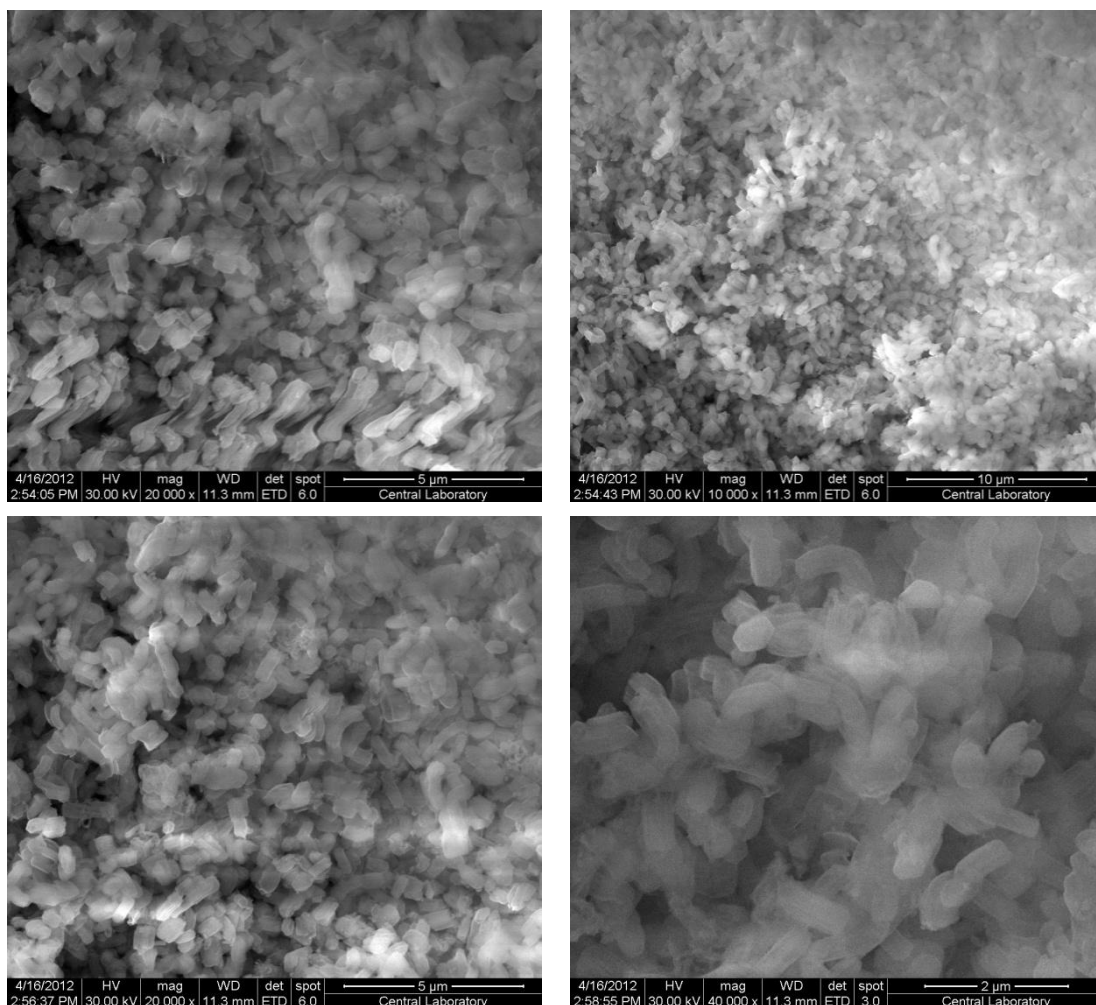


Figure 9.2.13. SEM images of nickel and ceria impregnated SBA-15 supported catalyst, NiCe(0.50)@SBA-15

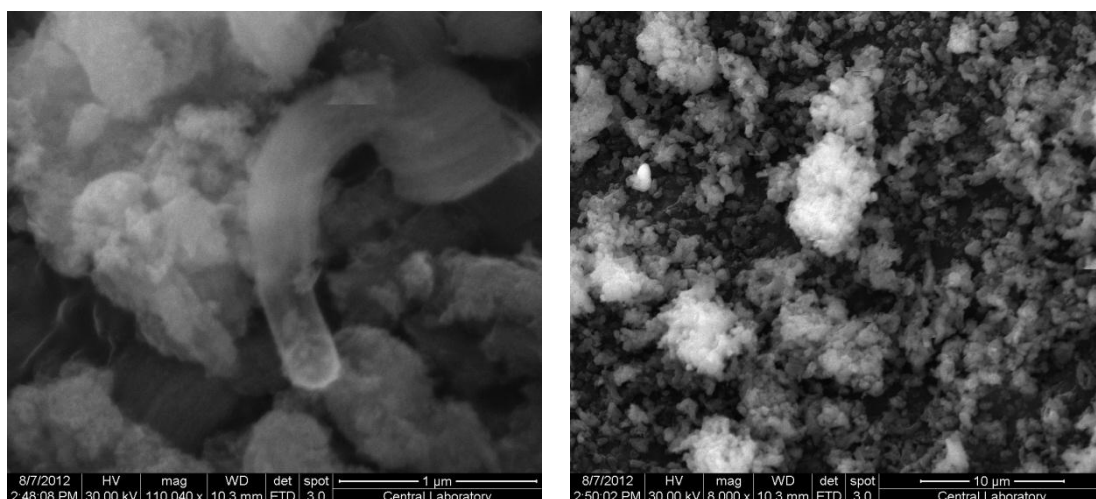


Figure 9.2.14. SEM images of nickel, ceria and palladium impregnated SBA-15 supported catalyst, NiCe(0.50)@SBA-15

9.2.2. ACTIVITIES OF SBA-15 SUPPORTED CATALYST IN ETHANOL STEAM REFORMING REACTION

Activities of SBA-15 supported catalysts were tested in steam reforming of ethanol reaction system. Unlike in the previous section, 0.15 g catalyst was used in the experiments and the system was modified with a condenser as explained in Section 8. The results are presented by means of ethanol conversion, hydrogen yield, composition of gas product stream and selectivity of each product. The activities SBA-15 supported catalysts in steam reforming of ethanol reaction are discussed in this section.

Ethanol conversion and hydrogen yield of Ni@SBA-15 is plotted against time at 600 °C in Figure 9.2.15. Ethanol conversion and hydrogen yield remained constant during 3 hours of reaction. Hydrogen yield is around 4 and it is quite a high value for ethanol steam reforming reaction. This corresponds to 75% Hydrogen in gas product stream (Figure 9.2.18). CO and CH₄ are produced as side products which reduce the hydrogen yield. In Figure 9.2.23, selectivities of CO₂, CO and CH₄ are shown. The product distribution also remains almost constant during the reaction period of 3 hours. These results indicated that SBA-15 incorporated catalysts were quite stable.

According to the activity studies, SBA-15 seems to have similar support properties with MCM-41. Characterization after reaction studies will be given in the next parts.

Nickel and ceria impregnated SBA-15 supported catalyst with a Ce/Si ratio of 0.10 (NiCe(0.10)@SBA-15) was tested for 5 hours in ethanol steam reforming reaction. Ethanol conversion and hydrogen yield changing with time at 600 °C are shown in Figures 9.3.16 and Figure 9.3.17 for NiCe(0.10)@SBA-15 and NiCe(0.50)@SBA-15, respectively. NiCe(0.10)@SBA-15 is found to be less active and stable than Ni@SBA-15. At 600 °C, thermal sintering occurs in ceria particles. Sintering may plug the active sites of the catalyst.

In the gas product stream, hydrogen percentage is 60% for NiCe and PdNiCe impregnated catalysts which is lower than that of Ni@SBA-15 (Figures 9.3.20, 9.3.21 and 9.3.22).

Addition of palladium prevents the formation C₂H₄ in the product stream which was produced in the case of NiCe impregnated catalyst with Ce/Si=0.50 (Figures 9.3.21 and 9.3.2).

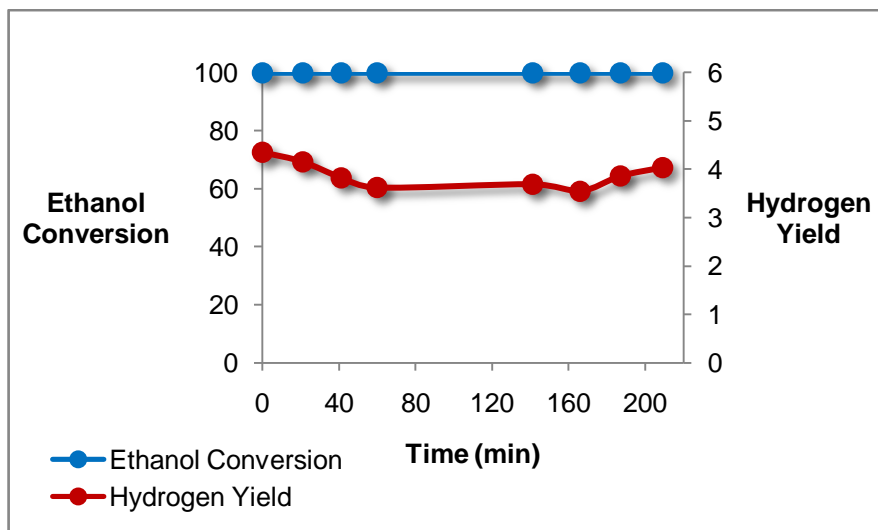


Figure 9.2.15 . Ethanol conversion and hydrogen yield of Ni impregnated SBA-15 catalyst, Ni @ SBA-15 at 600 °C

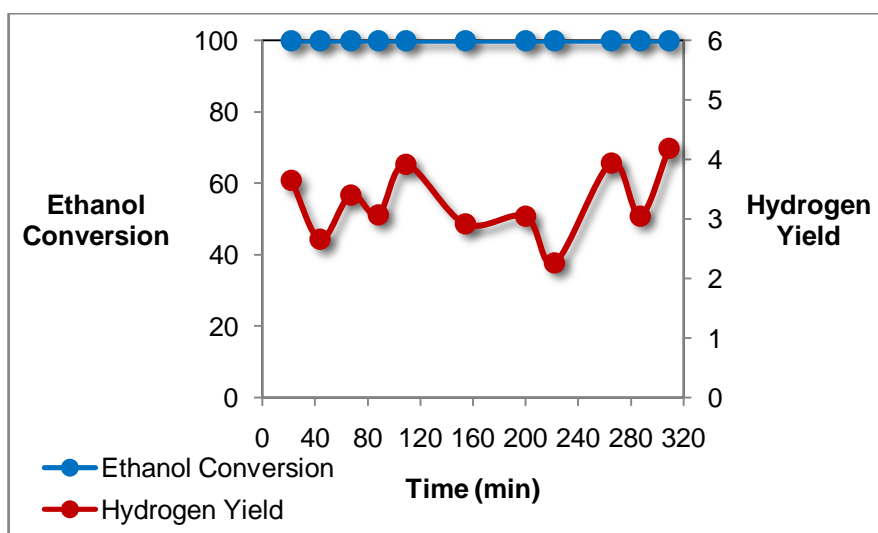


Figure 9.2.16. Ethanol conversion and hydrogen yield of Ni and Ce impregnated SBA-15 catalyst with Ce/Si=0.10, NiCe(0.10)@SBA-15 at 600 °C

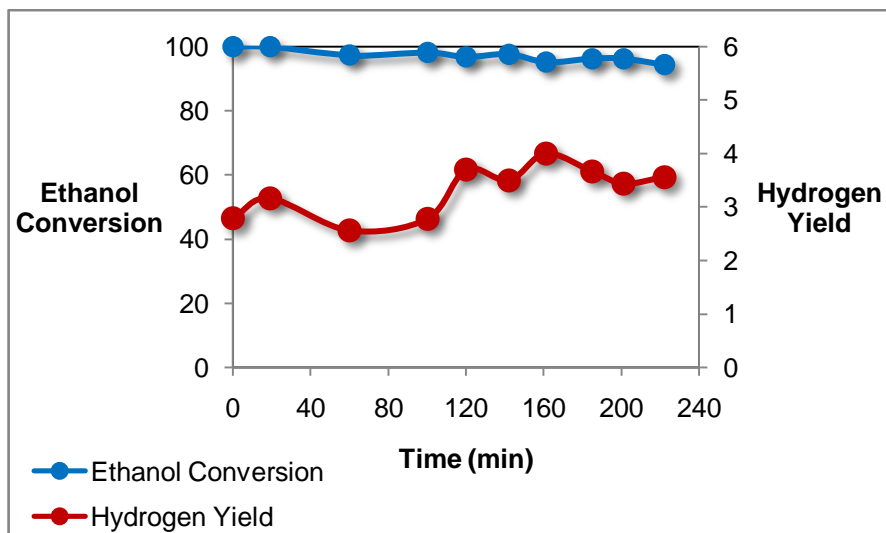


Figure 9.2.17. Ethanol conversion and hydrogen yield of Ni and Ce impregnated SBA-15 catalyst with Ce/Si=0.50, NiCe(0.50)@SBA-15 at 600 °C

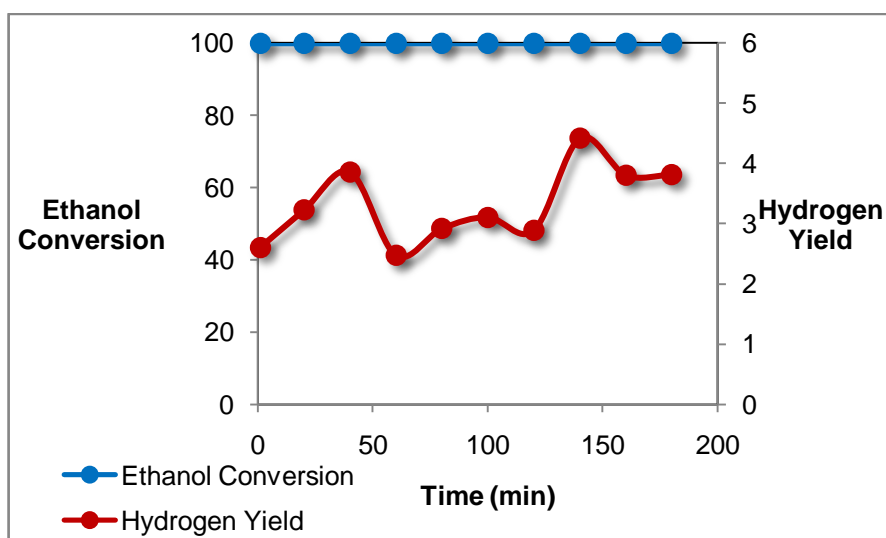


Figure 9.2.18. Ethanol conversion and hydrogen yield for Pd, Ni and Ce impregnated SBA-15 catalyst, PdNiCe(0.5)@SBA-15 at 600 °C

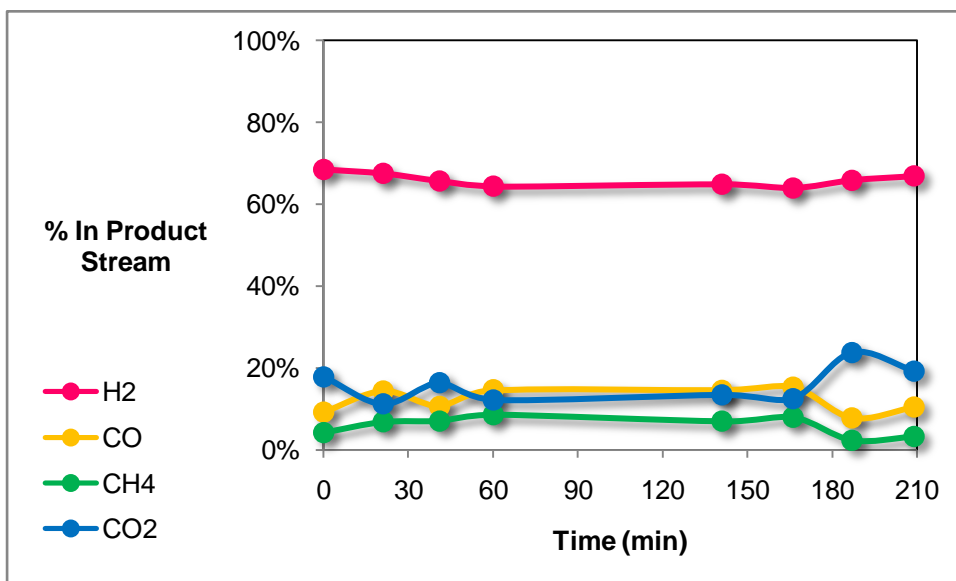


Figure 9.2.19. Composition of gas product stream for Ni impregnated SBA-15 catalyst, Ni@SBA-15

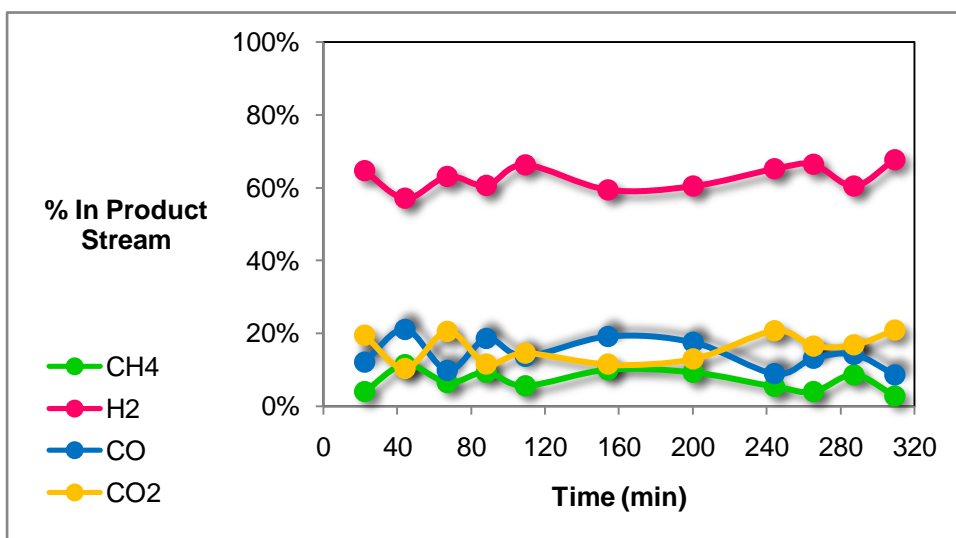


Figure 9.2.20. Composition of gas product stream of Ni and Ce impregnated SBA-15 catalyst with Ce/Si=0.10, NiCe(0.10)@SBA-15

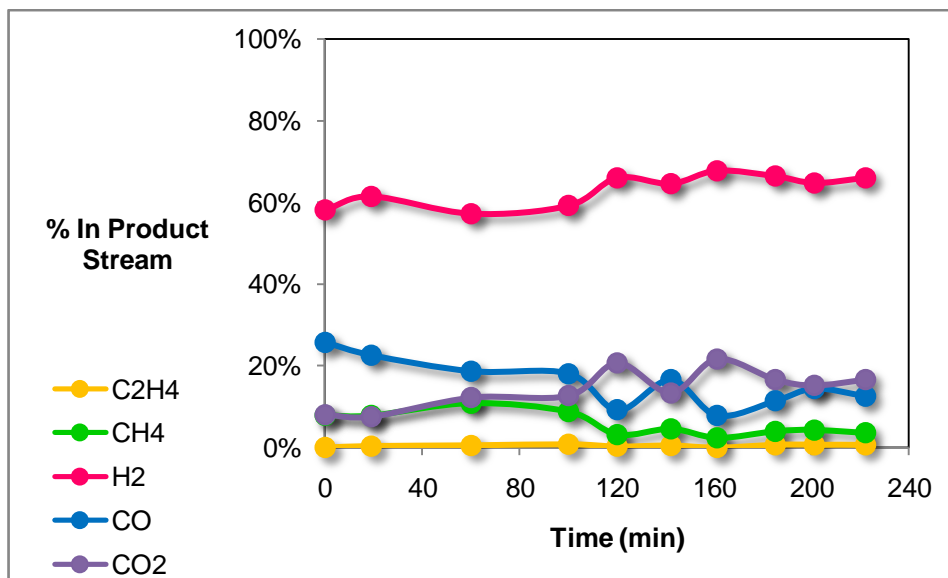


Figure 9.2.21. Composition of gas product stream for Ni and Ce impregnated SBA-15 catalyst, NiCe(0.5)@SBA-15.

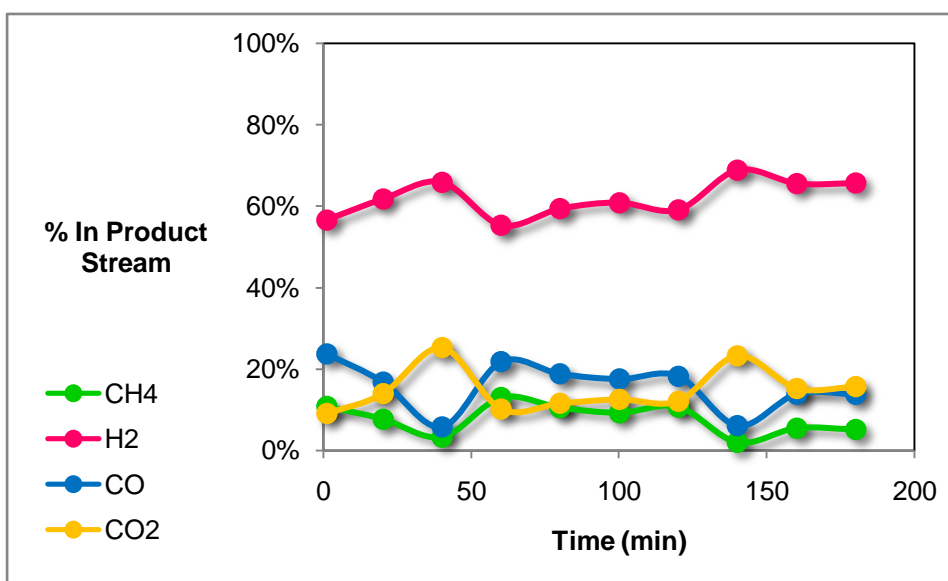


Figure 9.2.22. Composition of gas product stream for Pd, Ni and Ce impregnated SBA-15 catalyst, PdNiCe(0.5)@SBA-15.

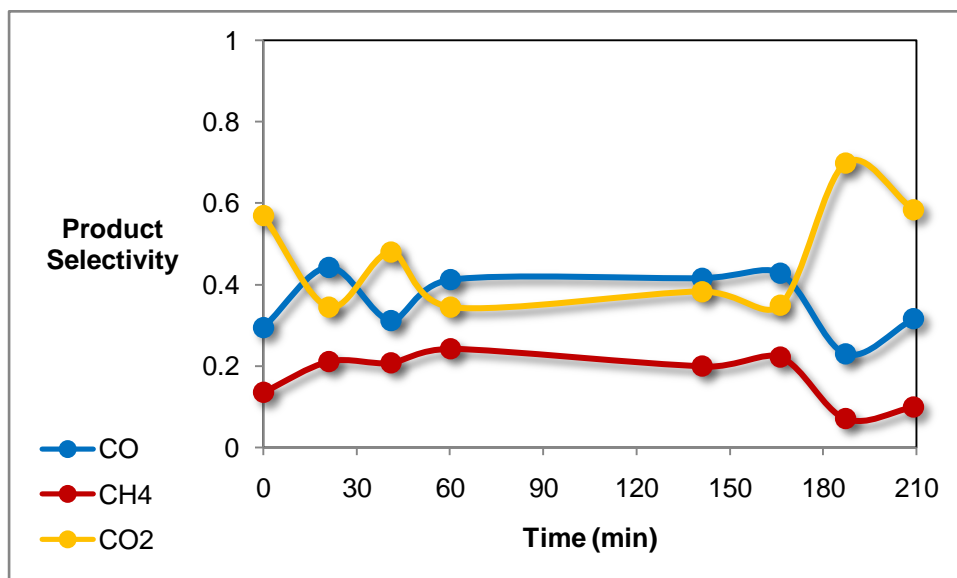


Figure 9.2.23. Selectivities of products for Ni impregnated SBA-15 catalyst, Ni@SBA-15 at 600 °C

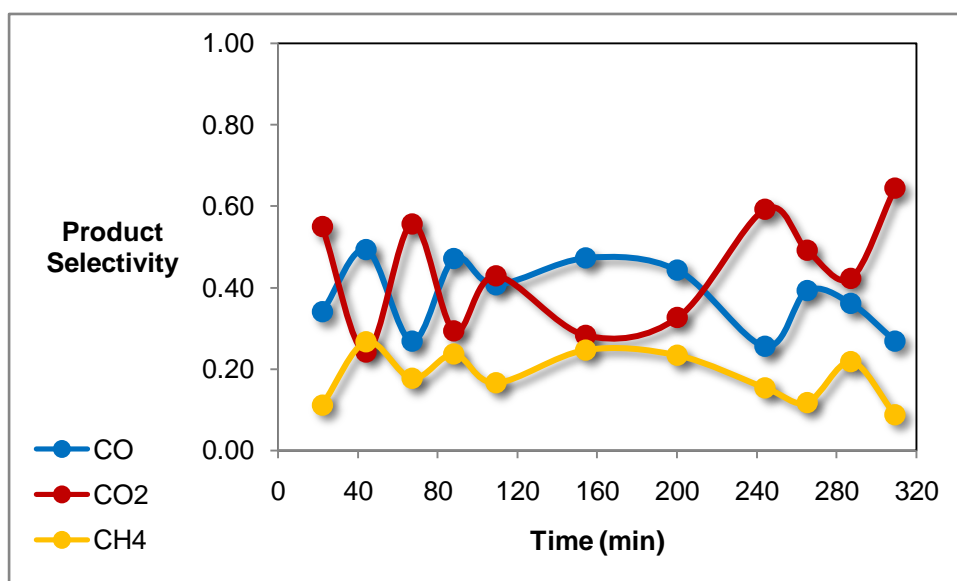


Figure 9.2.24. Product selectivities of Ni and Ce impregnated SBA-15 catalyst with Ce/Si=0.10, NiCe(0.10)@SBA-15 at 600 °C

Ni, NiCe and PdNiCe impregnated SBA-15 catalysts are compared in Figures 9.3.35, 9.3.36, 9.3.37 and 9.3.38. According to the plots, most stable catalyst was Ni@SBA-15.

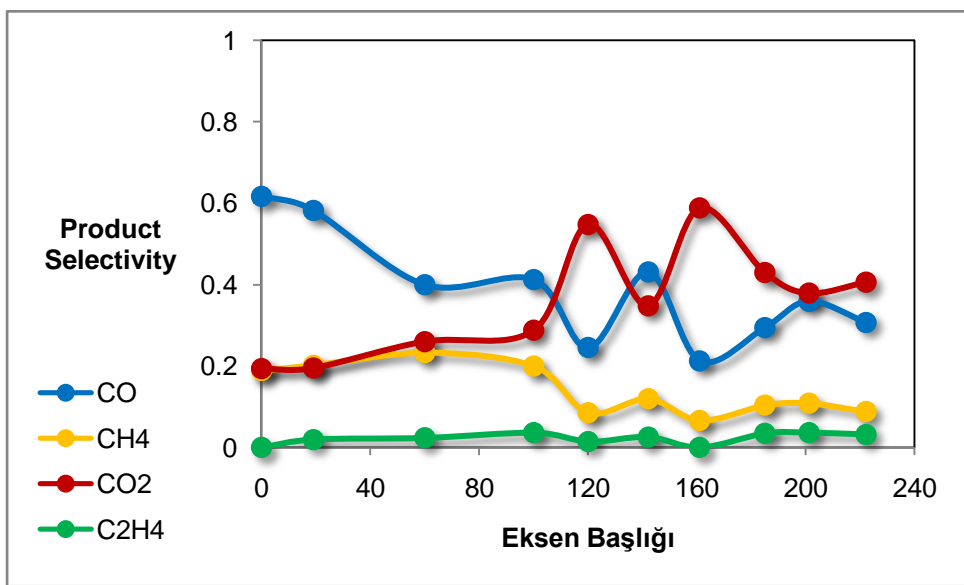


Figure 9.2.25. Product selectivities for Ni and Ce impregnated SBA-15 catalyst, NiCe(0.5)@SBA-15. At 600 °C

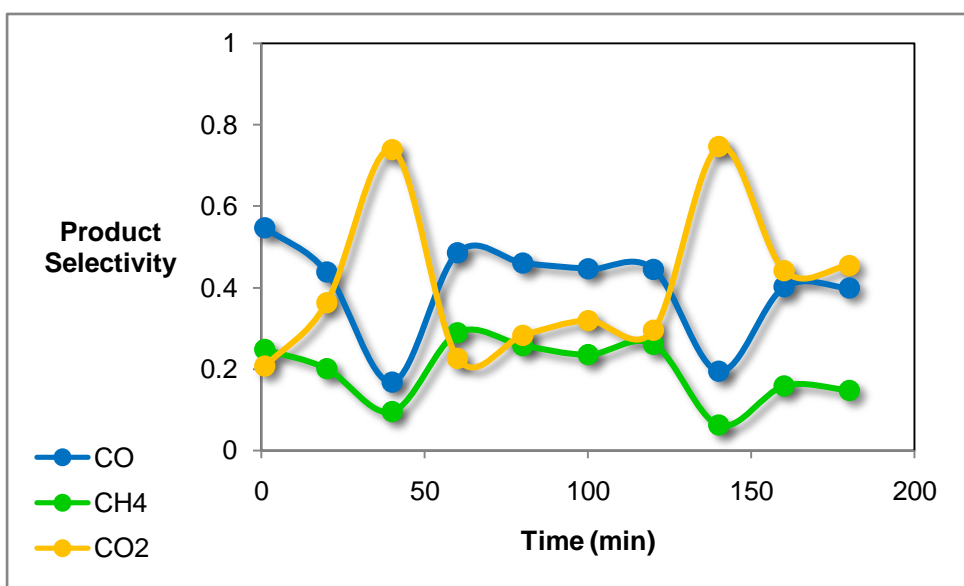


Figure 9.2.26. Product selectivities for Pd, Ni and Ce impregnated SBA-15 catalyst, PdNiCe(0.5)@SBA-15 at 600 °C

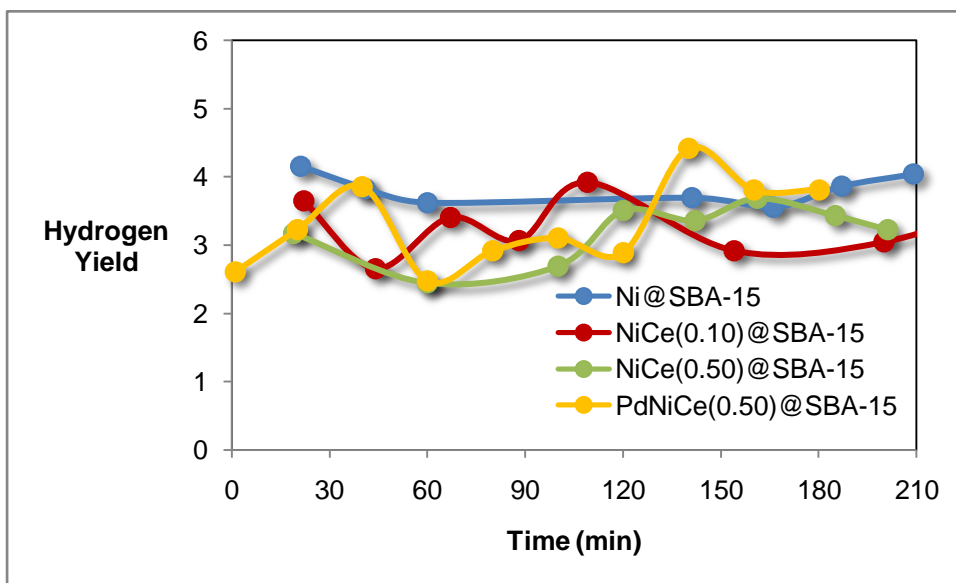


Figure 9.2.27. Comparison of hydrogen yield of SBA-15 supported catalysts at 600 °C

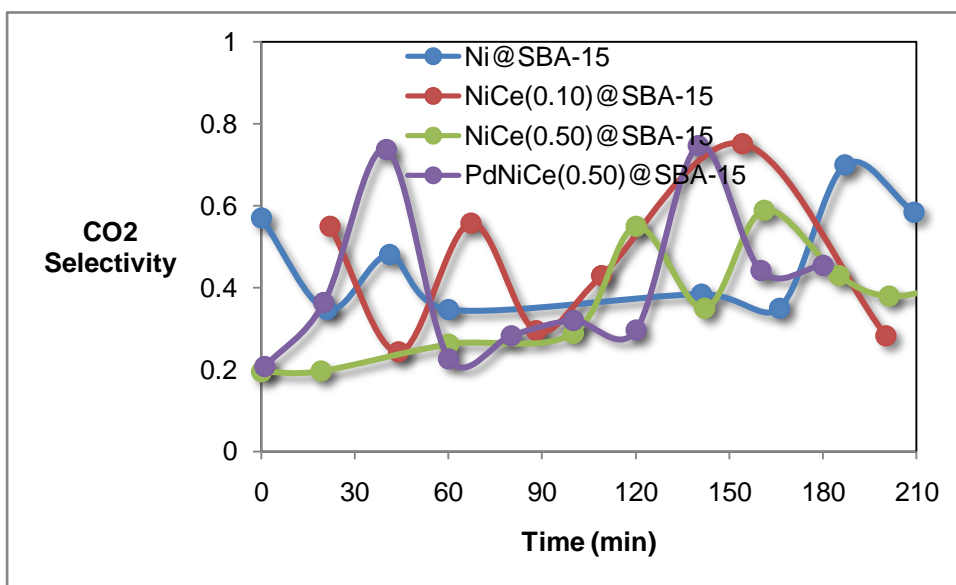


Figure 9.2.28. Comparison of carbon dioxide selectivity of SBA-15 supported catalysts at 600 °C

9.2.3. CHARACTERIZATION OF SBA-15 SUPPORTED CATALYSTS AFTER STEAM REFORMING OF ETHANOL REACTION

SBA-15 supported catalysts were characterized after activity tests in ethanol steam reforming reaction. X-ray diffraction analysis provides information about the deformation of the structure of the catalyst during reaction. In wide angle x-ray diffraction pattern, coke formation can be observed by carbon peaks. Change in surface area and pore diameter determines the catalyst stability. The most significant information about coke formation is obtained by thermal gravimetric analysis, i.e. amount of carbon deposited is estimated.

In Figure 9.2.29, x-ray diffraction patterns of reduced and used Ni@SBA-15 are shown. After ethanol steam reforming reaction at 600 °C, two dimensional hexagonal structure was preserved, slight decrease in intensity is observed. This result clearly showed that SBA-15 was a much more stable catalyst support than MCM-41.

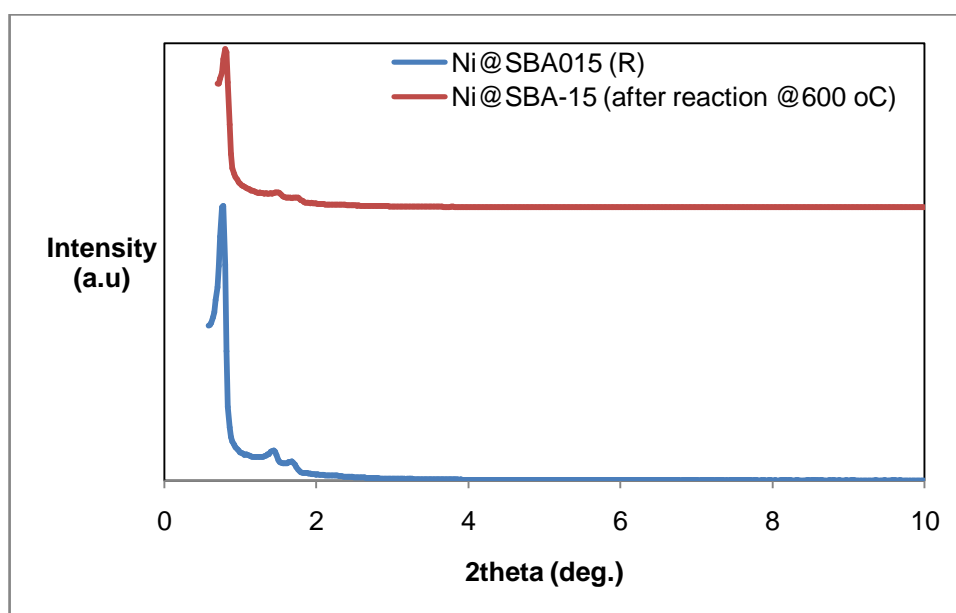


Figure 9.2.29. Low angle x-ray diffraction pattern of reduced Ni@SBA-15 and after reaction at 600 °C

Wide angle x-ray diffraction pattern of Ni@SBA-15 after reaction indicates coke formation on the surface of the catalyst with (002) and (101) peaks.

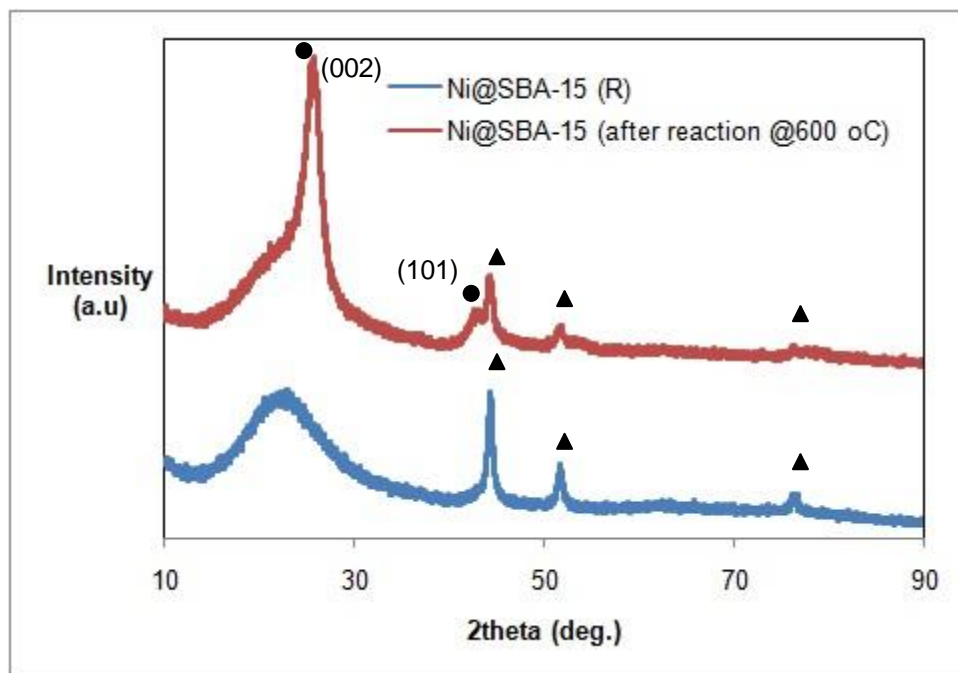


Figure 9.2.30. High angle x-ray diffraction pattern of Ni@SBA-15 before and after reaction at 600 °C (▲ NiO, ● C)

X-ray diffraction patterns of reduced and used NiCe(0.10)@SBA-15 is shown in Figure 9.2.31. In the case of ceria impregnation, peak of carbon (002) is not observed (Figure 9.2.32 and Figure 9.2.33). This is an important result, indicating that Ce incorporation caused significant reduction in coke formation, although it did not increase the activity of the catalyst in steam reforming of ethanol.

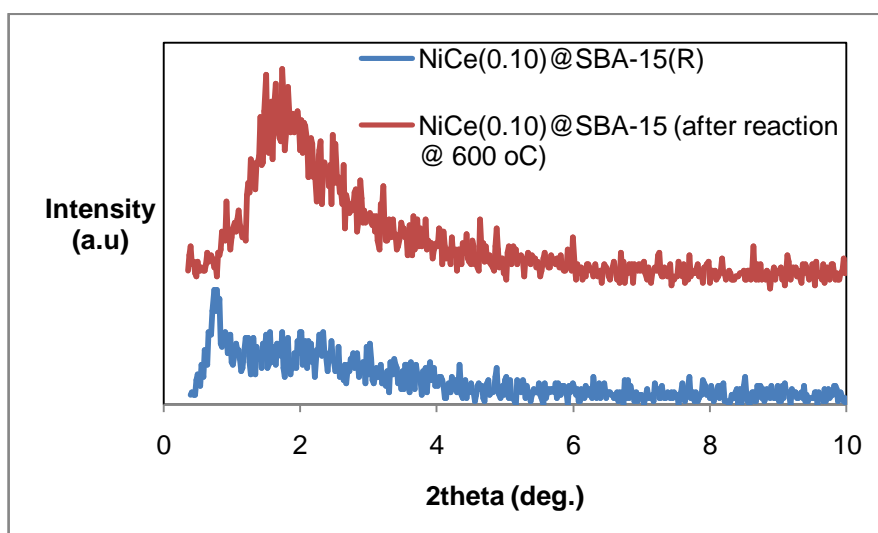


Figure 9.2.31. Low angle x-ray diffraction pattern of NiCe(0.10)@SBA-15 before and after reaction at 600 °C

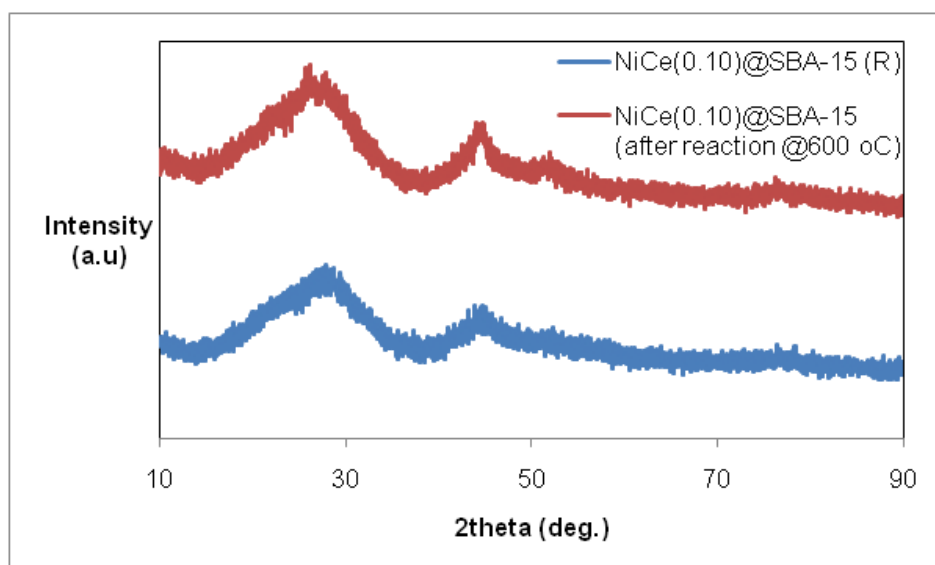


Figure 9.2.32. High angle x-ray diffraction pattern of NiCe(0.10)@SBA-15 before and after reaction at 600 °C

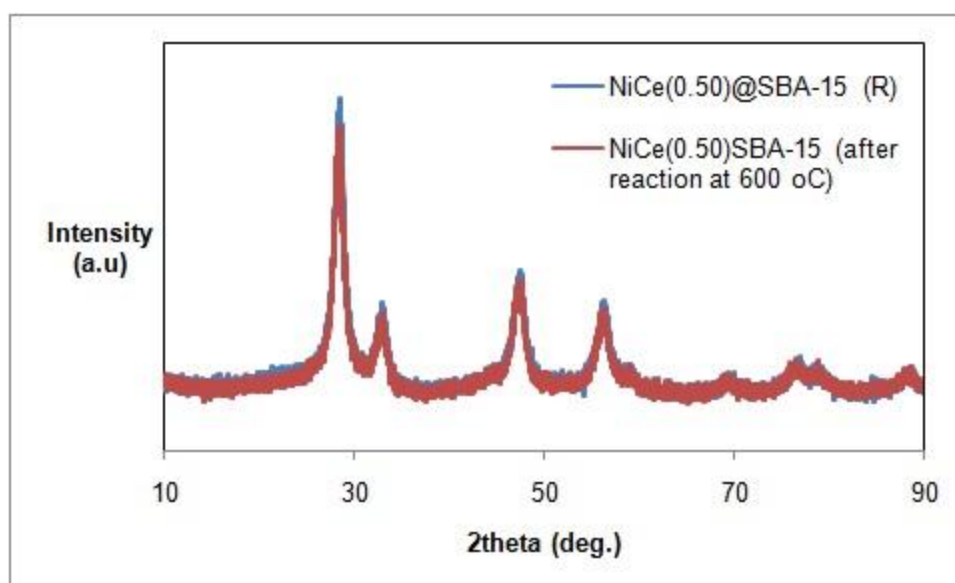


Figure 9.2.33. Wide angle x-ray diffraction pattern of NiCe(0.50)@SBA-15 before and after reaction at 600 °C

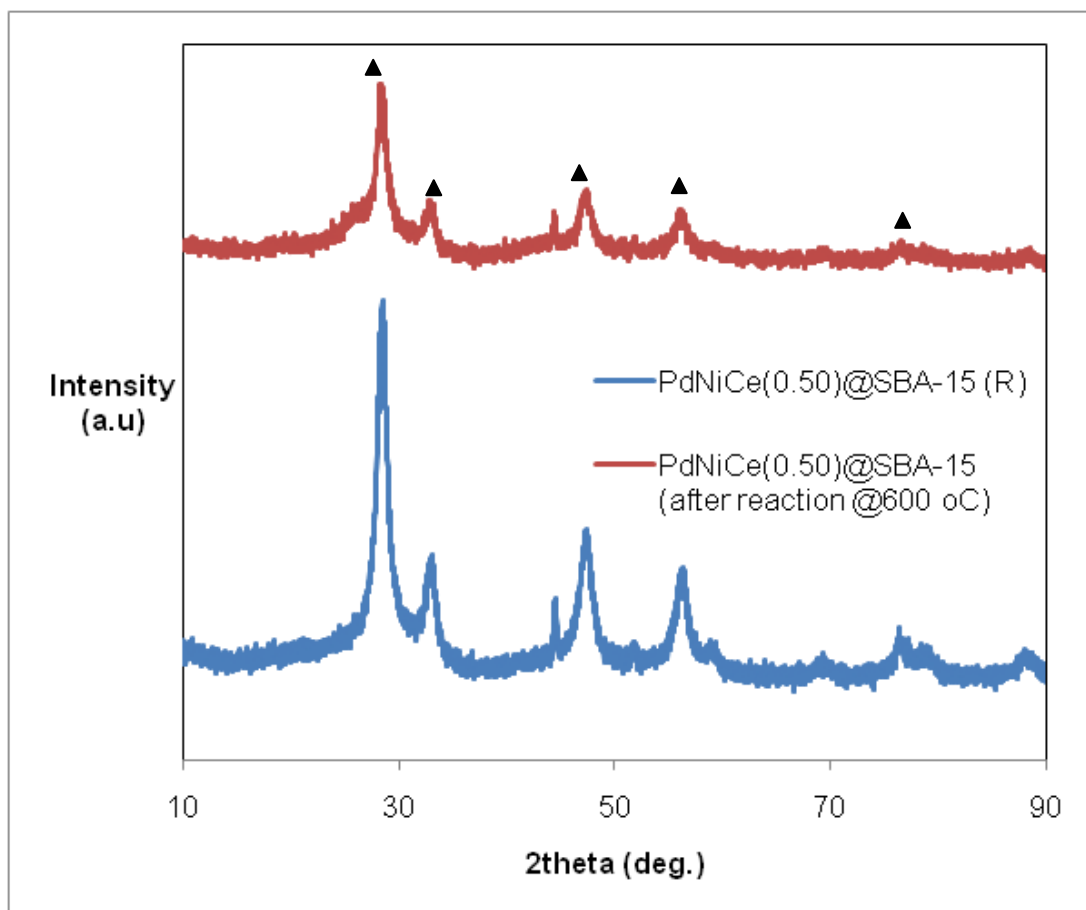


Figure 9.2.33. High angle x-ray diffraction pattern of PdNiCe(0.50)@SBA-15 before and after reaction at 600 °C.

SEM images of NiCe(0.50)@SBA-15 and PdNiCe(0.50)@SBA-15 are presented in Figures 9.2.34 and 9.2.25, respectively.

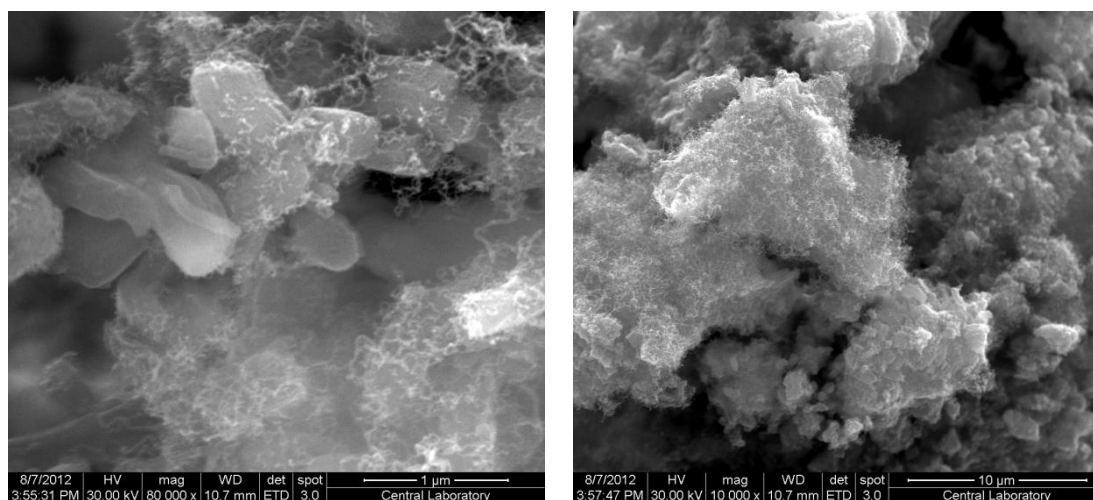


Figure 9.2.34. SEM images of NiCe(0.50)@SBA-15 after reaction at 600 °C

Filamentous carbon fibers (i.e. coke) are clearly seen in Figures 9.2.34 and 9.2.35.

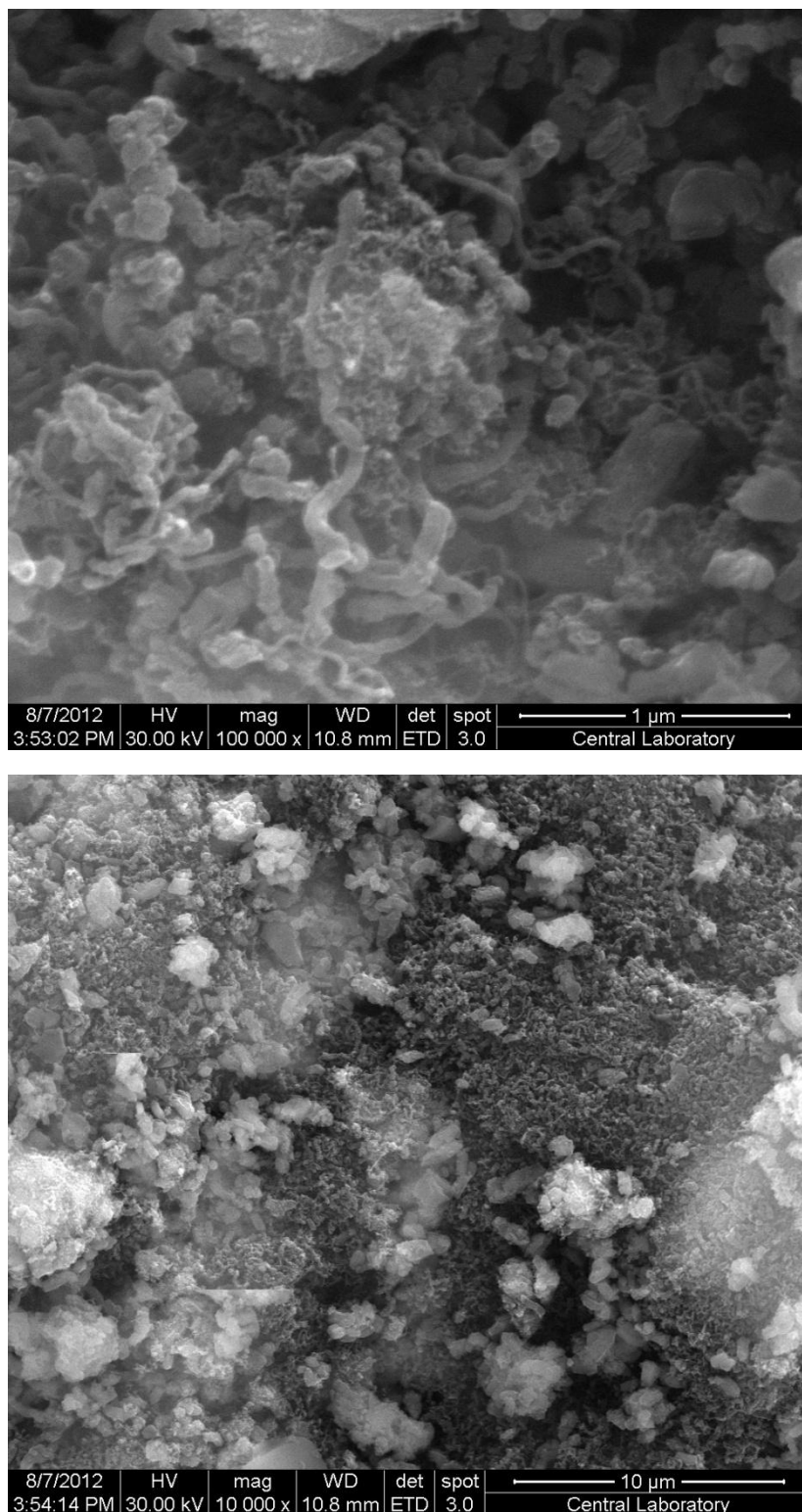


Figure 9.2.35. SEM images of PdNiCe(0.50)@SBA-15 after reaction at 600 °C

Thermal gravimetric analyses of Ni@SBA-15, NiCe(0.10)@SBA-15 and NiCe(0.50)@SBA-15 are shown in Figures 9.2.36, 9.2.37 and 9.2.38, respectively. Around 600 °C, the deposited carbon removes the surface. Weight loss percents of the catalysts are presented in Table 9.2.9. By increasing ceria amount, coke formation was eliminated due to the oxygen donor properties of ceria.

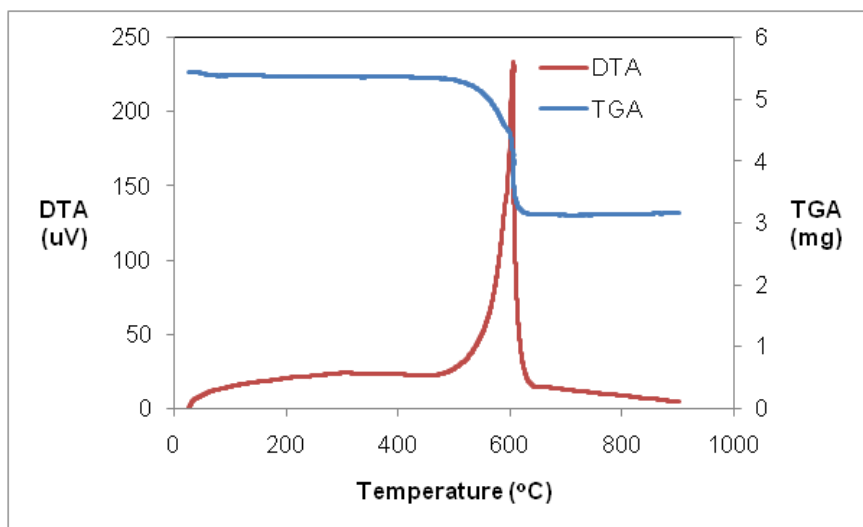


Figure 9.2.36. TGA profile of Ni@SBA-15 after reaction at 600 °C

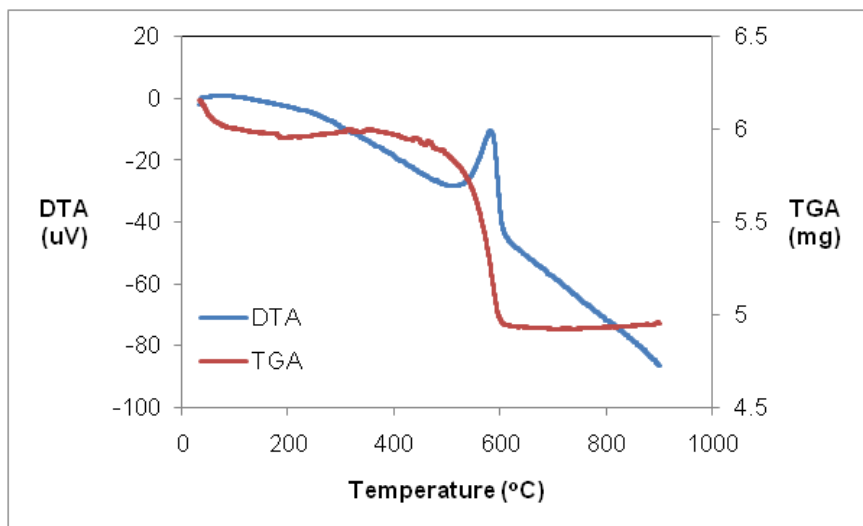


Figure 9.2.37. TGA profile of NiCe(0.10)@SBA-15 after reaction at 600 °C

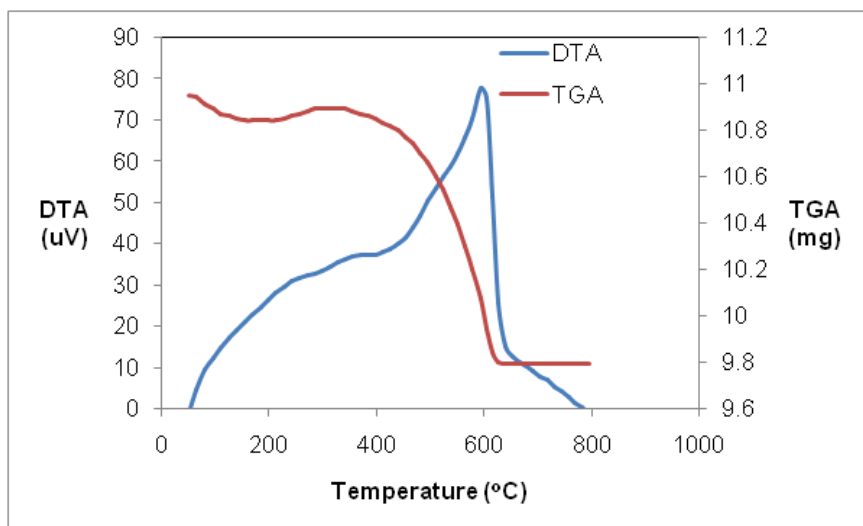


Figure 9.3.38. TGA profile of NiCe(0.50)@SBA-15 after reaction at 600 °C

Table 9.2.9. Weight loss of Ni and NiCe impregnated SBA-15 catalysts by TGA after reaction at 600 °C

Catalyst	% Weight Loss
Ni@SBA-15	40
NiCe(0.10)@SBA-15	16
NiCe(0.50)@SBA-15	11

9.3. Ni, Ce and NiCe IMPREGNATED COMMERCIAL AIMCM-41 CATALYSTS

In this part, impregnation of nickel, ceria and nickel-ceria to the commercial AIMCM-41 material and activity testing in ethanol steam reforming reaction is discussed. Obviously, Aluminum incorporation to the mesoporous silicate framework creates acidic sites. Effect of acidic sites to the catalyst activity for ethanol steam reforming reaction is inspected in this section.

Commercial AIMCM-41 (Sigma-Aldrich) was used as the support. It is in the structure of $\text{Al}_2\text{O}_3/\text{SiO}_2$ with the Al content of 3%. Similar to the previous section, effect of ceria

incorporation, effect of ceria loading and effect of the consequence of the impregnation is examined. Prepared catalysts are listed in Table 9.3.1.

Table 9.3.1. AIMCM-41 supported catalysts

Catalyst	Ni/Si	Ce/Si	Procedure
Ni@AIMCM-41	0.10	0	Standard impregnation
NiCe(0.10)@AIMCM-41	0.10	0.10	Simultaneous impregnation
NiCe(0.50)@AIMCM-41	0.10	0.50	Simultaneous impregnation
Ce@AIMCM-41	0	0.10	Standard impregnation
Ni@[Ce@AIMCM-41]	0.10	0.10	Consecutive impregnation

9.3.1. CHARACTERIZATION OF AIMCM-41 SUPPORTED CATALYSTS

Nickel and ceria impregnated AIMCM-41 catalysts were characterized by x-ray diffraction, nitrogen physisorption, scanning electron microscopy.

9.3.1.1. Characterization of Commercial AIMCM-41

Commercial AIMCM-41 (Sigma-Aldrich) is in the structure of $\text{Al}_2\text{O}_3/\text{SiO}_2$ with the Al content of 3%. X-ray diffraction spectroscopy pattern is shown in Figure 9.3.1. It gives a major peak at 2θ of 2.055 degrees and two reflections indicating two dimensional hexagonal structure with P6mm space group. Locations of peaks, $d(100)$ spacing and lattice parameter are presented in Table 9.3.2. These parameters are close to that of MCM-41 discussed in section 9.1.

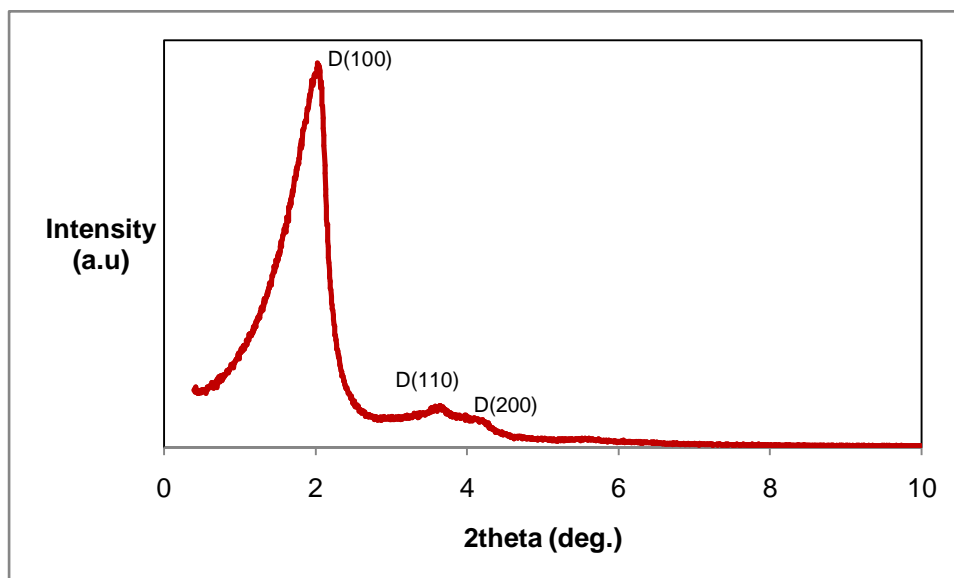


Figure 9.3.1. Low angle x-ray diffraction pattern of AIMCM-41

Table 9.3.2. X-ray diffraction peaks and related parameters for AIMCM-41

Sample	1 st peak (deg.)	2 nd peak (deg.)	3 rd peak (deg.)	D(100) (Å)	Lattice Parameter (Å)
AIMCM-41	2.055	3.72	4.21	42.83	49.46

Surface morphology can be observed by SEM images presented in Figure 9.3.2. Particles with different sizes agglomerated in the images. Average particle size can be estimated as around 100 nm. Composition of AIMCM-41 was determined by Energy Dispersive Spectroscopy (EDS) analysis (Table 9.3.3). According to the EDS analysis, atomic ration of silica to oxygen is around 2 and weight percent of aluminum is 3, as expected.

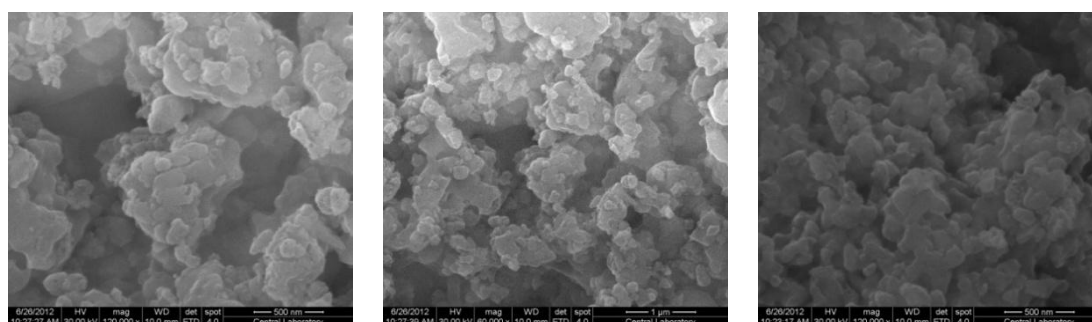


Figure 9.3.2. SEM images of AIMCM-41

Table 9.3.3. Composition of AIMCM-41 obtained by EDS

Element	Wt %	At %
O	49.66	63.34
Al	2.99	2.26
Si	47.35	34.40

Nitrogen adsorption-desorption isotherm is type IV indicating mesoporous structure (Figure 9.3.3) and the pore size distribution curve is narrow with a maximum at 3.08 nm (Figure 9.3.4). Surface area of AIMCM-41 is very high as shown in Table 9.3.4.

Table 9.3.4. Nitrogen physisorption analysis of AIMCM-41

Sample	BET Surface Area (m ² /g)	BJH	BJH	BJH
		Desorption Surface Area (m ² /g)	Desorption Pore Volume (cc/g)	Desorption Pore Diameter (nm)
AIMCM-41	1008	1306	1.29	3.08

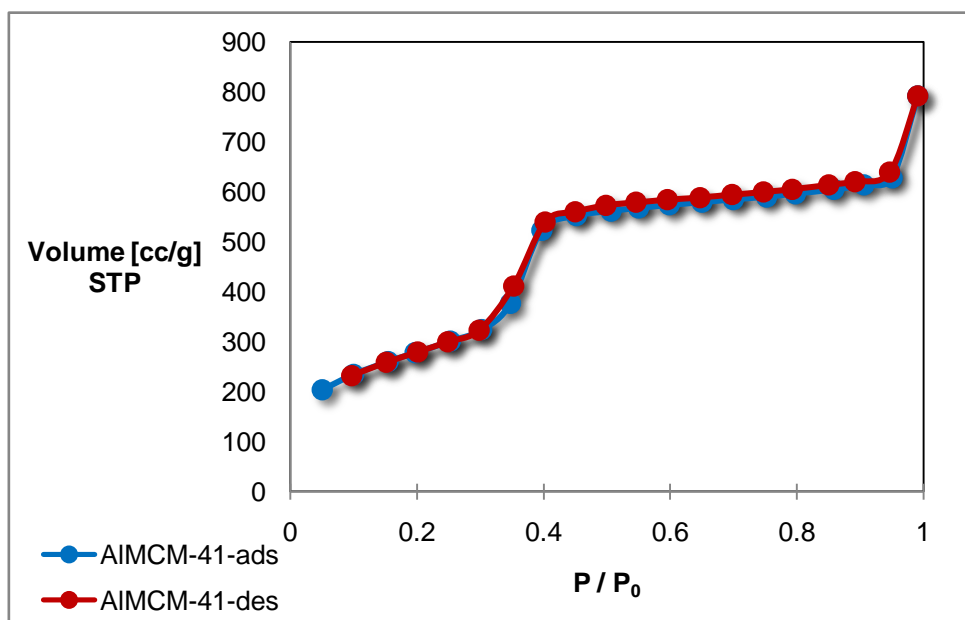


Figure 9.3.3. Nitrogen adsorption-desorption isotherm of AIMCM-41

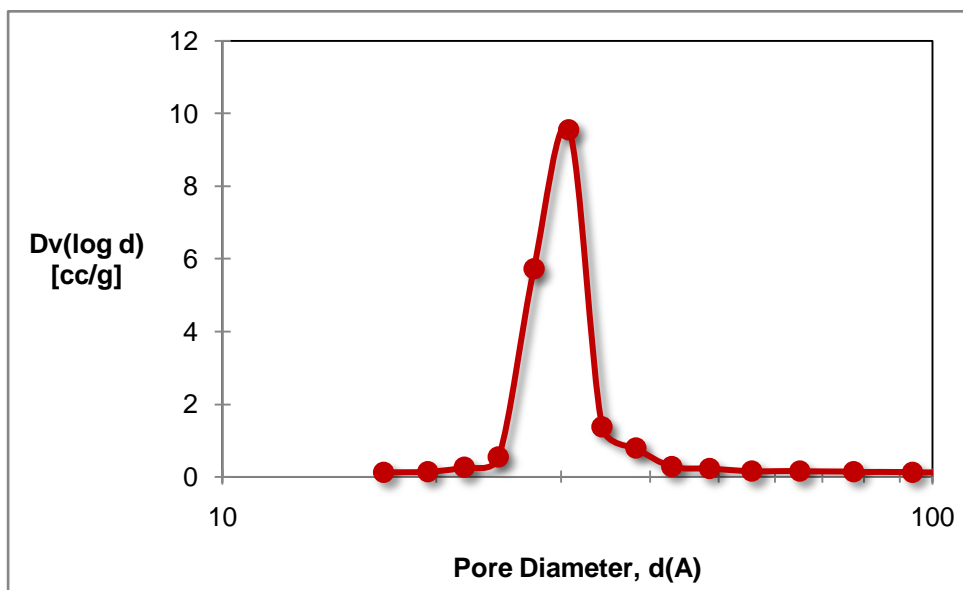


Figure 9.3.4. Pore size distribution curve of AIMCM-41

9.3.1.2. Characterization of Ni, Ce and NiCe Impregnated AIMCM-41 Supported Catalysts

Figure 9.3.5 shows the low angle x-ray diffraction pattern of nickel impregnated AIMCM-41 and that of nickel-ceria impregnated AIMCM-41 with different loadings is presented in Figure 9.3.6. Nickel impregnation to AIMCM-41 destructed the mesoporous structure very slightly. First and second peaks of AIMCM-41 are observed in Ni@ALMCM-41 sample. After impregnation with nickel and ceria, peak intensities decrease, i.e. mesoporous structure deformed. First and second peaks are still observed after nickel and ceria impregnation with the Ce/Si of 0.10. Increasing Ce/Si ratio to 0.50, more significantly deforms aluminasilicate framework. For NiCe(0.50)@AIMCM-41 catalysts, only the major peak was obtained with a low signal.

Peak locations, $d(100)$ spacings and lattice parameters for nickel and nickel-ceria impregnated catalysts are listed in Table 9.3.5. Samples with both nickel and ceria give major peak at higher 2 theta degrees. This is a result of contraction in the pores after impregnation with high loading.

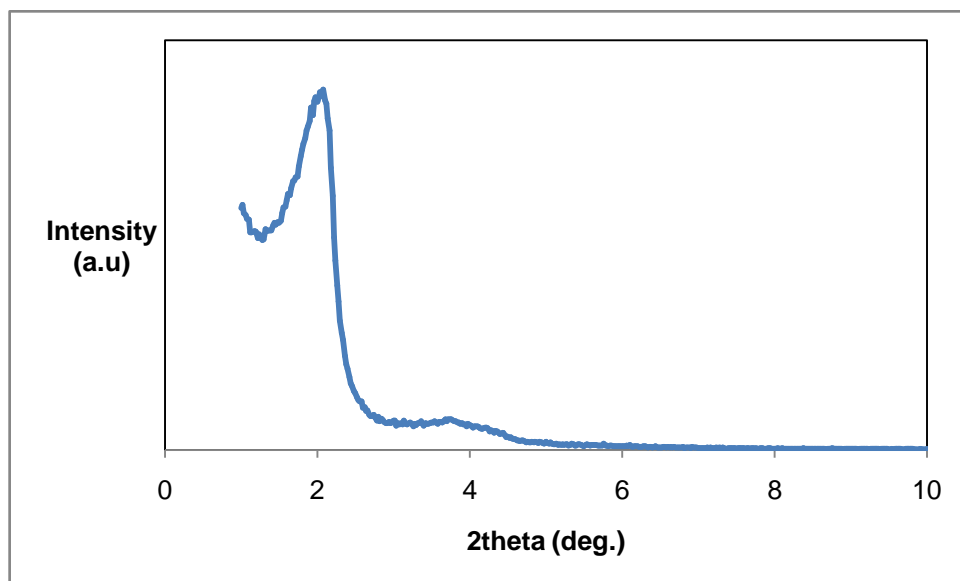


Figure 9.3.5. Low angle x-ray diffraction pattern of reduced nickel impregnated AIMCM-41, Ni@AIMCM-41

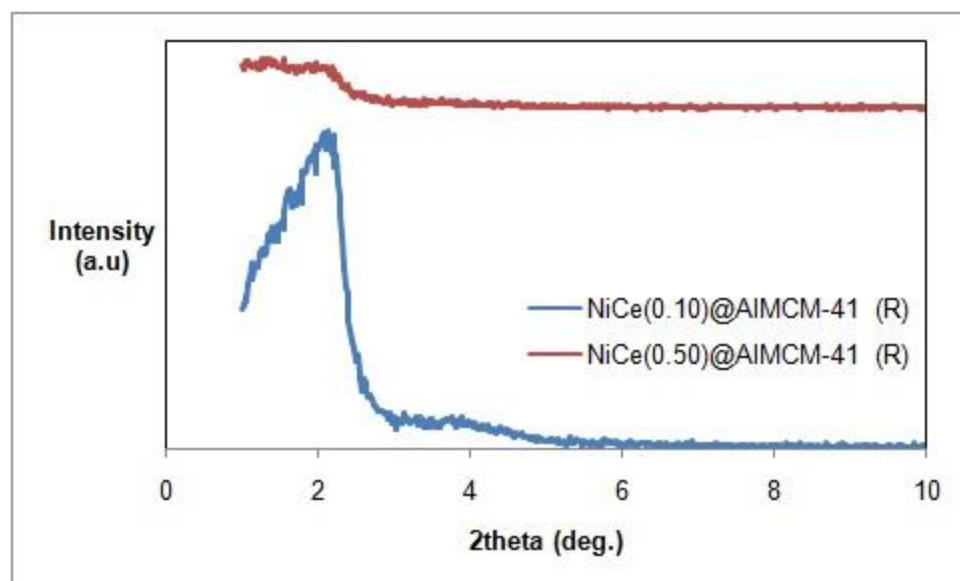


Figure 9.3.6. Low angle x-ray diffraction pattern of reduced nickel impregnated AIMCM-41, Ni@AIMCM-41

Table 9.3.5. X-ray diffraction analysis of nickel and nickel-ceria impregnated AIMCM-41 catalysts

Sample	1 st peak (deg.)	2 nd peak (deg.)	3 rd peak (deg.)	D(100) (Å)	Lattice Parameter (Å)
Ni@AIMCM-41 (R)	2.12	3.84	4.21	41.6	48.1
NiCe(0.10)@AIMCM-41 (R)	2.20	3.96	-	40.1	46.3
NiCe(0.50)@AIMCM-41 (R)	2.20	-	-	-	-

Crystalline peaks of NiO and CeO₂ species are shown in Figure 9.3.7. Peaks of (111), (200) and (220) of NiO were signed for Ni@AIMCM-41 and (111) peak was used for particle size determination by Scherrer equation. For NiCe(0.10)@AIMCM-41 sample, peaks of CeO₂ and NiO species are clearly seen. However for the sample NiCe(0.50)@AIMCM-41 CeO₂ peaks disable the observation of NiO peaks. Particle size of NiO for NiCe(0.50)@AIMCM-41 could not calculated. As listed in Table 9.3.6, particle size of CeO₂ species is very small, indicating a good dispersion with small nanoparticles. NiO species has also particles size around 13-16 nm, dispersed in the aluminasilicate network.

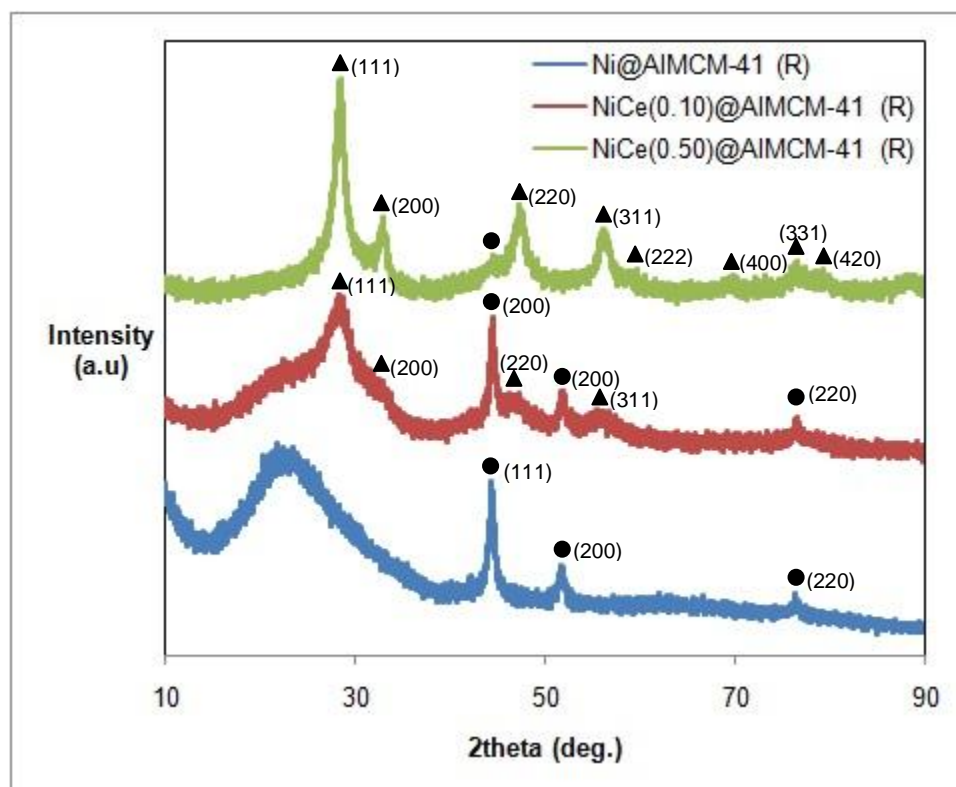


Figure 9.3.7. High angle x-ray diffraction patterns of Ni and NiCe impregnated AIMCM-41 supported catalysts (▲ CeO₂, ● NiO)

Table 9.3.6. NiO and CeO₂ particle sizes

Catalyst	NiO Particle Size (nm)	CeO ₂ Particle size (nm)
Ni@AIMCM-41 (R)	13.0	-
NiCe(0.10)@AIMCM-41 (R)	16.4	0.9
NiCe(0.50)@AIMCM-41 (R)	NA	6.5

Impregnation of nickel to AIMCM-41 with Ni/Si ratio of 0.10, decreased the surface area of AIMCM-41 by 20%. Nitrogen adsorption-desorption isotherm of the catalysts lost their type IV isotherm by increasing metal loading (Figure 9.3.8). Pore sizes of nickel and nickel-ceria impregnated AIMCM-41 catalysts remained constant after impregnation (Table 9.3.7), giving similar pore size distributions (Figure 9.3.9) .

Table 9.3.7. Nitrogen physisorption analysis of nickel and nickel-ceria impregnated AIMCM-41 samples

Catalyst	BET Surface Area (m ² /g)	BJH Desorption Surface Area (m ² /g)	BJH Desorption Pore Volume (cc/g)	BJH Desorption Pore Diameter (nm)
Ni@AIMCM-41 (U)	737.5	924.7	0.85	2.76
Ni@AIMCM-41 (R)	820.2	1068	1.02	2.73
NiCe(0.10)@AIMCM-41 (R)	594.2	755.9	0.69	2.74
NiCe(0.50)@AIMCM-41 (R)	237.3	309.8	0.27	2.73

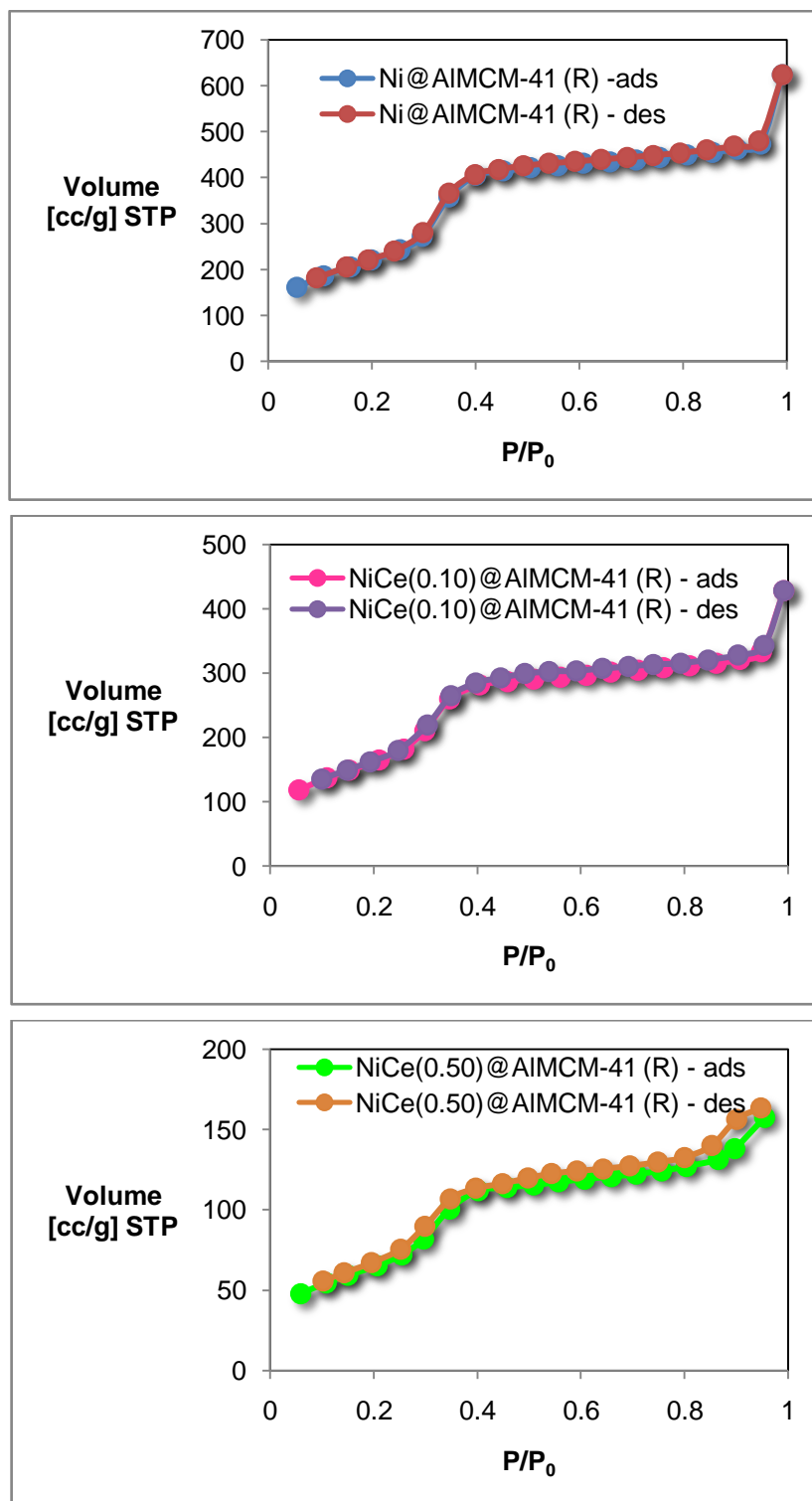


Figure 9.3.8. Nitrogen adsorption-desorption isotherms of Ni, and NiCe impregnated AIMCM-41 catalysts

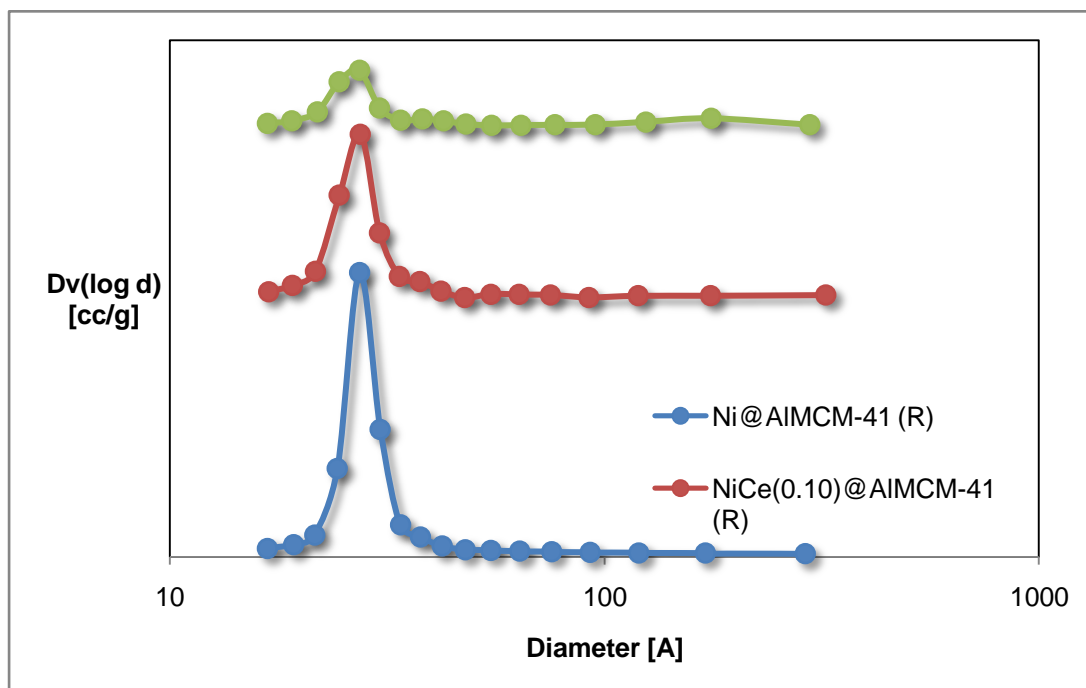


Figure 9.3.9. Low angle x-ray diffraction patterns of Ce, Ni and NiCe impregnated AIMCM-41.

Table 9.3.5. X-ray diffraction analysis of nickel and nickel-ceria impregnated AIMCM-41 catalysts

Sample	1 st peak (deg.)	2 nd peak (deg.)	3 rd peak (deg.)	D(100) (Å)	Lattice Parameter (Å)
Ni@AIMCM-41 (R)	2.12	3.84	4.21	41.6	48.1
NiCe(0.10)@AIMCM-41 (R)	2.20	3.96	-	40.1	46.3
NiCe(0.50)@AIMCM-41 (R)	2.20	-	-	-	-

SEM images of Ni@(Ce@AIMCM-41), Ce@AIMCM-41, NiCe(0,10)@AIMCM-41 and NiCe(0.50)@AIMCM-41 are shown in Figures 9.3.12, 9.3.13, 9.3.14 and 9.3.15, respectively. All the catalysts show very similar surface morphologies. Since the particles sizes of the samples are very small, agglomerated particles are observed.

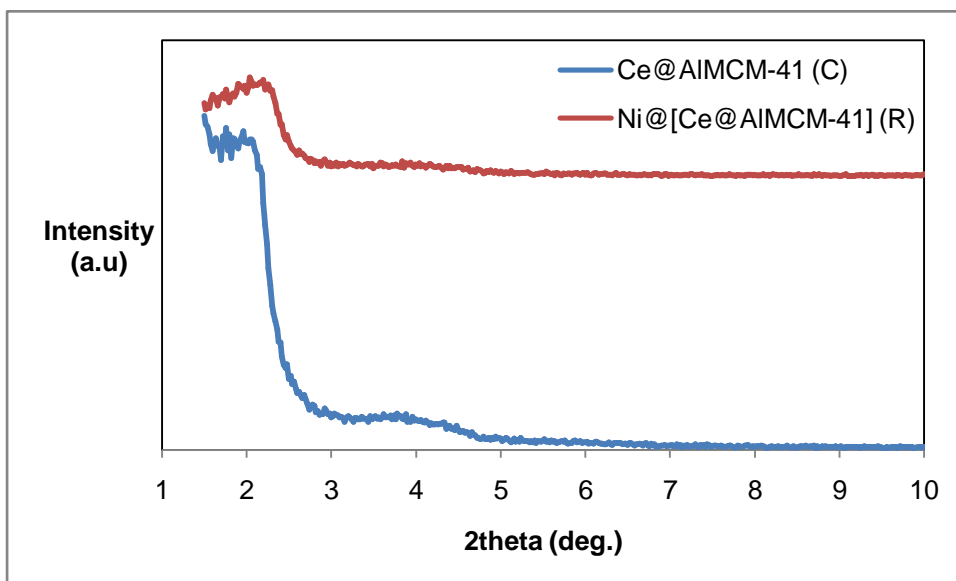


Figure 9.3.10. High angle x-ray diffraction patterns of Ce and NiCe impregnated AIMCM-41 catalysts

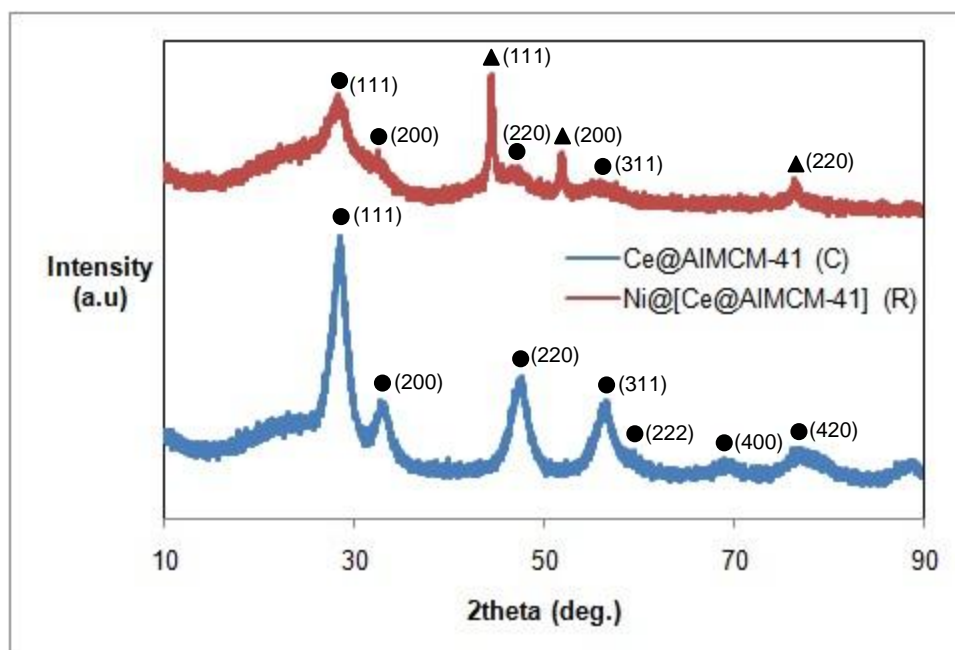


Figure 9.3.11. High angle x-ray diffraction pattern of cerium impregnated and consequently cerium and nickel impregnated AIMCM-41 catalysts

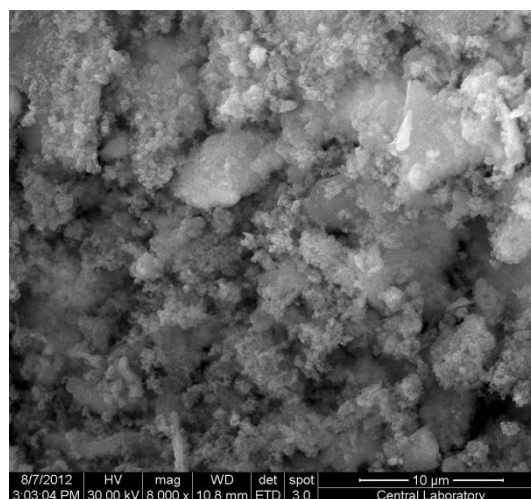
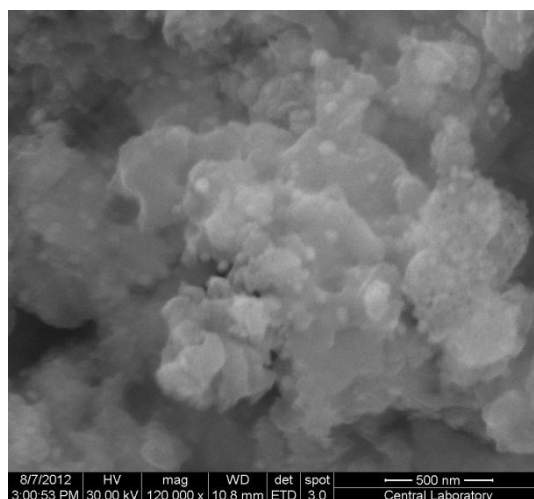
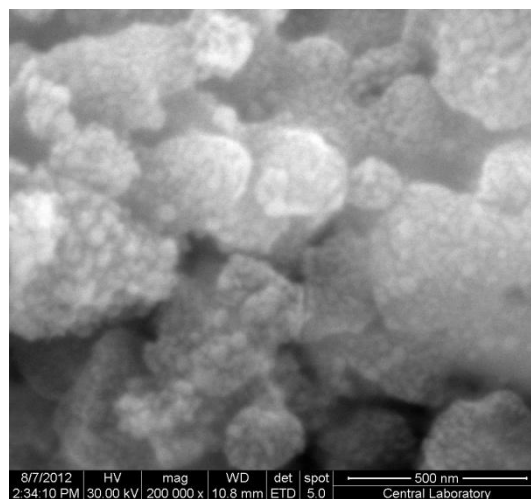
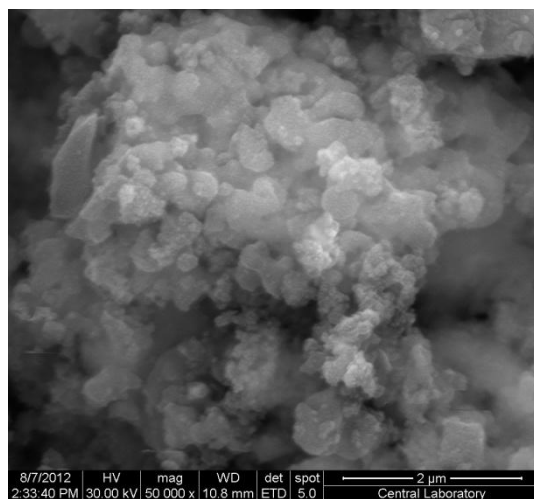


Figure 9.3.12. SEM images of Ni@[Ce@AIMCM-41]

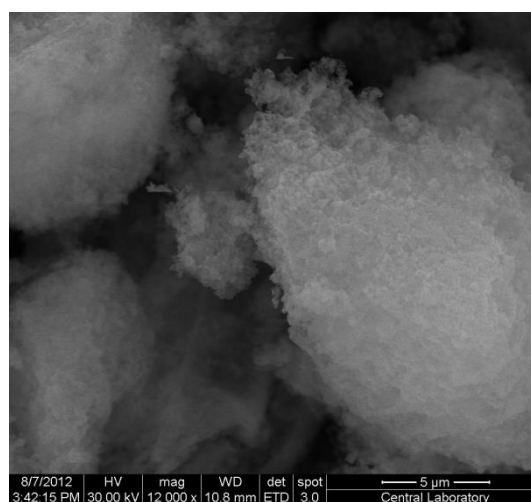
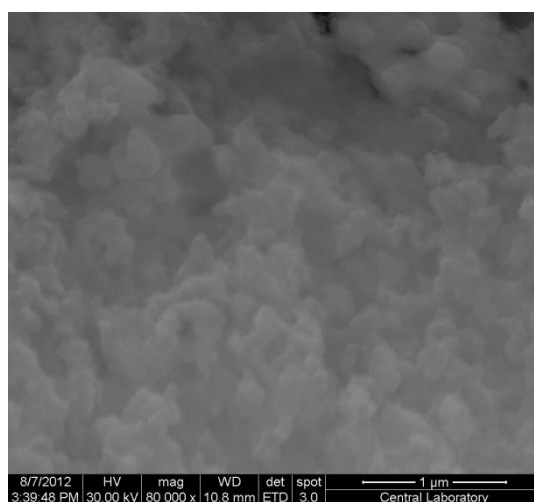


Figure 9.3.13. SEM images of Ce@AIMCM-41

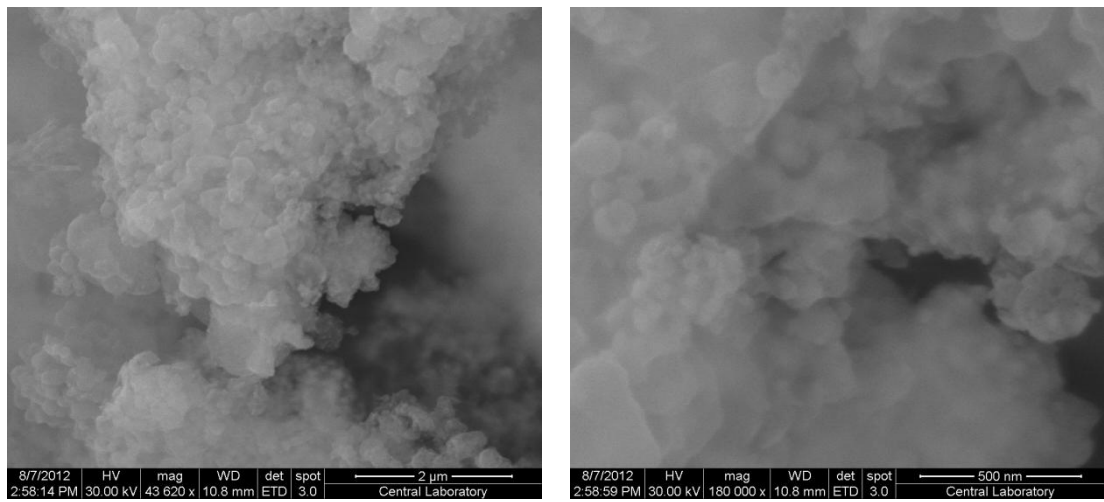


Figure 9.3.14. SEM images of NiCe(0.10)@AIMCM-41

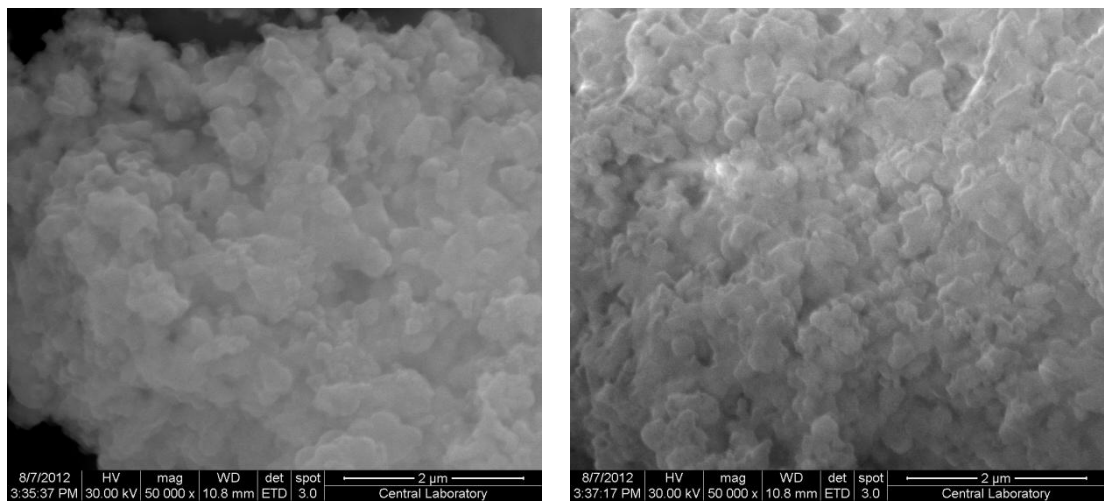


Figure 9.3.15. SEM images of NiCe(0.50)@AIMCM-41

9.3.1.3. Ethanol-Steam Reforming Reaction Results

Ethanol conversion and hydrogen yield values obtained with Ni@AIMCM-41 at 600 °C for 5 hours are plotted on Figure 9.3.15. Complete conversion was achieved and hydrogen yield is very high. At the beginning of the reaction hydrogen yield is 5.8, during 5 hours of reaction, the catalyst deactivates quickly and hydrogen yield decreases to 3.6.

In Figure 9.3.16, ethanol conversion and hydrogen yields with Ni@(Ce@AIMCM-41) for 5 hours reaction is presented. Hydrogen yield is 5.7/6.0 and after 5 hours it decreases to 4.3 which is also a high hydrogen yield value. Catalyst seems to be active and stable, after 2 hours, yield remains constant. Consecutively Ni and Ce impregnated catalyst shows higher activity and stability by means of hydrogen yield. NiCe(0.10)@AIMCM-41 catalyst shows similar behavior of Ni@AIMCM-41 and Ni@(Ce@AIMCM-41), however its deactivation is more significant (Figure 9.3.17).

Ce impregnated AIMCM-41 catalyst shows high activity by means of ethanol conversion. But different from Ni and NiCe impregnated catalysts, hydrogen yield is very low (Figure 9.3.18).. This is due to C_2H_2 formation by ethanol decomposition reaction.

Ethanol conversion and hydrogen yield at 600 °C for NiCe(0.50)@AIMCM-41 catalyst are shown in Figure 9.3.19 and 9.3.18 for 5 hours. Due to the blocking of pores by high amount of Ce, the catalyst shows a very unstable and less active behavior.

Different behaviors of the Ni, Ce and NiCe impregnated Al-MCM-41 catalysts can be explained by Ni-Ce and Ce-support interactions. Cerium incorporation reduces coke formation when dispersed on the surface of the support in the NiCe impregnated catalysts. If a consecutive impregnation procedure is applied, Ce disperses on the support and does not block Ni active sites. In the simultaneously impregnated catalyst, due to the Ni-Ce interaction, hydrogen yield is lower than that of consecutively NiCe impregnated catalyst. By increasing Ce loading, the pores of AIMCM-41 and Ni active sites are blocked by Ce particles, so the catalyst show low activity and stability.

Hydrogen yields of Ni@AIMCM-41, NiCe(0.10)@AIMCM-41 and Ni@(Ce@AIMCM-41) catalysts are compared in Figure 9.3.20 for 5 hours of reaction at 600 °C. Discussed trends of the catalysts are seen more clearly.

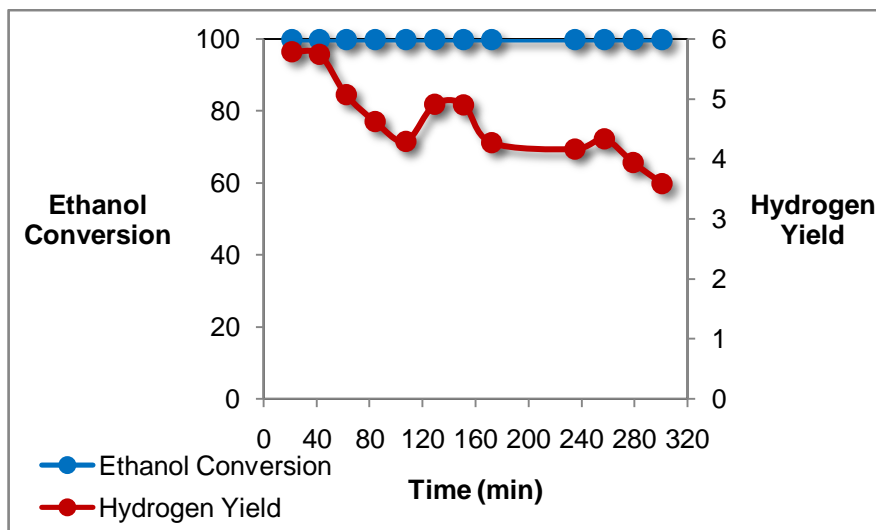


Figure 9.3.15. Ethanol conversion and hydrogen yield of Ni impregnated AIMCM-41 catalyst, Ni@AIMCM-41 at 600 °C

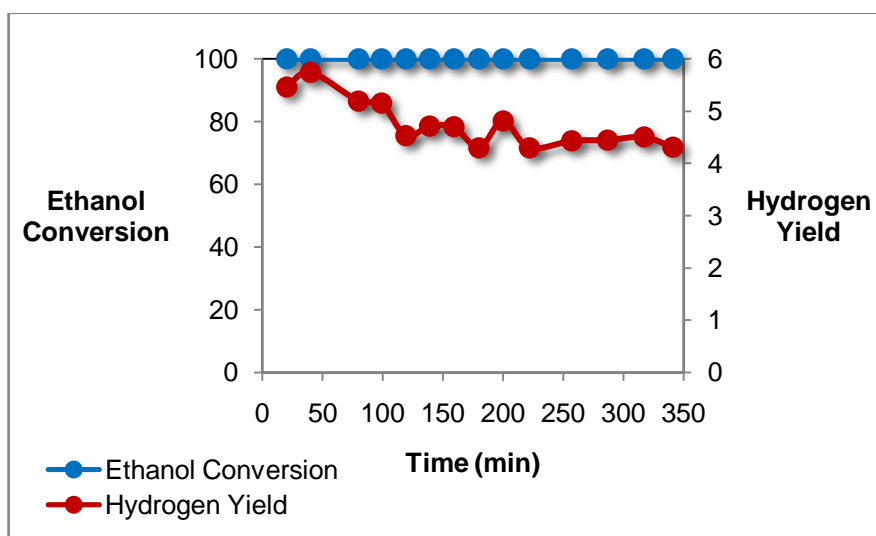


Figure 9.3.16. Ethanol conversion and hydrogen yield of sequentially Ni and Ce impregnated AIMCM-41 catalyst, Ni@[Ce@AIMCM-41] at 600 °C

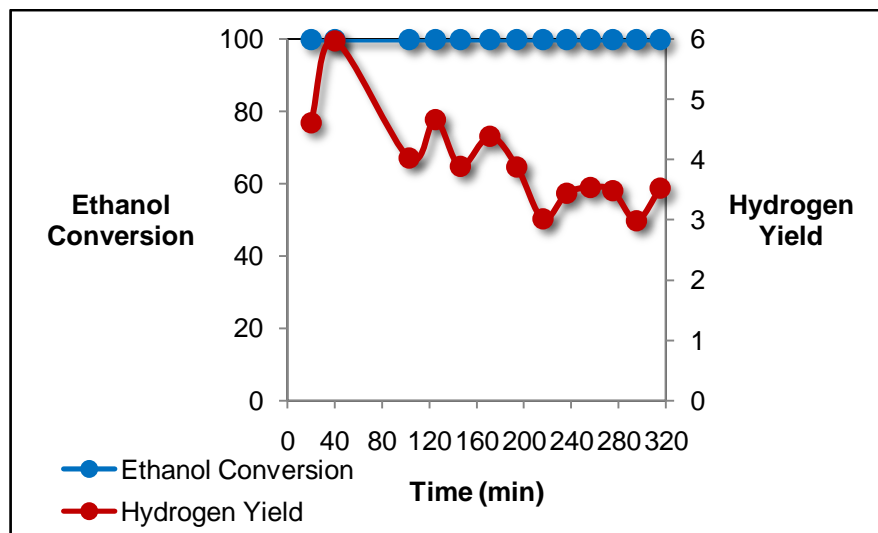


Figure 9.3.17. Ethanol conversion and hydrogen yield of Ni and Ce impregnated AIMCM-41 with Ce/Si=0.10, NiCe(0.10)@AIMCM-51 at 600 °C

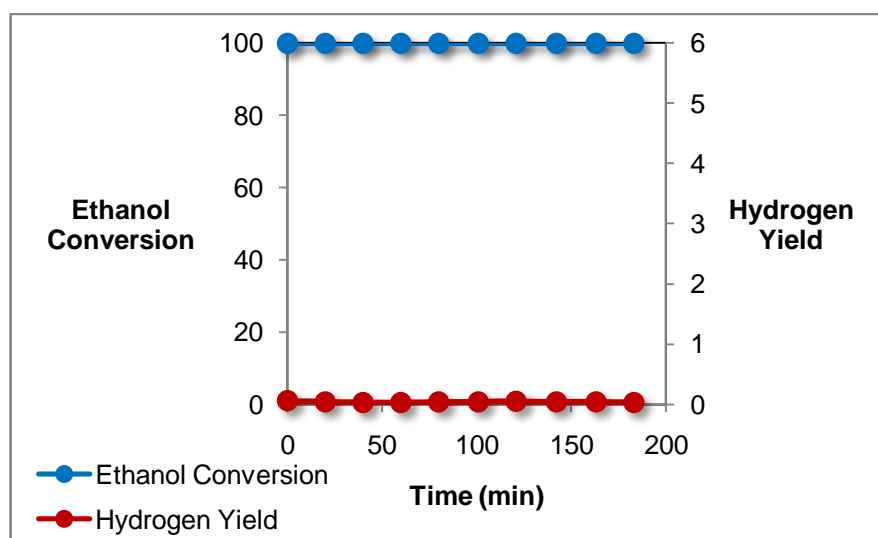


Figure 9.3.18. Ethanol conversion and hydrogen yield of Ce@AIMCM-41 at 600 °C

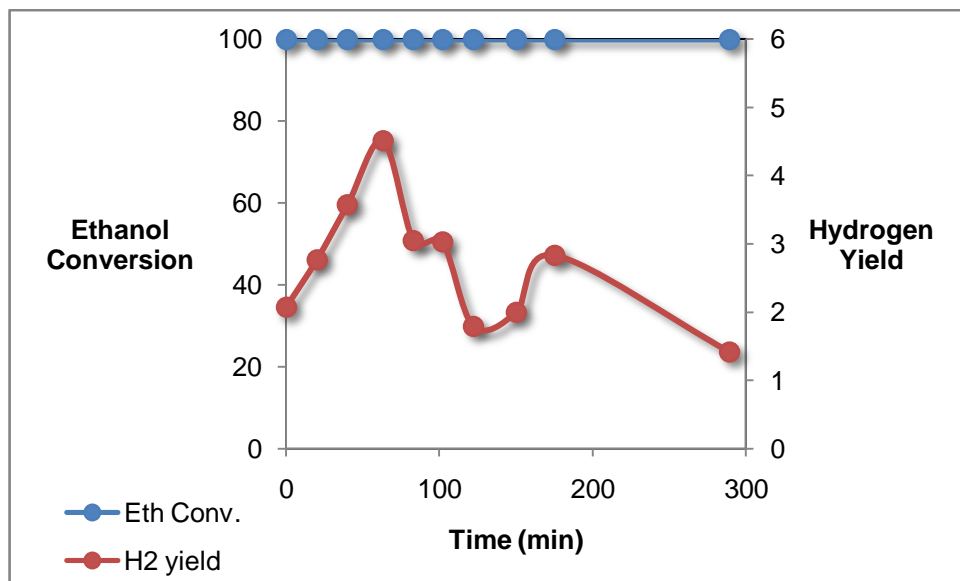


Figure 9.3.19. Ethanol conversion and hydrogen yield of NiCe(0.50)@AIMCM041 at 600 °C

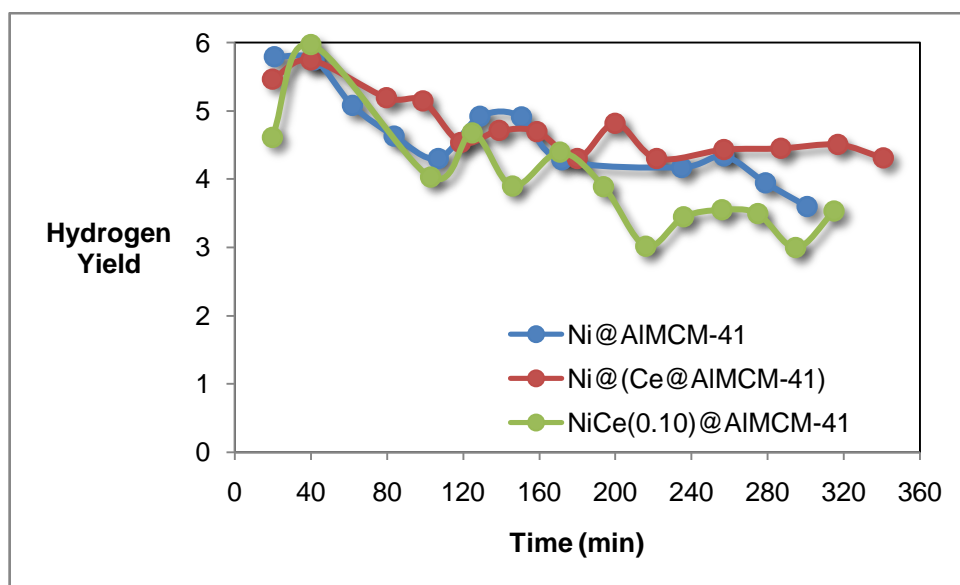


Figure 9.3.20. Comparison of hydrogen yields of Ni and NiCe impregnated AIMCM-41 supported catalysts

Figure 9.3.21 is the plot of gas phase composition versus time. With Ni@AIMCM-41 catalyst. Hydrogen composition decreases from 74% to 64% during 5 hours of reaction at 600 °C. CO₂, CH₄, CO and trace amount of CH₂O compose the gas product stream.

Gas product composition with Ne@(Ce@AIMCM-41) catalyst is shown in Figure 9.3.22. All the product compositions remains almost constant for 5 hours. In the product stream, 74%-68% hydrogen exists, this is the maximum percentage of hydrogen that can be achieved in steam reforming of ethanol. Gas product stream composition with NiCe(0.10)@AIMCM-41 is similar to that of Ni@AIMCM-41. In the consecutively impregnated catalyst, CH₂O formation is also prevented.

Gas product stream composition of NiCe(0.50)@AIMCM-41 is presented in Figure 9.3.24. In the stream, C₂H₂ concentration is higher.

Ce impregnated AIMCM-41 catalyst shows activity in decomposition of ethanol to C₂H₂ and H₂O. C₂H₂ concentration in the gas product stream is over 90% (Figure 9.3.25).

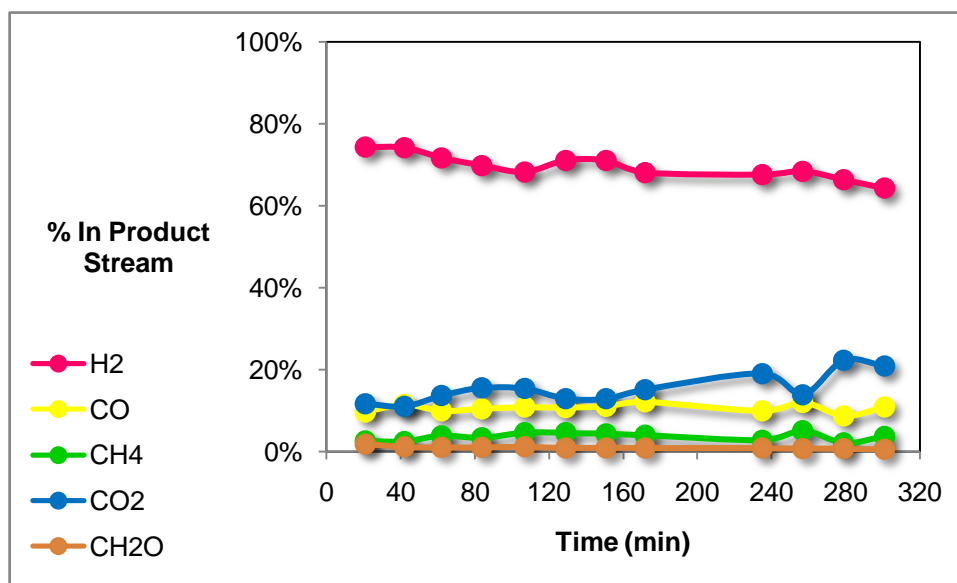


Figure 9.2.21. Composition of gas product stream of Ni impregnated AIMCM-41 catalyst, Ni@AIMCM-41 at 600 °C

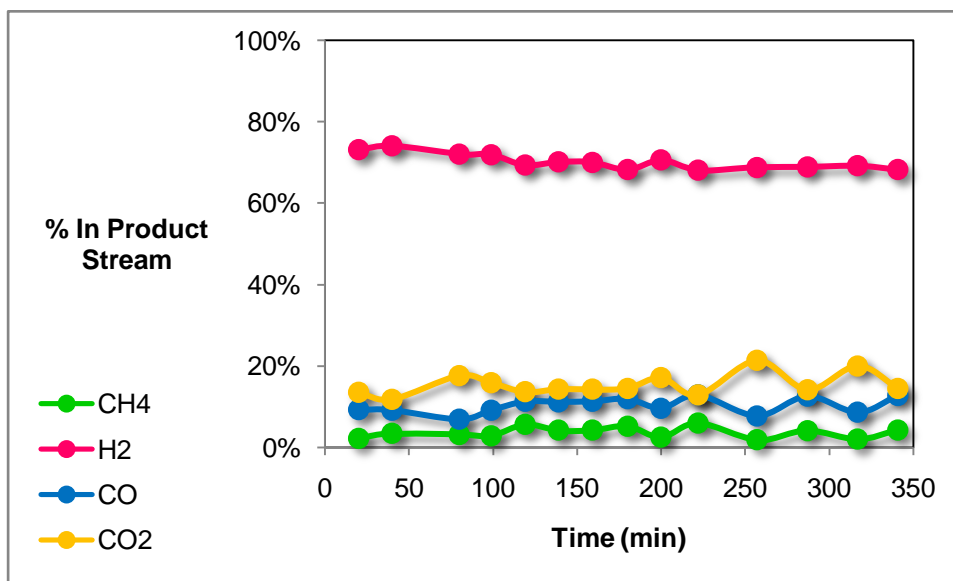


Figure 9.3.22 . Composition of gas product stream of sequentially Ni and Ce impregnated AIMCM-41 catalyst, Ni@[Ce@AIMCM-41] at 600 °C

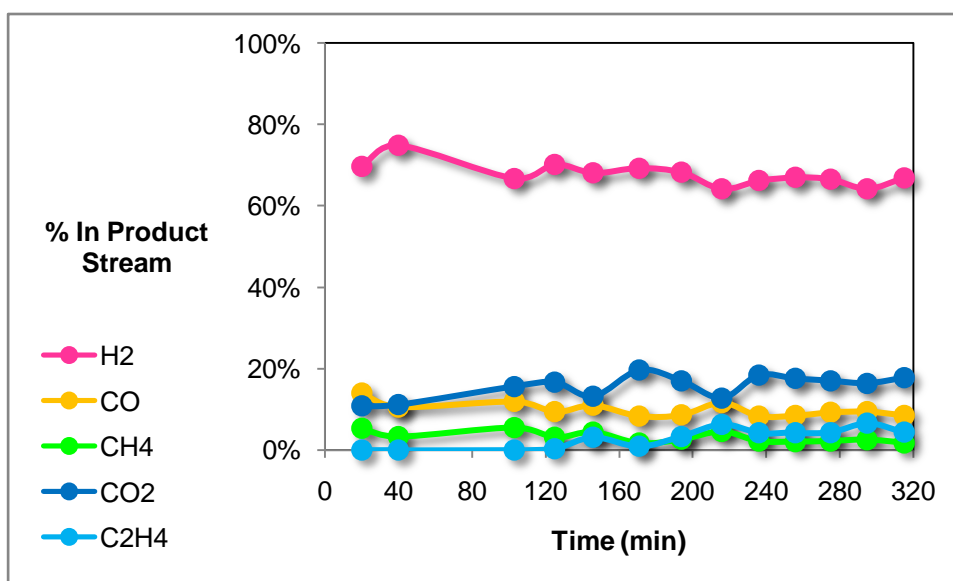


Figure 9.3.23. Composition of gas product stream of Ni and Ce impregnated AIMCM-41 with Ce/Si=0.10, NiCe(0.10)@AIMCM-51 at 600 °C

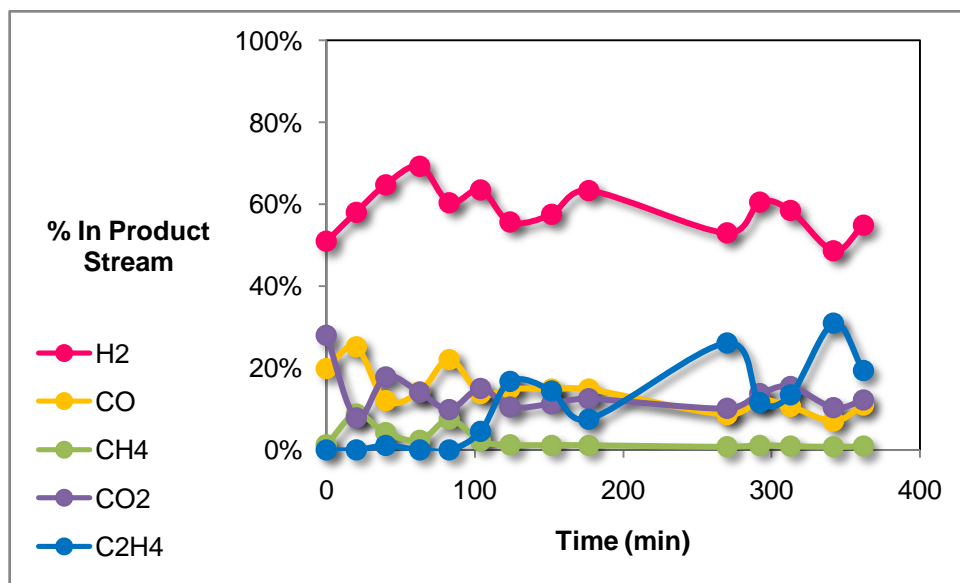


Figure 9.3.24. Composition of gas product stream of Ni and Ce impregnated AIMCM-41 with Ce/Si=0.50, NiCe(0.50)@AIMCM-51 at 600 °C

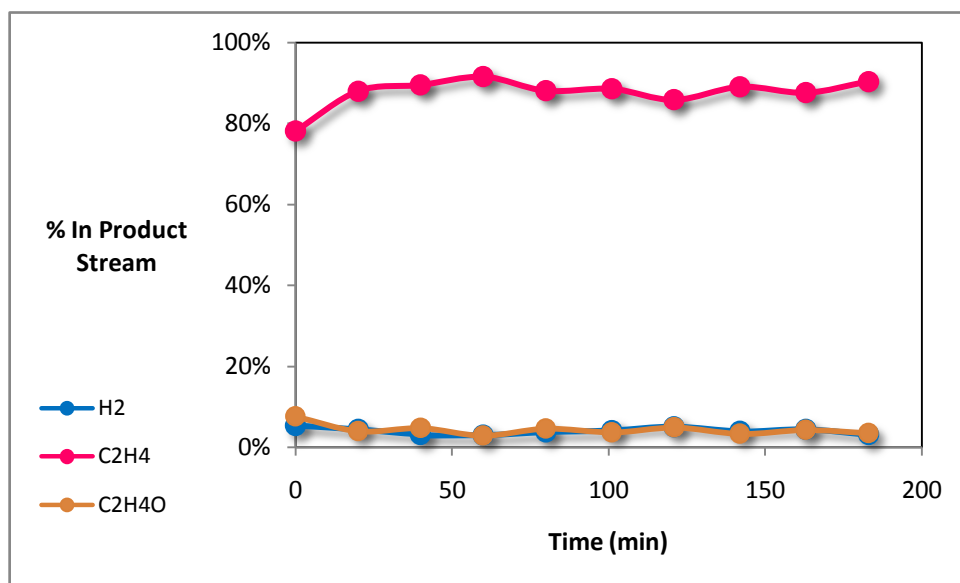


Figure 9.3.25. Composition of gas product stream of Ce@AIMCM-41 at 600 °C

Product selectivities for Ni@AIMCM-41, Ni@(Ce@AIMCM-41), NiCe(0.10)@AIMCM-41, NiCe(0.50)@AIMCM-41 and Ce@AIMCM-41 are shown in Figures 9.3.26, 9.3.27, 9.3.28, 9.3.29 and 9.3.30, respectively.

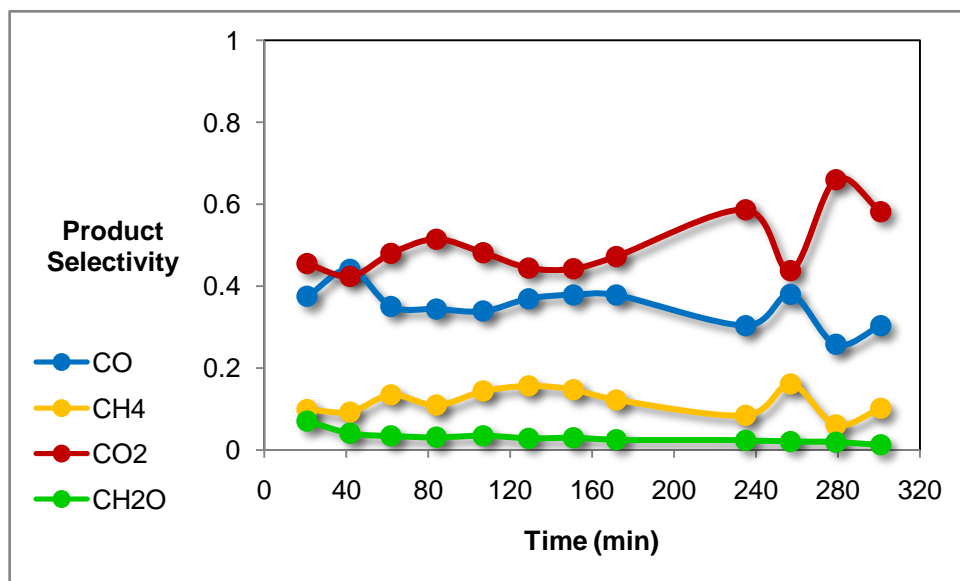


Figure 9.3.26. Selectivities of products with the catalyst Ni@AIMCM-41 at 600 °C

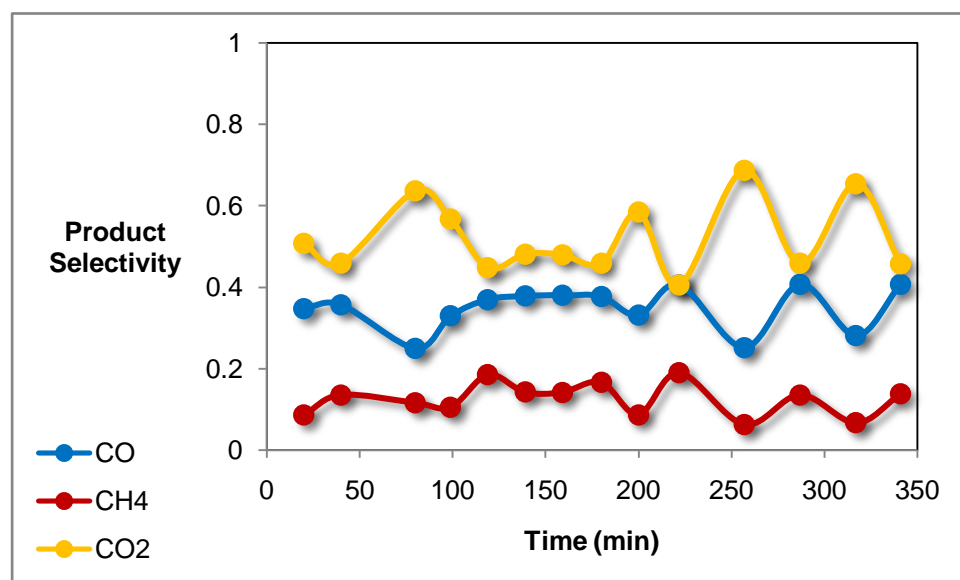


Figure 9.3.27 . Product selectivities of sequentially Ni and Ce impregnated AIMCM-41 catalyst, Ni@[Ce@AIMCM-41] at 600 °C

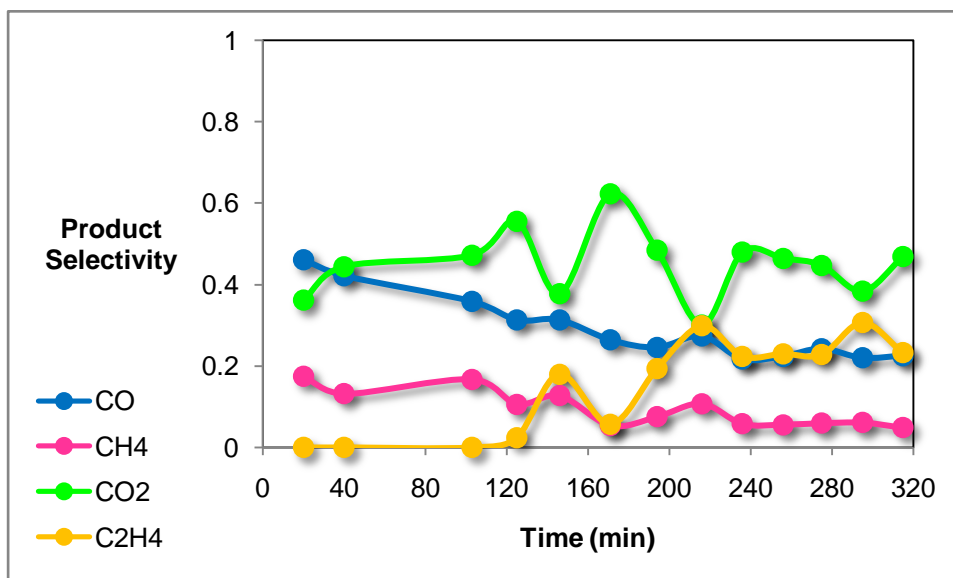


Figure 9.3.28. Product selectivities of Ni and Ce impregnated AIMCM-41 with Ce/Si=0.10, NiCe(0.10)@AIMCM-41 at 600 °C

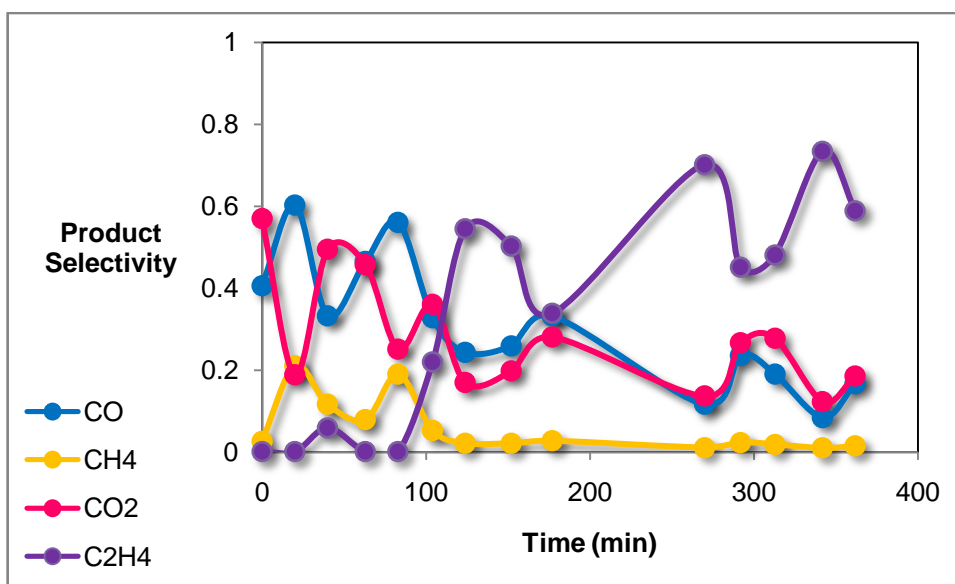


Figure 9.3.29. Product selectivities of Ni and Ce impregnated AIMCM-41 with Ce/Si=0.50, NiCe(0.50)@AIMCM-41 at 600 °C

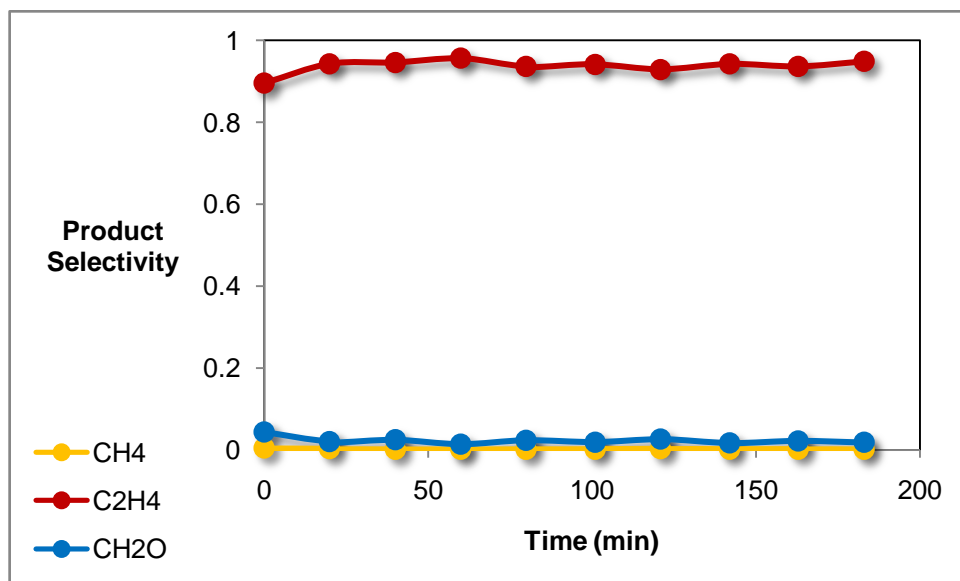


Figure 9.3.30. Product selectivities of Ce impregnated AIMCM-41 with Ce@AIMCM-41 at 600 °C

9.3.1.4. Characterization of AIMCM-41 Supported Catalysts After Ethanol Steam Reforming Reaction

Due to the high coke formation, removal of used catalysts from the reactor for characterization after reaction was difficult. Ni@(Ce@AIMCM-41) was characterized by x-ray diffraction, scanning electron microscopy and thermal gravimetric analysis.

Low angle and wide angle X-ray diffraction pattern of Ni@(Ce@AIMCM-41) after reaction at 600 °C is presented in Figure 9.3.31 and Figure 9.3.32, respectively. According to the low angle x-ray diffraction pattern, mesoporous structure is deformed significantly after reaction. In the wide angle x-ray diffraction pattern, filamentous carbon peak is observed.

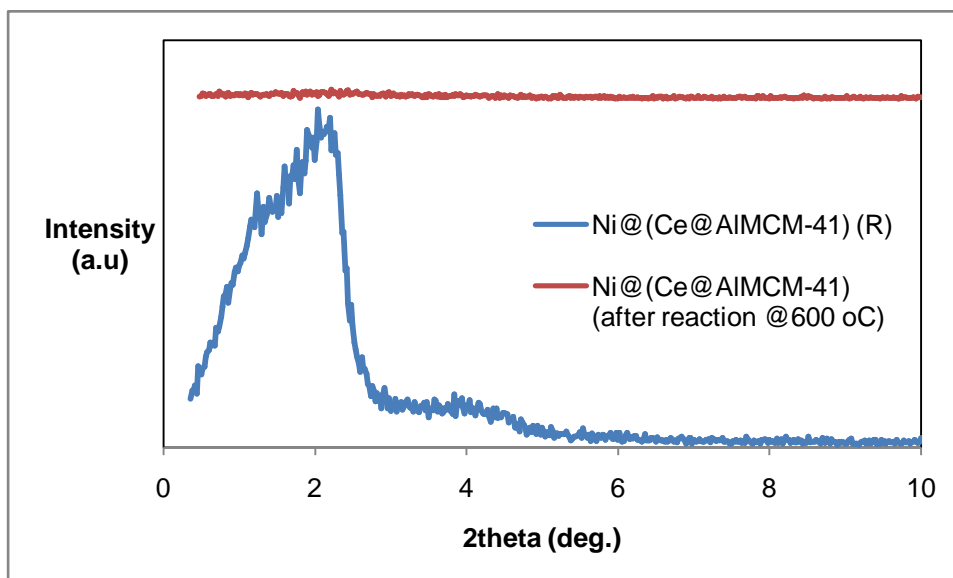


Figure 9.3.31. Low angle x-ray diffraction pattern of reduced Ni@[Ce@AIMCM-41] and after reaction at 600 °C

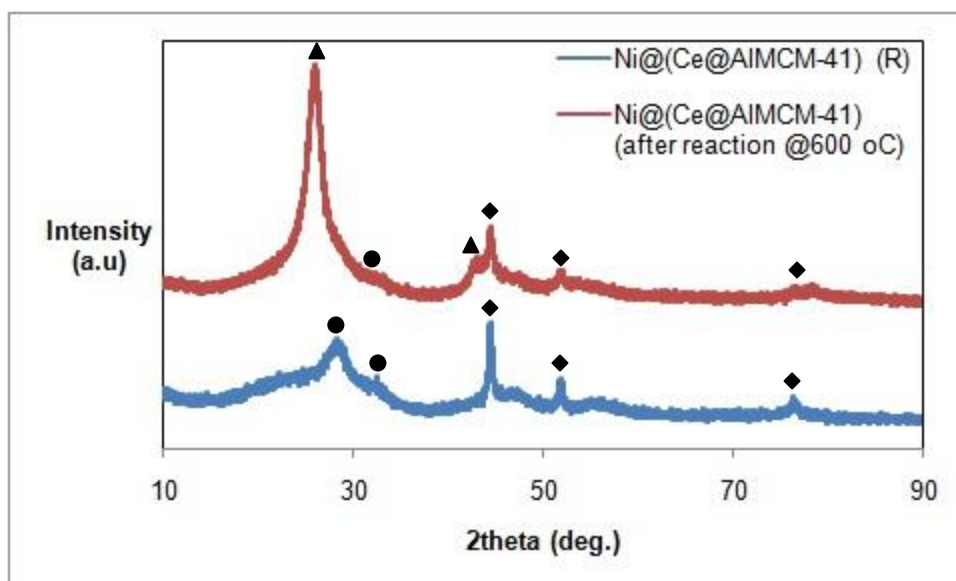


Figure 9.3.32. Wide angle x-ray diffraction pattern of reduced Ni@[Ce@AIMCM-41] and after reaction at 600 °C (▲ C, ◆NiO)

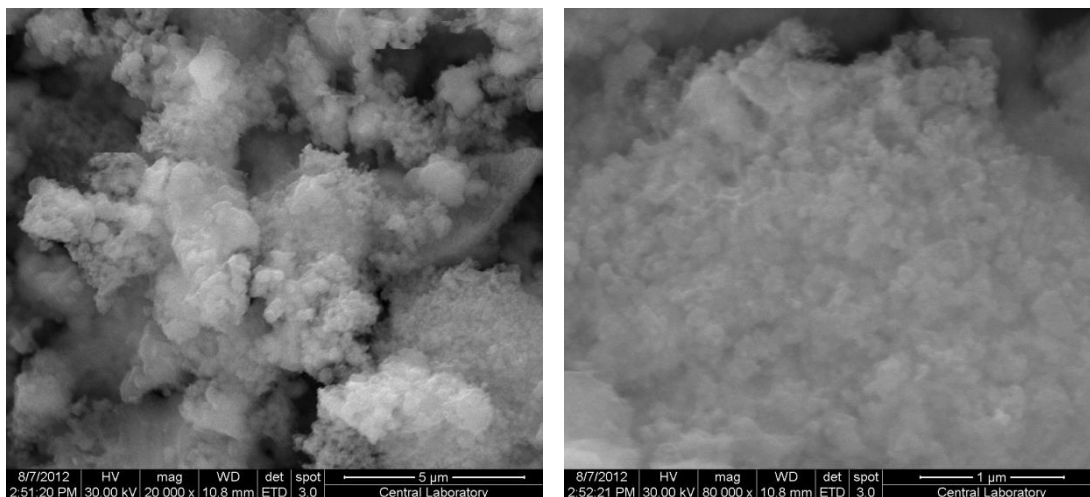


Figure 9.3.33. SEM images of NiCe(0.10)@AIMCM-41 after reaction at 600 °C

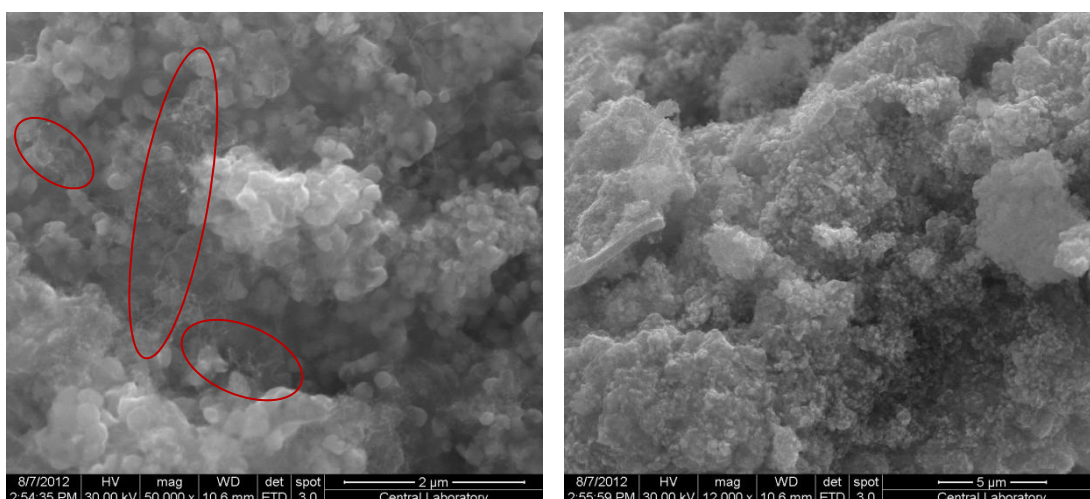


Figure 9.3.34. SEM images of NiCe(0.50)@AIMCM-41 after reaction at 600 °C

In Figures 9.3.33 and 9.3.34, carbon deposition is observed on the surface. In Figure 9.3.35, since ethanol steam reforming reaction was not achieved by Ce@AIMCM-41 catalyst, coke formation is not observed.

In Figure 9.3.36, thermal gravimetric analysis of Ni@(Ce@AIMCM-41) is presented. Deposited carbon is removed between 500 °C-600 °C, and the weight loss is determined as 70%.

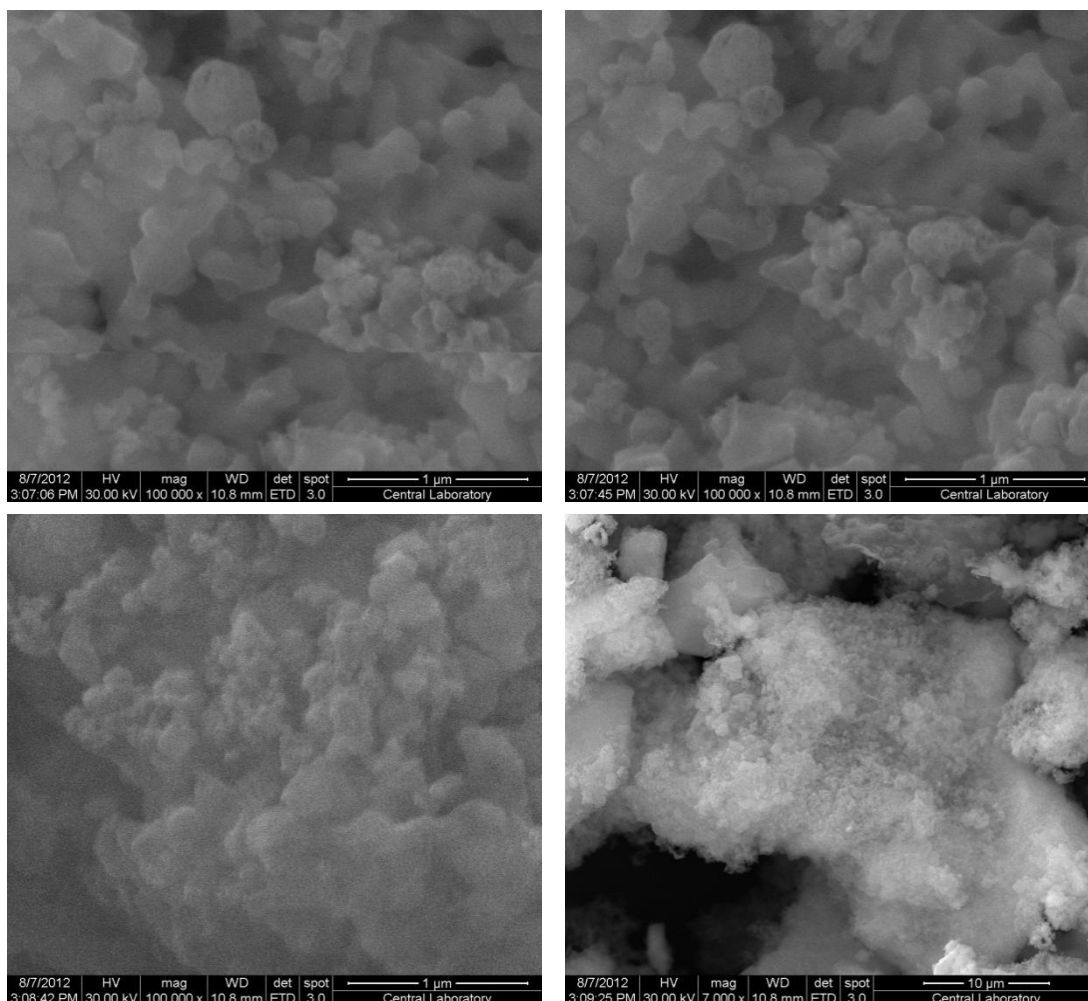


Figure 9.3.35. SEM images of Ce@AIMCM-41 after reaction at 600 °C

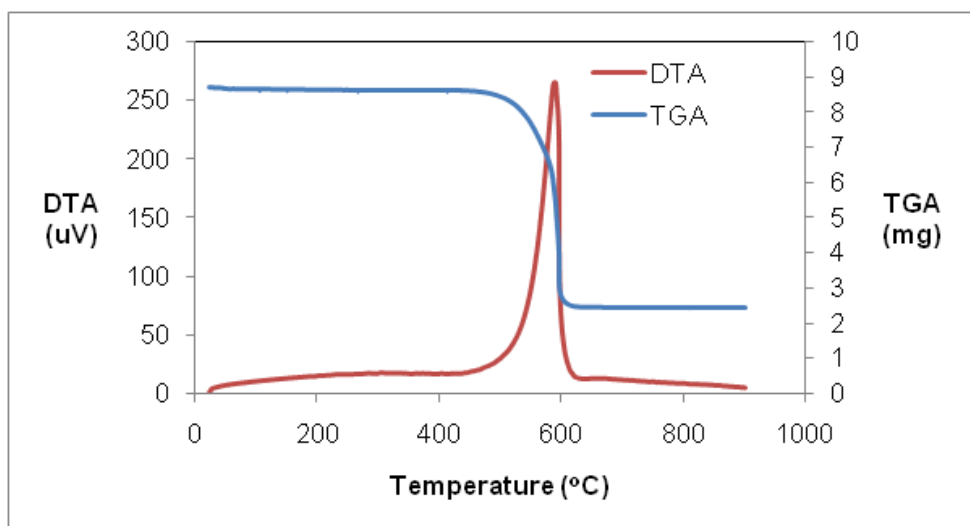


Figure 9.3.36. Thermal gravimetric analysis of consecutively ceria and nickel impregnated AIMCM-41 supported catalyst, Ni@[Ce@AIMCM-41] after reaction at 600 °C

9.4. Ni IMPREGNATED COMMERCIAL CeO₂ CATALYST

In this part of the study, another approach for support was applied. Firstly, a mesoporous structure composed of pure ceria was tried to be synthesized. Due to the thermal sintering problem of ceria, calcination could not be applied. As discussed in Section 4, mesoporous ceria structures were synthesized by calcining lower temperatures. Since the ethanol steam reforming reaction takes place over 500 °C, the material must be calcined at at least this temperature.

Due to the difficulty of synthesizing a porous structure by ceria, commercial non-porous ceria nanoparticles were used as support. An impregnation technique was applied and tested for its activity in steam reforming of ethanol reaction.

9.4.1. CHARACTERIZATION OF THE CATALYST

The support material was commercial ceria (Sigma-Aldrich) with a particle size of – nm. It was characterized before and after impregnation with nickel. The wide angle x-ray diffraction patterns of commercial untreated ceria and nickel impregnated are presented in Figure 9.4.1. Crystalline peaks of cerium oxide are seen clearly in the pattern. Since the nickel impregnated CeO₂ is in calcined form, nickel peaks are not observed in the figure. Particle size of CeO₂ is estimated as 16.8 nm.

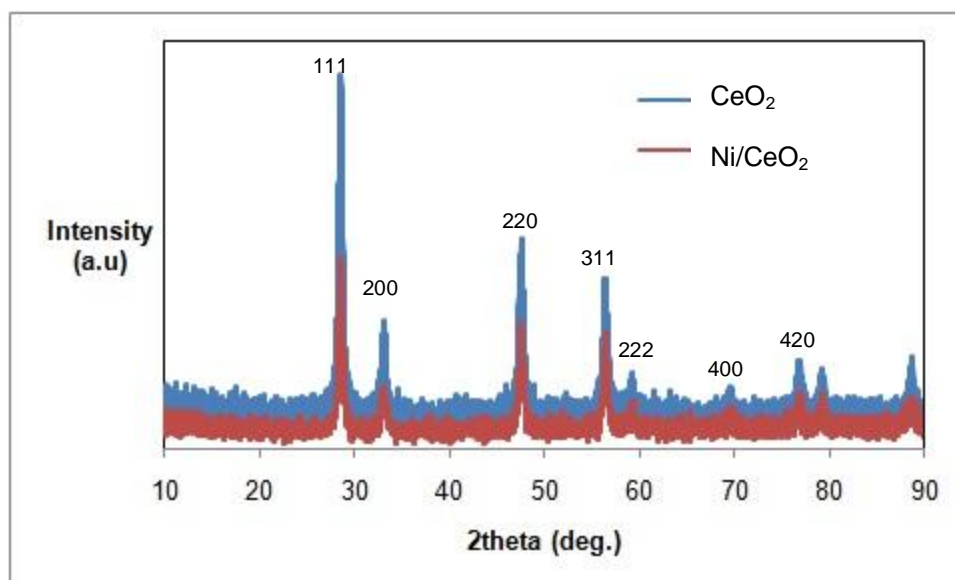


Figure 9.4.1. X-ray diffraction pattern of CeO₂ and Ni@CeO₂

Nitrogen adsorption-desorption isotherms of CeO_2 and Ni/CeO_2 are shown in Figure 9.4.2. typical isotherms for nonporous structures are seen in the figure.

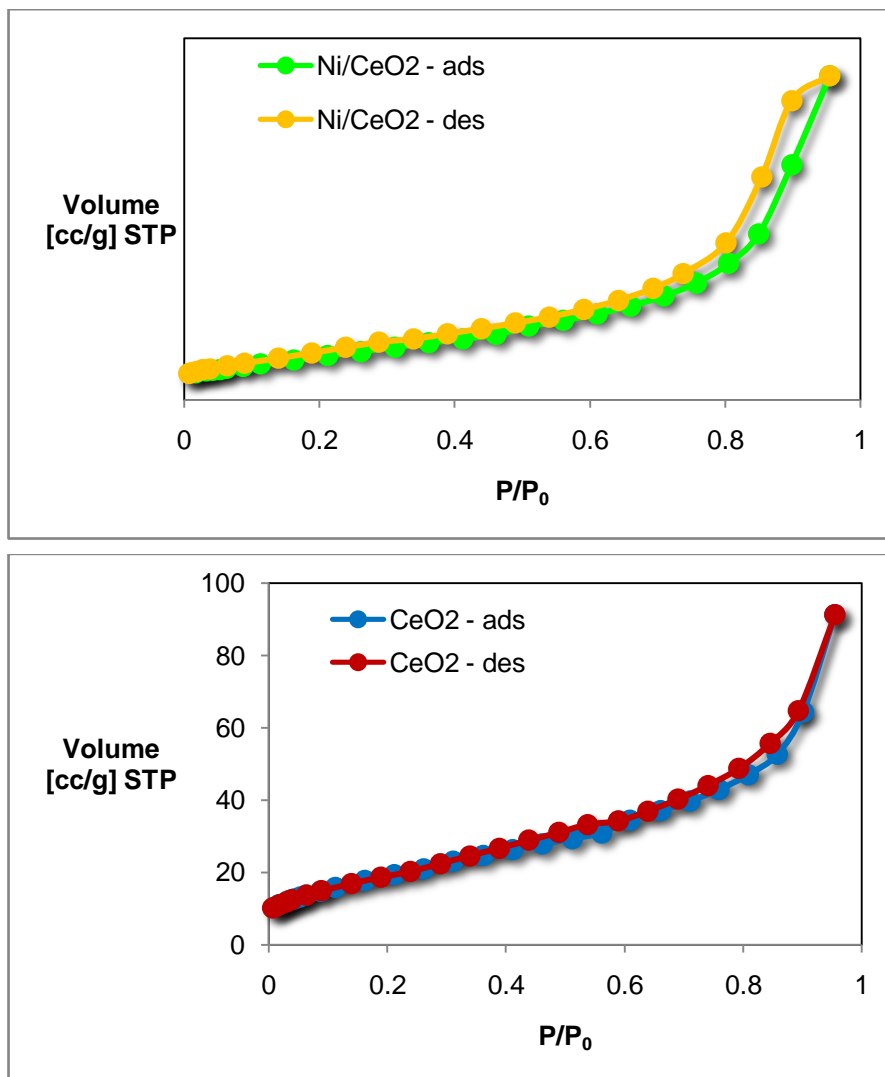


Figure 9.4.2. Nitrogen adsorption-desorption isotherms of commercial CeO_2 and as-synthesized Ni/CeO_2

After impregnation of Ni, surface area of the commercial CeO_2 decreased slightly. (Table 9.4.1)

Table 9.4.1 Surface area of CeO₂ and Ni/CeO₂

Sample	BET Surface Area (m ² /g)
CeO₂	71.6
Ni@CeO₂	54.4

SEM images of CeO₂ and Ni@CeO₂ are shown in Figure 8.4.3 and 8.4.4. Surface morphology of CeO₂ and Ni@CeO₂ are very similar. Agglomerated particles have a diameter of 2-3 nm, approximately.

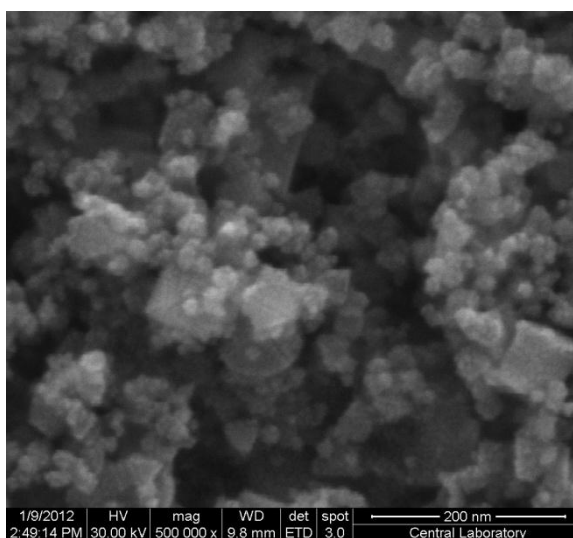


Figure 9.4.3. SEM image of reduced CeO₂

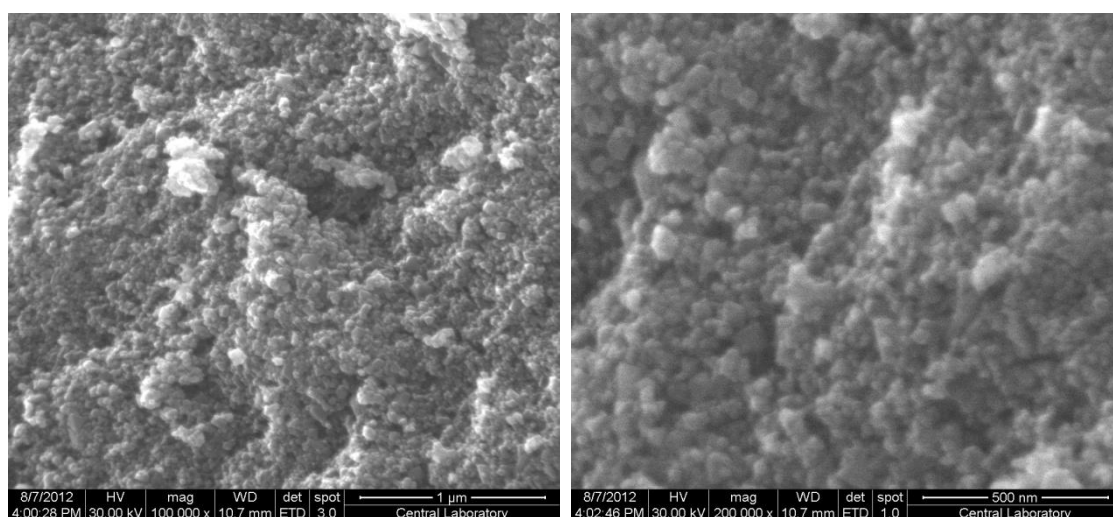


Figure 9.4.4. SEM images of reduced Ni/CeO₂

EDS analysis of Ni@CeO₂ gives Ni/Ce molar ratio as 0.1 which equals to the adjusted ratio in the synthesis.

9.4.1.2. Activity of Ni Impregnated CeO₂ Catalyst

Ni/CeO₂ catalyst was tested in steam reforming of ethanol reaction at 600 °C. Ethanol conversion and hydrogen yield of the catalyst are plotted as a function of time in Figure 9.4.4. Complete conversion was achieved at 600 °C. After reaching steady state, the catalyst shows quite high hydrogen yield. After 80 minutes of reaction, hydrogen yield decreased. This may be due to thermal sintering.

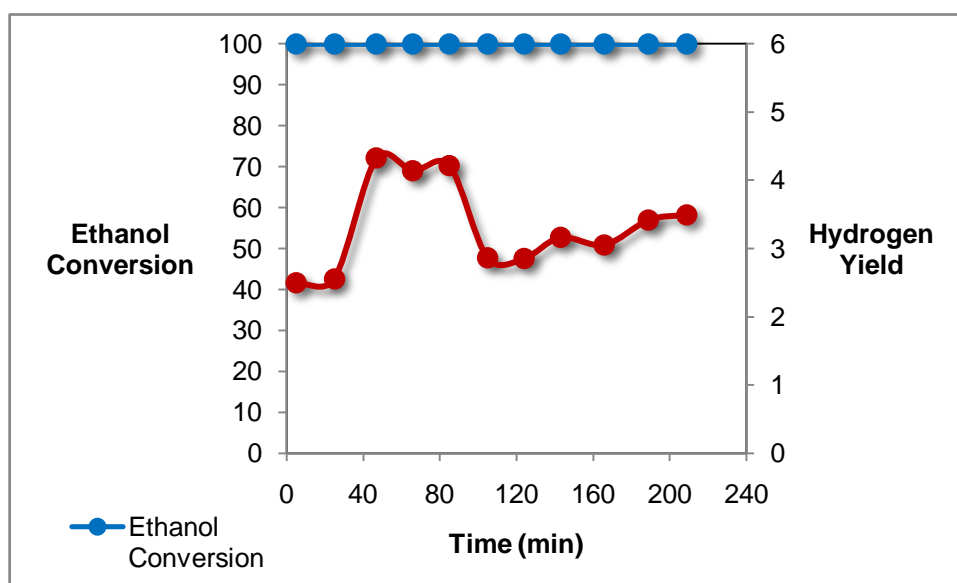


Figure 9.4.4.5. Ethanol conversion and hydrogen yield of NiCeO₂ at 600 °C

Composition of product steam is presented in Figure 9.4.6. In the first 80 minutes ethanol reforming reaction proceeds, accordingly CO₂ composition is high. After deactivation of the catalyst, CH₄ formation occurs, i.e. ethanol decomposes to CO and CH₄. Selectivities of the products also summarizes this behavior (Figure 9.4.7)

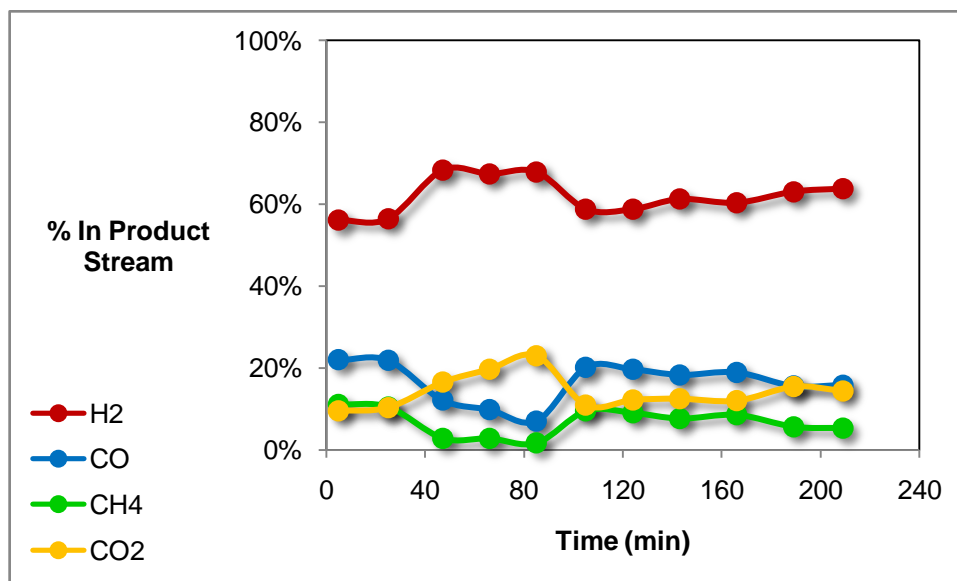


Figure 9.4.6. Composition of gas product stream yield of Ni/CeO₂ at 600 °C

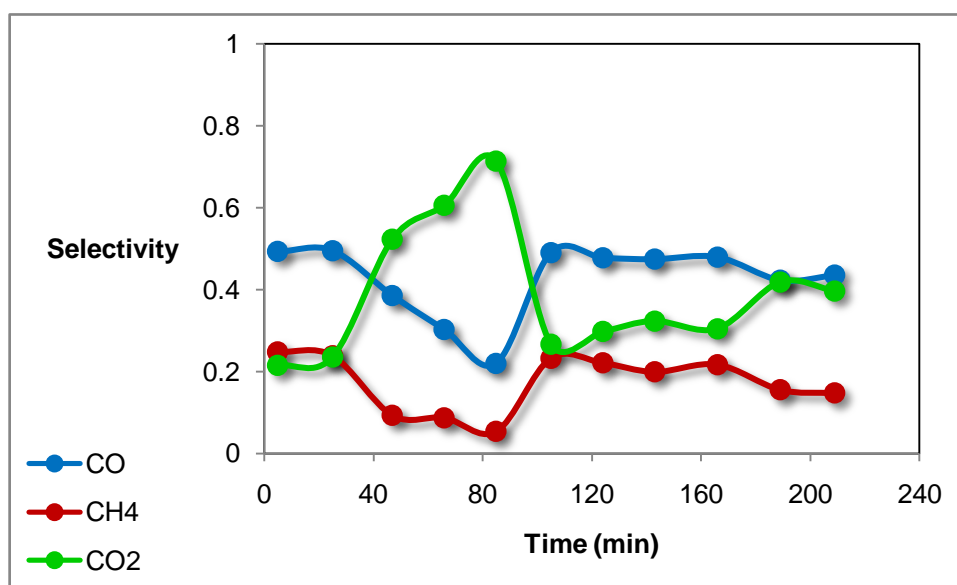


Figure 9.4.7. Selectivities of products with Ni/CeO₂ at 600 °C

9.4.3. Characterization of Ni/CeO₂ After Reaction

Since the volume of Ni/CeO₂ catalyst is small, reaction experiment was performed by mixing quartz particles in order to increase the length of the catalyst bed. Unfortunately, this procedure made the catalyst characterization difficult.

In Figure 9.4.8, SEM images indicate coke formation on the surface of the catalyst. Carbon filaments are seen clearly.

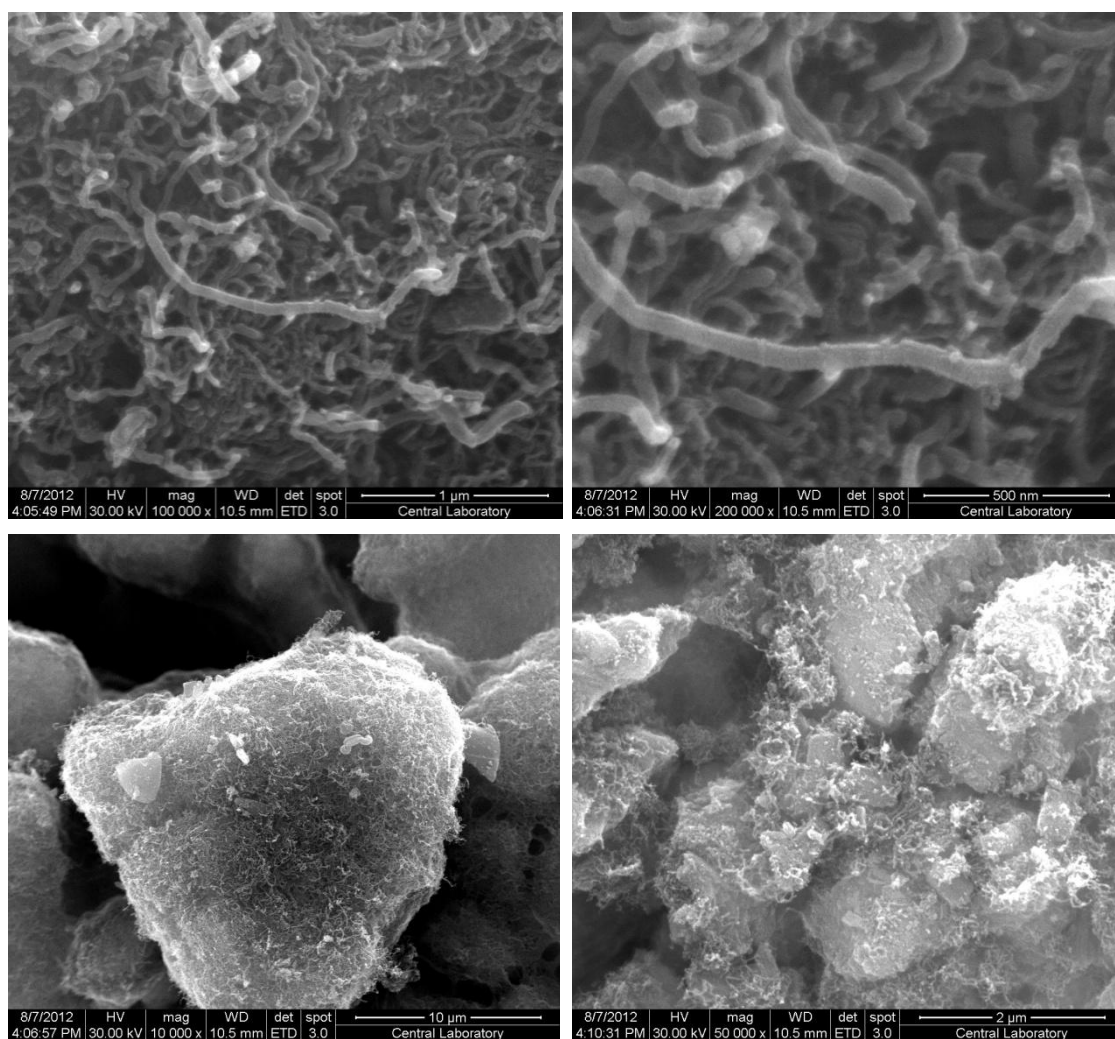


Figure 9.4.8. SEM images of Ni@CeO₂ after reaction at 600 °C

Thermal gravimetric analysis was performed and TGA and DTA curves are shown in Figure 9.4.9. By an approximate estimation, weight loss was found to be 11.4%.

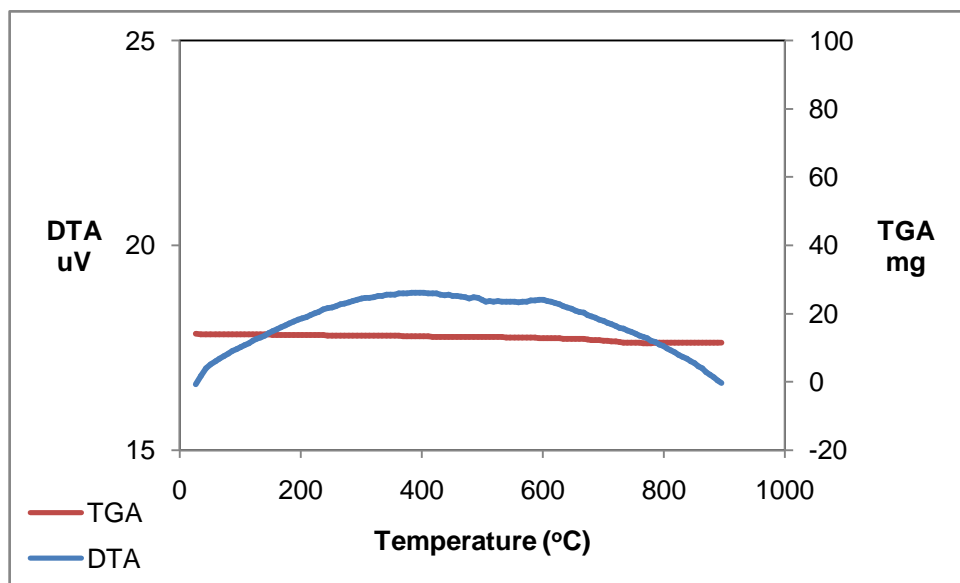


Figure 9.4.9. Thermal gravimetric analysis of Ni/CeO₂

CHAPTER 10

CONCLUSIONS

Ni@MCM-41, PdNi@MCM-41. Ni@SBA-15, NiCe@SBA-15, PdNiCe@SBA-15, Ni@AIMCM-41, NiCe@AIMCM-41 catalysts were synthesized successfully and tested in steam reforming of ethanol reaction. The catalysts were characterized before and after reaction and the concluded remarks are listed below:

- Synthesis of Ni@MCM-41 samples containing well dispersed nickel nanoparticles within the mesoporous MCM-41 matrix is achieved following a successive impregnation procedure. XRD analysis indicated some deformations in the characteristic MCM-41 structure after the impregnation procedure.
- Synthesis of bimetallic PdNi@MCM-41 samples containing well dispersed nickel and palladium nanoballs within the mesoporous MCM-41 matrix is achieved following two impregnation procedures, consecutively. XRD analysis indicated deformations in the characteristic MCM-41 structure after the impregnation procedure.
- Although some decrease of surface area and pore volume of MCM-41 was observed due to plugging of some of the mesopores by the nanoballs, the surface area values of about 600 m²/g obtained in the catalysts containing Ni/Si and Pd/Si values in the ranges of 0.10-0.16 and 0.006-0.008, respectively, were still quite high for catalytic applications. Besides the formation of Ni and Pd nanoballs of 5-25 nm size range, average pore diameter of the materials was decreased due to deposited metals. The decrease of the reduction temperature observed in the TPR experiments carried out with the bimetallic catalysts (as compared to catalysts containing only NiO_x) is concluded to be due to the reduction promoting effect of Pd. In the calcined materials nickel is in Ni⁺² and Ni⁺³ states and NiO_x crystals were formed after the calcination step. Well dispersion of Ni and Pd within the mesoporous matrix is highly attractive for catalytic applications, such as dry and steam reforming of methane and alcohols. These catalysts were shown to give good activity in steam reforming of ethanol. Pd incorporation into Ni-MCM-41 shifted the reforming reaction to lower

temperatures. However, product distributions indicated significant effect of catalyst composition of the significance of side reactions, like cracking, water gas shift reaction, dry reforming and coke formation. Pd incorporation increased the significance of cracking and methane formation. However, with the catalyst containing Ni/Si and Pd Si molar ratios of 0.134 and 0.008 (B6), respectively, increased activity of the catalyst for dry reforming of methane caused an increase in hydrogen yield at temperatures higher than 450°C.

- SBA-15 mesoporous silicate structure is synthesized successfully and impregnation of Ni, NiCe and PdNiCe to mesoporous SBA-15 is achieved. Ni impregnated SBA-15 catalyst is very stable in ethanol steam reforming reaction. For single metal incorporated (Ni impregnated) catalysts SBA-15 support found to be more stable support than MCM-41. Incorporation of Ceria with different loadings are also synthesized. Addition of Ce prevents coke formation very significantly, but does not increase the activity of the catalyst.,
- Ni and NiCe impregnated mesoporous AlMCM-41 supported catalysts were synthesized successfully. The most active catalysts are Ni and Ce impregnated AlMCM-41. Al sites in the silicate network give acidic properties to the support and Ce prevents coke formation. Impregnation technique have also a significant effect on the catalyst activity. Consecutive impregnation technique is better than sequential impregnation.
- Pure ceria supports are not successful due to the thermal sintering of Ce at high temperatures

REFERENCES

Aboudheir A., Akande A., Idem R.O., Dalai A., "Experimental studies and comprehensive reactor modelling of hydrogen production by the catalytic reforming of crude oil in a packed bed tubular reactor over a Ni/Al₂O₃ catalyst." *International Journal of Hydrogen Energy* 31, no. 6 (2006): 752-761.

Akande A.J., Idem R.O., Dalai A.K., "Synthesis, characterization and performance evaluation of Ni/Al₂O₃ catalysts for reforming of crude ethanol for hydrogen production." *Applied Catalysis A: General* 287, no. 2 (2005): 159-175.

Albertazzi S., Ganzeria R., Gobbi C., Lenarda M., Mandreoli M., Salatelli E., Savini P., Storaro L., Vaccari A. "Hydrogenation of naphthalene on noble-metal containing mesoporous MCM-41 aluminasilicates." *Journal of Molecular Catalysis A* 200 (2003): 261.

Arias A.M., Garcia M.F., Salamanca L.N., Valenzuela R.X. "Structural and redox properties of ceria in alumina-supported ceria catalyst supports." *J. Phys. Chem. B* 104 (2000): 4038.

Batista S.B., Santos R.K.S., Assaf E.M., Assaf J.M., Ticianelli E.A. "High efficiency steam reforming of ethanol by cobalt-based catalysts." *Journal of Power Sources* 134, no. 1 (2004): 27-32.

Beck J.S., Vartuli J.C., Roth W.J., Leonowicz M.E., Kresge C.T., Schmitt K.D., Chu C.T.W., Olson D.H., Sheppard E.W., McKullen S.B., Higgins J.B., Schlenker J.L., "A new family of mesoporous molecular sieves prepared with liquid crystal templates." *J. Am. Chem. Soc.* 114 (1992): 10834-10843.

Bumajdad A., Eastoe J., Mathew A., "Cerium oxide nanoparticles prepared in self-assembled systems." *Advances in Colloid and Interface Science* 147-148 (2009): 56-66.

Cavallaro S., Chiodo V., Freni S., Mondello N., Frusteri F. "Performance of Rh/Al₂O₃ catalyst in the steam reforming of ethanol: H₂ production for MC." *Applied Catalysis A* 249, no. 1 (2003): 119-128.

Cerovic L., Lair V., Lupan O., Cassir M., Ringuede A. "Electrochemical synthesis and characterization of nanorods, nano columnar ceria-based thin films on different glass substrates." *Chemical Physics Letters* 494, no. 4-6 (2010): 237-242.

Chane-Ching J.Y. European Patent Patent EP 208580. 1987.

Chane-Ching J.Y., Cobo F., Aubert D., Harvey H.G., Airiau M., Corma A., "General method for the synthesis of nanostructured large surface area materials through the self-assembly of functionalized nanoparticles." *Chem. Eur. J.* 11 (2005): 979.

Ciambelli P., Palma V., Ruggiero A., "Low temperature catalytic steam reforming of ethanol. 1. The effect of the support on the activity and stability of Pt catalyst." *Applied Catalysis B: Environmental* 96, no. 1-2 (2010): 18-27.

Ciesla U., Schuth F. "Review ordered mesoporous materials." *microporous and Mesoporous Materials* 27 (1999): 131-149.

Collart O. "Nanodesign of Aluminasilicate Framework in Mesoporous MCM-48 Architecture." *PhD Thesis*. University of Antwerpen, 2003.

Comas J., Marmo F., Laborde M., Amadeo N., "Bio-ethanol steam reforming on Ni/Al₂O₃ catalyst." *Chemical Engineering Journal* 98, no. 1-2 (2004): 61-68.

Damyanova S., Pawelec B., Arishtirova K., Fierro J.L.G., Sener C., Dogu T. "MCM-41 supported PdNi catalysts for dry reforming of methane." *Applied Catalysis B: Environmental* 92, no. 3-4 (2009): 250-261.

Demirbas, A. "Progress and recent trends in biofuels." *Progress in Energy and Combustion Science*, 2006.

Duan S., Senkan S. "Catalytic conversion of ethanol to hydrogen using combinatorial methods." *Ind. Eng. Chem. Res.* 44 (2005): 6381-6386.

Dumesic J.A., Rudd D.F., Aparicio L.M., Rekoske J.E., Trevino A.A. *The Microkinetics of Heterogeneous Catalysis*. American Chemical Society, 1993.

Erdohelyi A., Rasko J., Kecskes T., Toth M., Domok M., Baan K. "Hydrogen formation in ethanol reforming on supported noble metal catalysts." *Catalysis Today* 116 (2006): 367-376.

Fatsikostas A.N., Verykios X.E. "Reaction network of steam reforming of ethanol over Ni-based catalysts." *Journal of Catalysis* 225 (2004): 439.

Feio L.S.F., Hori C.E., Damyanova S., Noronha F.B., Cassinelli W.H., Marques C.M.P., Bueno J.M.C. "The effect of ceria content on the properties of Pd/CeO₂/ Al₂O₃ catalysts for steam reforming of methane." *Applied Catalysis A: General* 316 (2007): 107.

Ferreira A.P., Araujo J.C.S., Liberatori J.W.C., Damyanova S., Zanchet D., Noronha F.B., Bueno J.M.C. "Promoter effect of CeO₂ on the stability of supported Pt catalysts for methane-reforming as revealed by in-situ XANES and TEM analysis." *Natural Gas Conversion VIII* (2007): 433.

Firouzi D., Kumar D., Bull L.M., Besier T., Sieger P., Huo Q., Walker S.A., Zasadzinski J.A., Glinka C., Nicol J., Margolese D., Stucky G.D., Chmelka B.F. "Cooperative organization of inorganic-surfactant and biomimetic assemblies." *Science* 267 (1995): 1138.

Frusteri F., Freni S., Spadaro L., Chiodo V., Bonura G., Donato S., Cavallaro S. "H₂ production for MC fuel cell by steam reforming of ethanol over MgO supported Pd, Rh, Ni and Co catalysts." *Catalysis Communications* 5 (2004): 611-615.

Gao C. "Formation mechanism of anionic-surfactant-templated mesoporous silica (AMS)." *PhD Thesis*. Stockholm University, 2009.

Gheno S.M., Damyanova S., Riguetto B.A., Marques C.M.P., Leite C.A.P., Bueno J.M.C. "CO₂ reforming of CH₄ over Ru/zeolite catalysts modified with Ti." *Journal of Molecular Catalysis A: Chemical* 198 (2003): 263.

Gu F., Wang Z., Han D., Shi C., Guo G.,. "Reverse micelles directed synthesis of mesoporous ceria nanostructures." *Materials Science and Engineering B* 139, no. 1 (2007): 62-68.

Gucbilmez Y., Dogu T., Balci S. "Ethylene and acetaldehyde production by selective oxidation of ethanol using mesoporous V-MCM-41 catalysts." *Ind. Eng. Chem. Res.* 45 (2006): 3496-3502.

Gutierrez A., Karinen R., Airaksinen S., Kaila R., Krause A.O.I. "Autothermal reforming of ethanol on noble metal catalysts." *International Journal of Hydrogen Energy* 36 (2011): 8967-8977.

Halladay J.D., Hu J., King D.L., Wang Y. "An overview of hydrogen production technologies." *Catalysis Today* 139 (2009): 244-260.

Hirano M., Kato E., "Hydrothermal synthesis of cerium (IV) oxide." *J. Am. Ceram. Soc.* 79 (1996): 777.

Hsu W.P., Ronnqvist E., Matijevic E., "Preparation and properties of monodispersed colloidal particles of lanthanide compounds Cerium (IV)." *Langmuir* 4 (1988): 31.

Hsu Y-C., Hsu Y-T., Hsu H-Y., "Facile synthesis of mesoporous silica SBA-15 with additional into-particle porosities." *Chem. Mater.* 19, no. 5 (2007): 1120-1126.

Huo Q. "Synthetic Chemistry of the Inorganic Ordered Porous Materials." In *Modern Inorganic Synthetic Chemistry*, 339-373. Elsevier, 2011.

Huo Q.(***), Margolese D.I., Ciesla U., Feng P., Gler T.E., Sieger P., Leon R., Petroff P.M., Schuth F., Stucky G.D. "Generalized synthesis of periodic surfactant/inorganic composite materials." *Letters to Nature* 368 (1994): 317-321.

Association, Fuel Cell & Hydrogen Energy, ed. "Hydrogen Production Overview." *Hydrogen Production Overview_NEW.pdf*.
http://www.fchea.org/core/import/PDFs/factsheets/Hydrogen%20Production%20Overview_NEW.pdf (accessed June 2012).

Jacobs G., Keogh R.A., Davis B.H. "Steam reforming of ethanol over Pt/ceria with co-fed hydrogen." *Journal of Catalysis* 245 (2007): 326.

Jalowiecki-Duhamel L., Pirez C., Capron M., Dumeignil F., Payen E. "Hydrogen production from ethanol steam reforming over cerium and nickel based oxyhydrides." *International Journal of Hydrogen Energy* 35 (2010): 12741-12750.

Kosslick H., Monnich I., Paetzold E., Fuhrmann H., Fricke R., Muller D., Oehme G. "Suzuki reaction over palladium-complex loaded MCM-41 catalysts." *Microporous and Mesoporous Materials* 44 (2001): 537.

Kresge C.T., Leonowicz M.E., Roth W.J., Vartuli J.C., Beck J.S. "Ordered mesoporous molecular sieves synthesized by a liquid crystal template mechanism." *Nature* 359 (1992): 710.

Lattner J.R., Harold M.P. "Autothermal reforming of methanol: Experiments and modeling." *Catalysis Today* 120 (2007): 78.

Liang X., Wang X., Zhuang Y., Xu B., Kuang S.M., Li Y.D.,. "Formation of CeO₂-ZrO₂ solid solution nanocages with controllable structures via Kirkendall Effect." *J. Am. Chem. Soc.* 130 (2008): 2736.

Liberatori J.W.C., Ribeiro R.U., Zanchet D., Noronha F.B., Bueno J.M.C. "Steam reforming of ethanol on supported nickel catalysts." *Applied Catalysis A: General* 327 (2007): 197-204.
Liguras D.K., Kondarides D.I., Verykios X.E. "Production of hydrogen fuel cells by steam reforming of ethanol over supported noble metal catalysis." *Applied Catalysis B: Environmental* 43 (2003): 345-354.

Llorca J., Piscina P.R., Dalmon J.A., Sales J., Homs N.,. "CO-free hydrogen from steam reforming of bioethanol over ZnO-supported cobalt catalysts: effect of the metallic precursor." *Applied Catalysis B: Environmental* 43 (2003): 355-369.

Lundberg M., Skarman B., Cesar F., Wallenberg L.R.,. "Lundberg M., Skarman B., Cesar F., Wallenberg L.R." *Microporous and Mesoporous Materials* 54, no. 1-2 (2002): 97-103.

Luo J-X., Meng M., Yao J-S., Li X-G., Zha Y-Q., Wang X., Zhang T-Y.,. "One-step synthesis of nanostructured Pd-doped mixed oxides MO_x-CeO₂ (M=Mn, Fe,Co, Ni, Cu) for efficient CO and C₃H₈ total oxidation." *Applied Catalysis B: Environmental* 87, no. 1-2 (2009): 92-103.

Mamontov E., Egami T., Brezny R., Koranne M., Tyagi S.,. "Lattice defects and oxygen storage capacity of nanocrystalline ceria and zirconia." *J. Phys. Chem. B* 104 (2000): 1110-1116.

Matter P.H., Braden D.J., Ozkan U.S. "Steam reforming of methanol to H₂ over nonreduced Zr-containing CuO/ZnO catalysts." *Journal of Catalysis* 223 (2004): 463.

Matter P.H., Ozkan U.S. "Effect of pretreatment conditions on Cu/Zn/Zr-based catalysts for the steam reforming of methanol to H₂." *Journal of Catalysis* 234 (2005): 463.

Mbaraka J.K., Radu D.R., Lin V.S.Y., Shanks B.H. "Organosulfonic acid-functionalized mesoporous silicas for the esterification of fatty acids." *Journal of Catalysis* 219 (2003): 329-336.

Midilli A., Ay M., Dincer I., Rosen M.A. "On hydrogen and hydrogen energy strategies I: current status and needs." *Renewable and Sustainable Energy Reviews* 9 (2005): 255-271.

Monnier, Schuth F., Huo Q., Kumar D., Margolese D., Maxwell R.S., Stucky G.D., Krishnamurty M., Petroff P., Firouzi A., Janicke M., Chmelka B.F. "Cooperative formation of inorganic-organic interfaces in the synthesis of silicate mesostructures." *Science* 261 (1993): 1299.

Ni M., Leung D.Y.C., Leung M.K.H. "A review on reforming bio-ethanol for hydrogen production." *International Journal of Hydrogen Energy* 32 (2007): 3238-3247.

On D.T., Desplandier-Giscard D., Danumah C., Kaliaguine S. "Perspectives in catalytic applications of mesostructured materials." *Applied Catalysis A: General* 222 (2001): 299-357.

Otsuka-Yao-Matsuo S., Morikawa H., Izu N., Okuda K. "Photodegradation of methylene blue aqueous solution sensitized by pyrochlore-related k-CeZrO₄ oxide powder." *J. Japan Inst. Metals* 59 (1995): 1237.

Oye G., Sjoblom J., Stocker M. "Synthesis, characterization and potential applications of new materials in the mesoporous range." *Advances in Colloid and Interface Science* 89-90 (2001): 439-466.

Panwar N.L., Kaushik S.C., Kothari S. "Role of renewable energy sources in environmental protection: A review." *Renewable and Sustainable Energy Reviews* 15 (2011): 1513-1524.

Parizotto N.V., Rocha K.O., Damyanova S., Passos F.B., Zanchet D., Marques C.M.P., Bueno J.M.C. "Alumina-supported Ni catalysts modified with silver for the steam reforming of methane: Affect of Ag on the control of coke formation." *Applied Catalysis A: General* 12 (2007): 330.

Pawelec B., Damyanova S., Arishtirova K., Fiero J.L.G., Petrov L. "Structural and surface features of PtNi catalysts for reforming of methane with CO₂." *Applied Catalysis A: General* 323 (2007): 139.

Pengpanich S., Meeyoo V., Rirksomboon J., Bunyakiat K., "Catalytic oxidation of methane over CeO₂-ZrO₂ mixed oxide solid solution catalysts prepared via urea hydrolysis." *Applied Catalysis A: General* 234, no. 1-2 (2002): 221-233.

Pierre R. Roberge, PhD. *Corrosion Doctors*. 2012. www.corrosion-doctors.org (accessed June 2012).

Pompeo F., Nichio N.N., Gonzales M.G., Montes M. "Characterization of Ni/SiO₂ and Ni/Li-SiO₂ catalysts for methane dry reforming." *Catalysis Today* 107-108 (2005): 856.

Portugal U.L., Santos A.C.S.F., Damyanova S., Marques C.M.P., Bueno J.M.C. "CO₂ reforming of CH₄ over Rh-containing catalysts." *Journal of Molecular Catalysis A: Chemical* 184 (2002): 311.

Profeti L.P.R., Ticianelli E.A., Assaf E.A., "Production of hydrogen via steam reforming of biofuels on Ni/CeO₂-Al₂O₃ catalysts promoted by noble metals." *International Journal of Hydrogen Energy* 34 (2009): 5049-5060.

Puertolas B., Solsona B., Agouram S., Murillo R., Mastral A.M., Aranda A., Taylor S.H., Garcia T., "The catalytic performance of mesoporous cerium oxides prepared through a nanocasting route for the total oxidation of naphthalene." *Applied Catalysis B: Environmental* 93, no. 3-4 (2010): 395-405.

Rao G.R., Meher S.K., Mishra B.G., Charan P.H.K., "Surface and catalytic properties of Cu-Ce-O composite oxides prepared by combustion method." *Colloids and Surfaces A: Physicochemical and Engineering Aspects* 220 (2003): 1-3.

Sandler S.I. *Chemical and Engineering Thermodynamics*. New York: Wiley, 1999.

Sayari A. "Periodic mesoporous materials: synthesis, characterization and potential applications." *Studies in Surface Science and Catalysis* 102, no. 1-46 (1996).

Sener C.(*), Dogu T., Dogu G., "Effects of synthesis conditions on the structure of Pd incorporated MCM-41 type mesoporous nanocomposite catalytic materials with high Pd/Si ratios." *Microporous Mesoporous Materials* 94 (2006): 89-98.

Sener C., Arishtirova K., Nikolov R.N., Dogu T., Dogu G., Damyanova S. "MCM-41 supported Ni catalysts for dry reforming of methane." *Advanced Micro- and Mesoporous Materials* (Heron Press), 2008: 355-362.

Sener, C. *Synthesis and characterization of Pd-MCM-41 type mesoporous nanocomposite materials*. MSc Thesis-Middle East Technical University, 2006.

Sheng P.Y., Chiu W.W., Yee A., Morrison S.J., Idriss H. "Hydrogen production from ethanol over bimetallic Rh-M/CeO₂ (M=Pt or Pd)." *Catalysis Today* 129 (2007): 313-321.

Song H.(*), Ozkan U.S., "Ethanol steam reforming over Co-based catalysts: Role of oxygen mobility." *Journal of Catalysis* 261 (2009): 66-74.

Steinberg M., Cheng H.C., "Modern and prospective technologies for hydrogen production from fossil fuels." *International Journal of Hydrogen Energy* 14, no. 11 (1989): 797-820.

Sun J., Wang Y., Li J., Xiao G., Zhang L., Li H., Cheng Y., Sun C., Cheng Z., Dong Z., "H₂ production from stable ethanoil steam reforming over catalyst of NiO based on flower like CeO₂ microspheres." *International Journal of Hydrogen Energy* 35, no. 7 (2010): 3087-3091.

Taguchi, Schuth F. "Ordered mesoporous materials in catalysis." *Microporous and Meseoporous Materials* 77 (2005): 1.

Takahashi R., Sato S., Sodeawa T., Tomiyama S. "CO₂-reforming of methane over Ni/SiO₂ catalyst prepared by homogeneous precipitation in sol-gel-derived silica gel." *Applied Catalysis A: General* 286 (2005): 146.

Terribile D., Trovarelli A., Llorca J., Leitenburg C., Dolcetti G., "The preparation of high durface area CeO₂-ZrO₂ mixed oxides by a surfactant-assisted approach." *Catalysis Today* 43, no. 1-2 (1998): 79-88.

Tosti S., Basile A., Borgognoni F., Capaldo V., Cordiner S., Di Cave S., Gallucci F., Rizzello C., Santucci A., Traversa E., "Low-temperature ethanol steam reforming in a Pd-Ag membrane reactor. Part 1. Ru-based catalyst." *Journal of Membrane Science* 308 (2008): 250.

Wieslaw J., Roth W.J., Vartuli J.C., "Synthesis of mesoporous molecular sieves." *Studies in Surface Science and Catalysis* 157 (2005): 91-110.

Wiingaarden R.J., Kronberg A., Westerterp K.R. *Industrial Catalysis Optimizing Catalysts and Processes*. Wiley-vch, 1998.

Xu J. "Spectroscopic studies of synthesis, modification and characterization of novel mesoporous molecular sieves." *PhD Thesis*. University of Houston, 1999.

Ying F., Wang S., Au C-T., Lai S-Y., "Highly active and stable mesoporous Au/CeO₂ catalysts prepared from MCM-48 hard-template." *Microporous and Mesoporos Materials* 142, no. 1 (2011): 308-315.

Yuan Q., Duan H.H., Li L.L., Sun L.D., Zhang Y.W., Yan C.H. "Controlled synthesis and assembly of ceria-based nanomaterials." *Journal of Colloid and Interface Science* 335 (2009): 151-167.

Zhang F., Chan S.W., Spanier J.E., Apak E., Jin Q., Robinson R.D., Herman I.P. "Cerium oxide nanoparticles: Size-selective formation and structure analysis." *Applied Physics Letters* 80, no. 1 (2002): 127-129.

Zhao D., Yang P., Huo Q., Chmelka B.F., Stucky G.D. "Topological construction of mesoporous materials." *Current Opinion in Solid State & Materials Science* 3 (1998): 111-121.

APPENDICES

A.1. SUMMARY OF THE CATALYSTS

No	Catalyst ID	Synthesis Procedure	Comments
1	MCM-41	Hydrothermal Synthesis	Mesoporous silica
2	B1	Impregnation	Ni/Si=0.10, Pd/Si=0
3	B2	Impregnation	Ni/Si=0.18, Pd/Si=0
4	B3	Impregnation	Ni/Si=0.12, Pd/Si=0
5	B4	Impregnation	Ni/Si=0.10, Pd/Si=0.010
6	B5	Impregnation	Ni/Si=0.18, Pd/Si=0.004
7	B6	Impregnation	Ni/Si=0.10, Pd/Si=0.002
8	SBA-15-C	Hydrothermal Synthesis	Mesoporous silica Surfactant removed by calcination
9	SBA-15-E	Hydrothermal Synthesis	Mesoporous silica Surfactant removed by extraction
10	Ni@SBA-15	Impregnation	Ni/Si=0.10
11	NiCe(0.10)@SBA-15	Impregnation	Ni/Si=0.10, Ce/Si=0.10
12	NiCe(0.50)@SBA-15	Impregnation	Ni/Si=0.10, Ce/Si=0.50
13	PdNiCe(0.50)@SBA-15	Impregnation	Ni/Si=0.10, Ce/Si=0.50, Pd1wt.%
14	AlMCM-41	Commercial	Mesoporous aluminasilicate 3% Al
15	Ni@AlMCM-41	Impregnation	Ni/Si=0.10, Ce/Si=0.10
16	NiCe(0.10)@AlMCM-41	Impregnation	Ni/Si=0.10, Ce/Si=0.10
17	NiCe(0.50)@AlMCM-41	Impregnation	Ni/Si=0.10, Ce/Si=0.10
18	Ni@[Ce@AlMCM-41]	Impregnation	Ni/Si=0.10, Ce/Si=0.10
19	Ce@AlMCM-41	Impregnation	Ce/Si=0.10
20	CeO ₂	Commercial	Commercial ceria
21	Ni/CeO ₂	Impregnation	Ni/Ce=0.10

A.2. CALIBRATION OF GAS CHROMATOGRAPHY

The outlet stream emerging from the reactor is analyzed by an online gas chromatography. Gas chromatography was calibrated with respect to ethanol and calibration factor for ethanol, as a result, is one. For the species A, calibration factor is calculated by using the formula below:

$$\frac{X_A}{X_{C_2H_5OH}} = \frac{\text{Peak area of A} \times \beta_A}{\text{Peak area of } C_2H_5OH \times \beta_{C_2H_5OH}}$$

Retention times and calibration factors of the gas chromatography are given in Table A.2.1.

Table A.2.1. Calibration parameters of reaction gases

Gas	Retention Time	Calibration Factor
H ₂	0.98	0.35
CO	1.20	4.40
CH ₄	1.66	0.92
CO ₂	3.78	3.30
C ₂ H ₂	5.30	1.23
CH ₂ O	8.40	3.80
C ₂ H ₄ O	10.80	1.68
C ₂ H ₅ OH	12.80	1

A.3. SAMPLE CALCULATION

The data for 80. minute of Ni@(Ce@AIMCM-41) at 600 °C is used for the sample calculation. Raw data of this run is presented in Table A.3.1.

Table A.3.1. Raw data for 80. minute of Ni@(Ce@AIMCM-41) at 600 °C

Component	Peak Area
H ₂	39269.3
CO	300.3
CH ₄	662.8
CO ₂	1020

From the gas chromatography analysis, several peaks corresponding to different chemicals are obtained and each peak area is to be multiplied with their calibration factors as in equation A.3.1. Calculated numbers represent the mole numbers respective to ethanol.

$$n_{H_2} = \beta_{H_2} \times A_{H_2} \quad (\text{eqn. A.3.1})$$

Hand calculations for the mole numbers respective to ethanol are shown below.

$$n_{H_2} = \beta_{H_2} \times A_{H_2} = 0.35 \times 39269.3 = 13744.3$$

$$n_{CO} = \beta_{CO} \times A_{CO} = 4.4 \times 300.3 = 1321.3$$

$$n_{CH_4} = \beta_{CH_4} \times A_{CH_4} = 0.92 \times 662.8 = 609.8$$

$$n_{CO_2} = \beta_{CO_2} \times A_{CO_2} = 3.3 \times 1020 = 3366$$

Total mole number of inlet stream is calculated by the carbon balance of outlet stream flow as in equation 2 and hand calculations are given below.

$$n_0 = n_{C_2H_5OH} + 0.5 n_{CO_2} + 0.5 n_{CO} + 0.5 n_{CH_4} + n_{C_2H_4} + n_{C_2H_4O} \quad (\text{eqn. A.3.2})$$

$$n_0 = 0 + 0.5 \times 3366 + 0.5 \times 1321.3 + 0.5 \times 609.8 + 0 + 0 = 2648.4$$

To find the ethanol conversion, converted amount of ethanol is divided into the total carbon inlet stream and hydrogen yield is calculated by dividing mole numbers of hydrogen to mole numbers of inlet stream.

$$\text{Ethanol Conversion} = \frac{n_{\text{converted}}}{n_0} \times 100 = \frac{n_0 - n_{C_2H_5OH}}{n_0} \times 100 = \frac{2648.4 - 0}{2648.4} \times 100 = 100 \%$$

$$\text{Hydrogen Yield} = \frac{n_{H_2}}{n_0} = \frac{13744.3}{2648.4} = 5.19$$

The outlet stream product composition can be calculated by dividing the mole number of any component to total number of all components.

$$\% H_2 = \frac{n_{H_2}}{n_{\text{total}}}$$

Where $n_{\text{total}} = n_{H_2} + n_{C_2H_5OH} + n_{CO_2} + n_{CO} + n_{CH_4} + n_{C_2H_4} + n_{C_2H_4O}$

Hand calculations for composition calculations are shown below.

$$n_{\text{total}} = n_{H_2} + n_{C_2H_5OH} + n_{CO_2} + n_{CO} + n_{CH_4} + n_{C_2H_4} + n_{C_2H_4O}$$

$$= 13744.3 + 3366 + 1321.3 + 609.8 = 19041.4$$

$$\% H_2 = \frac{n_{H_2}}{n_{\text{total}}} = \frac{13744.3}{19041.4} = 72.2$$

Product selectivities are defined as the ratio of moles of product to total moles of ethanol converted to the products. According to this definition, CO methane and ethylene selectivities were expressed as;

$$S_{CO} = \frac{1}{2} \times \frac{n_{CO}}{n_0 - n_{C_2H_5OH}}$$

$$S_{CH_4} = \frac{1}{2} \times \frac{n_{CH_4}}{n_0 - n_{C_2H_5OH}}$$

$$S_{C_2H_4} = \frac{1}{2} \times \frac{n_{C_2H_4}}{n_0 - n_{C_2H_5OH}}$$

Hand calculations for selectivity calculations are shown below.

$$S_{\text{CO}} = \frac{1}{2} \times \frac{n_{\text{CO}}}{n_0 - n_{\text{C}_2\text{H}_5\text{OH}}} = \frac{1}{2} \times \frac{1321.3}{2648.4 - 0} = 0.25$$

$$S_{\text{CH}_4} = \frac{1}{2} \times \frac{n_{\text{CH}_4}}{n_0 - n_{\text{C}_2\text{H}_5\text{OH}}} = \frac{1}{2} \times \frac{609.8}{2648.4 - 0} = 0.15$$

$$S_{\text{C}_2\text{H}_4} = \frac{n_{\text{C}_2\text{H}_4}}{n_0 - n_{\text{C}_2\text{H}_5\text{OH}}} = \frac{0}{2648.4 - 0} = 0$$

$$S_{\text{CO}_2} = \frac{1}{2} \times \frac{n_{\text{CO}_2}}{n_0 - n_{\text{C}_2\text{H}_5\text{OH}}} = \frac{1}{2} \times \frac{3366}{2648.4 - 0} = 0.64$$

A.3. SELECTION OF FLOWRATE

Steam reforming of ethanol reaction was performed by increasing total flowrate to 100 ml/min for B5. Ethanol conversion of B5 catalyst .

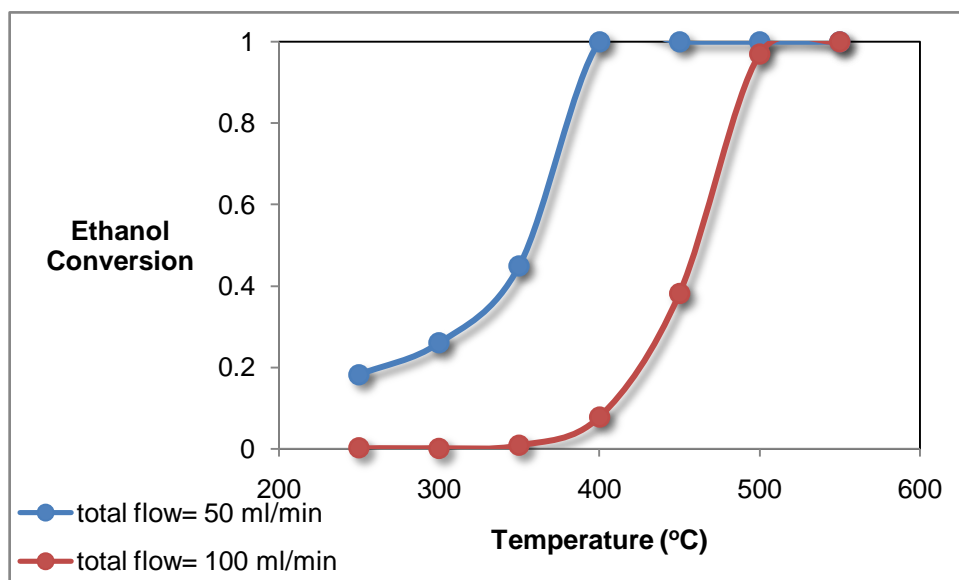


Figure A.3.1. Ethanol conversion versus temperature for different space times for B5 catalyst

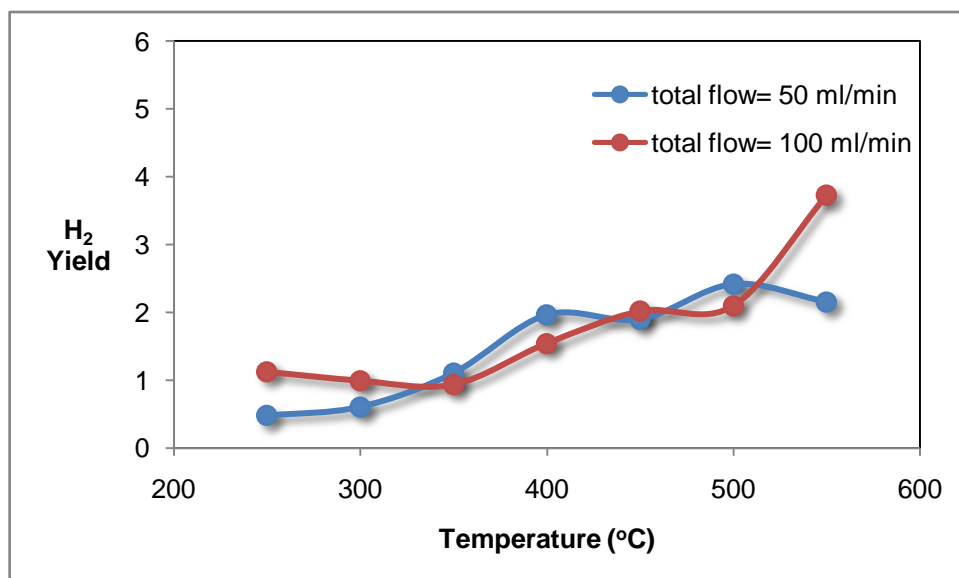


Figure A.3.2. Hydrogen yield versus temperature for different space times for B5 catalyst

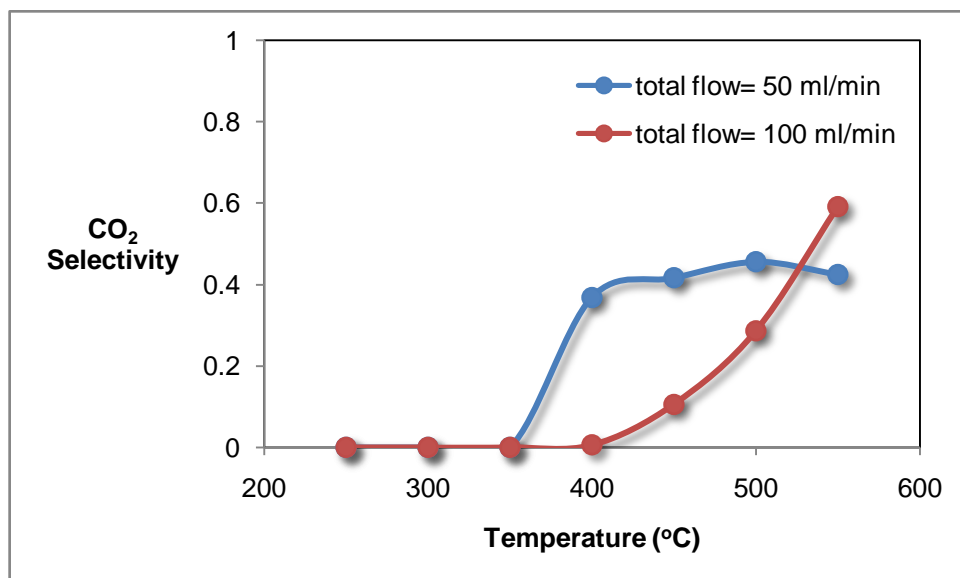


Figure A.3.3. Carbon dioxide selectivity versus temperature for different space times for B5 catalyst

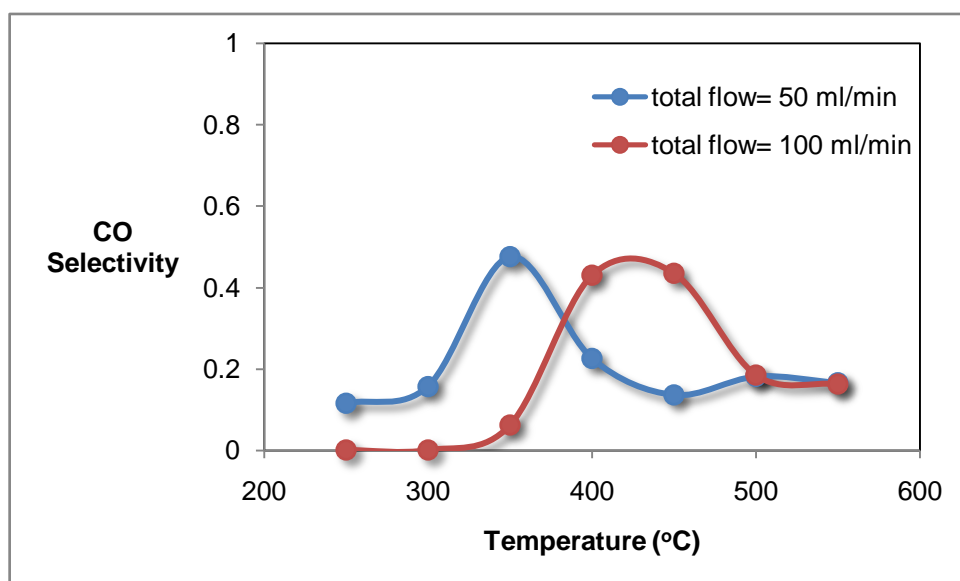


Figure A.3.4. Carbon monoxide selectivity versus temperature for different space times for B5 catalyst

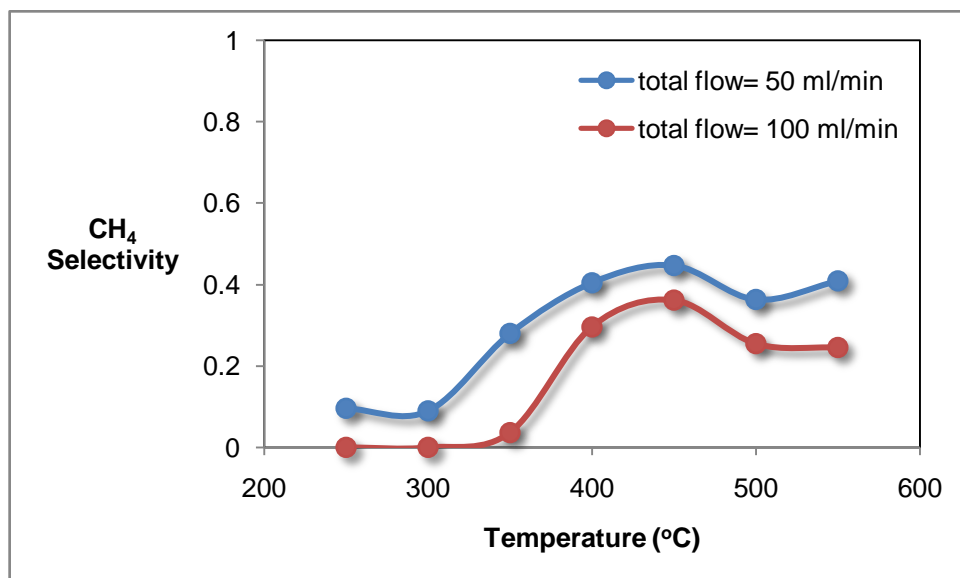


Figure A.3.5. Methane selectivity versus temperature for different space times for B5 catalyst

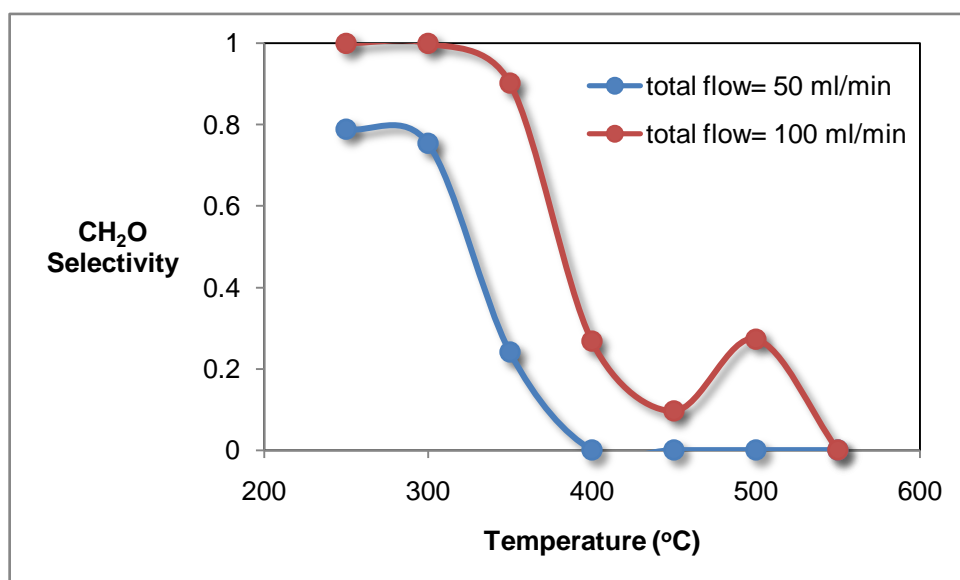


Figure A.3.6. Formaldehyde selectivity versus temperature for different space times for B5 catalyst

A.4. ACTIVITY OF Ni@MCM-41 AND PdNi@MCM-41 CATALYSTS IN DRY REFORMING OF METHANE REACTION

A.4.1. EXPERIMENTAL

Dry reforming of methane test reactions were performed in Bulgarian Academy of Sciences, Institute of Catalysis, Sofia.

The catalytic experiments in the reaction of reforming of CH₄ with CO₂ were conducted at atmospheric pressure in a fixed-bed continuous flow reactor consisting of a quartz tube with an inner diameter of 6 mm and a length of 300 mm. The tube was placed in a vertical tube furnace. The amount of the catalyst used during the catalytic runs was 0.05 g. The catalyst sample with particle diameter in the range from 0.2 to 0.25 mm was diluted with quartz (0.2-0.3 mm) and was packed in the reaction tube. Prior to each catalytic measurement the catalyst was reduced *in situ* in a flow of 10% H₂/N₂ (total flow rate 50 ml/min). The temperature was increased to 773 K for 1 h and kept at this temperature for 1 h. The catalyst was purged with flowing nitrogen (60 ml/min) for 40 min to remove adsorbed hydrogen from the surface. A reactant gas mixture of CH₄ (20%) and CO₂ (20%) diluted with N₂ has been used. The total flow rate was always kept at 100 ml/min. The reaction products were analyzed in a gas chromatograph (Varian 3700) equipped with a 3 m active carbon column (Carlo Erba) and a TCD (P. B. Damyanova S. 2009).

A.4.2. RESULTS

Incorporation of palladium, increased the stability and activity of the Ni@MCM-41 catalysts. Methane conversion of Ni@MCM-41 and PdNi@MCM-41 catalysts are presented in Figures A.4.1 and A.4.3.

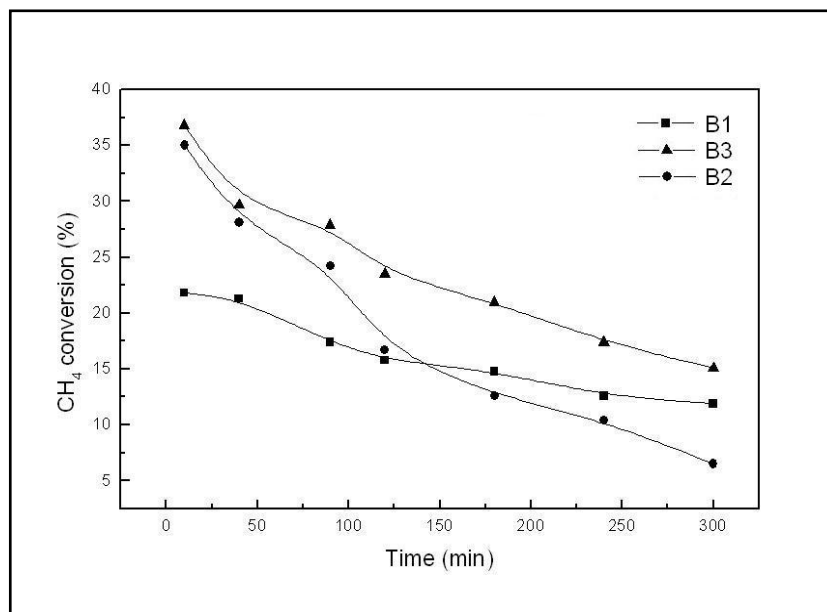


Figure A.4.1. Methane conversion of Ni@MCM-41 samples

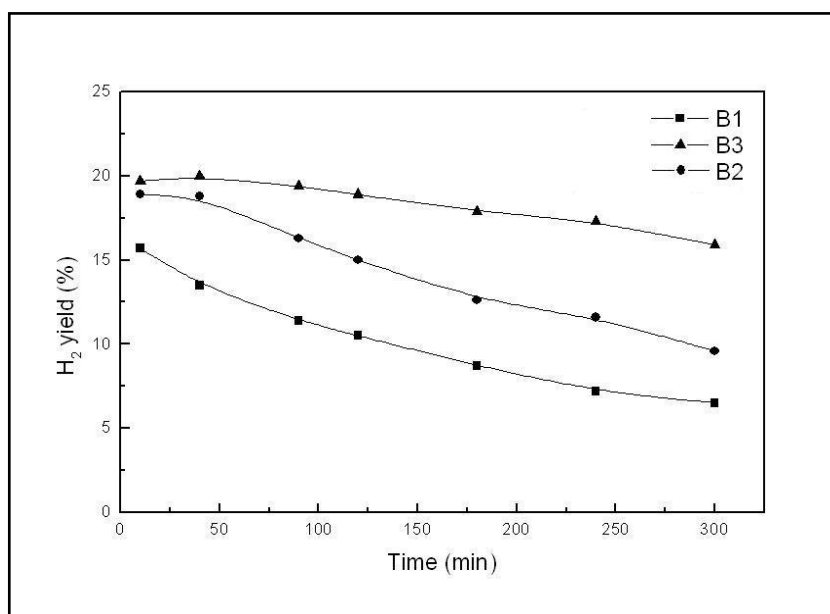


Figure A.4.2. Hydrogen yield of Ni@MCM-41 samples

Figures A.4.2 and A.4.4 show hydrogen yield versus time plots of Ni@MCM-41 and PdNi@MCM-41 catalysts.

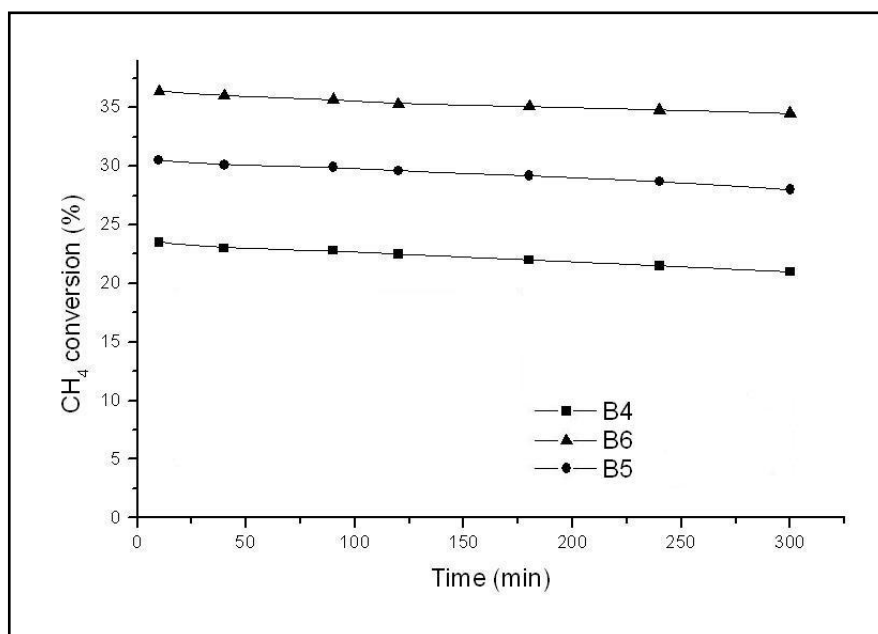


Figure A.4.3. Methane conversion of PdNi@MCM-41 samples

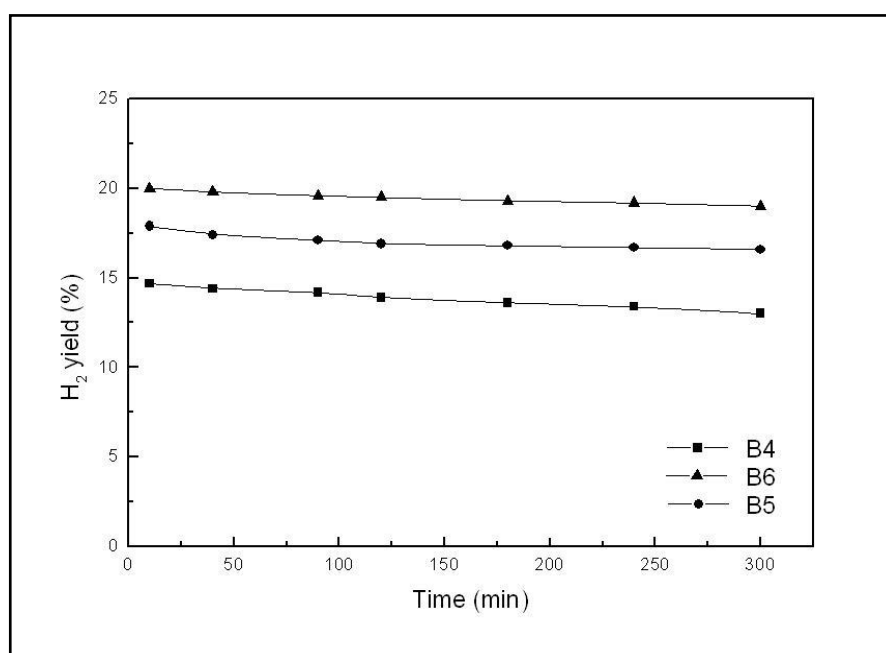


Figure A.4.4. Hydrogen yield of PdNi@MCM-41 samples

A.5. REACTION PARAMETERS OF THE CATALYSTS TESTED IN STEAM REFORMING OF ETHANOL REACTION

Table A.5.1. Reaction parameters of B1

Temperature (°C)	X _{C₂H₅OH}	S _{CO}	S _{CH₄}	S _{CO₂}	S _{C₂H₄}	S _{CH₂O}	S _{C₂H₄O}	Y _{H₂}
250	0.001	0	0	0	0	0	1	1.251
300	0.161	0.058	0.044	0	0	0	0.899	0.654
350	0.076	0.189	0.095	0	0	0	0.716	0.899
400	0.567	0.404	0.235	0.096	0	0	0.240	1.426
450	1	0.203	0.334	0.463	0	0	0	2.893
500	1	0.287	0.244	0.470	0	0	0	3.196
550	1	0.633	0.050	0.318	0	0	0	3.090

Table A.5.2. Reaction Parameters of B2

Temperature (°C)	X _{C₂H₅OH}	S _{CO}	S _{CH₄}	S _{CO₂}	S _{C₂H₄}	S _{CH₂O}	S _{C₂H₄O}	Y _{H₂}
250	0.003	0	0	0	0	0	1	1.363
300	0.006	0.007	0.004	0	0	0	0.989	0.964
350	0.059	0.160	0.120	0.044	0	0	0.647	1.343
400	1	0.222	0.442	0.336	0	0	0	2.313
450	1	0.047	0.544	0.409	0	0	0	1.957
500	1	0.096	0.380	0.524	0	0	0	3.498
550	1	0.447	0.109	0.445	0	0	0	4.556

Table A.5.3. Reactin parameters of B3

Temperature (°C)	X _{C₂H₅OH}	S _{CO}	S _{CH₄}	S _{CO₂}	S _{C₂H₄}	S _{CH₂O}	S _{C₂H₄O}	Y _{H₂}
250	0.002	0	0	0	0	0	1	0.397
300	0.058	0	0	0	0	0	1	0.197
350	0.039	0.007	0.007	0.025	0	0	0.943	0.311
400	0.956	0.237	0.444	0.320	0	0	0	2.359
450	1	0.034	0.554	0.412	0	0	0	1.746
500	1	0.028	0.549	0.423	0	0	0	1.741
550	1	0.027	0.527	0.446	0	0	0	1.890

Table A.5.4. Reaction parameters of B4

Temperature (°C)	$X_{C_2H_5OH}$	S_{CO}	S_{CH_4}	S_{CO_2}	$S_{C_2H_4}$	S_{CH_2O}	$S_{C_2H_4O}$	Y_{H_2}
250	0.123	0.220	0.206	0	0	0	0.574	1.207
300	0.165	0.109	0.093	0	0	0	0.799	0.564
350	0.681	0.476	0.371	0.020	0	0	0.133	1.290
400	1	0.148	0.456	0.397	0	0	0	2.101
450	1	0.069	0.555	0.377	0	0	0	1.698
500	1	0.020	0.480	0.500	0	0	0	2.388
550	1	0.046	0.470	0.485	0	0	0	2.443

Table A.5.5. Reaction parameters of B5

Temperature (°C)	$X_{C_2H_5OH}$	S_{CO}	S_{CH_4}	S_{CO_2}	$S_{C_2H_4}$	S_{CH_2O}	$S_{C_2H_4O}$	Y_{H_2}
250	0.182	0.115	0.096	0	0	0	0.789	0.481
300	0.260	0.157	0.090	0	0	0	0.754	0.610
350	0.450	0.476	0.280	0	0.004	0	0.240	1.108
400	1	0.226	0.405	0.369	0	0	0	1.967
450	1	0.136	0.448	0.417	0	0	0	1.901
500	1	0.181	0.363	0.456	0	0	0	2.420
550	1	0.165	0.409	0.425	0	0	0	2.159

Table A.5.6. Reaction parameters of B6

Temperature (°C)	$X_{C_2H_5OH}$	S_{CO}	S_{CH_4}	S_{CO_2}	$S_{C_2H_4}$	S_{CH_2O}	$S_{C_2H_4O}$	Y_{H_2}
250	0.010	0.047	0.046	0	0	0	0.908	0.898
300	0.026	0.106	0.084	0	0	0	0.811	0.973
350	0.103	0.326	0.245	0	0	0	0.429	1.238
400	0.836	0.499	0.426	0.075	0	0	0	1.755
450	1	0.044	0.449	0.508	0	0	0	2.625
500	1	0.107	0.389	0.504	0	0	0	3.039
550	1	0.343	0.242	0.415	0	0	0	3.063

Table A.5.7. Reaction parameters of Ni@SBA-15 at 600 °C

Time (min)	X _{C₂H₅OH}	S _{CO}	S _{CH₄}	S _{CO₂}	S _{C₂H₄}	S _{CH₂O}	S _{C₂H₄O}	Y _{H₂}
0	1	0.295	0.136	0.569	0	0	0	4.358
21	1	0.443	0.211	0.346	0	0	0	4.163
41	1	0.312	0.208	0.480	0	0	0	3.830
60	1	0.412	0.242	0.346	0	0	0	3.625
141	1	0.416	0.200	0.384	0	0	0	3.697
166	1	0.428	0.222	0.349	0	0	0	3.556
187	1	0.231	0.071	0.699	0	0	0	3.866
209	1	0.316	0.099	0.584	0	0	0	4.044

Table A.5.8. Gas stream product composition of Ni@SBA-15 at 600 °C

Time (min)	%H ₂	%CO	%CH ₄	%CO ₂	%C ₂ H ₄	%CH ₂ O	%C ₂ H ₄ O
0	68.5	9.3	4.3	17.9	0	0	0
21	67.5	14.4	6.8	11.2	0	0	0
41	65.7	10.7	7.1	16.5	0	0	0
60	64.4	14.7	8.6	12.3	0	0	0
141	64.9	14.6	7.0	13.5	0	0	0
166	64.0	15.4	8.0	12.6	0	0	0
187	65.9	7.9	2.4	23.8	0	0	0
209	66.9	10.5	3.3	19.3	0	0	0

Table A.5.9. Reaction parameters of NiCe(0.10)@SBA-15 at 600 °C

Time (min)	X _{C₂H₅OH}	S _{CO}	S _{CH₄}	S _{CO₂}	S _{C₂H₄}	S _{CH₂O}	S _{C₂H₄O}	Y _{H₂}
0	1	0.866	0.130	0.003	0	0	0	5.199
22	1	0.339	0.111	0.550	0	0	0	3.650
44	1	0.492	0.266	0.242	0	0	0	2.661
67	1	0.267	0.176	0.557	0	0	0	3.411
88	1	0.469	0.237	0.294	0	0	0	3.069
109	1	0.406	0.166	0.429	0	0	0	3.924
154	1	0.211	0.038	0.751	0	0	0	4.720
200	1	0.471	0.247	0.282	0	0	0	2.921
244	1	0.441	0.233	0.326	0	0	0	3.049
265	1	0.283	0.012	0.705	0	0	0	2.268
287	1	0.254	0.153	0.593	0	0	0	3.737
309	1	0.391	0.117	0.492	0	0	0	3.946

Table A.5.10. Gas stream product composition of NiCe(0.10)@SBA-15 at 600 °C

Time (min)	%H ₂	%CO	%CH ₄	%CO ₂	%C ₂ H ₄	%CH ₂ O	%C ₂ H ₄ O
0	72.2	24.1	3.6	0.1	0	0	0
22	64.6	12.0	3.9	19.5	0	0	0
44	57.1	21.1	11.4	10.4	0	0	0
67	63.0	9.9	6.5	20.6	0	0	0
88	60.5	18.5	9.3	11.6	0	0	0
109	66.2	13.7	5.6	14.5	0	0	0
154	59.4	19.1	10.0	11.5	0	0	0
200	60.4	17.5	9.2	12.9	0	0	0
244	65.1	8.9	5.3	20.7	0	0	0
265	66.4	13.1	3.9	16.6	0	0	0
287	60.4	14.2	8.6	16.7	0	0	0
309	67.7	8.7	2.8	20.8	0	0	0

Table A.5.11. Reaction parameters of NiCe(0.50)@SBA-15 at 600 °C

Time (min)	X _{C₂H₅OH}	S _{CO}	S _{CH₄}	S _{CO₂}	S _{C₂H₄}	S _{CH₂O}	S _{C₂H₄O}	Y _{H₂}
0	100	0.617	0.189	0.194	0	0	0	2.791
19	100	0.583	0.202	0.195	0.020	0	0	3.169
60	97.442	0.430	0.250	0.280	0.025	0	0	2.563
100	98.197	0.434	0.210	0.304	0.038	0	0	2.785
120	96.889	0.268	0.093	0.599	0.016	0	0	3.709
142	97.770	0.460	0.127	0.371	0.027	0	0	3.501
161	95.284	0.243	0.075	0.672	0	0	0	4.008
185	96.345	0.327	0.115	0.476	0.039	0	0	3.665
201	96.367	0.399	0.120	0.420	0.04	0	0	3.447
222	94.396	0.360	0.103	0.475	0.038	0	0	3.563

Table A.5.12. Gas stream product composition of NiCe(0.50)@SBA-15 at 600 °C

Time (min)	%H ₂	%CO	%CH ₄	%CO ₂	%C ₂ H ₄	%CH ₂ O	%C ₂ H ₄ O
0	58.3	26.0	8.0	8.1	0	0	0
19	61.5	23.0	8.0	7.6	0.4	0	0
60	57.3	19.0	11.0	12.2	0.6	0	0
100	59.3	18.0	9.0	12.7	0.8	0	0
120	66.1	09.0	3.0	20.7	0.3	0	0
142	64.6	17.0	5.0	13.4	0.5	0	0
161	67.9	08.0	2.0	21.7	0	0	0
185	66.5	11.0	4.0	16.6	0.7	0	0
201	64.9	14.0	4.0	15.2	0.7	0	0
222	66.1	13.0	4.0	16.6	0.7	0	0

Table A.5.13. Reaction parameters of PdNiCe(0.50)@SBA-15 at 600 °C

Time (min)	X _{C₂H₅OH}	S _{CO}	S _{CH₄}	S _{CO₂}	S _{C₂H₄}	S _{CH₂O}	S _{C₂H₄O}	Y _{H₂}
1	1	0.546	0.247	0.206	0		0	2.610
20	1	0.437	0.200	0.363	0		0	3.228
40	1	0.167	0.095	0.738	0		0	3.863
60	1	0.486	0.288	0.226	0		0	2.476
80	1	0.460	0.257	0.282	0		0	2.921
100	1	0.446	0.235	0.319	0		0	3.110
120	1	0.445	0.260	0.295	0		0	2.889
140	1	0.193	0.061	0.746	0		0	4.422
160	1	0.401	0.158	0.441	0		0	3.809
180	1	0.399	0.147	0.454	0		0	3.816

Table A.5.14. Gas stream product composition of PdNiCe(0.50)@SBA-15 at 600 °C

Time (min)	%H₂	%CO	%CH₄	%CO₂	%C₂H₄	%CH₂O	%C₂H₄O
1	56.6	23.7	10.7	8.9	0	0	0
20	61.7	16.7	7.6	13.9	0	0	0
40	65.9	5.7	3.2	25.2	0	0	0
60	55.3	21.7	12.9	10.1	0	0	0
80	59.4	18.7	10.5	11.5	0	0	0
100	60.9	17,5	9.2	12.5	0	0	0
120	59.1	18.2	10.6	12.1	0	0	0
140	68.9	6.0	1.9	23.2	0	0	0
160	65.6	13.8	5.4	15.2	0	0	0
180	65.6	13.7	5.1	15.6	0	0	0

Table A.5.15. Reaction parameters of Ni@AIMCM-41 at 600 °C

Time (min)	X _{C₂H₅OH}	S _{CO}	S _{CH₄}	S _{CO₂}	S _{C₂H₄}	S _{CH₂O}	S _{C₂H₄O}	Y _{H₂}
0	1	-	-	-	-	-	-	-
21	1	0.375	0.099	0.455	0	0.071	0	5.794
42	1	0.442	0.093	0.424	0	0.041	0	5.749
62	1	0.351	0.135	0.480	0	0.034	0	5.078
84	1	0.345	0.109	0.515	0	0.031	0	4.630
107	1	0.339	0.144	0.482	0	0.035	0	4.299
129	1	0.370	0.156	0.445	0	0.029	0	4.917
151	1	0.380	0.148	0.443	0	0.030	0	4.908
172	1	0.378	0.123	0.473	0	0.026	0	4.278
235	1	0.304	0.085	0.587	0	0.024	0	4.172
257	1	0.380	0.161	0.438	0	0.021	0	4.340
279	1	0.258	0.062	0.660	0	0.020	0	3.945
301	1	0.303	0.101	0.583	0	0.012	0	3.597

Table A.5.16. Gas stream product composition of Ni@AIMCM-41 at 600 °C

Time (min)	%H ₂	%CO	%CH ₄	%CO ₂	%C ₂ H ₄	%CH ₂ O	%C ₂ H ₄ O
0	-	-	-	-	-	-	0
21	74.3	9.6	2.5	11.7	0	1.8	0
42	74.2	11.4	2.4	10.9	0	1.1	0
62	71.7	9.9	3.8	13.6	0	1.0	0
84	69.8	10.4	3.3	15.5	0	0.9	0
107	68.3	10.8	4.6	15.3	0	1.1	0
129	71.1	10.7	4.5	12.9	0	0.8	0
151	71.0	11.0	4.3	12.8	0	0.9	0
172	68.1	12.1	3.9	15.1	0	0.8	0
235	67.6	9.9	2.7	19.0	0	0.8	0
257	68.5	12.0	5.1	13.8	0	0.7	0
279	66.4	8.7	2.1	22.2	0	0.7	0
301	64.3	10.8	3.6	20.8	0	0.4	0

Table A.5.17. Reaction parameters of NiCe(0.10)@AIMCM-41 at 600 °C

Time (min)	X _{C₂H₅OH}	S _{CO}	S _{CH₄}	S _{CO₂}	S _{C₂H₄}	S _{CH₂O}	S _{C₂H₄O}	Y _{H₂}
0	1	0.434	0.370	0.197	0	0	0	0.730
20	1	0.462	0.176	0.362	0	0	0	4.614
40	1	0.423	0.133	0.445	0	0	0	5.973
103	1	0.359	0.168	0.473	0	0	0	4.027
125	1	0.313	0.106	0.557	0.024	0	0	4.671
146	1	0.314	0.127	0.378	0.181	0	00	3.896
171	1	0.265	0.054	0.624	0.058	0	0	4.393
194	1	0.246	0.075	0.485	0.194	0	0	3.886
216	1	0.274	0.108	0.302	0.299	0	0.017	3.018
236	1	0.217	0.058	0.480	0.224	0	0.020	3.442
256	1	0.224	0.056	0.465	0.230	0	0.024	3.546
275	1	0.243	0.060	0.448	0.229	0	0.021	3.491
295	1	0.220	0.061	0.384	0.307	0	0.027	2.993
315	1	0.226	0.049	0.469	0.233	0	0.023	3.526

Table A.5.18. Gas stream product composition of NiCe(0.10)@AIMCM-41 at 600 °C

Time (min)	%H ₂	%CO	%CH ₄	%CO ₂	%C ₂ H ₄	%CH ₂ O	%C ₂ H ₄ O
0	-	-	-	-	-	-	-
20	69.8	14.0	5.3	10.9	0	0	0
40	74.9	10.6	3.3	11.2	0	0	0
103	66.8	11.9	5.6	15.7	0	0	0
125	70.3	9.4	3.2	16.8	0.4	0	0
146	68.2	11.0	4.5	13.2	3.2	0	0
171	69.3	8.4	1.7	19.7	0.9	0	0
194	68.3	8.6	2.6	17.0	3.4	0	0
216	64.2	11.7	4.6	12.8	6.4	0	0.4
236	66.2	8.4	2.2	18.5	4.3	0	0.4
256	67.0	8.5	2.1	17.6	4.4	0	0.4
275	66.6	9.3	2.3	17.1	4.4	0	0.4
295	64.2	9.5	2.6	16.5	6.6	0	0.6
315	66.9	8.6	1.8	17.8	4.4	0	0.4

Table A.5.19. Reaction parameters of Ni@[Ce@AIMCM-41] at 600 °C

Time (min)	X _{C₂H₅OH}	S _{CO}	S _{CH₄}	S _{CO₂}	S _{C₂H₄}	S _{CH₂O}	S _{C₂H₄O}	Y _{H₂}
0	-	-	-	-	-	-	-	-
20	1	0.347	0.085	0.506	0	0.062	0	5.461
40	1	0.356	0.135	0.459	0	0.050	0	5.741
80	1	0.249	0.115	0.635	0	0	0	5.190
99	1	0.329	0.104	0.567	0	0	0	5.149
119	1	0.369	0.184	0.447	0	0	0	4.533
139	1	0.378	0.141	0.481	0	0	0	4.712
159	1	0.380	0.141	0.479	0	0	0	4.695
180	1	0.377	0.166	0.458	0	0	0	4.302
200	1	0.330	0.086	0.584	0	0	0	4.812
222	1	0.405	0.189	0.405	0	0	0	4.299
257	1	0.251	0.062	0.687	0	0	0	4.429
287	1	0.406	0.135	0.459	0	0	0	4.447
317	1	0.281	0.066	0.653	0	0	0	4.503
341	1	0.406	0.137	0.458	0	0	0	4.307

Table A.5.20. Gas stream product composition of Ni@[Ce@AIMCM-41] at 600 °C

Time(min)	%H ₂	%CO	%CH ₄	%CO ₂	%C ₂ H ₄	%CH ₂ O	%C ₂ H ₄ O
0	-	-	-	-	-	-	-
20	73.2	9.3	2.3	13.6	0	1.7	0
40	74.2	9.2	3.5	11.9	0	1.3	0
80	72.2	6.9	3.2	17.7	0	0	0
99	72.0	9.2	2.9	15.9	0	0	0
119	69.4	11.3	5.6	13.7	0	0	0
139	70.2	11.3	4.2	14.3	0	0	0
159	70.1	11.3	4.2	14.3	0	0	0
180	68.3	12.0	5.3	14.5	0	0	0
200	70.6	9.7	2.5	17.1	0	0	0
222	68.2	12.9	6.0	12.9	0	0	0
257	68.9	7.8	1.9	21.4	0	0	0
287	69.0	12.6	4.2	14.2	0	0	0
317	69.2	8.6	2.0	20.1	0	0	0
341	68.3	12.9	4.3	14.5	0	0	0

Table A.5.21. Reaction parameters of Ce@AIMCM-41

Time (min)	$X_{C_2H_5OH}$	S_{CO}	S_{CH_4}	S_{CO_2}	$S_{C_2H_4}$	S_{CH_2O}	$S_{C_2H_4O}$	Y_{H_2}
0	1	0.033	0.006	0.006	0.896	0.044	0	0.061
20	1	0.002	0.003	0.002	0.944	0.021	0	0.046
40	1	0	0.002	0	0.947	0.025	0	0.033
60	1	0	0.002	0	0.957	0.014	0	0.030
80	1	0	0.002	0	0.937	0.024	0	0.039
101	1	0.001	0.002	0	0.943	0.019	0	0.043
121	1	0.002	0.003	0	0.930	0.026	0	0.054
142	1	0	0.002	0	0.943	0.017	0	0.040
163	1	0	0.002	0	0.937	0.022	0	0.046
183	1	0	0.001	0	0.949	0.018	0	0.031

Table A.5.22. Gas stream product composition of Ce@AIMCM-41

Time(min)	%H ₂	%CO	%CH ₄	%CO ₂	%C ₂ H ₄	%CH ₂ O	%C ₂ H ₄ O
0	5.3	6.0	1.0	1.1	78.0	7.6	0
20	4.3	0	0.5	0.3	87.9	4.0	0
40	3.1	0	0.3	0	89.4	4.7	0
60	2.9	0	0.3	0	91.4	2.8	0
80	3.6	0	0.3	0	88.0	4.5	0
101	4.0	0	0.4	0	88.4	3.7	0
121	5.0	0	0.6	0	85.7	4.9	0
142	3.8	0	0.4	0	88.9	3.3	0
163	4.3	0	0.4	0	87.5	4.2	0
183	3.0	0	0.3	0	90.3	3.5	0

Table A.5.23. Reaction parameters of NiCe(0.50)@AIMCM-41

Time (min)	X _{C₂H₅OH}	S _{CO}	S _{CH₄}	S _{CO₂}	S _{C₂H₄}	S _{CH₂O}	S _{C₂H₄O}	Y _{H₂}
0	1	0.405	0.025	0.570	0	0	0	2.077
20	1	0.603	0.209	0.188	0	0	0	2.774
40	1	0.333	0.115	0.494	0.058	0	0	3.580
63	1	0.464	0.078	0.458	0	0	0	4.517
83	1	0.560	0.189	0.251	0	0	0	3.053
104	1	0.328	0.052	0.360	0.219	0	0	3.033
124	1	0.243	0.021	0.169	0.544	0	0	1.798
152	1	0.258	0.021	0.197	0.502	0	0	2.002
177	1	0.332	0.027	0.280	0.338	0	0	2.836
270	1	0.115	0.010	0.136	0.701	0	0	1.422
292	1	0.236	0.023	0.266	0.451	0	0	2.348
313	1	0.190	0.018	0.277	0.481	0	0	2.091
342	1	0.084	0.009	0.123	0.734	0	0	1.154
362	1	0.167	0.014	0.185	0.589	0	0	1.67

Table A.5.24. Gas stream product composition of NiCe(0.50)@AIMCM-41

Time(min)	%H ₂	%CO	%CH ₄	%CO ₂	%C ₂ H ₄	%CH ₂ O	%C ₂ H ₄ O
0	50.9	19.9	1.2	28.0	0	0	0
20	58.1	25.3	8.8	7.9	0	0	0
40	64.8	12.0	4.2	17.9	1.1	0	0
63	69.3	14.3	2.4	14.0	0	0	0
83	60.4	22.2	7.5	9.9	0	0	0
104	63.6	13.7	2.2	15.1	4.6	0	0
124	55.7	15.0	1.3	10.5	16.8	0	0
152	57.6	14.9	1.2	11.3	14.4	0	0
177	63.4	14.8	1.2	12.5	7.5	0	0
270	53.0	8.6	0.8	10.1	26.1	0	0
292	60.6	12.2	1.2	13.7	11.6	0	0
313	58.5	10.6	1.0	15.5	13.5	0	0
342	48.7	7.1	0.8	10.4	31.0	0	0
362	55.0	11.0	0.9	12.2	19.4	0	0

CURRICULUM VITAE

Name :CANAN SENER
Title :Research Assistant
Employer :Middle East Technical University (METU), Ankara, Turkey
Telephone :(90) 312 2104363
Fax :(90) 312 2102600
Mobile :(90) 533 5500501
E-mail :scanan@metu.edu.tr
Date of birth :24.08.1980

Education

- | | | |
|----------|---|------|
| 1. Ph.D. | METU, Chem. Eng. Department, Ankara (in | 2012 |
| 2. M.S. | METU, Chem. Eng. Department, Ankara | 2006 |
| 3. B.S. | Hacettepe University, Chem. Eng. Department, Ankara | 2002 |

Academic Positions/Titles

- | | | |
|-----------------------|--|-----------|
| 1. Research Assistant | METU, Chem. Eng. Department, Ankara | 2004- |
| 2. Visiting Scholar | Iowa State Univ, Dept. of Chem.&Bio Eng. | 2008-2009 |

Awards-Scholarships

- | | |
|--|-----------|
| 1. Turkish Scientific and Technical Research Council (TUBITAK) Scholarship | 2006-2008 |
| 2. Prof.Dr. Mustafa Parlar Foundation Best Thesis Award (MS) | 2006 |
| 3. METU Institute of Natural and Applied Sciences, Performance Award | 2007 |
| 4. TUBITAK Research Scholarship | 2008 |
| 5. Turkish State Planning Organization Scholarship | 2008 |
| 6. TUBITAK Research Scholarship | 2011- |

Research Interests:

Synthesis and characterization of nanostructured mesoporous catalysts; chemical reaction engineering; heterogeneous catalysis; steam reforming of ethanol, dry reforming of methane.

Projects:

1. TUBITAK and Bulgarian Academy of Sciences Joint Project "Novel Catalysts for Producing Hydrogen from Biomass Derivatives" (TUBITAK Project No. 105M373) 2006-2009.
2. TUBITAK Project "Developing Pd, Ni, Silicotungstic Acid Incorporated MCM-41 Type Mesoporous Nanocomposite Catalysts for Producing Hydrogen and Ethylene from Ethanol" (Project No. 106M073), 2006-2008.
3. Iowa State University and University of Wisconsin-Madison Joint Project (CBIRC Project) "Coupled Acid/Base Catalysts" 2008-2009.
4. TUBITAK Project "Sorption Enhanced Catalytic Reforming of Ethanol for High Hydrogen Yield and Development of Suitable Mesoporous Catalysts", 2011-2012.

Computer Skills:

Programming: FORTRAN, MATLAB, MATHCAD

Teaching Experience:

Served as a Teaching Assistant for the following courses at METU:

ChE 203 - Chemical Process Calculations

ChE 203 - Thermodynamics I

ChE 220 – Principles of Transport Phenomena

ChE 222 - Fluid Mechanics

ChE 320 - Chemical Engineering Laboratory I

ChE 327 - Heat and Mass Transfer Operations

ChE 328 - Separation Processes

ChE 410 - Chemical Engineering Laboratory II

ChE 420 - Chemical Engineering Laboratory III

ChE 423 - Chemical Engineering Economics

ChE 426 - Reactor Design

ChE 510 - Advanced Chemical Reaction Engineering

Equipment Skills:

Physisorption (Quantachrome 1C, Micromeritics ASAP 2020)

Chemisorption (Micromeritics Chemisorb 2750)

TGA (Perkin Elmer TGA7)

PUBLICATIONS

THESIS

1. MSc Thesis: "Synthesis and Characterization of Pd-MCM-Type Mesoporous Nanocomposite Materials", Middle East Technical University, Ankara, 2006.
2. PhD Thesis: "Novel Bimetallic Mesoporous Catalysts for Hydrogen Production Through Steam Reforming of Ethanol", Middle East Technical University, Ankara, 2012.

ARTICLES PUBLISHED IN INTERNATIONAL JOURNALS

1. C. Sener, T. Dogu, G. Dogu, "Effects of Synthesis Conditions on the Structure of Pd Incorporated MCM-41 Type Mesoporous Nanocomposite Catalytic Materials with High Pd/Si Ratios", Microporous Mesoporous Materials, 94, 89-98 (2006).
2. Sener, C., Dogu, T., Dogu, G. "Direct hydrothermal synthesis of palladium-incorporated silicate-structured mesoporous catalysts", Turkish Journal of Chemistry, 31, 473-478 (2007).
3. Sener C., Arishtirova K., Nikolov R.N., Dogu T., Dogu G., Damyanova S., "MCM-41 Supported Ni Catalysts for Dry Reforming of Methane", Advanced Micro- and Mesoporous Materials, Heron Press, Sofia, 355-362 (2008).
4. Damyanova S., Pawelec B., Arishtirova K., Fierro J.L.G., Sener C., Dogu T., "MCM-41 supported PdNi catalysts for dry reforming of methane", Applied Catalysis B: Environmental, in press (2009).

5. Sener C., Dogu T., Dogu G., Arishtirova K., Damyanova S., "Hydrogen production by steam reforming of ethanol over Pd-Ni incorporated bimetallic MCM-41-like mesoporous catalysts", to be submitted.

INTERNATIONAL SYMPOSIUM PRESENTATIONS/PUBLICATIONS

1. Sener, C., Dogu, T., Dogu, G. "Novel Pd-MCM-41 Nanocomposite Materials for Hydrogen Storage Applications", Int. Hydrogen Energy Congress, Istanbul, proceedings 15, July (2005).
2. Sener, C., Dogu, T., Dogu, G., "Synthesis and Characterization of Pd-MCM-41 Type Mesoporous Nanocomposite Catalytic Materials", Int. Symp. Catalytic Processes on Advanced Micro-, Mesoporous Materials, proceedings 143, Bulgaria, Sept. (2005).
3. Dogu, T., Gucbilmez, Y., Sener, C., Nalbant, A., Balci, S., Dogu, G., "Metal and Metal Oxide Incorporated MCM-41 Type Mesoporous Materials and their Catalytic Applications", EMCC-4 East Mediterranean Chem. En. Conf., Proceedings 378, Israel, January (2006).
4. Dogu, T., Gucbilmez, Y., Sener, C., Balci, S., Dogu, G., "V, Mo and Pd Incorporated MCM-41 Catalysts for Selective Oxidation and Reforming of Ethanol", 1. European Chemistry Congress, proceedings 43, Budapest, August (2006).
5. Sener, C., Dogu, T., Dogu, G., "Mesoporous Pd-Si Nanocomposite Sponge Catalysts by Direct Acidic Hydrothermal Synthesis Route", IMMS2006 5th International Mesostructured Materials Symp., Proceedings p. 228-229, Shanghai, China, (2006).
6. Varisli D., Sener C., Ozdogan E., Dogu T., "Novel Mesoporous Nanocomposite Catalysts for Reforming and Dehydrogenation Reactions", SOMER Symposium 1, Proceedings 82, Ankara, Turkey (2007).
7. Sener C., Arishtirova K., Nikolov R.N., Dogu T., Dogu G., Damyanova S., "MCM-41 Supported Ni Catalysts for Dry Reforming of Methane", Micro 2007, Varna, Bulgaria (2008).

8. Sener C., Dogu T., Dogu G., Arishtirova K., Damyanova S., "Steam Reforming of Ethanol and Dry Reforming of Methane on Ni@MCM-41 and Pd-Ni@MCM-41 Catalysts", 6th EFCATS Summer School, Izmir, Turkey (2010).
9. Sener C., Dogu T., Dogu G., "Novel Mesoporous Catalysts for Hydrogen Production by Steam Reforming of Ethanol", 7th Chemical Engineering Conference for Collaborative Research in Eastern Mediterranean Countries – EMCC7, Corfu, Greece (2012).

NATIONAL SYMPOSIUM PRESENTATIONS/PUBLICATIONS

1. Şener, C., Dogu, T., Dogu, G., "Pd-MCM-41 Mesoporous Composite Nanostructures and Pd Nanoballs in MCM-41 Hosts", NANOTR-1 Nanoscience and Nanotechnology, Ankara (2005).
2. Dogu, T., Şener, C., Gucbilmez, Y., Dogu, G., Balci, S., "Characterization and Application Areas of Activated MCM-41 Type Mesoporous Nanocomposite Catalytic Materials", GAP V. Engineering Symposium, p. 253-255 Urfa (2006) (in Turkish)
3. Sener C., Dogu T., Dogu G., "Palladium Incorporated Silicate Structured Mesoporous Catalysts for Ethanol Reforming", 1. National Catalysis Congress, Northern Cyprus (2007).
4. Sener Marti C., Arishtirova K., Nikolov R.N., Dogu T., Dogu G., Damyanova S., "Dry Reforming of Methane Over Pd-Ni-MCM-41 Dual Catalysis", 2. National Catalysis Congress, Erzurum (2008).
5. Sener Marti C., Arishtirova K., Dogu T., Dogu G., Damyanova S., "Synthesis and Characterization of Pd and Ni Incorporated Mesoporous Catalysts for Hydrogen Production by Ethanol-Steam and Methane-Carbon Dioxide Reforming Reactions", National Chemical Engineering Congress, Malatya (2008).
6. Sener C., Dogu T., Dogu G., "Ni Incorporated Ceria Catalysts by Different Routes for Hydrogen Production by Steam Reforming of Ethanol", 4th National Catalysis Conference – NCC-4, Kocaeli (2012).

ATTENDED SCHOOLS:

1. IMMS2006 5th International Mesostructured Materials Symposium Pre-School “The Fundamental Practices on Mesostructured Materials”, Shanghai, China (2006)
2. First Anatolian School of Catalysis, ASC-1, Ankara, Turkey (2006).
3. 6th EFCATS Summer School “Catalysis&Surface Science for Renewables & Energy”, Izmir, Turkey (2008).